ISSN 2408-2384 (ONLINE)

Environment and Natural Resources Journal

Volume 24 Number 1 January - February 2026

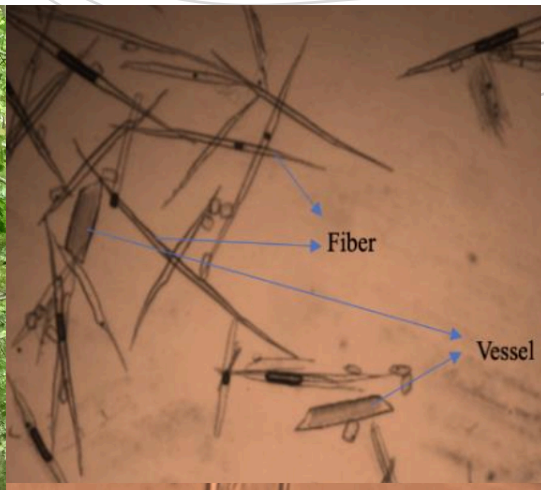

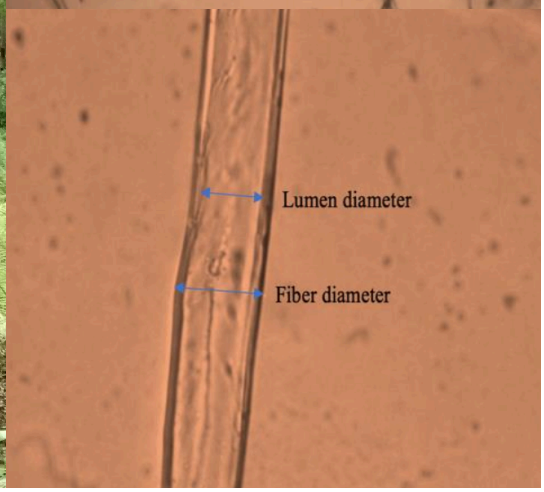

Clones of rubber wood (*Hevea brasiliensis*) in Naga, Zamboanga Sibugay, Philippines. The assessment of their anatomical, physical, and mechanical properties demonstrates their potential as raw materials for the Philippine timber industry and local utilization.

Source: Marasigan OS, Alipon MA. Assessment of wood properties of Hevea brasiliensis clones grown in Zamboanga Sibugay Philippines for their potential applications. Environ. Nat. Resour. J. 2026;24(1):58-76.

Environment and Natural Resources Journal (EnNRJ)
Volume 24, Number 1, January -February 2026 ISSN: 2408-2384 (Online)

FOCUS AND SCOPE

Environment and Natural Resources Journal (EnNRJ) is a peer-reviewed journal which provides a platform for exchanging and distributing knowledge and cutting-edge research in environmental science and natural resource management to academicians, scientists, and researchers.

The scope of the journal covers the integration of multidisciplinary sciences for prevention, control, treatment, environmental clean-up, and restoration. The study of existing or emerging problems related to the environment and natural resources in Southeast Asia and the development of innovative knowledge and/or creative recommendations for mitigation measures and sustainable development are emphasized. The subject areas are diverse, but specific topics of interest include:

- Biodiversity
- Climate change
- Detection and monitoring of pollutants and their sources (e.g., agriculture, industry, mining, urban activities, accidents)
- Disaster (e.g., forest fires, flooding, earthquakes, tsunamis or tidal waves)
- Ecological/Environmental modelling
- Emerging contaminants/hazardous wastes investigations and remediation
- Environmental dynamics (e.g., coastal erosion, rising sea levels)
- Environmental assessment tools, policy, and management [e.g., GIS, remote sensing, and Environmental Management Systems (EMS)]
- Pollution control and innovative solutions for pollution reduction
- Remediation technology in contaminated environments
- Transboundary pollution
- Waste and wastewater treatments and disposal technology

Schedule
Environment and Natural Resources Journal (EnNRJ) is published 6 issues per year in January-February, March-April, May-June, July-August, September-October, and November-December.

Publication Fees
An article publication fee in the Environment and Natural Resources Journal is set at a rate of 250 USD per article, payable after the final acceptance of the manuscript.

Ethics in publishing
EnNRJ follows closely a set of guidelines and recommendations published by Committee on Publication Ethics (COPE).

Environment and Natural Resources Journal (EnNRJ)
Volume 24, Number 1, January -February 2026 ISSN: 2408-2384 (Online)

Editorial Office Address
Research and Academic Service, Research Management Unit,
Faculty of Environment and Resource Studies, Mahidol University
999, Phutthamonthon Sai 4 Road, Salaya, Phutthamonthon, Nakhon Pathom, Thailand, 73170
Phone +662 441 5000 ext. 2108
Website: https://ph02.tci-thaijo.org/index.php/ennrj/index
E-mail: ennrjournal@gmail.com

Environment and Natural Resources Journal (EnNRJ)

Volume 24, Number 1, January -February 2026 ISSN: 2408-2384 (Online)

CONTENT

Environment and Natural Resources Journal

Volume 24
Issue 1
2026

Enzymatic Processing of Grouper Bone Waste as Fish Protein Hydrolysate Potential Bioactive Peptides

Nuniek Herdyastuti[1*], Rudiana Agustini[1], Tukiran[1], Titik Taufikurohmah[1], Intan Fatma Listiandari[1], Nur Indah Syamsiati[1], Mohammad Dhimas Adiputra[1], Ireniza Liano[1], and Tan Wen Nee[2]

[1]Department of Chemistry, Faculty of Mathematics and Natural Sciences, Universitas Negeri Surabaya. Jl. Ketintang Surabaya 60231, East Java, Indonesia
[2]Chemistry Section, School of Distance Education, Universiti Sains Malaysia, 11800 Penang, Malaysia

ARTICLE INFO

Received: 11 Jan 2025
Received in revised: 13 Jun 2025
Accepted: 8 Aug 2025
Published online: 13 Nov 2025
DOI: 10.32526/ennrj/24/20250016

Keywords:
Fish protein hydrolysate/ Grouper/ Protease enzyme/ Bioactive peptide

*** Corresponding author:**
E-mail:
nuniekherdyastuti@unesa.ac.id

ABSTRACT

Grouper fish is a type of reef fish that has high economic value and is widely used as fillets in the industry. It is estimated that 50% of the total fish catch is not used as food. Fish solid waste has been utilized as a source of protein and essential amino acids with high nutritional value over the last decade. Enzymatic hydrolysis is the most recommended method to produce fish protein hydrolysates. Enzymatic hydrolysis with various enzymes and hydrolysis time can determine the characteristics of the hydrolysate obtained. The results of hydrolysis of fish bone powder using variations of Papain, Bromelain, and alcalase enzymes, along with time variations of 30-300 minutes, showed the highest yield with papain enzymes at a hydrolysis time of 240 minutes. The degree of hydrolysis above 88% was achieved at an incubation time of 120 minutes with papain enzyme and alkalase and 3 hours with bromelain enzyme. The proximate content of protein hydrolysates from fish bones showed a moisture content of between 7% and 15%, an ash content below 0.5%, and a protein content of 0.46%. The results of protein hydrolysis molecular weight analysis using SDS-PAGE revealed that each enzyme yielded peptides at sizes of 5 and 3.4 kDa, which are expected to have potential as bioactive peptides.

HIGHLIGHTS

This study highlights the potential of grouper bone waste as a source of bioactive peptides through enzymatic hydrolysis.

1. INTRODUCTION

Indonesia is a major producer of reef fish that is traded as food, including grouper. According to FAO data, before 2016, Indonesia contributed 26.5% of the world's grouper catch. Groupers are caught for export and local consumption and are marketed alive and dead in fresh or frozen form (Amiin et al., 2023; Efendi et al., 2021; Khasanah et al., 2020; Petrova et al., 2018). The grouper fish is a significant export commodity to several countries, including Hong Kong, Japan, Singapore, and China (Mo et al., 2018; Nurhayati et al., 2014; Rumondang et al., 2023; Tirtadanu et al., 2023). In the industry, grouper fish is mainly utilized as fillets, taking only the meat, which results in the rest being discarded as fish waste, around 45-65%. The fish waste is not suitable for consumption or use as food and has not been widely utilized despite its high protein content. Fish waste produced includes muscle components (15-20%), skin and fins (1-3%), bones (9-15%), head (9-12%), viscera (12-18%), and scales around 5% (Coppola et al., 2021; Kumar et al., 2018; Martínez-Alvarez et al., 2015; Palla et al., 2022). Fish waste is typically not marketed due to low consumer acceptance or sanitary regulations that restrict its use, so it is primarily used for ensilage, fertilizer production, or disposal (Ishak

Citation: Herdyastuti N, Agustini R, Tukiran, Taufikurohmah T, Listiandari IF, Syamsiati NI, Adiputra MD, Liano I, Nee TW. Enzymatic processing of grouper bone waste as fish protein hydrolysate potential bioactive peptides. Environ. Nat. Resour. J. 2026;24(1):1-9. (https://doi.org/10.32526/ennrj/24/20250016)

and Sarbon, 2018). In China, fish and shrimp waste are currently used in conjunction with trash fish, anchovies, and lantern fish (*Benthosema pterotum*) to produce fishmeal (Mo et al., 2018; Raeesi et al., 2023). However, the utilization of fish waste for the production of fishmeal, fertilizer, and fish oil still yields a low level of profit. It can cause environmental pollution, which has a negative impact on society (Nguyen et al., 2022).

Over the last decade, solid waste from fish has gained attention from researchers by potentially utilizing fish by-products as a source of essential amino acids, collagen, gelatin, anti-inflammatory, blood pressure lowering, antidiabetic, antihypertensive, antimicrobial, and enzymes (Ahn et al., 2015; Gao et al., 2021; Henriques et al., 2021; Ishak and Sarbon, 2018; Korkmaz and Tokur, 2022; Zhang and Huang, 2019). Currently, research interest in fish waste is focused on the production of protein hydrolysates that are treated chemically, physically, enzymatically, or in combination. This is because it is more cost-effective and offers solutions that reduce environmental problems (Harnedy and FitzGerald, 2012; Korkmaz and Tokur, 2022). Enzymatic treatment of fish waste has been widely practiced to obtain fish protein hydrolysates (FPH) (Annisa et al., 2017; Araujo et al., 2021; Honrado et al., 2024; Nguyen et al., 2022). Enzymatic hydrolysis is the most recommended method for FPH production in the pharmaceutical and food industries because this method does not leave residual organic solvents or chemical compounds in the resulting product, is more efficient, inexpensive, produces fish protein hydrolysates without loss of essential amino acids, and avoids non-hydrolytic product changes or damage (Siddik et al., 2021; Zhang et al., 2020). Proteolytic enzymes that are endopeptidases break peptide bonds within protein molecules, while exopeptidases hydrolyze peptide bonds from the N or C terminus (Bernadeta et al., 2012; Clemente, 2000). Enzymatic hydrolysis with protease enzymes such as trypsin, chymotrypsin, flavourzyme, alcalase, ficin, papain, and bromelain on fish proteins can produce peptides and amino acids with different molecular weights depending on the degree of enzyme hydrolysis (Gao et al., 2021; Korkmaz and Tokur, 2022; Raksakulthai and Haard, 2003; Udenigwe and Aluko, 2012). Several studies have been conducted to obtain protein hydrolysate from tilapia (*Oreochromis niloticus*) using a combination of bromelain and pepsin enzymes, yielding 12.68% with a degree of hydrolysis of 61.46% (Nasution and Nasution, 2024). Chemical and enzymatic hydrolysis of tuna fish skin, scales, and bones yield 2.6-16.7% of dry matter (Ahmed et al., 2019). The results of research from Kaveh et al. 2024 showed that hydrolysis using alcalase and pancreatin on skipjack fish (*Katsuwonus pelamis*) with a hydrolysis time of 146.9 and 171.67 minutes and enzyme concentrations of 1.94 and 2.17% obtained a degree of hydrolysis of 25.12% and 20.35%, respectively.

2. METHODOLOGY

2.1 Grouper bone pretreatment

Grouper bones obtained from fish collectors in the Sidoarjo area of East Java, Indonesia, were stored at -20°C until needed. The steps taken to obtain fish bone powder involve separating the meat from the bones by boiling. The clean bones are then dried in an oven at 60°C for 24 h. After drying, the bones are ground into powder using a homogenizer.

2.2 Enzymatic production of fish protein hydrolysate (FPH)

Hydrolysis of fish bones was carried out enzymatically using three commercially available protease enzymes: papain, bromelain, and alcalase, according to the method modification by Pires et al. (2024). In an Erlenmeyer flask, 1 g of fish bone powder was added to the enzyme papain, bromelain, or alkaline phosphatase with an activity of 0.7 U. Then, phosphate buffer (pH 7) was added to a volume of 8 mL. The Erlenmeyer flask was closed using aluminum foil and incubated for 3 h at room temperature. Incubation was continued at 40°C with time variations of 30, 60, 120, 180, 240, and 300 min, followed by an additional incubation at 90°C for 5 min. The results of the incubation were filtered, and the filtrate was collected and then dried at 70°C for 24 h to obtain powder FPH.

2.3 Analysis of protein

Protein content was determined using the Bradford method (Walker, 2002). A total of 0.5 mL protein sample was added to 2.5 mL of biuret reagent and vortexed. The solution was incubated at room temperature (25°C) for 10 min. The solution was added 0.25 mL of Folin-Ciocalteu and vortexed again. The solution was incubated at room temperature for 20 min and then measured the absorbance with a UV-Vis Spectrophotometer (Shimadzu-1800) at a wavelength of 595 nm.

2.4 Degree of hydrolysis (DH)

Determination of the DH of FPH was carried out by measuring the soluble protein content of liquid FPH treated with the addition of trichloroacetic acid (TCA) and without the addition of TCA. This method is a modification of the total nitrogen method (Hoyle and Merritt, 1994). The TCA addition treatment was carried out by adding FPH dissolved in distilled water and 6.25% (v/v) TCA in a ratio of 3:2. The mixture was allowed to stand at room temperature for 15 min and then centrifuged at 8,000 × g for 15 min. The supernatant formed was measured for soluble protein by the Bradford method and compared with the protein content without TCA addition treatment. DH value was measured with the equation:

$$\text{DH (\%)} = \frac{\text{TCA}-\text{Soluble N in sample}}{\text{total N in Sample}}$$

2.5 Determination of molecular weight

Molecular weight determination was performed using electrophoresis (Biorad mini protean II) with the Laemmli Method. The initial step of electrophoresis is the preparation of a separating gel with a concentration of 12% made from the following components: 3.35 mL of distilled water, 2.5 mL of Tris-Cl (pH 8.8), 100 µL of SDS (10%), 4 mL of polyacrylamide (30%), 100 µL of ammonium persulfate (10%), and 5 µL of TEMED. Furthermore, a 4% concentration stacking gel was made with a composition of 1.525 mL aquabidesh; 650 µL Tris-Cl pH 6.8; 25 µL SDS 10%; 333.5 µL polyacrylamide 30%; 25 µL ammonium persulfate 10% and 5 µL TEMED. Samples with a volume of 20 µL were added 10 µL of 5x sample buffer (Tris-Cl, 60 mM, pH 6.8; glycerol, 25%; SDS, 2%; 2-mercaptoethanol, 14.4 mM; and bromophenol blue, 0.1%). The denatured mixture was loaded into wells on the stacking gel and placed in a tank containing running buffer at pH 8.3 (Tris-base, glycine, and SDS). Electrophoresis was carried out at a voltage of 150 volts for 50 min. After electrophoresis is complete, the gel is stained with Coomassie blue or silver nitrate.

3. RESULTS AND DISCUSSION

3.1 Preparation of gouper bone powder

In the fish processing industry, demersal fish, such as grouper, are typically processed into fish fillets, which generate a considerable amount of by-products, including heads, scales, bones, skeletons, skin, fins, and viscera. These by-products can reach 45-65% of the total fish weight (Ishak and Sarbon, 2018; Palla et al., 2022). Bone and skeletal by-products, as well as other materials, have the potential to be utilized for FPH production. The FPH consists of relatively short peptides (2-20 amino acids) that can be produced by breaking proteins into peptides either by chemical or enzymatic hydrolysis (Patil et al., 2020). The dried bones were made into coarse powder, as shown in Figure 1(c), and produced as much as 25.3% of the initial grouper bone sample (Figure 1(b)). Bone generally has a lower moisture content compared to skin (Binsi et al., 2009).

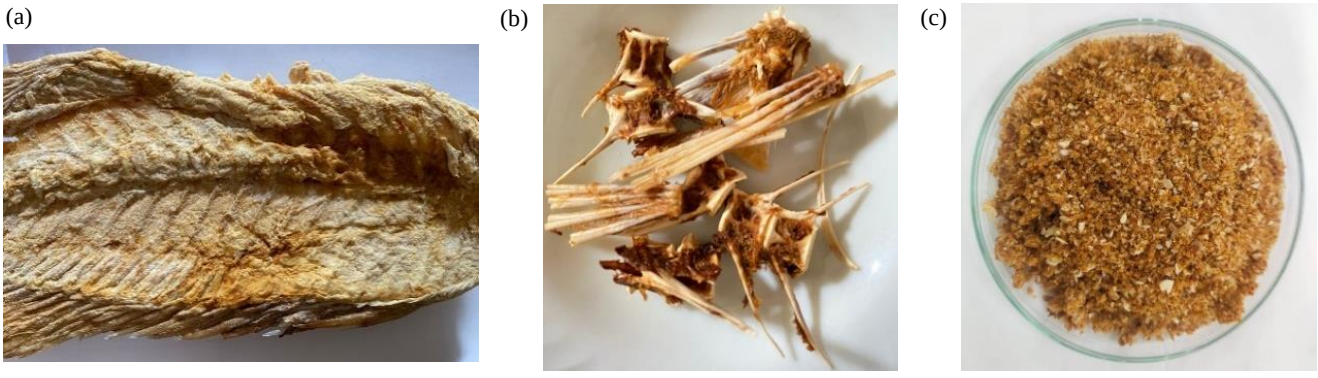

Figure 1. Grouper fish waste in the form of bones (a), boiled bones (b), and bones that have been made into powder (c)

Protein content ranges from 13 to 15 g/100 g based on wet weight, with grouper having higher protein than red snapper (Shakila et al., 2012). The high protein content is an advantage of fish waste that can be utilized in high-value products. With the rapid development of marine fisheries, grouper production is increasing year by year, producing by-products rich in protein, lipids, and minerals. It is a good source for the development of natural active ingredients (Liu et al., 2024). Fish bones, as a by-product, are considered waste and have low economic value. With special treatment, fish bone is a good source of protein and

bio-calcium, which can be leveraged to enhance its potential in food products (Dong et al., 2021). The utilization of fish bones as FPH is one of the alternatives that can be done as a promising solution to overcome the challenge of turning by-products into high-value products. This aligns with SDG 12, which aims to halve waste (Sapatinha et al., 2025). Grouper fish in addition to having a high selling value has been reported to have antiproliferative benefits from giant grouper (*Epinephelus lanceolatus*) egg hydrolysate against oral cancer cells (Yang et al., 2016); grouper bone hydrolysate (GBH) as a potential candidate for applications in health promotion and sports performance enhancement (Kao et al., 2024); enzymatic hydrolysis of fish waste can be used as a viable solution to obtain high value-added products such as collagen (Araujo et al., 2021).

3.2 Enzyme hydrolysis of fish bone grouper with different protease

Fishbone powder was hydrolyzed using three different types of protease enzymes, namely Bromelin, Papain, and Alcalase, with a variation of hydrolysis time of 30-300 min. Based on the results (Table 1), it is evident that the mass of hydrolyzate is proportional to the yield obtained, which increases with different hydrolysis times. In hydrolysis with papain and alcalase enzymes, the highest yield was obtained in 240 min, while the bromelain enzyme gave the highest yield in 30 min. The results of the one-way ANOVA test analysis showed a probability of $p<0.05$, indicating a significant difference in hydrolysis time and the resulting hydrolysate yield. The results of Duncan's further test showed that at an interval of 30 and 240 min, there was a significant difference in the yield of hydrolyzate produced.

Table 1. Effect of enzyme and time variation on the yield produced

Hydrolysis time (minutes)	Papain		Bromelain		Alcalase	
	Hydrolyzate mass (g)	Percent Yield (%)	Hydrolyzate mass (g)	Percent Yield (%)	Hydrolyzate mass (g)	Percent Yield (%)
30	0.914	18.28^{b}	1.978	39.56^{e}	1.675	33.50^{b}
60	0.980	19.60^{c}	0.886	17.72^{d}	1.713	34.26^{c}
120	0.867	17.34^{a}	0.846	16.92^{c}	1.480	29.60^{a}
180	1.061	21.22^{d}	0.842	16.84^{c}	1.488	29.76^{a}
240	2.007	40.14^{e}	0.646	12.92^{b}	1.794	35.88^{d}
300	0.908	18.16^{b}	0.587	11.74^{a}	1.710	34.20^{c}

Numbers followed by the same letter in the same column indicate no significant difference in the 0.05 Duncan test.

Protease enzymes have specific abilities on the cutting side of proteins, allowing for the production of different peptides with varying molecular weights, depending on the level of hydrolysis achieved with the enzyme used (Nguyen et al., 2022). Proteolytic enzymes are classified as endo and exopeptidases. Endopeptidases hydrolyze peptide bonds at specific residues and produce large peptides. The enzyme bromelain hydrolyzes proteins containing peptide bonds into simpler amino acids. In this case, cysteine endopeptidase specifically cuts peptide bonds on carbonyl groups, such as those found in arginine or aromatic amino acids, namely phenylalanine or tyrosine (Masri, 2013). Alcalase enzymes are endopeptidase proteases that belong to the serine protease group, which cleave the internal bonds of peptide chains that contain active sites with phenylalanine, tyrosine, and leucine (Jaziri et al., 2017). Meanwhile, the papain enzyme, which has a sulfhydryl functional group, is capable of hydrolyzing peptide bonds in lysine and glycine amino acids (Nilna et al., 2021).

The results of proximate analysis of protein hydrolysates from each hydrolysis of bromelain, papain, and alcalase enzymes (Table 2). Data on ash content and water content for each enzyme showed significant differences, whereas the protein content yielded nearly identical results. The protein yield in the hydrolysate obtained is minimal compared to several other studies, which is likely due to the suboptimal amount of enzyme used. Haslaniza et al. (2013) stated that the increasing concentration of proteolytic enzymes in the hydrolysis process will cause an increase in soluble nitrogen content in fish protein hydrolysate.

The results of research by Kristinsson and Rasco (2000) showed that FPH from Salmon fish muscle, using alcalase enzymes, obtained 88.39% protein, 0.92% water content, and 8.96% ash content. Another study reported that the results of chemical

hydrolysis of grouper skin waste aimed at obtaining gelatin showed an ash content of 1.32%, a protein content of 79.9691%, and a water content of 4.61% (Azara, 2017). The protein contained in this hydrolysate product is soluble, whereas the undissolved protein is wasted during the separation process. During hydrolysis, insoluble proteins are converted into soluble nitrogen compounds, which then break down into simpler compounds, such as peptides, amino acids, and ammonia. The protein content of catfish protein hydrolysate increased due to an increase in the concentration of enzymes used, resulting in a corresponding increase in soluble nitrogen content (Baehaki et al., 2015).

Table 2. Proximate analysis of fish bone protein hydrolysate

Hydrolysis results with enzyme	Ash content (%)	Moisture content (%)	Protein content (%)
Alcalase	0.295[a]	7.10[a]	0.425[a]
Papain	0.445[b]	15.20[c]	0.430[a]
Bromelain	0.285[a]	9.50[b]	0.460[a]

Numbers followed by the same letter in the same column indicate no significant difference in the 0.05 Duncan test

3.3 Degree of hydrolysis

The degree of hydrolysis (DH) is the level of protein breakdown into short-chain compounds, as measured by the ratio of α-amino nitrogen to total nitrogen (AN/TN), so the higher the level of protein breakdown into short-chain compounds, including α-amino nitrogen compounds, causes the higher the degree of hydrolysis. Conversely, the lower the rate of protein breakdown into short-chain compounds, the lower the degree of hydrolysis (Jaziri et al., 2017). Figure 2 shows that the best results with DH and papain enzyme were obtained at 180 min, while those with bromelain enzyme and alcalase were achieved at 120 min of hydrolysis time. The results of statistical test analysis, with $p<0.05$, showed a significant difference in hydrolysis time for DH with all enzymes. During the hydrolysis process with papain, bromelain, and alcalase enzymes, these enzymes cleave the peptide bonds in the initial protein into smaller protein molecules and peptides with increased solubility (Tacias-Pascacio et al., 2020). Hydrolytic enzymes break peptide bonds of protein substrates through their active sites, which can initiate catalysis through covalent interactions with protein substrates (Nothling et al., 2019).

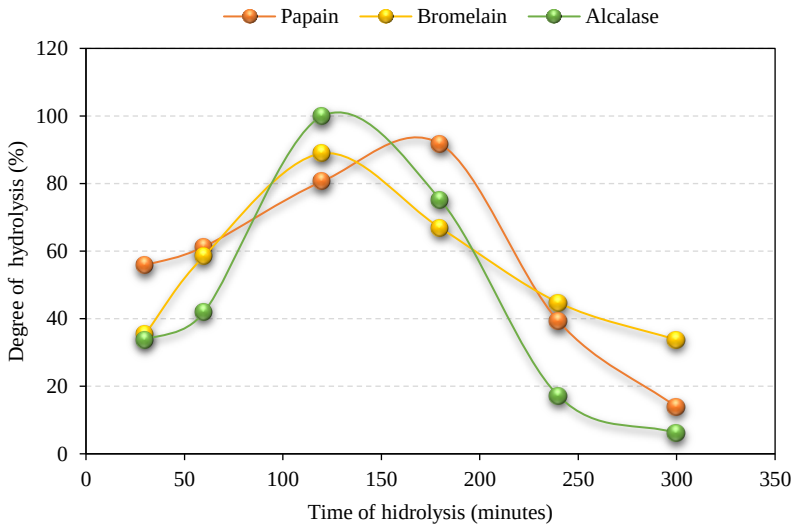

Figure 2. Effect of hydrolysis time with papain, bromelain, and alkalize enzymes on Hydrolysis Degree

The extent of proteolysis is quantified as DH, which refers to the percentage of peptide bonds broken down (Wang et al., 2007). The method used to evaluate the degree of hydrolysis of peptide bonds is based on the amount of nitrogen released by protein hydrolysis in the presence of precipitating agents, such as trichloroacetic acid (TCA) (Haslaniza et al., 2013). The degree of hydrolysis is the percentage (%) of free

amino groups released during the hydrolysis process to the total nitrogen contained in the substrate (Restiani, 2017). The degree of hydrolysis (DH) of protein is determined by several factors, including the type of protease used, enzyme concentration, temperature, pH, and hydrolysis time (Haslaniza et al., 2013; Liaset et al., 2000). Therefore, it is crucial to optimize certain factors to achieve the optimal DH. Enzymes exhibit different of DH when the same feedstock is used, which can be explained by the affinity of the enzyme for the substrate. Enzymes are highly efficient catalysts because they bind substrates (and cofactors) in the active site of a peptide bond that is stereospecifically oriented to the proximity of the group performing the catalytic reaction, forming an enzyme-substrate complex. A study conducted by Silva et al. (2014) using Alcalase showed a 15.5% of DH in fish bones. Hydrolysis of catfish protein with 0.04% bromelain enzyme and incubation time of 2.8 hours resulted in DH, pH, and antioxidant activity of 35.88, 7.07, and 29.86%, respectively, at optimum conditions (Nurdiani et al., 2024). Production of fish protein hydrolysate from chef carp (*Hypophthalmichthys nobilis*) using ficin enzyme at optimum conditions showed that hydrolysate yield increased with increasing DH, and the highest yield was obtained at DH 20.15% (Alahmad et al., 2022). Production of protein hydrolysate from Giant mudskippers using alkaline enzyme at optimum conditions, with a hydrolysis time of 2 hours, resulting in a hydrolysis degree of 67.44% (Edison et al., 2020). Zavareze et al. (2009) used chopped Bluewing searobin (*Prionotus punctatus*) to achieve a 25.41% of DH with Alcalase. Research by Gajanan et al. (2016) showed that the ability of papain to hydrolyze protein from curry fish bone waste was higher than that of bromelain, as indicated by the DH value (Gajanan et al., 2016). Restiani (2017) stated that the time of bromelain hydrolysis of protein hydrolysates influenced the degree of hydrolysis, where 240 minutes yielded the highest DH. The increase in hydrolysis speed at the beginning of the reaction is likely due to the rapid cleavage of peptide bonds, which reaches its maximum speed. The activity of cutting peptide bonds by the bromelain enzyme begins to decrease as the available substrate decreases. The soluble peptides or free amino acids produced from the hydrolysis process can cause inhibition of the active side of the enzyme so that the enzyme is unable to carry out the activity of cutting peptide bonds, causing the hydrolysis rate to reach a stationary phase (Zavareze et al., 2009; Dong et al., 2008; Gajanan et al., 2016; Restiani, 2017; Silva et al., 2014). Some studies report that increasing temperature can improve hydrolysis efficiency by resulting in greater release of amino acids or peptides. This phenomenon could be attributed to the higher ionization constant of water (Pires et al., 2024).

3.4 Protein pattern FPH based on molecular weight by SDS-PAGE

The results of the protein cutting pattern based on molecular weight using SDS-PAGE on each enzyme based on the best degree of hydrolysis, as shown in Figure 3. The results of hydrolysis with the three enzymes showed an almost identical pattern, where peptides were obtained at sizes ranging from around 30 to 10 kDa. Papain and alcalase enzymes were able to show hydrolyzed peptides at 5 and 3.4 kDa. The use of different enzymes can significantly impact the molecular weight (MW) of the peptides and the resulting amino acid sequence. In general, increasing the hydrolysis time can increase the degree of hydrolysis (DH), thereby reducing the molecular weight (MW) of the peptide, which can enhance its biopeptide activity. For example, biopeptides with high antioxidant activity are peptides of lower molecular weight (<3,000 Da), as it is easier for them to donate electrons or hydrogen atoms and react with free radicals to form more stable compounds (Honrado et al., 2024). Some studies have shown a relationship between the molecular weight (MW) size of peptides and their biological activity. The active peptide obtained has ACE (Angiotensin-I Converting Enzyme) activity with a size of less than 1,000 Da (Ngo et al., 2014). FPH from Blue Whiting (*Micromesistius poutassou*) fish waste with lower Mw resulted in outstanding production yield (12% w/b substrate), most excellent protein content (77% w/b), most excellent in vitro digestibility (>95%), highest presence of essential amino acids (43%), best antioxidant (DPPH=62%) and antihypertensive properties (IC_{50}-ACE=80 mg/L) (Vàzquez et al., 2024). Protein hydrolysates from fish waste, enzymatically broken down with alkaline-producing low-molecular-weight peptides (<13.7 kDa), can exhibit antioxidant and ACE inhibitor activities (Borges et al., 2023). Molecular weight is one of the important characteristics of FPH that needs to be considered, as it provides information on the expected physical and bioactive properties of the product. More than 50% of the molecules in protein hydrolysates

from sardine have a molecular weight of less than 10 kDa (Chiodza and Goosen, 2024). Another research attempted to improve the functional peptides of mackerel (*Scomber scombrus*) protein hydrolysates by reducing the particle size of the peptides via ultrasonication and obtained small size (<200 Da) and small peptides (500-2,000 Da) in FPH samples (Cropotova et al., 2024).

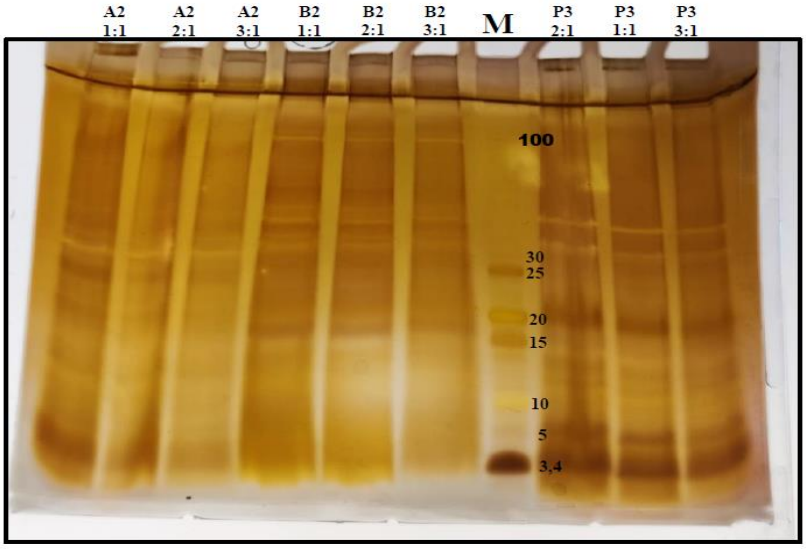

Figure 3. Electrophoresis results of protein hydrolysates at the best degree of hydrolysis using alcalase (A), bromelain (B) and papain (P) enzymes with various sample dilutions of 1:1 to 1:3; M is a protein marker of size 3.4-100 kDa.

4. CONCLUSION

Based on the results of hydrolysis using various types of enzymes in grouper bones, the best hydrolysis degree value was achieved at a 2-hour incubation time using papain and alcalase and at 3 hours with bromelain, with a hydrolysis degree above 88%. The protein pattern of electrophoresis results from papain enzymes that can produce sizes below 5.4 kDa and are expected to have activity as a biopeptide compound. The proximate content of protein hydrolysates from fish bones showed water content between 7-15%, ash content below 0.5%, and the yield of protein hydrolysate from each enzyme hydrolysis was 36-40%.

ACKNOWLEDGEMENTS

We thank Universitas Negeri Surabaya for the facilities and research support funds that enabled this research to be carried out.

AUTHOR CONTRIBUTIONS

Experimental run and Data Collection, Intan Fatma Listiandari, Browi Nugroho, Nur Indah Syamsiati, Mohammad Dhimas Adiputra, Ireniza Liano; Methodology, Validation, Supervision and Writing Original Draft Preparation, Nuniek Herdyastuti, Rudiana Agustini, Titik Taufikurohmah; Formal Analysis; Data Curation, Visualization, Writing-Review and Editing, Nuniek Herdyastuti, Tukiran, Tan Wen Nee.

DECLARATION OF CONFLICT OF INTEREST

The authors declare no conflicts of interest.

REFERENCES

Ahmed R, Haq M, Chun BS. Characterization of marine-derived collagen extracted from the by-products of bigeye tuna (*Thunnus obesus*). International Journal of Biological Macromolecules 2019;135:668-76.

Ahn CB, Cho YS, Je JY. Purification and anti-inflammatory action of tripeptide from salmon pectoral fin byproduct protein hydrolysate. Food Chemistry 2015;168:151-6.

Alahmad K, Xia W, Jiang Q, Xu Y. Effect of the degree of hydrolysis on nutritional, functional, and morphological characteristics of protein hydrolysate produced from bighead carp (*Hypophthalmichthys nobilis*) using ficin enzyme. Foods 2022;11:Article No. 1320.

Amiin MK, Subekti S, Masithah ED, Nirmala D, Yunus M, Santanumurti MB, et al. First microphological and molecular parasitological survey of Benedenia in humpback grouper (*Cromileptes altivelis*) of Lampung and Situbondo, Indonesia. Biodiversitas 2023;24(12):6858-67.

Annisa S, Darmanto YS, Amalia U. The effect of various fish species on fish protein hydrolysate with the addition of papain enzyme. Fisheries Science: Indonesian Journal Of Fisheries Science And Technology 2017;13(1):Article No. 2430 (in Indonesian).

Araujo J, Sica P, Costa C, Márquez, MC. Enzymatic hydrolysis of fish waste as an alternative to produce high value-added products. Waste and Biomass Valorization 2021;12(2):847-55.

Azara R. Preparation and analysis of physicochemical properties of gelatin from grouper fish skin waste (*Ephhinephelus* sp.). Journal of Food Design 2017;11(1):62-9 (in Indonesian).

Baehaki A, Lestari SD, Romadhoni AR. Hydrolysis of catfish protein using papain enzyme and antioxidant activity of its hydrolysate. Indonesian Fishery Products Processing 2015;18(3):230-9 (in Indonesian).

Bernadeta, Ardiningsih P, Silalahi IH. Determination of optimum conditions for protein hydrolysate from yellowtail fish waste (*Caesio cuning*) based on organoleptic characteristics. Journal of Equatorial Chemistry 2012;1(1):26-30.

Binsi PK, Shamasundara BA, Dileepa AO, Badiib F, Howell NK. Rheological and functional properties of gelatin from the skin of Bigeye snapper (*Priacanthus hamrur*) fish: Influence of gelatin on the gel-forming ability of fish mince. Food Hydrocolloids 2007;23(2009):132-45.

Borges S, Odila J, Voss G, Martins S, Rosa A, Couto JA, et al. Fish by-products: A source of enzymes to generate circular bioactive hydrolysates. Molecules 2023;28:Article No. 1155.

Chiodza K, Goosen NJ. Emulsion formation during enzymatic protein hydrolysis and its effect on protein recovery and molecular weight distribution of protein hydrolysates from sardine (*Sardina pilchardus*) by-products. Biomass Conversion and Biorefinery 2024;14(19):24069-80.

Clemente A. Enzymatic protein hydrolysates in human nutrition: A review. Trends in Food Science and Technology 2000;11(7):254-62.

Coppola D, Lauritano C, Esposito FP, Riccio G, Rizzo C, de Pascale D. Fish waste: From problem to valuable resource. Marine Drugs 2021;19:Article No. 116.

Cropotova J, Kvangarsnes K, Stangeland J, Rustad T. Effect of ultrasound pretreatment prior to enzymatic hydrolysis on physicochemical parameters of fish protein hydrolysates (FPH) extracted from side streams of Atlantic mackerel (*Scomber scombrus*). Frontiers in Sustainable Food Systems 2024;8:Article No. 1500359.

Da Rosa Zavareze E, Silva CM, Salas-Mellado M, Prentice-Hernandez C. Functionality of bluewing searobin (*Prionotus Punctatus*) protein hydrolysates obtained from different microbial proteases. Quimica Nova 2009;32(7):1739-43.

Dong S, Zeng M, Wang D, Liu Z, Zhao Y, Yang H. Antioxidant and biochemical properties of protein hydrolysates prepared from Silver carp (*Hypophthalmichthys molitrix*). Food Chemistry 2008;107(4):1485-93.

Dong Y, Yan W, Zhang X, Di Dai ZY, Zhang YQ. Steam explosion-assisted extraction of protein from fish backbones and effect of enzymatic hydrolysis on the extracts. Foods 2021;10(8):1-15.

Edison, Dewita, Karnila R, Yoswaty D. The hydrolysis of fish protein from giant mudskipper (*Periophthalmodon schlosseri*) using alcalase enzyme. Current Research in Nutrition and Food Science 2020;8(3):1056-63.

Efendi DS, Adrianto L, Yonvitner, Wardiatno Y. An evaluation of grouper and snapper fisheries management policy in Saleh Bay, Indonesia. IOP Conference Series: International Symposium on Aquatic Sciences and Resources Management; 2021 Nov 16-17; Bogor, West Java: Indonesia; 2020.

Gajanan PG, Elavarasan K, Shamasundar BA. Bioactive and functional properties of protein hydrolysates from fish frame processing waste using plant proteases. Environmental Science and Pollution Research 2016;23(24):24901-11.

Gao R, Yu Q, Shen Y, Chu Q, Chen G, Fen S, et al. Production, bioactive properties, and potential applications of fish protein hydrolysates: Developments and challenges. Trends in Food Science and Technology 2021;110:687-99.

Harnedy PA, FitzGerald RJ. Bioactive peptides from marine processing waste and shellfish: A review. Journal of Functional Foods 2012;4(1):6-24.

Haslaniza H, Maskat MY, Wan Aida WM, Mamot S, Saadiah I. Optimization of enzymatic hydrolysis of cockle (*Anadara granosa*) meat wash water precipitate for the development of seafood flavor. International Food Research Journal 2013;20(6):3053-9.

Henriques A, Vázquez JA, Valcarcel J, Mendes R, Bandarra NM, Pires C. Characterization of protein hydrolysates from fish discards and by-products from the north-west Spain fishing fleet as potential sources of bioactive peptides. Marine Drugs 2021;19:Article No. 338.

Honrado A, Miguel M, Ardila P, Beltrán JA, Calanche JB. From waste to value: Fish protein hydrolysates as a technological and functional ingredient in human nutrition. Foods 2024;13:Article No. 3120.

Hoyle NT, Merritt JH. Quality of fish protein hydrolysates from herring (*Clupea harengus*). Journal of Food Science 1994;59(1):76-9.

Ishak NH, Sarbon NM. A review of protein hydrolysates and bioactive peptides deriving from wastes generated by fish processing. Food and Bioprocess Technology 2018;11(1):2-16.

Jaziri AA, Sukoso. Characterization of protease from marine clam coarse extract and its activity in hydrolyzing groundfish protein. Journal of Fisheries and Marine Science 2017;1(2):78-87 (in Indonesian).

Kao YF, Chai HJ, Tsai CJ, Tsai TY, Liu TH, Yi TK, et al. Development of functional foods from grouper fish-bone residues to enhance muscle strength and exercise endurance in mice. Frontiers in Sustainable Food Systems 2024;8:1-12.

Kaveh S, Mahoonak AS, Erfanimoghadam V, Ghorbani M, Gholamhosseinpour A, Reisi M. Evaluation the effect of hydrolysis conditions and type of protease on the degree of hydrolysis and antioxidant properties of the protein hydrolysate from the skipjack fish (*Katsuwonus pelamis*) viscera by the response surface methodology. Journal of Food Science and Technology 2024;20(144):131-52.

Khasanah M, Nurdin N, Sadovy de Mitcheson Y, Jompa J. Management of the grouper export trade in Indonesia. Reviews in Fisheries Science and Aquaculture 2020;28(1):1-15.

Korkmaz K, Tokur B. Optimization of hydrolysis conditions for the production of protein hydrolysates from fish wastes using response surface methodology. Food Bioscience 2022;45: Article No. 101312.

Kristinsson HG, Rasco BA. Biochemical and functional properties of Atlantic salmon (*Salmo salar*) muscle proteins hydrolyzed with various alkaline proteases. Journal of Agricultural and Food Chemistry 2000;48(3):657-66.

Kumar V, Muzaddadi AU, Mann S, Balakrishnan R, Bembem K, Kalnar Y. Utilization of fish processing waste: A waste to wealth approach. Compendium of ICAR Summer School: Emerging Post-Harvest Engineering and Technological Interventions for Enhancing Farmer's Income; 2018. p. 127-31.

Liaset B, Lied E, Espe M. Enzymatic hydrolysis of by-products from the fish-filleting industry; chemical characterisation and nutritional evaluation. Journal of the Science of Food and Agriculture 2000;80(5):581-9.

Liu M, Li Z, Chen Q, Yang X, Chen J, Zhang L, et al. Preparation and characterization of grouper bone peptides-calcium complex by lactic acid bacteria fermentation. Lwt-Food Science and Technology 2024;201:Article No. 116224.

Martínez-Alvarez O, Chamorro S, Brenes A. Protein hydrolysates from animal processing by-products as a source of bioactive molecules with interest in animal feeding: A review. Food Research International 2015;73:204-12.

Masri M. Isolation and measurement of bromelin enzyme activity from crude extract of pineapple stem (*Ananas comosus*) at variation of pH. Biosel: Biology Science and Education 2013;2(2):Article No. 80 (in Indonesian).

Mo WY, Man YB, Wong MH. Use of food waste, fish waste and food processing waste for China's aquaculture industry: Needs and challenge. Science of the Total Environment 2018;(613-614):635-43.

Nasution EZ, Nasution LM. Enzymatization of nila fish (*Oreochromis niloticus*) protein hydrolysate by combination of bromelin and pepsin enzymes. Journal of Chemical Natural Resources 2024;6(2):122-30.

Ngo DH, Ryu BM, Kim SK. Active peptides from skate (*Okamejei kenojei*) skin gelatin diminish angiotensin-i converting enzyme activity and intracellular free radical-mediated oxidation. Food Chemistry 2014;143:246-55.

Nguyen HT, Bao HND, Dang HTT, Tómasson T, Arason S, Gudjónsdóttir M. Protein characteristics and bioactivity of fish protein hydrolysates from Tra Catfish (*Pangasius hypophthalmus*) side stream isolates. Foods 2022;11(24): Article No. 4102.

Nilna FNM, Muyassaroh, Azizah W, Sabrina M. Effect of temperature variation and drying time on the preparation of papain enzyme from papaya leaf extract. Journal Atmosphere 2021;2(2):15-21.

Nothling MD, Xiao Z, Bhaskaran A, Blyth MT, Bennett CW, Coote ML, et al. Synthetic catalysts inspired by hydrolytic enzymes. ACS Catalysis 2019:9(1):168-87.

Nurdiani R, Firdaus M, Prihanto AA, Jaziri AA, Jati MR, Abdurrahman TR, et al. Enzymatic hydrolysis of protein hydrolysate from *Pangasius* sp. by-product using Bromelain. Current Research in Nutrition and Food Science 2024; 12(1):125-36.

Nurhayati T, Salamah E, Cholifah, Nugraha R. Process optimization of hydrolysate preparation of white Snapper Offal. Indonesian Journal of Fishery Product Processing 2014;17(1):42-52 (in Indonesian).

Palla ANF, Metusalach, Amir N. Protein hydrolyzate of grouper viscera: Effects of crude bromelain extract concentration and hydrolysis time on yield and degree of hydrolysis. International Journal of Applied 2022;6(2):222-9.

Patil SP, Goswami A, Kalia K, Kate AS. Plant-derived bioactive peptides: A treatment to cure diabetes. International Journal of Peptide Research and Therapeutics 2020;26(2):955-68.

Petrova I, Tolstorebrov I, Eikevik TM. Production of fish protein hydrolysates: A step-by-step approach to technological aspects, equipment used, significant energy costs, and methods for minimizing them. International Aquatic Research 2018;10(3):223-41.

Pires C, Leitão M, Sapatinha M, Gonçalves A, Oliveira H, Nunes ML, et al. Protein hydrolysates from salmon heads and cape hake by-products: Comparing enzymatic method with subcritical water extraction on bioactivity properties. Foods 2024;13:Article No. 2418.

Raeesi R, Shabanpour B, Pourashouri P. Use of fish waste to silage preparation and Its application in animal nutrition. Online Journal of Animal and Feed Research 2023;13(2):79-88.

Raksakulthai R, Haard NF. Exopeptidases and their application to reduce bitterness in food: A review. Critical Reviews in Food Science and Nutrition 2003;43(4):401-45.

Restiani R. Enzymatic hydrolysis of Nyamplung (*Calophyllum inophyllum*) seed cake protein using Bromelain. Biota: Scientific Journal of Life Sciences 2017;1(3):103-10.

Rumondang R, Mulyani I, Aulia P. Feeding an artificial rush fish for the growth and survival of mud grouper (*Epinephelus lanceolatus*). AACL Bioflux 2023;16(1):259-69.

Sapatinha M, Camacho C, Pais-Costa AJ, Fernando AL, Marques A, Pires C. Enzymatic hydrolysis systems enhance the efficiency and biological properties of hydrolysates from frozen fish processing co-products. Marine Drugs 2025; 23:Article No. 14.

Shakila RJ, Jeevithan E, Varatharajakumar A, Jeyasekaran G, Sukumar D. Functional characterization of gelatin extracted from bones of red snapper and grouper in comparison with mammalian gelatin. LWT - Food Science and Technology 2012;48(1):30-6.

Siddik MAB, Howieson J, Fotedar R, Partridge GJ. Enzymatic fish protein hydrolysates in finfish aquaculture: A review. Reviews in Aquaculture 2021;13(1):406-30.

Silva CM, da Fonseca RA dos S, Prentice C. Comparing the hydrolysis degree of industrialization byproducts of Withemout croaker (*Micropogonias furnieri*) using microbial enzymes. International Food Research Journal 2014; 21(5):1757-61.

Tacias-Pascacio VG, Morellon-Sterling R, Siar EH, Tavano O, Berenguer-Murcia Á, Fernandez-Lafuente R. Use of Alcalase in the production of bioactive peptides: A review. International Journal of Biological Macromolecules 2020;165:2143-96.

Tirtadanu, Prihatiningsih, Yusuf HN, Zamroni A, Amri K, Chodrijah U. Assessing the stock status of areolate grouper (*Epinephelus areolatus*) in Java Sea, Indonesia. Regional Studies in Marine Science 2023;66:Article No. 103116.

Udenigwe CC, Aluko RE. Food protein-derived bioactive peptides: Production, processing, and potential health benefits. Journal of Food Science 2012;77(1):11-24.

Vàzquez JA, Comesa˜na S, Soengas JL, Bermúdez MPR, Rotllant J, Varcalcel J. Optimal and sustainable production of tailored fish protein hydrolysates from tuna canning wastes and discarded blue whiting: Effect of protein molecular weight on chemical and bioactive properties. Science of the Total Environment 2024;939:Article No. 173461.

Walker JM. The Protein Protocols Handbook. Totowa, New Jersey: Humana Press Inc; 2002.

Wang JS, Zhao MM, Zhao QZ, Bao Y, Jiang YM. Characterization of hydrolysates derived from enzymatic hydrolysis of wheat gluten. Journal of Food Science 2007;72(2):103-7.

Yang JI, Tang JY, Liu YS, Wang HR, Lee SY, Yen CY, et al. Roe protein hydrolysates of giant grouper (*Epinephelus lanceolatus*) inhibit cell proliferation of oral cancer cells involving apoptosis and oxidative stress. BioMed Research International 2016;2016:Article No. 8305073.

Zhang M, Huang TS, Mu TH. Production and in vitro gastrointestinal digestion of antioxidant peptides from enzymatic hydrolysates of sweet potato protein affected by pretreatment. Plant Foods for Human Nutrition 2019;74:225-31.

Zhang X, He H, Xiang J, Yin H, Hou T. Selenium-containing proteins / peptides from plants : A review of the structures and functions. Journal of Agricultural and Food Chemistry 2020;68(51):15061-73.

Environment and Natural Resources Journal

Volume 24
Issue 1
2026

Suitability and Evaluation of the Quality of Groundwater Used in Irrigation, Case of the Region of Oum El-Bouaghi (Northeast Algeria)

Khater Ibtissem[1], Zair Nadjet[2*], Khechekhouche Abderrahmane[3], Attoui Badra[4], and Miloudi Abdelmonem[5]

[1]Hydraulic and Civil Engineering Department, university of El-Oued, Algeria
[2]Hydraulic and Civil Engineering Department, University of El-Oued, Algeria
[3]Faculty of Technology, University of El-Oued, Algeria
[4]Laboratory of geology, Badji Mokhtar University of Annaba.BP12, 23000 Annaba, Algeria
[5]New Technology and local Development Laboratory, University of Eloued, Algeria

ARTICLE INFO

Received: 26 May 2025
Received in revised: 21 Aug 2025
Accepted: 27 Aug 2025
Published online: 8 Oct 2025
DOI: 10.32526/ennrj/24/20250135

Keywords:
Irrigation/ Salinity/ Spatial Autocorrelation/ Groundwater/ Wilcox/ Richards

*** Corresponding author:**
E-mail: nadjetzair@hotmail.fr; zair-nadjet@univ-eloued.dz

ABSTRACT

This study assesses the quality of groundwater for irrigation in the plains of Bir Chouhada, Souk Naamane, and Ouled Zouai, focusing on physico-chemical parameters including Electrical Conductivity (EC), Sodium Adsorption Ratio (SAR), sodium percentage (%Na), and chloride toxicity. Results show EC values ranging from 993 to 9,322 µS/cm, indicating poor to unsuitable water quality for irrigation in most wells. The SAR values vary between 8.86 and 43.6 meq/L, reflecting a high risk of soil sodification. The %Na ranges from 19.18% to 61.41%, with over 66% of samples exhibiting high mineralization. Using Richards classification, 58.78% of samples fall in the highly unsuitable C4S4 class, while Wilcox classification indicates 48.78% of dry season samples as unsuitable for irrigation. Seasonal variation shows slight quality improvement during the wet season, with good-quality water increasing from 4.87% (dry) to 7.31% (wet). Hydrochemical facies analysis identifies 46.34% of samples as calcic chloride type, linked to mineralization from gypsiferous formations. Spatial autocorrelation using Moran's I reveals moderate positive clustering of SAR (0.21-0.27) and %Na (0.15-0.23), with stable patterns across seasons. Statistical analysis via ANOVA confirms the significance of the model with $F=29.48$ ($p<0.000005$) and explains 43% of variation in water quality parameters. These findings highlight the critical challenges of irrigation water quality in the region and underscore the need for integrated management strategies including the use of salt-tolerant crops and soil drainage improvements.

HIGHLIGHTS

This study evaluated groundwater quality for irrigation using EC, SAR, %Na, and chloride toxicity. Classification by Richards and Wilcox methods showed that over 58% of samples were highly unsuitable for irrigation. Spatial analysis using Moran's I revealed moderate clustering of SAR and %Na values, consistent across seasons. ANOVA confirmed the model's significance, explaining 43% of the variation in water quality. The findings highlight serious salinity and sodicity risks, emphasizing the need for integrated water management and salt-tolerant agricultural practices.

1. INTRODUCTION

Irrigation water supply in arid and semi-arid areas is crucial for agricultural production, influencing both crop intensification and the expansion of irrigated areas (Jabeen et al., 2022; Jarray et al., 2023; Khechekhouche et al., 2020). While surface water is the main source of irrigation in temperate regions, groundwater is increasingly relied upon in semi-arid areas where surface water is scarce or absent (DHW, 2004; Ayers and Westcot, 1988; Person, 1978). However, agriculture development in such regions faces significant challenges, primarily due to water scarcity and emerging issues like soil salinization and alkalization. These problems directly affect soil fertility and crop productivity, posing serious obstacles to sustainable agricultural practices. Soil salinization occurs when soluble salts accumulate in the soil to levels that hinder plant growth, often

Citation: Ibtissem K, Nadjet Z, Abderrahmane K, Badra A, Abdelmonem M. Suitability and evaluation of the quality of groundwater used in irrigation, case of the region of Oum El-Bouaghi (Northeast Algeria). Nat. Resour. J. 2026;24(1):10-28. (https://doi.org/10.32526/ennrj/24/20250135)

resulting from improper irrigation practices or the use of saline water (Gouaidia, 2011; Pan et al., 2024). Alkalization, involving the buildup of exchangeable sodium in the soil, deteriorates soil structure and reduces permeability, further complicating water management and crop growth. To address these challenges in semi-arid agricultural regions, integrated water management strategies and innovative agricultural practices are essential to maintain soil health and ensure long-term sustainability (Liu et al., 2024; Miloudi et al., 2024; Zair et al., 2024; Attoui et al., 2024a). These issues mainly arise from ionic exchanges between irrigation water and soil, altering soil chemistry and reducing fertility over time (Bremond and Perredon, 1979; Devez, 2004; Zair et al., 2024; Attoui et al., 2024b). Effective mitigation requires proper irrigation management, soil amendments, and the use of salt-tolerant crops (Lado et al., 2024; Anyango et al., 2024). Similar challenges related to groundwater quality, salinity, and sustainable irrigation have been extensively documented in Pakistan's Punjab Province, a key agricultural region heavily dependent on groundwater resources (Khan et al., 2024; Malik et al., 2023; Baloch et al., 2025; Meng et al., 2024; Iqbal et al., 2023; Hussein et al., 2023; Baloch et al., 2022a; Baloch et al., 2022b). These studies reveal widespread contamination issues such as fluoride and nitrate pollution, risks associated with land use changes, and the potential of machine learning for water quality prediction and risk assessment. Collectively, they underscore the importance of integrated approaches combining groundwater quality monitoring, adaptive irrigation strategies, and crop selection to mitigate soil degradation and sustain agricultural productivity under increasing environmental pressures. Placing the present study within this global and regional framework emphasizes the crucial role of comprehensive water quality assessments such as those employing Wilcox and Richards's methods in informing water management policies that protect agricultural livelihoods and ecosystem health. Understanding seasonal variations in water quality, as done here over dry and wet seasons, further aids in developing targeted strategies to limit the negative impacts of salinization and alkalization, ensuring long-term agricultural sustainability in semi-arid regions such as Bir Chouhada, Souk Naamane, and Ouled Zouai. The accumulation of water-soluble salts in the root zone negatively impacts plant growth by altering soil permeability and aeration, as well as disrupting the plants' osmotic processes (Sousa et al., 2017; Attoui et al., 2024a; Zair et al., 2024). Regions like Bir Chouhada, Souk Naamane, and Ouled Zouai face significant risks of soil salinization (Zair, 2017; Rouabhia and Djabri, 2010). These areas are characterized by low rainfall, high evaporation rates, and groundwater rich in chlorides and sulfates, which exacerbate salinization and alkalization risks. Understanding the water and saline regimes in these regions is essential for sustainable water and soil resource management (Habiba et al., 2024; Zair et al., 2024). Various methods can help evaluate the type and quality of water intended for irrigation, including the Water Quality Index, Wilcox method, and Sodium Adsorption Ratio (SAR) method (Richards, 1954). In this study, we assessed irrigation water quality using the Wilcox and Richards methods. The Wilcox method focuses on salinity issues by assessing sodium percentage and electrical conductivity (Habiba et al., 2024; Miloudi et al., 2024; Zair et al., 2025), while the Richards method evaluates water quality based on sodium concentration (Na^+), a key indicator of water suitability for agriculture (Zair et al., 2021). Both methods rely on the chemical composition of water, which directly impacts plant growth and human health. We applied both the Wilcox (Na%) and Richards (SAR) methods to evaluate potential alterations in irrigation water quality, aiming to identify and mitigate issues that may affect irrigated soils and crops. Evaluations were conducted over dry and wet seasons to understand seasonal variations and better inform sustainable water management practices in the region. In the context of scarce water resources and risks of soil salinization and alkalization, this study addresses: How can we assess the quality of water intended for irrigation in Bir Chouhada, Souk Naamane, and Ouled Zouai? What strategies can be implemented to limit the negative effects of these phenomena on agriculture?

2. METHODOLOGY

2.1 Geographic situation of the study region

The study area includes the communes of Bir Chouhada, Souk Naamane and Ouled Zouai. These communes are located at the south-eastern end of the city of Oum El Bouaghi, located in the northeast of Algeria. Administratively, these communes are bordered by the cities of Mila to the north and Batna to the south as shown in Figure 1.

According to the hydrogeological study of the plain of Bir Chouhada, Souk Naamane and Ouled

Zouai, carried out by the Directorate of Hydraulics of the Wilaya (DHW) of Oum El Bouaghi in 2004, the geology of the region has four stratigraphic sets:

- The allochthonous Setifian in Djebel Amsid (northwest of Bir Chouhada), it consists of marls and gypsiferous clays of Miocene age and massive limestone of middle Cretaceous age.
- The autochthonous north Aurassian, represented by the djebels of Ain Yagout, Hanout, Harshel and Terbenut. The grounds are constituted of conglomerate, marl and marl-limestone.
- The Constantine neritic nappe and the nappe moi-plio quaternary extends on the plain, they are especially represented by the formations mio-plio-quaternary, represented by the alluvium, clays, marls, conglomerates, gravels, sands and dolomitic limestones as shown in Figure 2.

Figure 3 illustrates the piezometric map of the water table in the studied region. The area is characterized by a semi-arid climate, with cool winters and hot, dry summers. The average annual precipitation is approximately 465.30 mm, while the average annual temperature is around 16°C (DHW, 2004; Zair et al., 2017; Gouaidia et al, 2020). From a hydrogeological perspective, the piezometric surface observed during the wet season indicates that the general direction of groundwater flow is from west to east. The main drainage axes are located near the limestone massifs of the Lower Cretaceous and along the edge of the Miocene lacustrine limestone, particularly west of Bir Chouhada.

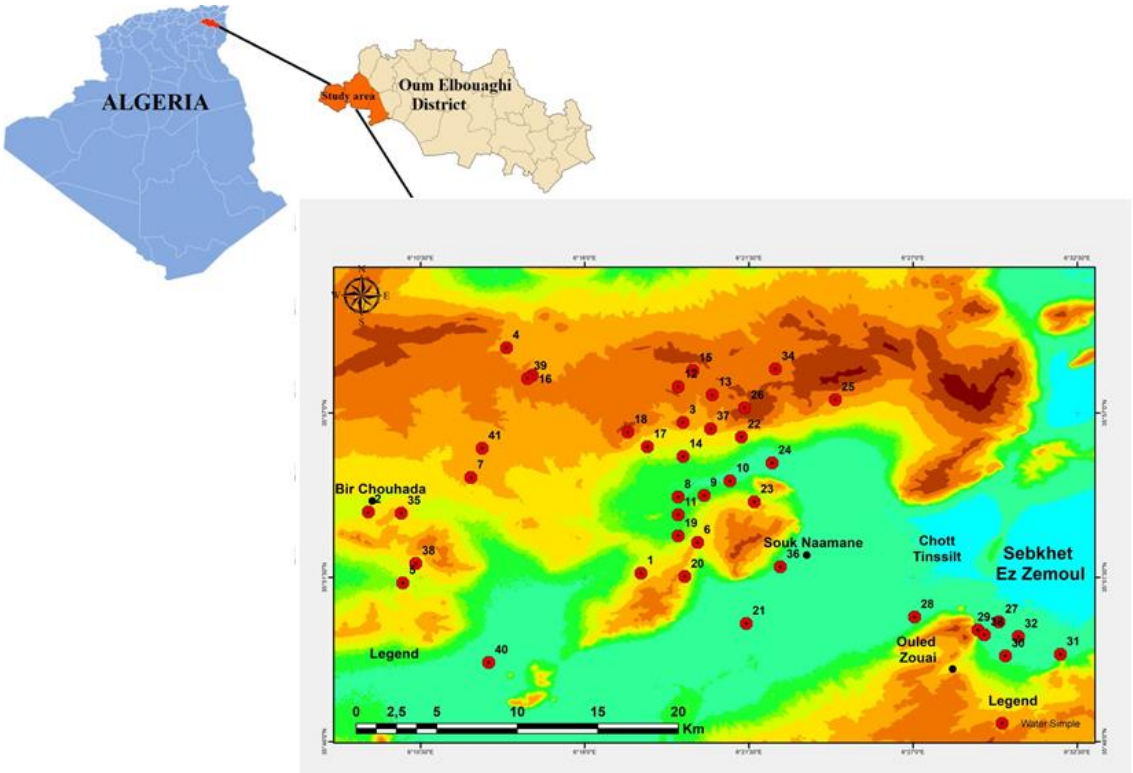

Figure 1. Geographic situation of the study region and well sampling repartition

As part of our study on groundwater quality for irrigation, we selected more than 40 water points strategically distributed across different geographical areas: near chotts, upstream (in the mountains), and in agricultural areas. This distribution provides a better understanding of the impact of geological and hydrological characteristics on water quality. Areas near chotts, often rich in dissolved salts due to evaporation, can have high sodium levels, increasing the risk of soil salinization and sodification. In contrast, water from the mountains, naturally filtered by the soil, should have lower sodium levels. Agricultural areas, depending on irrigation practices and local characteristics, offer another perspective on water salinity. By measuring SAR and Na% indices, you will be able to accurately assess soil degradation risks and recommend appropriate solutions, such as specific irrigation techniques or water management strategies to preserve soil fertility and optimize agricultural production. In situ measurements of pH,

and electrical conductivity (EC) were conducted using a WWT 82 362 multi-parameter probe. Geographic coordinates of each sampling point were recorded with the GPS Status device. The sampling network is illustrated in Figure 1. Water samples were stored at 4°C in a cooler during transportation to the laboratory. In addition, major ions (Na^+, K^+, HCO_3^-, Cl^-, Ca^{2+}, Mg^{2+}, SO_4^{2-}) were analyzed in the laboratory following APHA (1989) standard methods during May and September 2019 sampling campaign.

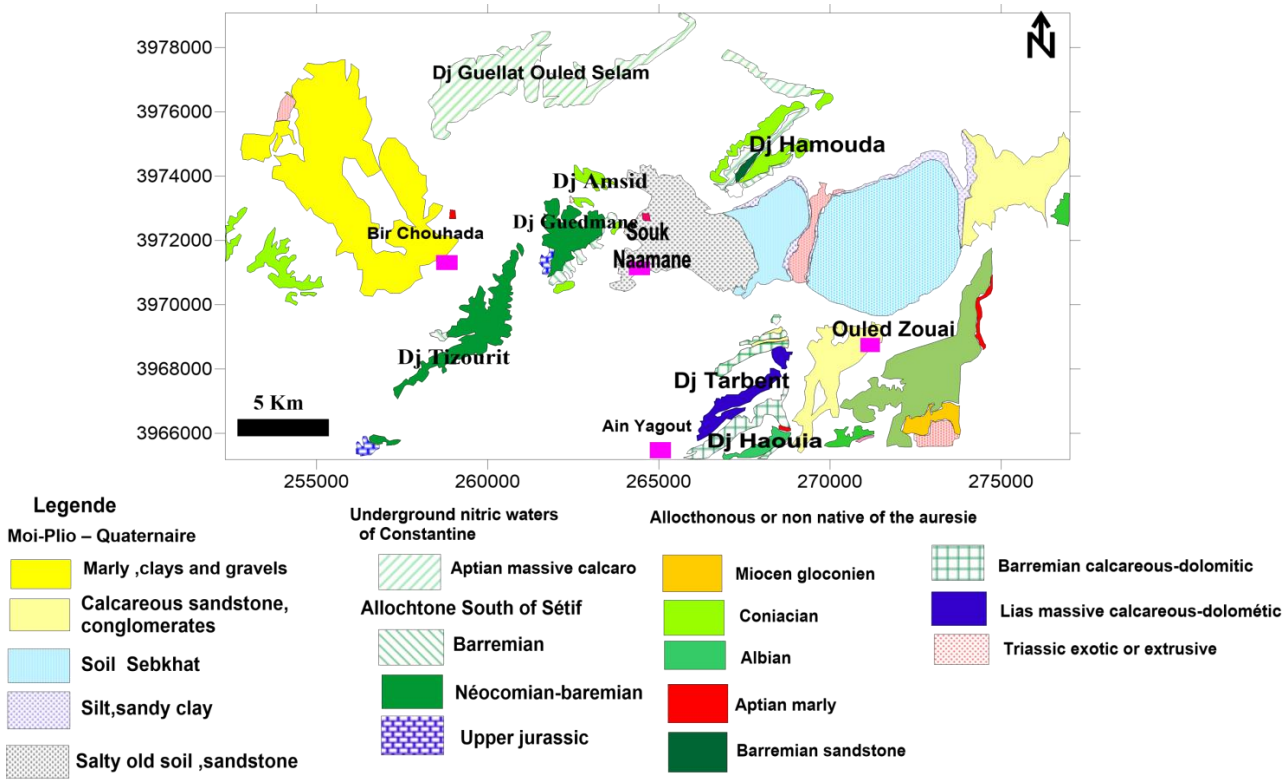

Figure 2. Extract of the geological map of the study area (DHW, 2004)

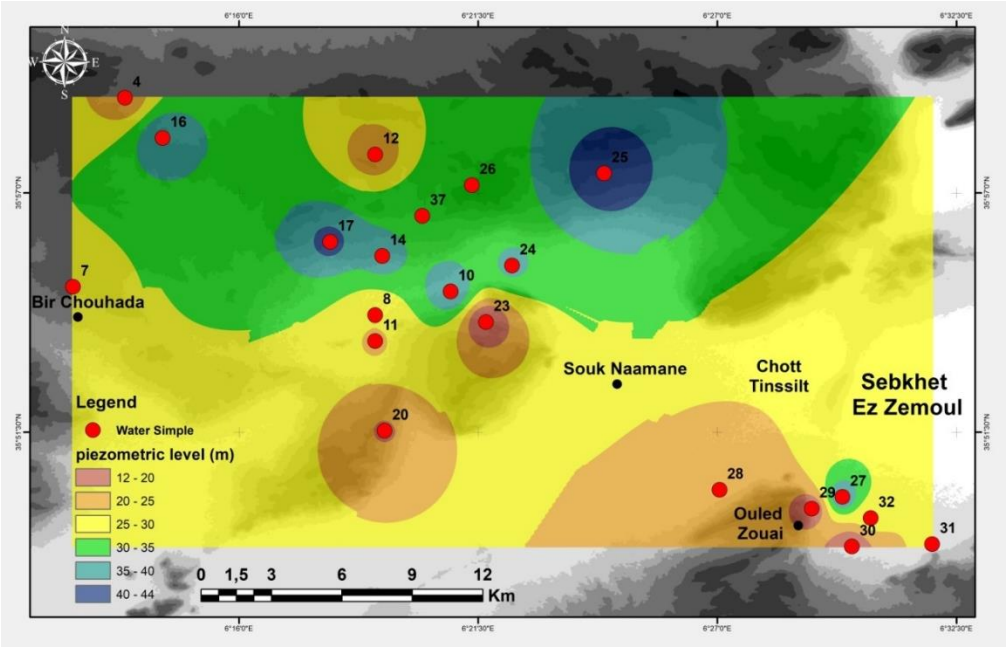

Figure 3. Water table of the phreatic aquifer

Different agricultural practices and the implementation of many irrigation systems have had an effect on the quality of groundwater, particularly that which returns to the aquifer after irrigation (Hemila, 1988; Zair at al., 2025). It should be noted that mineral salts in water have an impact on soil and plants. Indeed, salts can cause changes in soil structure (on its permeability and aeration), directly affecting plant development (Zair et al., 2017; Zair, 2017; Gouaidia, 2011). In this study, we have highlighted the evaluation of the quality of groundwater in Bir Chouhada, Souk Namaane and Ouled Zouai for agricultural purposes. This assessment is based on the Piper diagram for the determination of chemical facies, and on the universal diagrams of Riverside and Wilcox to assess the risk of salinization and sodisation of soils (Figure 4). The SAR (Sodium Adsorption Ratio) method and the Na% (sodium percentage) method are commonly used tools to assess the quality of groundwater intended for irrigation. Each of these methods allows measuring the compatibility of water with soils and identifying the potential risk of deterioration of agricultural land due to excess sodium, which can harm soil structure and affect plant growth. The Wilcox approach and the Riverside approach are widely used to assess the suitability of water for irrigation based on salinity and sodicity (SAR) (Sumner, 1993; Devez, 2004; Eaton, 1950). The Riverside and Wilcox methods are widely used to assess the quality of water for irrigation. The Riverside method plots the Sodium Adsorption Ratio (SAR) against Electrical Conductivity (EC), categorizing water into Good, Acceptable, Marginal, and Hazardous based on levels of salinity and sodicity (Table 1). The Wilcox method uses sodium percentage (Na%) and EC to classify water into four categories: Excellent, Good, Fair, and Unsuitable, based on the salinity and sodium content of the water (Wilcox, 1955) (Table1). Both methods provide critical insights into water quality, helping guide water management practices and crop selection by highlighting risks to soil structure and crop health.

Table 1. Summary table for classification of water quality

Diagram	Parameter	Classification	EC (µS/cm)	SAR	Na%
Wilcox	Salinity and Sodicity	Excellent	≤700	≤3	≤20
		Good	700-1,400	3-6	20-40
		Fair	1,400-2,800	6-12	40-60
		Unsuitable	>2,800	>12	>60
Riverside	Salinity and SAR	Good	≤2,000	≤6	
		Acceptable	2,000-4,000	6-9	
		Marginal	4,000-6,000	9-12	
		Hazardous	>6,000	>12	

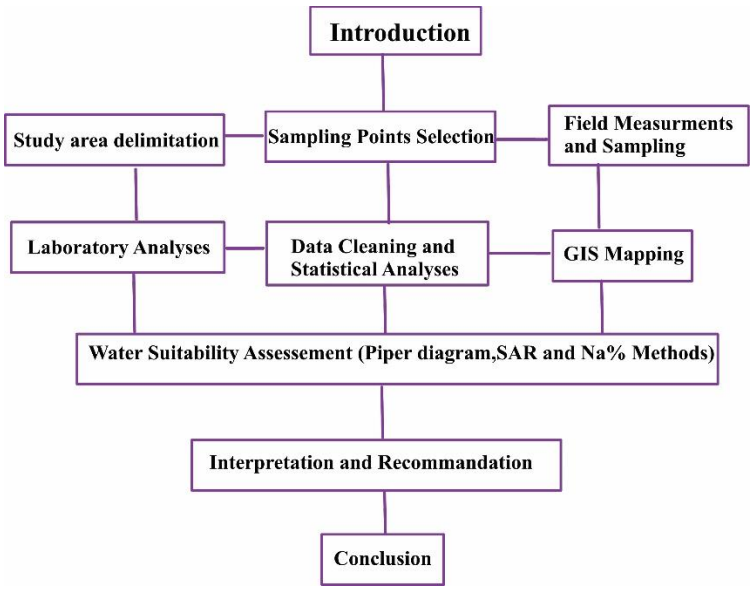

Figure 4. General Diagram presenting the study approaches

2.2 Limitations and sources of uncertainty

While the applied hydrochemical methods provide valuable insights into the groundwater facies and geochemical processes, several limitations and sources of uncertainty should be acknowledged. Firstly, measurement errors associated with field instrumentation (electrical conductivity, pH, and ion-selective electrodes) and laboratory analyses (ion chromatography, titration methods) may affect the accuracy and precision of the chemical data. Additionally, the temporal variability of groundwater chemistry particularly influenced by seasonal changes in recharge, evapotranspiration, and anthropogenic inputs could lead to inconsistencies if the sampling was conducted during a single season or over a short time frame. The spatial coverage of sampling points may also limit the representativeness of the interpreted facies, especially in heterogeneous geological settings where local lithology, permeability, and water-rock interaction can vary significantly. Furthermore, potential mixing of groundwater from multiple sources (deep versus shallow aquifers) could obscure geochemical signatures, complicating facies classification. Lastly, the interpretation of facies is based on the dominant ion composition and does not always account for trace elements, isotopic data, or redox-sensitive species, which can provide critical complementary information for understanding groundwater evolution and contamination processes. Future studies should consider incorporating multitemporal sampling, and modeling approaches to reduce these uncertainties and improve the reliability of hydrochemical interpretations.

2.3 Statistical analysis

Analysis of variance (ANOVA) is a widely used statistical method designed to determine whether the differences observed among the means of multiple groups are statistically significant. It compares the between-group variance, which reflects the effects of explanatory factors (facies type, season), to the within-group variance, associated with natural sample variability (Montgomery, 2017). In hydrogeology, ANOVA is particularly useful for assessing whether variations in physicochemical parameters such as concentrations of major ions (Ca^{2+}, Mg^{2+}, SO_4^{2-}, Cl^-) are significantly influenced by qualitative variables like hydrochemical facies, seasonal changes, or spatial distribution (Helena et al., 2000; Subba Rao, 2006). The null hypothesis (H_0) assumes all group means are equal, while the alternative hypothesis (H_1) suggests at least one group mean differs; a p-value less than 0.05 indicates statistically significant differences unlikely due to random chance (Hair et al., 2014). Valid ANOVA requires assumptions of normality (tested by Shapiro-Wilk), homogeneity of variances (Levene's or Bartlett's test), and independence; violations may necessitate non-parametric alternatives like the Kruskal-Wallis test (Zar, 2010). In this study, ANOVA provides a robust framework to test temporal variability in groundwater chemistry and validate facies classifications from multivariate or classical analyses. Complementing this, Moran's I is a spatial statistic that evaluates whether the values of a variable, such as SAR salinity, exhibit spatial clustering. Ranging from -1 to +1, Moran's I indicates strong positive spatial autocorrelation at +1 (similar values are spatially clustered), zero spatial autocorrelation at 0 (random distribution), and strong negative spatial autocorrelation at -1 (neighboring values differ greatly), helping to reveal geographic clustering patterns in the data.

2.4 Comparison of classes from the Riverside and Wilcox methods

In this comparative study, the Riverside classification method will be the one used as the reference for determining the evaluation of spatial variations in classes. A statistical method will be used to make this comparison: Statistical analysis of class areas. This analysis compares the areas of the different classes produced by the two methods (Riverside and Wilcox), according to a 100 m × 100 m grid. The analysis is based on the two maps and the number of grid cells per class. The evaluation and visualization of the results were carried out using Excel 2010 software, Diagram software, software for the geographic information system GIS (Arc GIS, QGIS) and golden surfer 20 logiciel.

3. RESULTS AND DISCUSSION

The results of physico-chemical analysis of the water of study area, during the observation period, have brought out the parameters usually used for the estimation of the quality of irrigation water. Among these parameters, we count the salinity expressed by the Electrical Conductivity (EC), the %Na, the SAR (Sodium Absorption Ratio) and the toxicity of chlorides. These parameters have been reported in Table 2.

The average value of conductivity between 37,012 and 3,371 (µS/cm) in dry and wet periods.

These values indicate that the groundwater of Bir Chouhada, Souk Namaan and Ouled Zouai is of poor to Unsuitable quality. Nevertheless, several water points are of average quality with an EC below 1050 (µS/cm). However, the average SAR value varies between 15.9 (Dry period) and 17.7 meq/L (Wet period), showing a high risk of sodisation .These results are similar to what was found by (Benmrabet et al., 2025) in the Tebessa region (Algeria). According to the guidelines, there is a problem of toxicity by chlorine if the concentration is between 4 and 10 meq/L, beyond 10 meq/L of Cl^-, the problems become serious. The %Na values of the groundwater samples range from 38 to 40. Most of the groundwater samples are of poor water quality with high mineralization (66%) These results are compatible with those found in the Tebessa region (Algeria) (Benmerabet et al., 2025), with regard to the results found (Table 2) their toxicity is clear, since we find more than half (68.2%) of the wells with contents that greatly exceed 10 meq/L representing the maximum permissible threshold for plants (Ayers and Westcot, 1988; Bremond and Perredon, 1979).

Table 2. Statistical parameters of some groundwater variables in the study area

	CE	Dry			CE	Wet		
		SAR	Cl^-	Na%		SAR	Cl^-	Na%
Unit	µS/cm	meq/L	meq/L	meq/L	meq/L	meq/L	meq/L	meq/L
Min	1,056	9.44	8.02	26.67	993	8.86	7.61	19.18
Max	9,322	43.60	72.11	61.41	9,000	31.40	68.54	61.06
Mean	3,712.821	15.90	1,796.294	38.43	3,371.923	17.70	17.93555	40.01

3.1 Determination of the Hydrochimique facies of the waters

Analysis of the scatterplots shown in Figures 5(a) and 5(b) does not indicate a clear dominance of either cations (such as calcium, magnesium, sodium, potassium) or anions (such as chloride, sulfate, and bicarbonate). This lack of ion dominance suggests that multiple hydrochemical processes influence the groundwater composition in the study area. However, the classification of hydrochemical facies reveals a relatively dominant calcic chloride facies, representing 46.34% of the analyzed samples. This facies typically reflects more advanced mineralization, likely linked to deeper or longer groundwater circulation through evaporitic formations rich in chlorides. A moderate proportion of calcic sulfate facies (25.15%) is also observed. This indicates a significant contribution from rocks containing gypsum or anhydrite, which is consistent with the presence of gypsiferous marls of Triassic age in the geological substratum. These formations release calcium and sulfate through dissolution, thereby influencing the groundwater chemistry. In addition, two calcic bicarbonate facies are present at lower proportions (18% and 10.5%), suggesting the influence of more recent or less mineralized recharge waters. These facies are generally associated with peripheral zones, where infiltration of rainwater or input from shallow aquifers dilutes major ion concentrations, resulting in less chemically evolved water types (Figures 5(a) and 5(b)). The significant presence of sodium in several samples can be attributed to the Triassic gypsiferous marls that form the aquifer's substratum. These formations contribute sodium through processes such as mineral dissolution or cation exchange, which further complicates the hydrochemical signature of the groundwater. In summary, the distribution of hydrochemical facies reflects a complex interplay of geological substrate, recharge mechanisms, and water-rock interactions. No single ion type (cationic or anionic) clearly dominates across the dataset, underscoring the heterogeneous nature of the groundwater system.

3.2 Water quality status for agricultural use

Potassium (K^+) is not usually included in the traditional SAR because its concentration is low and has less effect on soil sodicity. However, when K^+ is significant, it can be measured in the laboratory and added to the SAR to better assess water quality and its impact on soil. The concentration of sodium ions (Na^+) in the soluble state of the soil plays a crucial role in Base Exchange processes, particularly when sodium levels are high. In such cases, Na^+ ions often replace calcium (Ca^{2+}) ions in the soil's absorbing complex, which can adversely affect soil structure and reduce its

permeability to water and air. This phenomenon is particularly common when irrigation water is rich in salts a frequent condition in arid and semi-arid regions where groundwater is the main source for agriculture. To assess this risk, the Sodium Adsorption Ratio (SAR) is commonly used. It is a key agronomic indicator defined by the following equation (1):

$$SAR = \frac{(Na + K)}{\sqrt{(\frac{(Ca + Mg)}{2})}} \quad (1)$$

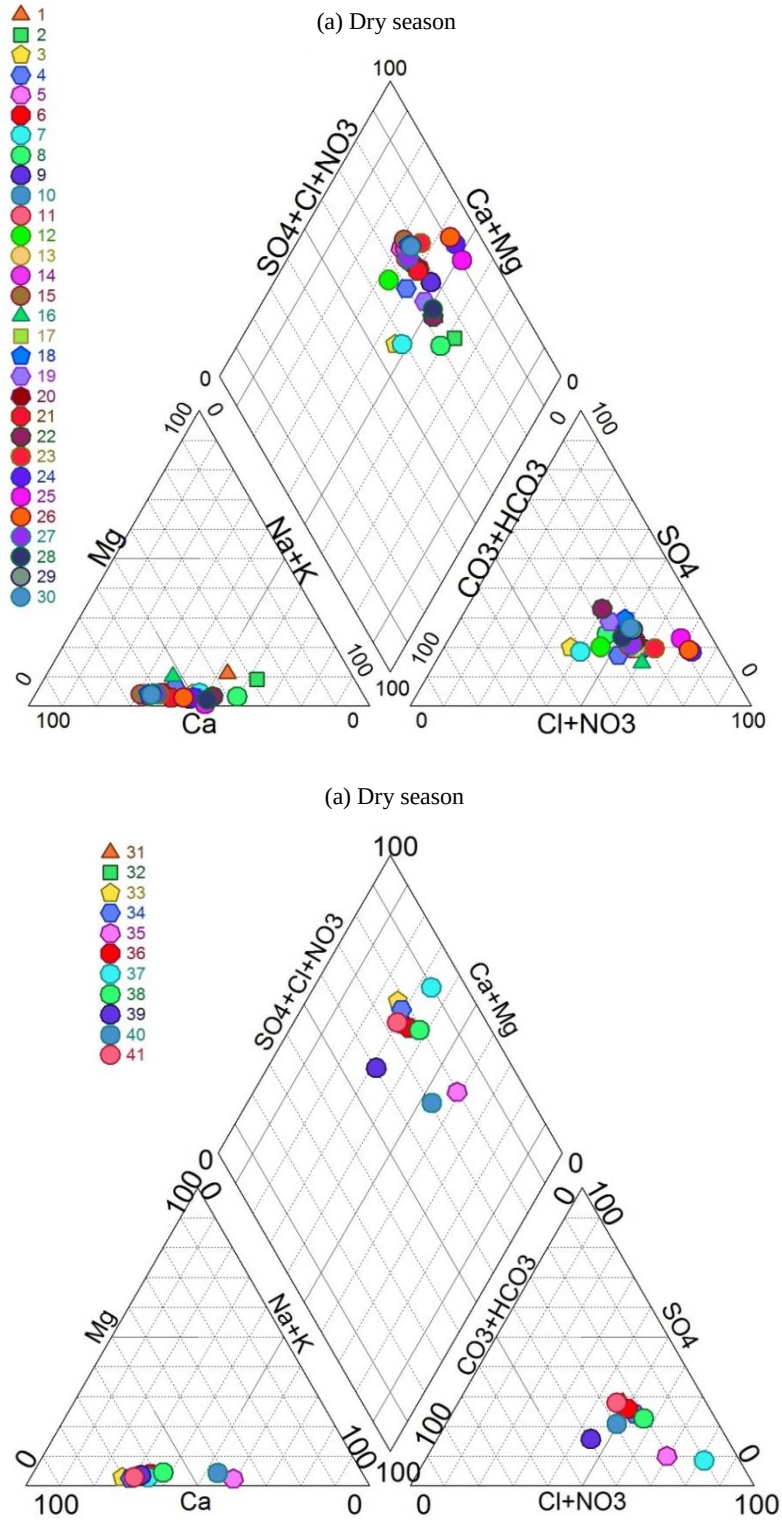

Figure 5. Piper diagram of groundwater in the plain; (a) dry season, (b) wet season

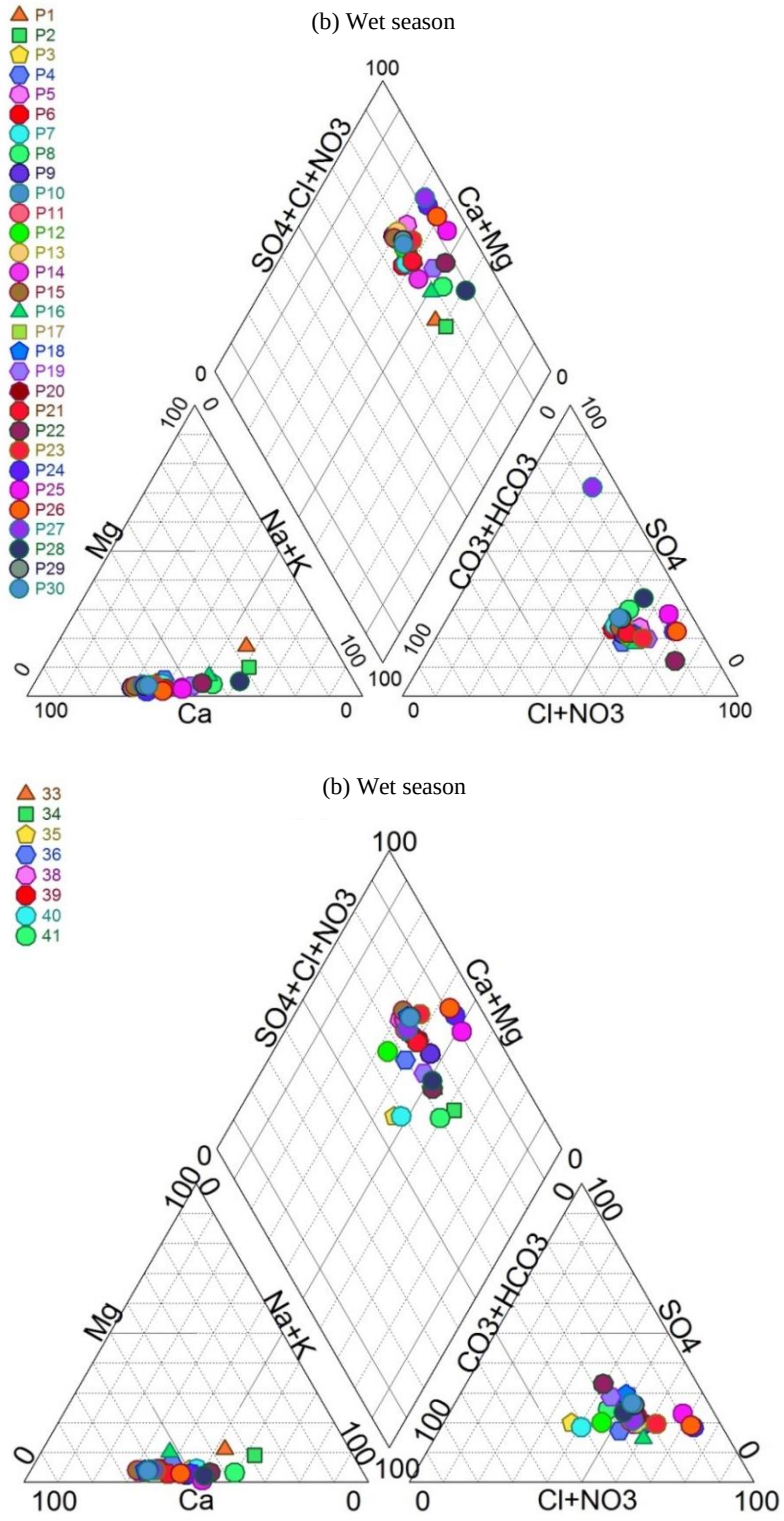

Figure 5. Piper diagram of groundwater in the plain; (a) dry season, (b) wet season (cont.)

In the case study of groundwater from the plains of Bir Chouhada, Souk Naamane, and Ouled Zouai, all water samples from different field campaigns were plotted on the Richards diagram (Figures 6(a) and 6(b)), using their electrical conductivity (EC) and SAR values. This classification allowed for the identification of five water quality classes, ranging from acceptable to poor for irrigation purposes. Classes C3S2 and C3S3 represent water that is acceptable for the irrigation of salt-tolerant crops, provided that the soils are well-drained or exhibit good permeability. Nevertheless, salinity must be regularly monitored to avoid long-term accumulation. Class C3S2 corresponds to wells mainly located in the

western part of the plain and the Bir Chouhada area, accounting for 2.43% of the total water points sampled. Class C3S3 accounts for 4.89% and represents a slightly higher salinity level but remains within the acceptable range (Table 3). In contrast, C4S3 and C4S4 represent poor to very poor quality waters, highly mineralized, and only suitable for the irrigation of highly salt-tolerant species on well-drained and frequently leached soils. C4S4 is the most dominant class, making up 58.78% of all sampled water points, mostly located between Souk Naamane and Ouled Zouai (Table 3). This class shows severe salinity and sodicity risks, which could harm agricultural productivity if not properly managed. C4S3, with moderate sodicity compared to C4S4, is found in the central region of Souk Naamane and the southeastern part of the plain. It represents 34.14% of samples in the wet season and rises to 41.46% in the dry season, indicating a relative deterioration in water quality due to seasonal evaporation (Table 3). The comparison of results across the two campaigns indicates that water quality remained relatively stable over time, suggesting no significant short-term changes in the aquifer's composition. However, a slight degradation trend was observed, likely due to the presence of gypsum and clay minerals, which naturally release ions into the water, and evaporation, which increases the concentration of dissolved salts, particularly during the dry season. These waters can only be used for irrigation on permeable soils with good natural drainage. If these soil conditions are not met, there is a significant risk of alkalization, particularly in fine-textured soils such as clays, where sodium accumulation can lead to soil structure deterioration and reduced infiltration. Under such constraints, only salt-tolerant crops should be considered for cultivation. Suitable species include tobacco, cotton, barley, artichoke, and date palms, which have demonstrated resilience under saline or sodic irrigation conditions. The choice of these crops, combined with appropriate soil and water management strategies, is essential to mitigate the long-term impacts of using highly mineralized water for irrigation.

Table 3. Evolution of irrigation classes according to Riverside

	Wet season	Dry season
C3S2	2,43%	2,56%
C3S3	4,89%	4,89%
C4S3	34,14%	41,46%
C4S4	58,78%	51,12%

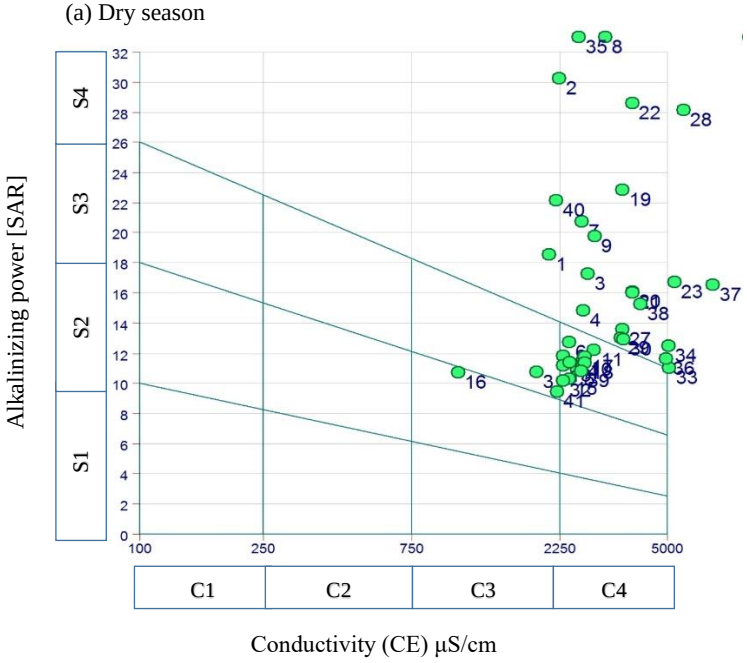

Figure 6. Riverside diagram (a) dry season, (b) wet season

(b) Wet season

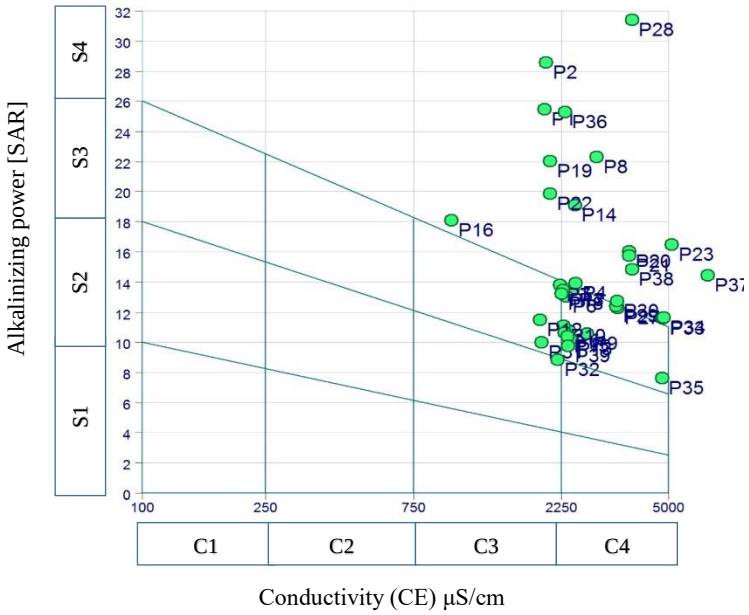

Figure 6. Riverside diagram (a) dry season, (b) wet season (cont.)

The Wilcox classification is based on the electrical conductivity and the sodium content in water expressed in percentage. The representation of the different samples on this diagram allows the characterization of the waters for their suitability for irrigation (Figures 7(a) and 7(b)). The $\%Na^+$ is defined by the relation (2):

$$Na\% = \frac{(Na+K)}{(Ca+Mg+Na+K)} \quad (2)$$

The classification of irrigation water quality across seasons reveals a concerning trend in the region (Table 4). During the dry season, only 4.87% of the water is classified as good, while the majority falls into the fair/poor (46.34%) and unsuitable (48.78%) categories. In the wet season, water quality shows a slight improvement, with good water increasing to 7.31% and unsuitable water decreasing to 39.02%, likely due to the dilution effect of rainfall (Table 4). However, the overall situation remains problematic, as no water samples fall into the acceptable category in either season, indicating a lack of moderately safe water for irrigation. More than 90% of the water in both seasons is considered either marginal or entirely unsuitable for most crops. This highlights the serious limitations imposed by water quality on agricultural productivity in the region. The dominance of poor and unsuitable water especially during the dry season suggests that evaporation and mineral accumulation significantly worsen water conditions. These findings emphasize the urgent need for integrated management practices, such as improving soil drainage, adopting salt-tolerant crops, and exploring water treatment or blending strategies to ensure the sustainability of irrigated agriculture in this area.

Table 4. Evolution of irrigation classes according to Wilcox (Na%)

	Dry season	Wet season
Good	4,87%	7,31%
Acceptable	00%	00%
Fair/Poor	46,34%	51,41%
Unsuitable	48,78%	39,02%

The analysis of groundwater quality throughout the entire observation period, based on the Wilcox classification (Figures 7(a) and 7(b)), reveals that the waters of Bir Chouhada, Souk Naamane, and Ouled Zouai predominantly fall into three categories: Good**,** Poor, and unsuitable. However, during the dry season, a fourth class acceptable also appears, indicating a slight expansion in water quality variability. Despite this, the majority of water samples across both dry and wet seasons consistently fall within the poor to unsuitable categories, accounting for over 90% of the samples. This widespread degradation in water quality significantly limits its suitability for irrigation. The underlying cause of this poor water quality is primarily natural, linked to the geological composition of the region. The aquifer systems are embedded in

Miocene-aged formations rich in bicarbonate and gypsiferous clays, which contribute high levels of dissolved salts to the groundwater. These geological characteristics, combined with evaporation processes, promote salinity and sodicity, further reducing the irrigation potential of the water.

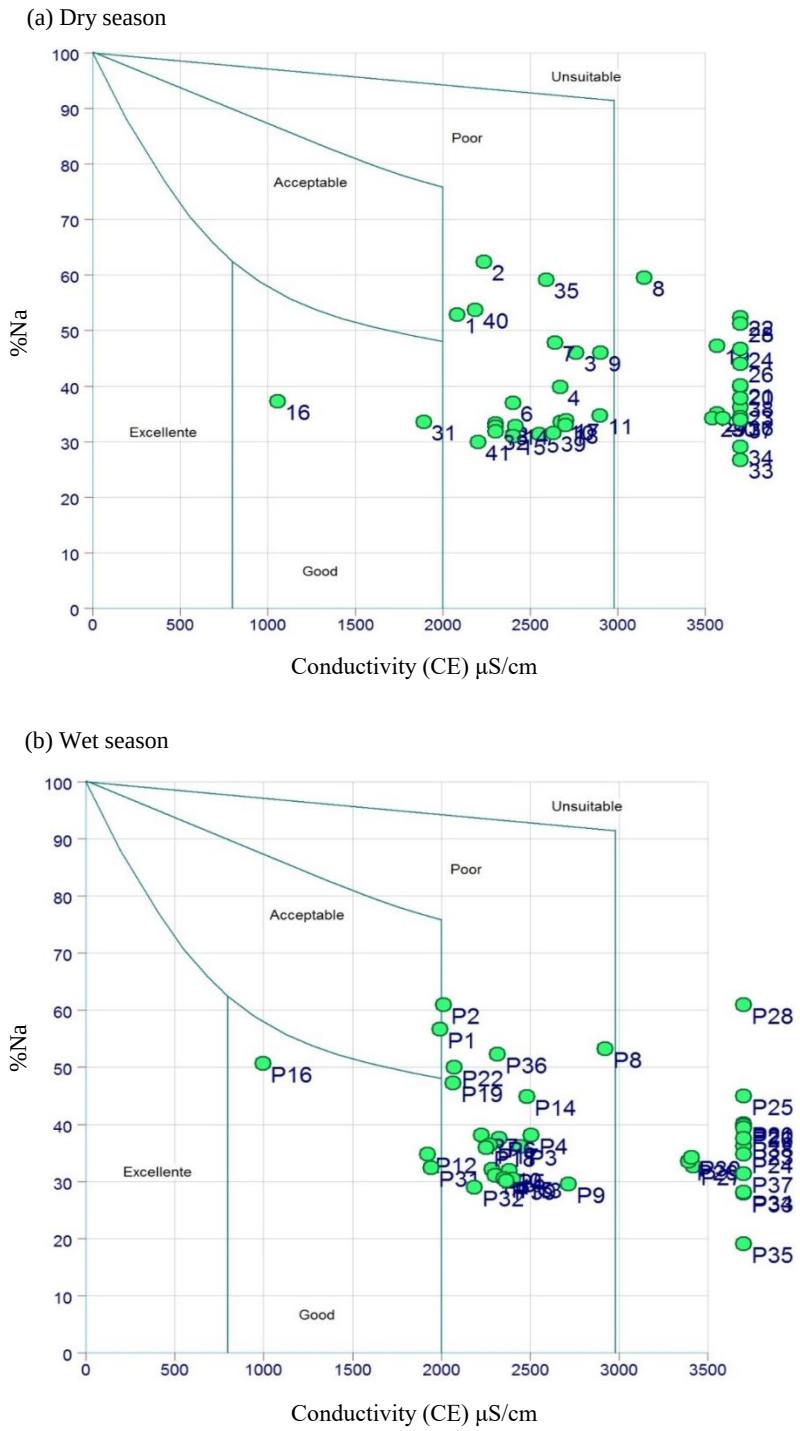

Figure 7. Wilcox diagram (a) dry season, (b) wet season

3.3. Mapping of water suitability classes for irrigation

With the objective of highlighting the effect of lithology on agricultural water quality, we mapped the respective SAR (Riverside) and %Na (Wilcox) values for the dry season, which includes the maximum number of wells (Figures 8(a), 8(b) and Figure 9(a), 9(b)):

3.3.1. Irrigation suitability map based on Richards's classification (dry and wet season)

According to the classification of irrigation water quality during the dry season, two major groups were identified within the study area. The Marginal class (C3S2 and C3S3) is primarily located in the northwest, upstream of the plain (samples 16, 39, 12, 13, 15, 17, 18, and 41), as well as in the southwest portion of the aquifer (wells 30, 32, and 31). These waters are characterized by moderate mineralization and average alkalinity, and are largely derived from the carbonate formations that border the basin (Figure 8(a)). In contrast, the Unsuitable class (C4S3 and C4S4) includes highly mineralized waters that pose serious risks for most crops unless specific irrigation conditions are applied. These waters can only be used with salt-tolerant crops and require well-drained and leached soils to prevent degradation. A similar distribution was observed during the wet season (Figure 8 (b)), with the Marginal class extending across the northwest, the Bir Chouhada zone, the southwest (wells 30, 32, 31, 33, and 29), and parts of the central plain. This group represented 39.02% of the total study area and maintained similar characteristics to those identified in the dry season. However, the Unsuitable class remained dominant, covering approximately 61% of groundwater samples during the wet season. The widespread occurrence of unsuitable water underlines the significant constraints that natural hydrogeological conditions impose on agricultural activities in the region.

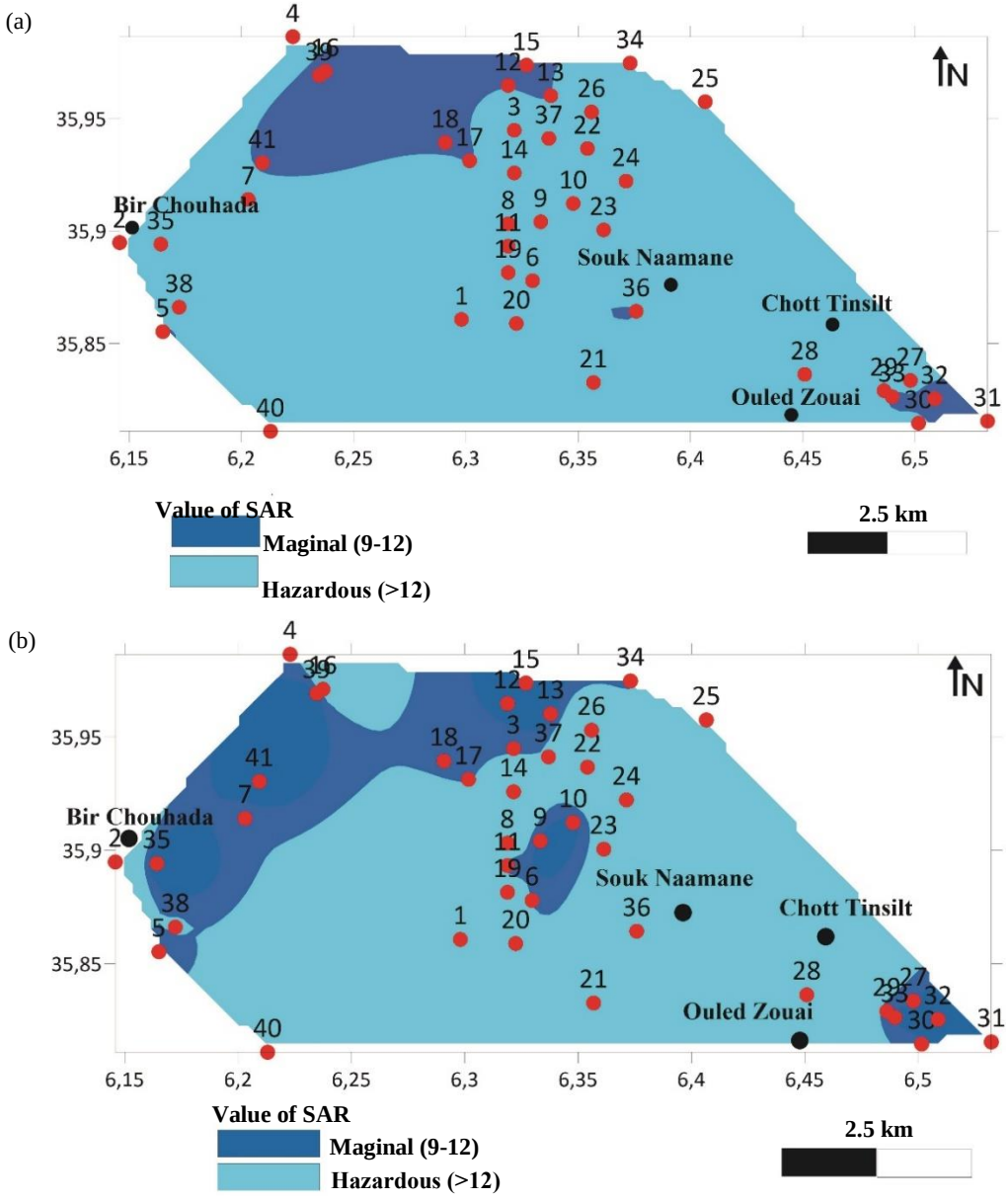

Figure 8. Irrigation suitability map based on Richards classification (a) dry season, (b) wet season

3.3.2 Water suitability map for irrigation in the study area according to Wilcox classification (dry and wet season)

The Wilcox classification applied to groundwater samples from both the dry and wet seasons revealed a predominance of good to poor water quality for irrigation. In the dry season (Figure 9(a)), three classes were identified: Good (58.53%), Poor (36.58%), and Unsuitable (4.87%) of the well sampling. Similarly, in the wet season (Figure 9(b)), the same three classes were observed, although the distribution shifted slightly: Good quality water became the dominant category (65.85%), followed by Poor (31.72%) and Unsuitable (2.43%) of the points water. In both cases, a clear trend of water quality degradation along the direction of groundwater flow was observed, illustrating the influence of lithological factors particularly the interaction with gypsiferous and clay-rich geological formations on mineralization and alkalinity levels. Furthermore, the spatial mapping of irrigation water suitability using both the Riverside and Wilcox methods, applied over a 100 m × 100 m grid, provided a detailed classification of surface areas by water quality classes, as shown in Table 5. The comparison between the Riverside and Wilcox methods for evaluating mesh quality reveals notable differences in classification outcomes. According to the Riverside method, 25% of the meshes fall into the "Good" class, while the remaining 75% are categorized as "Poor," with no meshes classified as "Acceptable" or "Unsuitable." In contrast, the Wilcox method shows a more favorable distribution, with 40.44% of meshes classified as "Good," 58.36% as "Poor," and a small proportion (1.18%) deemed "Unsuitable." Neither method identifies any meshes in the "Acceptable" category. These results suggest that the Wilcox method applies less restrictive criteria than Riverside, resulting in a higher percentage of meshes being considered suitable for use. However, the identification of a small number of "Unsuitable" meshes by Wilcox, which are not detected by Riverside, indicates that it may offer better sensitivity at the lower end of the quality scale. Overall, while both methods highlight significant limitations in mesh quality, Wilcox presents a slightly more optimistic assessment.

Table 5. Percentage of class areas produced by Riverside and Wilcox methods

	Riverside		Wilcox	
	Number of meshes	%	Number of meshes	%
Good class	125	25	200	40,44
Acceptable class	0	0	0	0
Poor class	375	75	294	58,36
Unsuitable class	0	0	6	1,18
Total	500	100	500	100

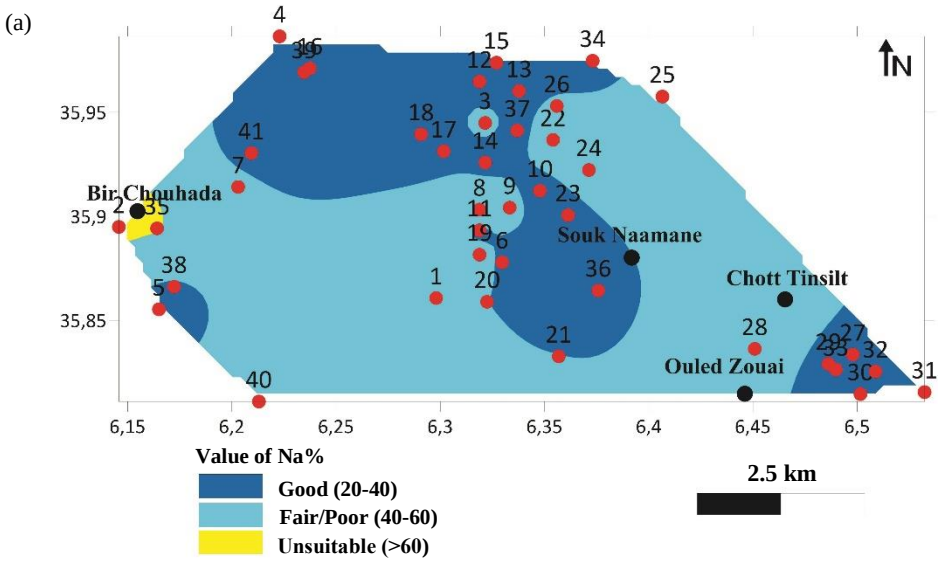

Figure 9. Water suitability map for irrigation in the study area according to Wilcox classification (a) dry season, (b) wet season

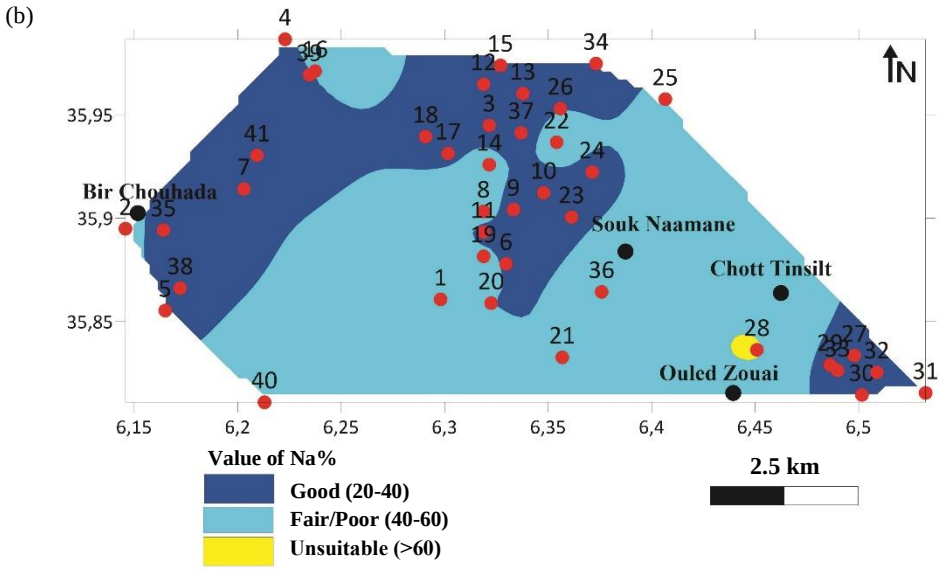

Figure 9. Water suitability map for irrigation in the study area according to Wilcox classification (a) dry season, (b) wet season (cont.)

Table 5. Percentage of class areas produced by Riverside and Wilcox methods

	Riverside		Wilcox	
	Number of meshes	%	Number of meshes	%
Good class	125	25	200	40,44
Acceptable class	0	0	0	0
Poor class	375	75	294	58,36
Unsuitable class	0	0	6	1,18
Total	500	100	500	100

3.3 Statistical analysis

Table 6 shows the analysis of variance (ANOVA) conducted for our simple linear regression model indicates that the model is statistically significant. The F-test, used to assess the contribution of the independent variable, yields an F-statistic of 29.48 with 1 degree of freedom for the regression and 39 degrees of freedom for the residuals. This F-value is associated with a very small p-value ($p \approx 0.000005$), which is far below the conventional significance threshold of 0.05. This means that the likelihood of observing such a result by chance is extremely low. Consequently, we reject the null hypothesis and conclude that the independent variable has a significant effect on the dependent variable. Moreover, the model's coefficient of determination (R^2) is 0.43, indicating that approximately 43% of the total variation in the dependent variable is explained by the predictor. This is considered a moderately strong relationship for a simple regression model, suggesting that the model provides a reasonably good fit to the data. However, it also implies that 57% of the variation remains unexplained, possibly due to other variables not included in the model. In summary, the ANOVA results confirm that the regression model is statistically valid, and the selected independent variable makes a meaningful and significant contribution to explaining the variation in the outcome variable.

Table 6. SAR ANOVA

Source	df	Sum of Square	Mean square	F	p
Regression	1	1,303.75	19.08	29.48	0.000005
Residual	39	1,724.78	44.24	/	/
Total	40	3,027.96	/	/	/

The ANOVA results for the simple linear regression model indicate a highly significant relationship between the independent variable and the dependent variable (Table 7). The regression explains a sum of squares of 1,305.975 with 1 degree of freedom, while the residual variance accounts for 2,498.529 across 39 degrees of freedom, resulting in a total variance of 3,804.504 (Table 7). The mean square for the regression is therefore 1305.975, compared to a residual mean square of 64.06. This yields an F-statistic of 20.38, associated with a p-value of 0.000057, which is well below the conventional significance threshold of 0.05 (Table 7). This strong statistical evidence allows us to reject the null hypothesis that the independent variable has no effect. The model explains approximately 34.3% of the variance in the dependent variable, as indicated by the coefficient of determination (R^2). Overall, these results demonstrate that the predictor variable significantly contributes to explaining the variability of the outcome, making the regression model a valid tool for prediction in this context.

Table 7. Na% ANOVA

Source	df	Sum of Square	Mean square	F	p
Regression	1	1,305.975	69.10	20.38	0.000057
Residual	39	2,498.529	64.06	/	/
Total	40	3,804.504	/	/	/

The spatial autocorrelation analysis based on Moran's I (Table 8) reveals consistent positive spatial clustering patterns in both SAR and Na% values across the dry and wet seasons. Most Moran's I values for SAR range between 0.21 and 0.27 in both seasons, indicating a moderate to strong positive spatial autocorrelation suggesting that wells with similar salinity levels are spatially clustered rather than randomly distributed. The Na% values also show positive autocorrelation, though slightly lower on average, with Moran's I typically ranging from 0.15 to 0.23. The stability of Moran's I across seasons suggest that the spatial distribution of salinity and sodium concentration does not significantly change between wet and dry periods. Notably, the highest Moran's I values for both SAR and Na% are observed in well 41 (0.333-0.351 for SAR and 0.367-0.350 for Na %), indicating particularly strong spatial clustering in that area. These results confirm that spatial processes likely driven by hydrogeological structures or anthropogenic influences govern the distribution of salinity and sodium across the study area.

Table 8. Indice of Moran for SAR and Na% (dry and wet season)

Wells	I Moran's SAR dry season	I Moran's SAR wet season	I Moran's Na% dry season	I Moran's Na% wet season
1	0.214	0.209	0.157	0.155
2	0.216	0.221	0.163	0.171
3	0.234	0.239	0.185	0.195
4	0.234	0.235	0.192	0.193
5	0.240	0.240	0.198	0.197
6	0.232	0.239	0.185	0.193
7	0.213	0.229	0.166	0.179
8	0.219	0.237	0.172	0.191
9	0.240	0.250	0.195	0.211
10	0.247	0.249	0.205	0.209
11	0.246	0.248	0.204	0.206
12	0.248	0.249	0.207	0.207
13	0.248	0.241	0.207	0.198
14	0.249	0.241	0.208	0.198
15	0.246	0.238	0.201	0.189
16	0.243	0.234	0.198	0.183
17	0.245	0.241	0.203	0.198

Table 8. Indice of Moran for SAR and Na% (dry and wet season) (cont.)

Wells	I Moran's SAR dry season	I Moran's SAR wet season	I Moran's Na% dry season	I Moran's Na% wet season
18	0.235	0.234	0.192	0.189
19	0.231	0.232	0.187	0.187
20	0.240	0.240	0.195	0.195
21	0.228	0.237	0.185	0.187
22	0.228	0.237	0.188	0.190
23	0.221	0.236	0.194	0.205
24	0.198	0.225	0.183	0.198
25	0.201	0.220	0.184	0.194
26	0.232	0.240	0.202	0.208
27	0.241	0.239	0.199	0.192
28	0.241	0.238	0.199	0.191
29	0.258	0.259	0.217	0.217
30	0.263	0.264	0.219	0.220
31	0.266	0.268	0.222	0.225
32	0.264	0.264	0.227	0.228
33	0.255	0.256	0.224	0.223
34	0.219	0.246	0.181	0.219
35	0.220	0.233	0.177	0.197
36	0.245	0.233	0.206	0.192
37	0.233	0.213	0.196	0.198
38	0.234	0.196	0.194	0.196
39	0.229	0.183	0.181	0.183
40	0.230	0.182	0.182	0.182
41	0.333	0.351	0.367	0.350

3.4. Recommendation

To reduce the risks associated with high salinity, local farmers can implement several effective strategies. Selecting salt-tolerant crops such as barley, cotton, olive trees, date palms, or sorghum can help maintain productivity despite saline conditions. Crop rotation is also beneficial to prevent excessive salt buildup in the soil. Improving irrigation methods by shifting from traditional flood irrigation to more efficient systems like drip or sprinkler irrigation minimizes salt accumulation near plant roots. Additionally, periodic leaching with excess water can flush salts away if good drainage is available. Soil management techniques, including the use of gypsum to neutralize sodium and the addition of organic matter to enhance soil structure, further mitigate salinity effects. Enhancing drainage through subsurface systems or preserving natural drainage pathways helps prevent waterlogging and salt concentration. Mixing saline groundwater with higher quality water sources and storing rainwater during wet seasons can also reduce irrigation water salinity. Finally, regular monitoring of water quality, especially salinity levels and Sodium Adsorption Ratio (SAR), allows farmers to adapt their irrigation practices and crop selection to current conditions, ensuring more sustainable agricultural production in the face of salinity challenges.

4. CONCLUSION

This study demonstrates that groundwater quality in the Bir Chouhada, Souk Naamane, and Ouled Zouai plains is strongly influenced by geological formations and seasonal variations, significantly affecting its suitability for irrigation in this semi-arid region. According to the Wilcox classification, during the dry season, 58.53% of wells provide good-quality water, 36.58% are poor, and 4.87% are unsuitable for irrigation. In the wet season, water quality improves with 65.85% good, 31.72% poor and only 2.43% unsuitable, reflecting dilution effects from rainfall. Spatial mapping on a 100 m × 100 m grid reveals notable heterogeneity linked to lithology, with 25% of the area classified as good by the Riverside method compared to 40.44% by Wilcox, which also identifies 58.36% poor and 1.18% unsuitable zones. Geological factors, particularly Miocene gypsiferous and clay-rich

formations, play a key role in water mineralization and sodicity, causing progressive water quality degradation along groundwater flow paths. Moran's I spatial autocorrelation analysis shows moderate to strong clustering of SAR and sodium percentage (%Na), especially near well 41, indicating geographically concentrated salinity and sodicity likely related to hydrogeological structures or human activities. These conditions pose significant agronomic risks, as elevated SAR and sodium promote clay dispersion, degrading soil structure and permeability, which restricts water and air movement. Consequently, irrigation is sustainable mainly on well-drained soils with salt-tolerant crops such as tobacco, cotton, barley, artichoke, and date palms. Regression and ANOVA analyses confirm the significance of key variables with R^2 values between 34.3% and 43%, indicating moderate explanatory power and suggesting other factors remain to be explored. Despite these insights, the study is limited by the number of analyzed parameters, sampling points, and seasonal coverage, lacking continuous monitoring and detailed consideration of anthropogenic and seasonal influences. Future research should incorporate more comprehensive, year-round monitoring, a broader range of physico-chemical indicators, advanced hydrogeological modeling, and socio-economic data integration to support sustainable groundwater management in this vulnerable semi-arid agricultural zone.

AUTHOR CONTRIBUTIONS

Conceptualization: N. Zair, I. Khater; Methodology: N. Zair; Software: I. Khater; Validation: I. Khater, N. Zair, A. Miloudi; Formal analysis: I. Khater; Investigation: I. Khater, N. Zair; Resources: A. Khechekhouche; Data curation: I. Khater; Writing original Draft: I. Khater, N. Zair; Writing Review and Editing: A. Khechekhouche, B. Attoui; Visualization: I. Khater, N. Zair, A. Miloudi; Supervision: N. Zair; Project administration: N. Zair; Funding acquisition: N. Zair.

DECLARATION OF CONFLICT OF INTEREST

The authors declare that they have neither conflict nor competing of interests.

REFERENCES

Attoui B, Sayad L, Majour H, Harizi K, Drouiche N, Bouguerra H. Water quality index, risk assessment in a coastal aquifer: The Djendjen aquifer (Jijel, Algeria). Journal of Coastal Conservation 2024a;28:Article No. 1031.

Attoui B, Sayad L, Majour H, Boudjebieur E, Boulahia A, Lamrou W. Impact of technical landfill Bouguerguer on water resources and the environment (North-East Algeria). Carpathian Journal of Earth and Environmental Sciences 2024b;19(1):Article No. 287.

Ayers RS, Westcot DW. Water Quality in Agriculture. FAO Irrigation and Drainage Paper 29. FAO; 1988. p. 1-165.

Anyango GW, Bhowmick GD, Bhattacharya NS. A critical review of irrigation water quality index and water quality management practices in micro-irrigation for efficient policy making. Desalination Water Treat 2024;318:Article No. 100304.

Baloch MYJ, Zhang W, Cha J, Al Shoumi BA, Tariq A, Iqbal J, et al. Groundwater contamination, fate, and transport of fluoride and nitrate in Western Jilin, China: Implications for water quality and health risks. Environmental Economics and Policy Studies 2025;7:Article No. 1189.

Baloch MYJ, Zhang W, Zhang D, Al Shoumi BA, Iqbal J, Li S, et al. Evolution mechanism of arsenic enrichment in groundwater and associated health risks in Southern Punjab, Pakistan. International Journal of Environmental Research and Public Health 2022a;19:Article No. 13325.

Baloch MYJ, Zhang W, Al Shoumi BA, Nigar A, Elhassa AAM, Elshekh AEA, et al. Hydrogeochemical mechanism associated with land use land cover indices using geospatial, remote sensing techniques, and health risks model. Sustainability 2022b;14(24):Article No. 16768.

Benmerabet N, Sedrati N, Djabri L. Hydrogeochemical processes, water-rock interactions, and the suitability of groundwater in a semi-arid region, Northeastern Algeria. Water Supply 2025;25(3):Article No. 404.

Bremond R, Perredon C. Water Quality Parameters. Paris: Ministère de l'Environnement; 1979.

Devez A. Characterization of the Risks Induced by Agricultural Activities on Aquatic Ecosystems [dissertation]. Montpellier: Ecole Nationale du Génie Rural des Eaux et des Forêts (ENGREF); 2004.

Hydraulic Department of the Wilaya of Oum El Bouaghi (DHW). Hydrogeological Study of the Plain of Bir Chouhada - Souk Naamane - Ouled Zouai (Wilaya of Oum El Bouaghi). DHW; 2004.

Eaton FM. Significance of carbonates in irrigation waters. Soil Science 1950;69:123-33.

Jarray H, Azaza FH, Zammouri M, Ouessar M, Barbieri M, Carrey R, et al. Geochemical evaluation of groundwater quality and its suitability for drinking and irrigation purposes in arid and semiarid regions: The case of Zeuss-Koutine and a part of Mio-Plio-Quaternary aquifers (SE Tunisia). Physics and Chemistry of the Earth 2023;132:Article No. 103483.

Jabeen M, Ahmed SR, Ahmed M. Enhancing water use efficiency and grain yield of wheat by optimizing irrigation supply in arid and semi-arid regions of Pakistan. Saudi Journal of Biological Sciences 2022;29(2):878-85.

Habiba M, Attoui B, Bouguerra H. Hydrochemical dynamics of the denitrification process of the aquifer: Case of the lower plain of the Seybouse watershed, North-eastern Algeria. Doklady Earth Sciences 2024;514:161-8.

Hair JF, Black WC, Babin BJ, Anderson RE. Multivariate Data Analysis. 7th ed. Pearson; 2014.

Hemila ML. Hydrogeology, Modeling and Management of Water Resources of the Alluvial Plain of the Meskiana Basin, Haut Mellègue, East Algeria [dissertation]. Besançon: University of Besançon; 1988.

Helena B, Pardo R, Vega M, Barrado E, Fernández JM, Fernández L. Temporal evolution of groundwater composition in an

alluvial aquifer (Pisuerga River, Spain) by principal component analysis. Water Research 2000;34(3):807-16.

Hussei EE, Baloch MYJ, Nigar A, Abualkhair HF, Aldawood FK, Tageldin E. Machine learning algorithms for predicting the water quality index. Water 2023;15(20):Article No. 3540.

Iqbal J, Amin G, Su C, Haroon E, Baloch MYJ. Assessment of land cover impacts on the groundwater quality using hydrogeochemical and geospatial techniques. Environmental Science and Pollution Research 2023;31:Article No. 29628.

Gouaidia L. Evaluation of the vulnerability of a water table in a semi-arid environment and comparison of applied methods: Case of the Meskiana water table (East Algeria). Sécheresse 2011;22(1):35-42.

Gouaidia A, Bouchemal F, Kaddour Z, Khachena S, Miloudi A. Performance of a wastewater treatment plant in south-eastern Algeria. International Journal of Energetica 2020;5(2):47-51.

Khan MN, Fifield S, Power DM. The impact of the COVID-19 pandemic on stock market volatility: Evidence from a selection of developed and emerging stock markets. SN Business and Economics 2024;4:Article No. 63.

Khechekhouche A, Benhaoua B, Attia M E H, Driss Z, Manokar A, Ghodbane M. Polluted groundwater treatment in Southeastern Algeria by solar distillation. Environment and Natural Resources Journal 2020;6(1):1207-11.

Lado JJ, García-Quismondo E, Fombona-Pascual A, Mavrandonakis A, Cruz C, Oropeza FE, et al. Tuning mono-divalent cation water composition by the capacitive ion-exchange mechanism. Water Research 2024;255:Article No. 121469.

Liu Y, Li F, Liu H, Hou Y, Nazir N. Study and application of coupling relationship between water-salt-resistivity-soil structure in saline soils in arid and semi-arid areas of northwest China. Environmental Research 2024;241:Article No. 117608.

Malik MJ, Ahmad S, Ahmad R. Geological evidence of paleo-earthquakes on transverse right-lateral strike slip fault along the NW Himalayan front: Implications towards fault segmentation and strain partitioning. Journal of Asian Earth Sciences 2023;244:Article No. 105518.

Meng L, Yan Y, Jing H, Baloch MYJ, Du S. Large-scale groundwater pollution risk assessment research based on artificial intelligence technology: A case study of Shenyang City in Northeast China. Ecological Indicators 2024; 169:Article No. 112915.

Miloudi A, Zair N, Khechekhouche A, Attoui B, Mega N, Khechana S, et al. Assessment of groundwater quality using the Water Quality Index (WQI) and Nitrate Pollution Index (NPI) in the El-Oued region (South-East Algeria). Tobacco Regulatory Science 2024;10(1):1676-90.

Montgomery DC. Design and Analysis of Experiments. 9th ed. New York: Wiley; 2017.

Pan X, Zhang J, Zhou Y, Wan C. Effects of deficit winter irrigation with overwintering freezing on oases soil salinization and alkalization. Pedosphere 2024;35(2):569-79.

Person J. Irrigation and drainage in Tunisia problem of soil salinity and water. Bull BRGM, 2nd Series. 1978;3(2):143-51.

Richards LA. Diagnosis and Improvement of Saline and Alkali Soils (USDA Agriculture Handbook No. 60). Washington, DC: U.S. Department of Agriculture; 1954.

Rouabhia AEK, Djabri L. Irrigation and the risk of saline pollution: A case study of groundwater from the Miocene aquifer in the El Ma El Abiod plain. Larhyss Journal 2010;(8):55-67.

Sousa AF, Weber OB, Crisostomo LA, Escobar MEO, Oliveira TS. Changes in soil soluble salts and plant growth in a sandy soil irrigated with treated water from oil extraction. Agricultural Water Management 2017;193:Article No. 1016.

Sumner ME. Sodic soils: New perspectives. Australian Journal of Soil Research 1993;31:683-750.

Subba Rao N. Seasonal variation of groundwater quality in a part of Guntur District, Andhra Pradesh, India. Environmental Geology 2006;49:413-29.

Wilcox LV. Classification and Use of Irrigation Water. Circular 969. Washington DC: US Department of Agriculture; 1955.

Zar JH. Biostatistical Analysis. 5th ed. Upper Saddle River: Prentice Hall; 2010.

Zair N, Chaab S, Bertrand C. Aquifer vulnerability to pollution of Oum El-Bouaghi region in North East of Algeria. Management of Environmental Quality 2017;28(3):384-99.

Zair N. Hydrogeological Characteristics of Aquifers in the Region of Oum-El-Bouaghi: Problems of Depletion and Salinity of Their Waters [dissertation]. Annaba: University of Annaba; 2017.

Zair N, Attoui B, Miloudi A, Khechekhouche A. Evaluation of surface water quality and contamination status of the Zeremna Valley sub-basin in the Skikda Region (North-Eastern Algeria). Food and Environment Safety Journal 2021; 20(3):235-46.

Zair N, Attoui B, Miloudi A, Khechekhouche A, Souyei B. Assessing drinking water quality in Eloued, south-East Algeria, using the groundwater pollution index (GPI) and the synthetic pollution index (SPI) model. Environmental Monitoring and Assessment 2024;196:Article No. 1019.

Zair N, Attoui B, Miloudi A. Characterization of the state of pollution by nitrates in the groundwater in arid zones: Case of Eloued district, South-East Algeria. International Journal of Environmental and Ecological Engineering 2025;19(1):5-12.

Environment and Natural Resources Journal

Volume 24
Issue 1
2026

Vegetation Condition and Potential Seed Rain in a Fire-Affected Tropical Forest Ecosystem Dominated by the Endangered *Eucalyptus urophylla* in Mutis Forest, East Nusa Tenggara-Indonesia

Demak E.R. Damanik[1,2], Devi N. Choesin[3], and Endah Sulistyawati[3*]

[1]*Biology, School of Life Sciences and Technology, Institut Teknologi Bandung, Bandung, Indonesia*
[2]*Faculty of Science and Engineering, Nusa Cendana University, Kupang, Indonesia*
[3]*School of Life Sciences and Technology, Institut Teknologi Bandung, Bandung, Indonesia*

ARTICLE INFO

Received: 12 Jun 2025
Received in revised: 19 Aug 2025
Accepted: 28 Aug 2025
Published online: 21 Oct 2025
DOI: 10.32526/ennrj/24/20250151

Keywords:
Eucalyptus urophylla/ Mutis forest/ Seed production/ Vegetation diversity

*** Corresponding author:**
E-mail: endah@itb.ac.id

ABSTRACT

Global deforestation and climate change-induced forest fires disrupt tropical forest functions. On the other hand, fires can be ecologically beneficial by increasing seed rain diversity and regeneration. In the Mutis forest, Indonesia, recurrent fires and deforestation threaten the endangered native species *Eucalyptus urophylla*. This study compared vegetation and seed rain between burned and unburned areas of the Mutis forest. Vegetation data were collected from 50 plots (10×10 m), in each area by measuring trees with a diameter at breast height (DBH; 1.3 m above ground level) ≥3 cm. Seed rain was collected for seven months using 50 seed traps (Ø 50 cm) in each area. The results showed that *Eucalyptus urophylla* has a significant ecological role in the both sites, as shown by its highest Importance Value Index (IVI) in both burned (177.05%) and unburned sites (115.70%). Four seed species were found in both sites, i.e., *E. urophylla*, *Olea paniculata*, *Pittosporum timorense*, and *Rapanea hasseltii*. The most abundant seeds were *E. urophylla*, 435 seeds at the burned site and 314 seed at the unburned site, indicating their origin from local vegetation. Seed species diversity was low in both burned (Shannon H'=0.21) and unburned (H'=0.39) areas. Therefore, conservation are necessary to maintain the sustainability of this forest. Recommended actions included seed collection in April to May, cultivation of *E. urophylla* for post-fire restoration, and implementing fire management strategies in the Mutis forest area.

HIGHLIGHTS

Mutis forest shows apparent vegetation shifts due to fire disturbances. Burned plots are dominated by fire-tolerant *Eucalyptus urophylla*. Most of the seed rain collected originated from plants present in the area. Low seed diversity may hinder natural forest regeneration.

1. INTRODUCTION

Global deforestation is an escalating threat to biodiversity and the ecological integrity of tropical forests, driven primarily by human activities like extensive logging and land-use conversion (Gould et al., 2024). In addition, climate change exacerbates forest degradation through rising temperatures, irregular rainfall patterns, prolonged droughts, and increasingly intense wildfires (IPCC, 2023). There are three common types of fires, namely (1) underground fires that occur in the organic soil layer, (2) surface fires that occur just above the soil surface, and (3) crown fires that occur in the crowns of trees (Bond and van Wilgen, 2013). Wildfires can alter vegetation structure and composition, inhibit natural regeneration, and reduce the abundance and diversity

Citation: Damanik DER, Choesin DN, Sulistyawati E. Vegetation condition and potential seed rain in a fire-affected tropical forest ecosystem dominated by the endangered *Eucalyptus urophylla* in Mutis Forest, East Nusa Tenggara-Indonesia. Environ. Nat. Resour. J. 2026;24(1):29-41. (https://doi.org/10.32526/ennrj/24/20250151)

of plant species (Arasa-Gisbert et al., 2024; Chalermsri et al., 2020). Fires can significantly alter ecosystem processes across a landscape, including increasing soil erosion (Bond and Keane, 2017), changing forest composition, and directly impacting vegetation, which may lead to long-term changes in forest structure and ecosystem function (Armenteras et al., 2021).

Nevertheless, fires can also provide ecological benefits, such as increasing seed rain diversity in disturbed areas compared to undisturbed ones (Leder et al., 2022). Regularly occurring fires can eradicate invasive species and promote the growth of native plants. In addition, fire-adapted plants, such as certain grasses and shrubs, often emerge after a fire, creating opportunities for local wildlife to return and thrive (Pivello et al., 2021). Fire can also trigger flowering, seed dispersal, or seed germination (Bond and Keane, 2017) and seed development in Eucalyptus (Florence, 2004). Seeds from plant families including Anacardiaceae, Apiaceae, Cistaceae, Convolvulaceae, Fabaceae, Malvaceae, and Rhamnaceae are known to germinate when exposed to heat from fires (Keeley and Pausas, 2022).

Repeated deforestation and wildfires contribute to a decline in mature tree populations, disrupting natural seed rain potential (Arasa-Gisbert et al., 2024). Seed rain constitutes a crucial ecological process and serves as a key indicator of vegetation regeneration, reflecting the spatial distribution and abundance of seeds dispersed by abiotic and biotic agents, including wind, gravity, and animals (Baskin and Baskin, 2014; Rocha et al., 2021). It plays an essential role in facilitating natural regeneration, shaping initial species composition, and influencing successional pathways (Huanca Nuñez et al., 2021). Vegetation influences seed rain dynamics through various mechanisms (Rocha et al., 2021), and seed rain analysis offers valuable insights into ecosystem conditions (Procknow et al., 2020).

Indonesia ranks third in the world in terms of deforestation rates over the past decade (FAO, 2020). One of the most affected by deforestation and recurring forest fires is the Mutis forest, located in the East Nusa Tenggara Region. Fires in the Mutis Timau area are dominated by surface fires (Kaho and Marimpan, 2014). The dominant vegetation in this area is *Eucalyptus urophylla*, a species native to Indonesia and Timor-Leste (IUCN, 2019; Monk et al., 2000), which is naturally distributed throughout much of eastern Indonesia (Pepe et al., 2004). Despite its important ecological role in maintaining the structure and function of local ecosystems, this species has been categorized as Critically Endangered on the IUCN Red List, with a projected population decline exceeding 50% over the next century (IUCN, 2019).

Eucalyptus urophylla is a resilient species that grows rapidly in soils with limited organic matter content (Monk et al., 2000), making it commercially significant (Barros et al., 2022). It typically initiates flowering during the dry season, with seed maturation occurring within approximately six months. The species relies predominantly on biotic pollinators—such as insects, birds, and mammals—while wind contributes only marginally to the pollination process (Sein and Mitlöhner, 2011). Even though genus Eucalyptus was known to have limited distribution capacity (Booth, 2017), its epicormic resprouting structure facilitates regeneration after disturbance (Crisp et al., 2011), resulting in the resilience of *E. urophylla* to persist. Fire acts as an ecological driver influencing the spatial regeneration of Eucalyptus (Dorrough and Moxham, 2005). For example, seedlings of *Eucalyptus regnans* have been observed to regenerate vigorously after moderate to high-intensity fires in southeastern Australia, particularly in areas with adequate rainfall (Smith et al., 2016).

The potential of fire to affect vegetation dynamics, including seed rain production, and forest regeneration in a forest dominated by Eucalyptus, has been widely studied. However, no studies have yet been done in a forest dominated by *E. urophylla*, such as Mutis forest. Therefore, this study aimed to compare vegetation, forest structure, and seed rain conditions in burned and unburned areas within Mutis forest. The outcome of this study is expected to provide foundational insights into seed rain dynamics and also serve as basic information for conservation and restoration efforts in the Mutis Timau National Park Area.

2. METHODOLOGY

2.1 Study area

This study was conducted at the Mutis forest area, a part of Mutis Timau National Park, East Nusa Tenggara, Indonesia. Before being declared a national park, Mutis forest was a nature reserve covering an area of 12,315.61 ha. The status was officially changed on 8 September 2024, to Mutis Timau National Park following the issuance of Decree of the Minister of Environment and Forestry No. 946 of 2024. The national park covers a total area of 78,789 ha,

including Mutis forest and Mutis Timau Protection forest (Rahmat, 2024). Mutis forest receives the highest rainfall on Timor Island, with an annual average of 2,000-3,000 mm. The rainy season last from November to March, and temperatures ranging between 14°C to 29°C in normal conditions and reaching 9°C in extreme conditions (BBKSDA NTT, 2018; Putri et al., 2024). Fires in the Mutis forest area usually occur between August and October (Kaho and Marimpan, 2014).

Data collection was done from February to September 2023 in forested areas within the administrative boundaries of Fatumnasi Village. According to data from the Mutis Nature Reserve Resort Centre (unpublished), this region experienced a high incidence of forest fires in 2019. The research period was selected with consideration for environmental factors including weather conditions and rainfall. The study sites (Figure 1) were classified into burned areas and unburned areas based on the presence or absence of visible fire scars on the trunks of *Eucalyptus urophylla* trees, which served as indicators for site classification. A general description of the study site is presented in Table 1.

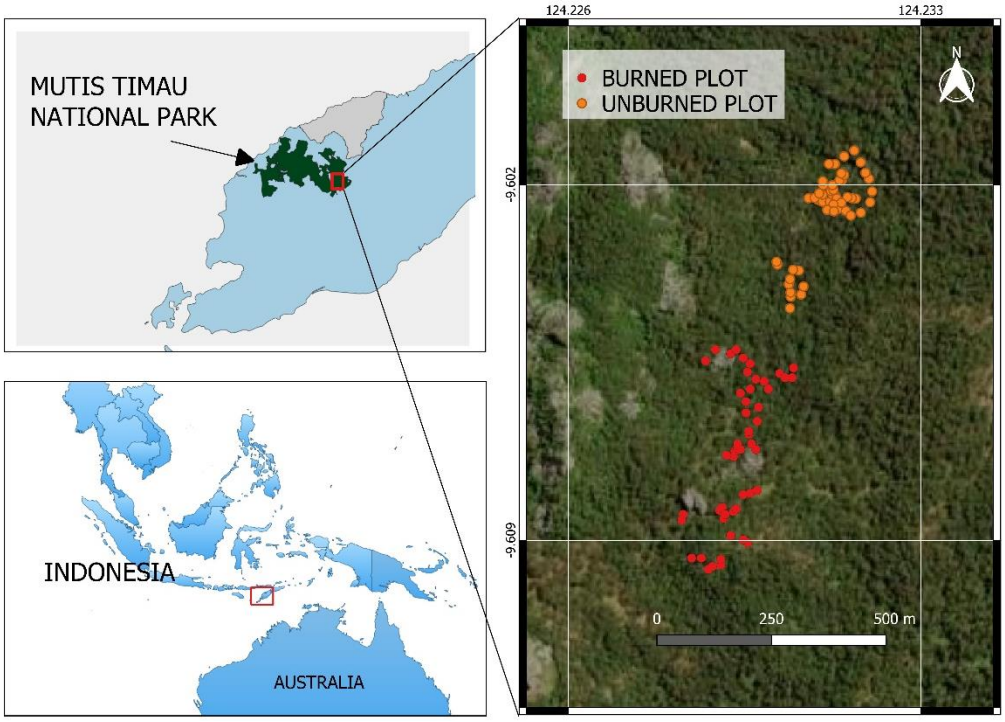

Figure 1. The location of study sites in Mutis Forest, East Nusa Tenggara, Indonesia

Table 1. General description of the study location

Description	Mutis Timau National Park Study Location	
	Burned area	Unburned area
Village	Fatumnasi	
Geologic conditions[a]	A mixture of volcanic rock and limestone[a]	
Annual rainfall (mm)[b]	2,000-3,000[b]	
Temperature conditions [b] (°C)	14-29[b]	
Longitude	124°13'41"- 124°13'49" E	124°13'46"- 124°13'53.6" E
Latitude	9°36'32.4" -9°36'21.6" S	9°36'06" -9°36'26.2" S
Soil conditions[c]		
- Average organic C (%)	9.16[c]	7.19[c]
- Average pH of soil	4.6[c]	3.9[c]
- Soil Humidity (%)	71.7[c]	81.3[c]

[a] (Fisher,L et al., 1999); [b] (Putri et al., 2024); [c] (Research documentation, analyzed in laboratory, unpublished data)

2.2 Vegetation survey

Due to limited accessibility and existing field conditions in the forest area, the site selection was influenced by resource limitations and environmental factors, including extreme weather and landslides that occurred during the data collection period. The lack of replication at the treatment level is a limitation of this study. Vegetation measurements were conducted in February to March 2023 using 10×10 m plots. A total of 50 plots were established in each area. Plots were randomly placed approximately 30 m from the trail to minimize edge effects. In each plot, all trees with a diameter at breast height (DBH, measured at 1.3 m above ground level) of at least 3 cm were measured, marked, and identified.

Soil pH and moisture were measured directly in the field. Soil samples were collected for analysis of organic carbon content at the Kupang State Polytechnic laboratory. Rainfall data during the study period were obtained from unpublished records provided by the Ministry of Public Works and Housing of Indonesia. Plant samples were collected and identification was done at Herbarium Bandungense, Institute of Technology Bandung, with assistance from a curator and a plant identification application (Yang et al., 2022).

2.3 Seed rain collection

Seed rain of tree species was collected by installing seed traps in the study area dominated by *E. urophylla*. The vegetation plots were located around the seed traps. Since the seeds of *E. urophylla* and several other species were relatively small, the seeds that were collected and analysed were the ones that were still in the capsule. Fifty traps on each site were installed in February 2023. Traps used were a conical or funnel-shaped seed trap made of mesh with a surface area of 0.196 m² each (Figure 2), resulting in a total seed capture area of 9.8 m². Each trap was tied to 3 poles at a height of 1 m above the ground. Seed traps were set randomly, and purposive sampling was performed with a minimum distance of 10 m between traps.

Seeds were collected from the traps from March to September 2023. The sampling process encountered significant challenges due to extreme weather, landslides, and the substantial loss of traps. Initially, seed collection was planned every 10 days. However, due to limited human resources in the field and unpredictable weather conditions, the seed collection intervals were not the same. Nonetheless, up to two seed collections were conducted in each month, resulted in a total of twelve collections. During the collection, some seed traps were unusable due damage caused by strong winds, heavy rainfall, and being stolen. These disruptions occurred sporadically during the collection period. More details on the seed collection period and the condition of seed traps are presented in Table 2.

Figure 2. The setup of the seed trap at the study site

The number of seed traps decreased significantly since the first data collection (S01). At the end of data collection (S12), only 14 seed traps remained, consisting of six seed traps in burned area and eight seed traps in unburned area. Even though the traps were set in areas that human rarely visited, the decrease in the number of functioning traps was mainly due to human activities, especially individuals entering the forest to collect wood. Subsequently, the data for seed rain presented in this study utilized data obtained from traps that could record data consistently from the first to the 12th data collection. There were 12 collections periods in total, with a minimum interval of 11 days between collections. The collected seeds were classified into three categories, i.e., category I: damaged or rotten fruits or seeds; category II: fruits or seeds that were intact, ripe, and had no damage or decay; category III: fruits or seeds that were young, small, and immature but not damaged or rotten.

Table 2. The seed collection period and the number of remaining seed traps

Sampling codes	Period	Burned area		Unburned area	
		Time range of seed collection	Number of remaining traps	Time range of seed collection	Number of remaining traps
S01	February	20 February - 8 March 2023	49	15 February-4 March 2023	50
S02	March - I	9 March-20 March 2023	45	5 March- 21 March 2023	50
S03	March - II	21 March - 3 April 2023	42	22 March- 3 April 2023	48
S04	April - I	4 April - 14 April 2023	38	4 April - 14 April 2023	48
S05	April - II	15 April - 5 May 2023	31	15 April-5 May 2023	43
S06	May - I	6 May - 19 May 2023	29	6 May-19 May 2023	41
S07	May - II	20 May - 2 June 2023	17	20 May-2 June 2023	33
S08	June	3 June - 26 June 2023	15	3 June-26 June 2023	33
S09	July - I	27 June-14 July 2023	13	27 June-14 July 2023	30
S10	July - II	15 July-5 August 2023	12	15 July-5 August 2023	28
S11	August	6 August -30 August 2023	11	6 August -31 August 2023	21
S12	September	31 August -21 September 2023	**6**	1 September-21 September 2023	**8**

2.4 Data analysis

- Vegetation structure and seed rain condition

The data analysis was done using Minitab® 21.4.3 (64-bit). The species density (Di) at the plot level was calculated using Equation (1) (Tebabal et al., 2024):

$$\text{Species Density (individual/ha)} = \frac{\text{The number of a species (individual)}}{\text{Total area sampled (ha)}} \quad (1)$$

The Mann-Whitney test was used to compare vegetation at burned and unburned locations.

The differences in forest structure, species composition, and forest similarity were measured using the Important Value Index (IVI), which was calculated as Equation (2):

$$\text{Important Value Index (IVI\%)} = (\text{RDi}) + (\text{RFi}) + (\text{RDo}) \quad (2)$$

Where; RDi is Relative density, RFi is Relative frequency, RDo is Relative dominance, which were calculated using Equation (3), (4), (5):

$$\text{Relative Density (RDi \%)} = \frac{\text{Density of a species}}{\text{Density of all species}} \times 100\% \quad (3)$$

$$\text{Relative Frequency (RFi \%)} = \frac{\text{Frequency of a species}}{\text{Frequency of all species}} \times 100\% \quad (4)$$

$$\text{Relative Dominance (RDo \%)} = \frac{\text{Dominance of a species}}{\text{Dominance of all species}} \times 100\% \quad (5)$$

The species diversity of an area and colected seeds were analyzed the Shannon-Wiener index for both burned and unburned area (Shannon and Weaver, 1949).

The Chi-square test was used for the analysis of differences in the distribution of DBH classes of *E. urophylla* and other species in burned and unburned sites.

The Kruskal Wallis test was used to analyse differences between seed categories (CI, CII, CIII) in burned and unburned locations.

The relationship between stand density and seed density in burned and unburned sites was analysed using Spearman correlation. This correlation was also used to analyse the relationship between rainfall and seed density.

3. RESULTS

3.1 Condition and structure vegetation in fire-affected and intact forest sites

Vegetation surveys of trees with DBH ≥3 cm revealed that the burned area has slightly less diverse trees (10 families, 12 species) with a lower density (702 individuals/ha) than the unburned area (11 families, 14 species, 790 individuals/ha. However, Mann-Whitney U test showed no significant difference between the sites ($p=0.201$; $p>0.05$). The burned area was dominated by *E. urophylla*, with a density of 364 individuals/ha (Figure 3). Meanwhile, *Dacrycarpus imbricatus* emerged as the most abundant species in the unburned area (230 individuals/ha). Nevertheless, based on IVI, *E. urophylla* was the dominant species at both sites (Table 3). Two tree species, i.e., *Cyathea contaminans* and *Euodia macrophylla* were only found in the unburned area.

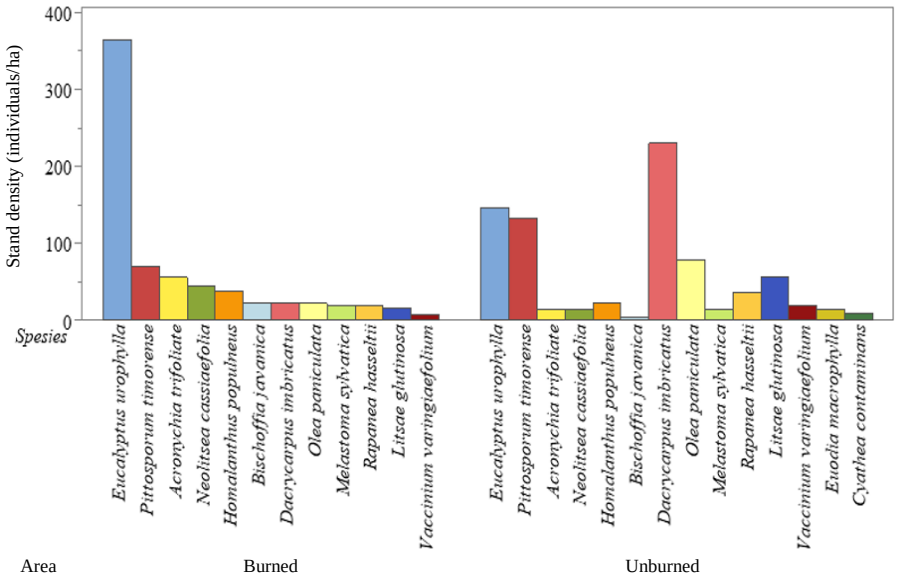

Figure 3. Stand density (individuals/ha) of tree vegetation in burned and unburned areas

Table 3. The Importance Value Index (IVI) of the most important species in burned and unburned site

Spesies	RDi (%)	RFi (%)	RDo (%)	IVI (%)
Burned Site				
Eucalyptus urophylla	51.85	32.89	92.31	177.05
Pittosporum timorense	9.97	14.47	0.53	24.98
Acronychia trifoliate	7.98	11.84	1.06	20.87
Neolitsea cassiaefolia	6.27	7.24	0.13	13.64
Homalanthus populneus	5.41	7.89	0.09	13.40
Dacrycarpus imbricatus	3.13	5.92	2.45	11.51
Olea paniculata	3.13	3.29	1.44	7.87
Acalypha caturus	2.85	4.61	0.02	7.48
Litsae glutinosa	2.28	4.61	0.02	6.91
Bischoffia javanica	3.13	2.63	1.09	6.86
Rapanea hasseltii	2.85	3.29	0.45	6.59
Vaccinium varingiaefolium	1.14	1.32	0.40	2.86
Unburned site				
Eucalyptus urophylla	18.48	21.96	75.25	115.70
Dacrycarpus imbricatus	29.11	21.50	17.56	68.17
Pittosporum timorense	16.71	15.42	0.57	32.70
Olea paniculata	9.87	10.28	3.26	23.41
Litsae glutinosa	7.09	8.88	0.63	16.59
Rapanea hasseltii	4.56	4.21	0.49	9.25
Vaccinium varingiaefolium	2.53	3.27	0.46	6.27
Homalanthus populneus	2.78	3.27	0.13	6.19
Euodia macrophylla	1.77	2.34	0.75	4.86
Neolitsea cassiaefolia	1.77	2.34	0.56	4.67
Acalypha caturus	1.77	2.34	0.08	4.19
Acronychia trifoliate	1.77	1.87	0.10	3.75
Cyathea contaminans	1.27	1.87	0.07	3.20
Bischoffia javanica	0.51	0.47	0.08	1.05

When comparing the size class distribution of *E. urophylla* to "other species", a pattern was observed. There was a higher density of *E. urophylla* in small size classes (Figure 4) in burned sites, indicating a higher regeneration capability under fire-affected conditions. Meanwhile, in the unburned sites, the stand density in the low and medium DBH classes was dominated by "other species" (Figure 4). The Chi-square test showed a statistically significant difference in the DBH class distribution between *Eucalyptus urophylla* and "other species" in both burned and unburned locations (χ^2=870.756; df=27; p<0.001).

3.2 Condition of seed rain

As previously mentioned several traps were lost due to theft or damaged by extreme weather. At the time of the last sampling (S12), only 14 seed traps were still functional—6 of which were located in the burned area and 8 in the unburned area. Data from the 14 remaining traps were used for seed rain analysis, since they were considered representative and could consistently record seed deposition dynamics throughout twelve sampling periods. Four seed species were identified and present at both sites, i.e., *E. urophylla*, *Olea paniculata*, *Pittosporum timorense*, and *Rapanea hasseltii.* The species composition, seed quantities, and seed density in each area are presented in Table 4.

From first (S01) to last (S12) sampling events in 14 seed traps, *E. urophylla* seeds had the highest density at both study sites (Table 4). The highest seed density was recorded in the last sampling period at the burned site (Figure 5). In contrast, the lowest density—indicated by the absence of seeds in the trap—was recorded in the first sample at the unburned site (Figure 5). The high density of *E. urophylla* seeds observed in both area was analysed further to explore differences in seed distribution between the two sites. The Mann-Whitney test revealed that the density of *E. urophylla* seeds between burned and unburned areas differs significantly (p=0.046). Figure 6 presents seed density data *E. urophylla* in three seed categories.

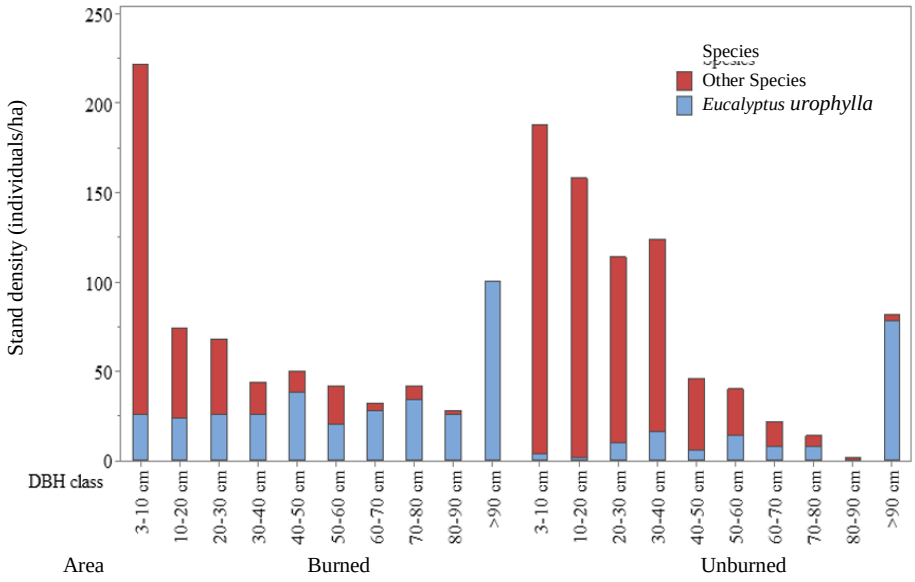

Figure 4. The DBH class distribution of *E. urophylla* and other species in burned and unburned areas

Table 4. The seed rain captured through twelve sampling periods in each sampling area

Spesies	Burned area		Unburned area	
	Quantities (seed)	Seed density (seed/m²)	Quantities (seed)	Seed density (seed/m²)
Eucalyptus urophylla	435	369,4	314	200
Olea paniculata	2	1,7	1	0,6
Pittosporum timorense	14	11,9	20	12,7
Rapanea hasseltii	3	2,5	12	7,6

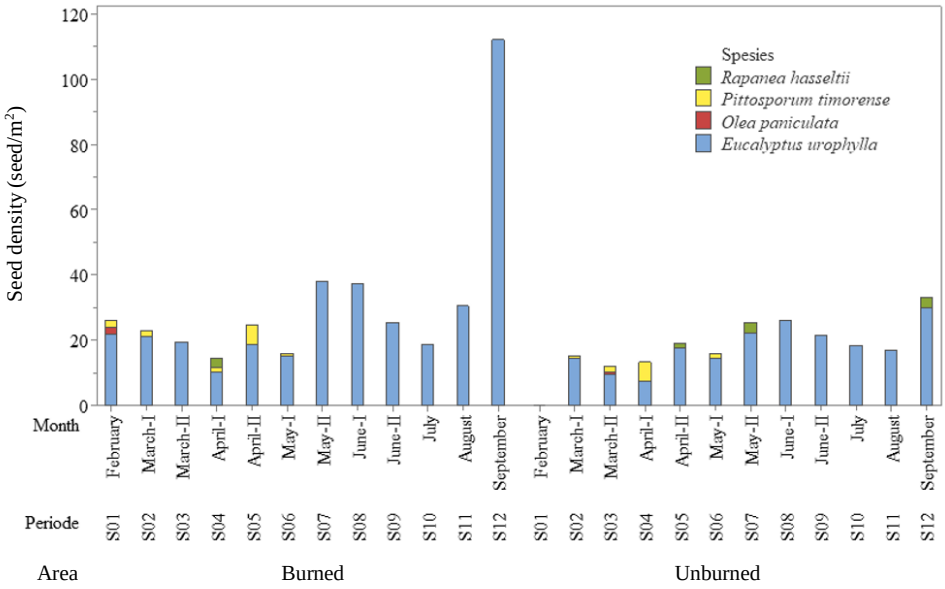

Figure 5. The seed density found in 14 seed traps (six traps in the burned area and eight in the unburned area) in each collection period

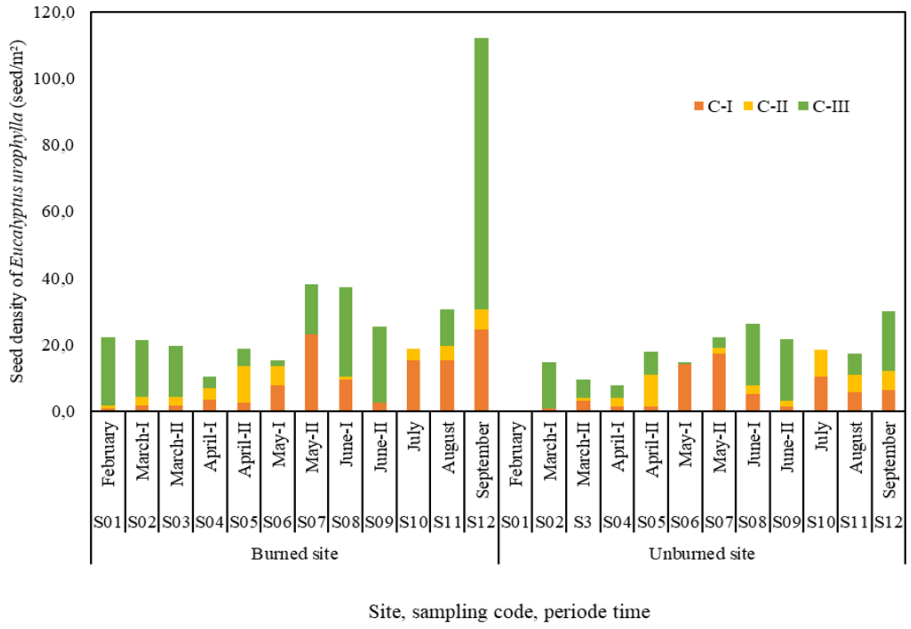

Figure 6. The seed density (seeds/m²) of *E. urophylla* based on their quality categories (C I, CII, or CIII) (Note: Category I (CI): Damaged or rotten fruits or seeds; Category II (C II): Fruits or seeds that were intact, ripe, and had no damage or decay; Category III (C III): Fruits or seeds that are young, small, and immature but not damaged or rotten.)

The Kruskal-Wallis test revealed a statistically significant difference among *E. urophylla* seed categories in the burned sites (p=0.029), indicating a non-uniform seed distribution. Category C-III, comprising small and physiologically immature seeds, exhibited the highest density relative to the other categories. In contrast, no significant difference was detected among *E. urophylla* seed categories in the unburned sites (p=0.241), suggesting a more homogeneous distribution pattern. On the other hand, seeds from Category C-II were the most abundant in the fifth sampling period (April-May), both in burned areas (11.0 seeds/m^2) and unburned areas (9.6 seeds/m^2). These seeds are believed to have natural regeneration potential.

3.3 Relationship among seed rain and vegetation

Eucalyptus urophylla exhibited the highest density in both vegetation and seed rain at both studied areas (Figure 7), suggesting that most of the *E. urophylla* seeds captured the seed rain originated from local vegetation, specifically mature trees surrounding the seed traps. Its highest stand density was found in the burned site, reaching 346 soil/ha. Similarly, the seed density of this species was also highest in the burned area (369.4 seeds/m^2). In the unburned site, although *E. urophylla* did not reach the highest stand density, it still showed the highest seed density (200 seeds/m^2) among other species. In contrast, *D. imbricatus*, which had the highest stand density in the unburned site, did not produce any seeds captured in the seed traps (Figure 7). The calculated Spearman correlation showed no correlation between stand density and seed density in the burned and unburned areas (Table 5).

Table 5. Spearman correlation between stand density and seed density in the burned and unburned site

Site	Variabel 1	Variabel 2	Correlation	p-value
Burned site	Stand density (individual/ha)	Seed density (seed/m²)	0..434	0.158
Unburned site	Stand density (individual/ha)	Seed density (seed/m²)	0.610	0.021

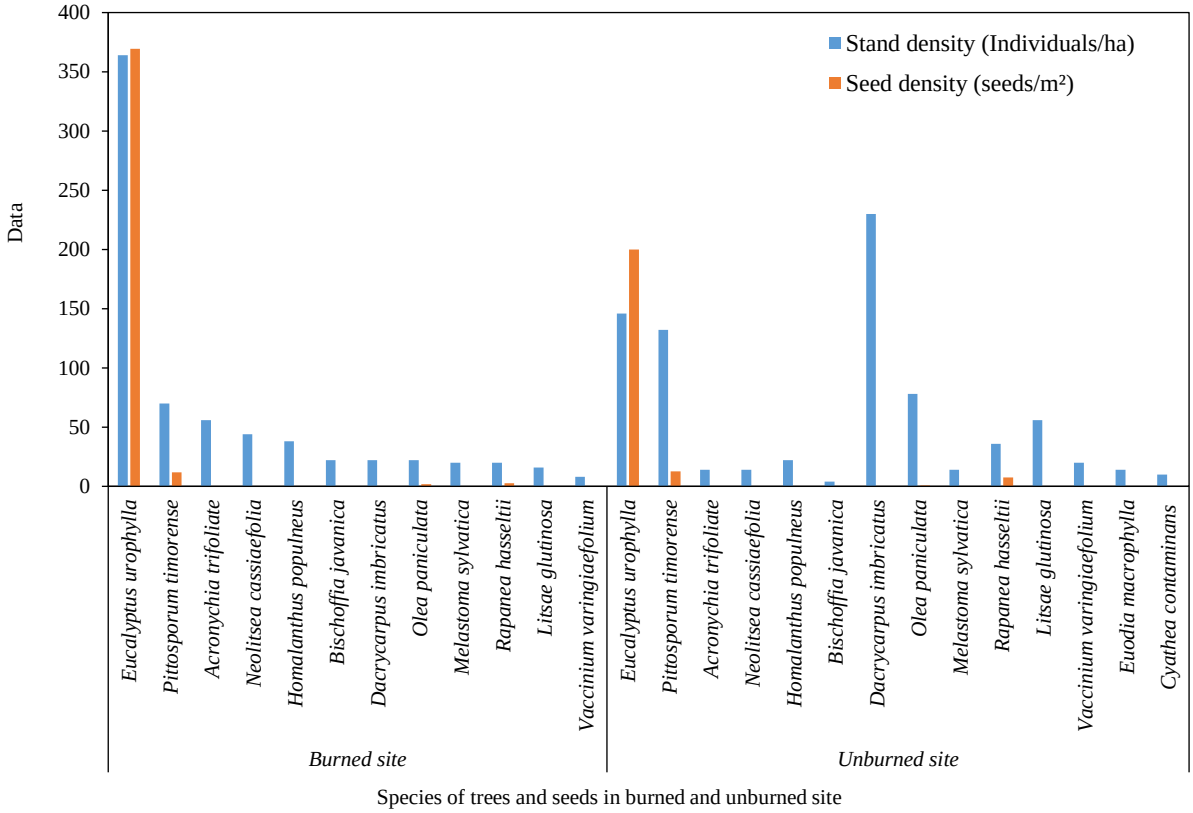

Figure 7. The density of trees and seeds of different species found in burned and unburned areas

The Shannon-Wiener index for vegetation at the unburned area indicated moderate diversity (H'=2.09), while the burned area had a lower index value (H'=1.76). Meanwhile, the Shannon-Wiener index for seed rain at both the burned (H'=0.21) and unburned (H' =0.39) area showed very low values. Additionally, by using rainfall data for the Fatumnasi village area, we analysed the relationship between rainfall and seed density in both sites (Figure 8).

Spearman correlation was used to analyse the correlation between rainfall and seed density in the burned and unburned area (Table 6).

Spearman's correlation analysis shows that when rainfall increases, seed density tends to decrease, although not strongly (r=-0.490), but this correlation is not significant (p-value>0.05). Meanwhile, in the unburned location, it was found that the higher the rainfall, the lower the seed density. This may indicate a decrease in the number of seeds falling into the traps.

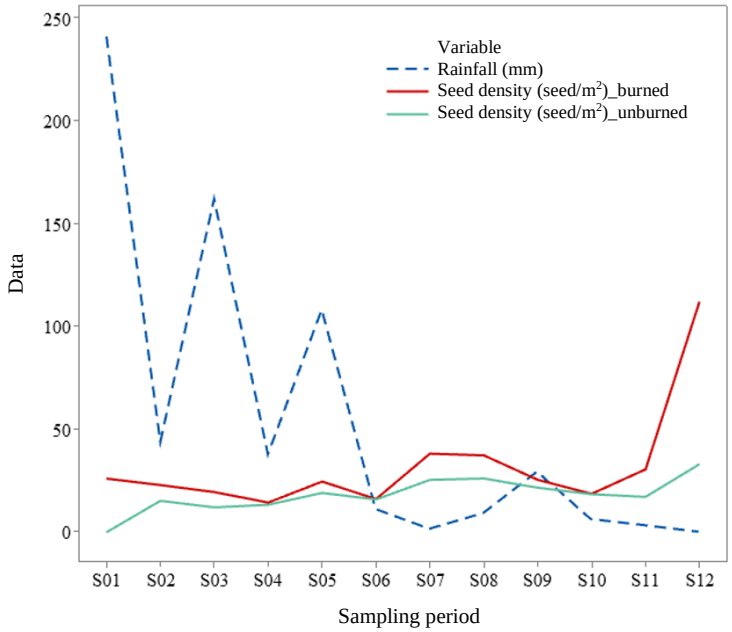

Figure 8. The relationship between rainfall in Fatumnasi Village and seed density in burned and unburned sites

Table 6. Spearman correlation between rainfall and seed density in the burned and unburned site

Site	Variabel 1	Variabel 2	Correlation	p-value
Burned site	Rainfall (mm)	Seed density (seed/m²)	- 0.490	0.106
Unburned site	Rainfall (mm)	Seed density (seed/m²)	- 0.748	0.005

4. DISCUSSION

This study found no significant difference in vegetation density between burned and unburned sites, indicating that fire disturbance did not directly affect overall vegetation density. A possible explanation is likely the severity and intensity of the fire, as well as the natural regeneration capacity of dominant species or the introduction of pioneer species that quickly colonise post-fire sites, allowing vegetation density to recover rapidly. These findings are consistent with a study in the tropical mountain forests of Vietnam, which found that although burned plots showed lower species diversity, tree density, and basal area than unburned areas, their vegetation showed signs of recovery towards unburned conditions within just a few years, especially if the fire was of low to moderate intensity and the burned areas located near the edge of unburned forest. (Trang et al., 2023).

The results of this study showed that *E. urophylla* has a significant ecological role in the burned and unburned sites. Its high IVI indicates that *E. urophylla* is a dominant species with the ability to adapt and dominate post-fire vegetation structure and an important role in the early successional phase and ecosystem restoration. This result suggests that forest fires have influenced the structure of plant communities, potentially leading to the dominance of pioneer or fire-resistant species in burned areas. The forest fires that occurred in tropical forests in South India have also indicated an impact on vegetation dynamics, forest structure and regeneration (Sathya and Jayakumar, 2017). The dominance of *E. urophylla* in the largest class in both area are likely related to its ability to withstand fire. Trees with larger-diameter stems generally have thicker bark, which provides greater resilience against fire compared to those with smaller-diameter stems (Pausas, 2015). In unburned areas, *E. urophylla* has few small trees, indicating future replacement. However, these areas are more diverse, so careful forest fire management is necessary to make it beneficial for the maintenance of *E. urophylla*.

In this study, seed production from trees in both sites was resilient and no longer affected by fire events. The seed rain in both study areas was dominated by *E. urophylla*, indicating that most of the

distributed seeds originated from surrounding mature forests of this species. Although, *E. urophylla* is an important component of the vegetation in Mutis forest, the dominance of this species is stronger in burned area. Meanwhile, in the unburned area, *D. imbricatus* was found co-dominants with *E. urophylla*. While fires occur almost every year in Mutis forest, the fire intensity should be considered when determine its the impact on vegetation and seed rain. We found that the diversity of vegetation and the seed potential for regeneration were very low. Similar findings have been reported in studies on forests dominated by Eucalyptus (Standish et al., 2007; Zivec and Johnston-Bates, 2024). However, because of limitations in this study, which only monitored seed rain over a short time period, long-term studies on seed rain and vegetation dynamics will be necessary to provide more information on this and to monitor the effects of climate change on the vegetation community.

The Mutis forest area is a diverse forest dominated by *E. urophylla*. However, the natural regeneration potential of *E. urophylla* is low, as indicated by the proportion of individuals with small DBH (3-10 cm), which is much smaller than that of large DBH (DBH>50 cm). Therefore, active restoration efforts in the form of planting Eucalyptus as the dominant species are needed. The post-fire restoration effort has also been implemented in many places (Scheper et al., 2021; Sorenson et al., 2025; Verma and Jayakumar, 2015). With the change in the area's status from Nature Reserve to National Park, such efforts are feasible if carried out in designated zones. To support the planting of *E. urophylla*, seeds are required. This study recommends collecting seeds from April to May, cultivating seedlings from these seeds, and planting *E. urophylla* as the dominant species. On the other hand, several preventive strategies for managing forest fires are crucial, for instance, implementing stricter law enforcement on intentional firesetting in surrounding forest areas and implementing payment for ecosystem services (PES). The payments for ecosystem services have been already implemented in some regions (Ottaviani, 2011). Collaboration among all stakeholders, including the government and local communities, is essential for the success of conservation efforts.

5. CONCLUSION

Fire is a recurring disturbance in the Mutis forest area, which occurrs almost every year. *E. urophylla* was identified as the dominant tree species as well as seed production in burned and unburned areas, suggesting that seed production could still occur despite the fires at the current fire intensity. However, more fire intensity needs to be anticipated because if fires coincide during the early stages of *E. urophylla* seed development during the dry season, this could threaten natural seed regeneration. Therefore, further study is needed to understand the mechanisms and mitigation strategies.

ACKNOWLEDGEMENTS

The authors would like to thank Beasiswa Pendidikan Indonesia (BPI) for the doctoral study scholarship (ID number 202101120844); Pusat Pelayanan Pembiayaan dan Asesmen Pendidikan Tinggi (PPAPT), Center for Higher Education Funding and Assessment, Ministry of Higher Education, Science, and Technology of Republic Indonesia doctoral study, and Lembaga Pengelola Dana Pendidikan (LPDP), Ministry of Finance of the Republic of Indonesia for supporting publication. The authors would also like to thank Institut Teknologi Bandung for providing support during research activities, to thank the East Nusa Tenggara Natural Resources Conservation Center (BBKSDA), South Central Timor District Forest Management Unit for granting the permission to carry out this study within their jurisdiction, and to thank Nuri Setiawan who has helped the author with many discussions during the research.

AUTHOR CONTRIBUTIONS

Conceptualization, Damanik DER, Choesin DN, Sulistyawati E; Methodology, Damanik DER, Choesin DN, Sulistyawati E; Software, Damanik DER; Validation, D Choesin DN, Sulistyawati E; Formal Analysis, Damanik DER, Choesin DN, Sulistyawati E; Investigation, Damanik DER, Sulistyawati E; Resources, Damanik DER; Data Curation, Damanik DER; Writing-Original Draft Preparation, Damanik DER; Writing-Review and Editing, Damanik DER, Choesin DN, Sulistyawati E; Visualization, Damanik DER; Supervision, Choesin DN, Sulistyawati E.

DECLARATION OF CONFLICT OF INTEREST

The authors declare no conflict of interest.

REFERENCES

Arasa-Gisbert R, Arroyo-Rodríguez V, Meave JA. The impact of human disturbances on the regeneration layer of tropical rainforests. Environmental Research Letters 2024;19:Article No. 123004.

Armenteras D, Meza MC, González TM, Oliveras I, Balch JK, Retana J. Fire threatens the diversity and structure of tropical gallery forests. Ecosphere 2021;12(1):e03347.

Barros IP, Da Costa LOS, Da Silva PHM, Araujo M, Novaes E. Genetic structure and diversity in wild and breeding populations of *Eucalyptus urophylla*. Silvae Genetica 2022;71:128-36.

Baskin CC, Baskin JM. Seeds: Ecology, Biogeography, and Evolution of Dormancy and Germination. 2nd ed. San Diego, CA: Elsevier; 2014.

East Nusa Tenggara Natural Resources Conservation Agency (BBKSDA NTT). Profile of Mutis Timau Nature Reserve [Internet]. 2018 [cited 2021 Dec 9] Available from: http://bbksdantt.menlhk.go.id/kawasan-konservasi/ca/ca-mutis/profil-ca-mutis-timau (in Indonesian).

Bond WJ, Keane RE. Fires, Ecological Effects of. Reference Module in Life Sciences, Elsevier; 2017.

Bond WJ, van Wilgen BW. Fire and Plants. London: Chaoman and Hall; 2013.

Booth TH. Going nowhere fast: A review of seed dispersal in eucalypts. Australian Journal of Botany 2017;65(5):401-10.

Chalermsri A, Ampornpan L, Purahong W. Seed rain, soil seed bank, and seedling emergence indicate limited potential for self-recovery in a highly disturbed, tropical, mixed deciduous forest. Plants 2020;9(10):Article No. 1391.

Crisp MD, Burrows GE, Cook LG, Thornhill AH, Bowman DMJS. Flammable biomes dominated by eucalypts originated at the Cretaceous-Palaeogene boundary. Nature Communications 2011;2:Article No. 193.

Dorrough J, Moxham C. Eucalypt establishment in agricultural landscapes and implications for landscape-scale restoration. Biological Conservation 2005;123:55-66.

Fisher L, Moeliono, I, Wodicka S. The nusa tenggara uplands, Indonesia: Multiple-site lessons in conflict management. In: Buckles D, editor. Cultivating Peace: Conflict and Collaboration in Natural Resource Management. New York, Ottawa, Washington, DC, USA: International Development Research Center; 1999.

Florence RG. Ecology and Silviculture of Eucalypt Forests. CSIRO Publishing; 2004.

Food and Agriculture Organization of the United Nations (FAO). Global Forest Resources Assessment, 2020: Main Report. Rome: Food and Agriculture Organization of the United Nations; 2020.

Gould WA, Álvarez-Berríos NL, Parrotta JA, McGinley K. Climate change and tropical forests. In: Future Forests: Mitigation and Adaptation to Climate Change. Elsevier; 2024. p. 203-19.

Huanca Nuñez N, Chazdon RL, Russo SE. Seed-rain-successional feedbacks in wet tropical forests. Ecology 2021;102:e03362.

Intergovernmental Panel on Climate Change (IPCC). Climate Change 2022-Impacts, Adaptation and Vulnerability: Working Group II Contribution to the Sixth Assessment Report of the Intergovernmental Panel on Climate Change. 1st ed. Cambridge University Press; 2023.

International Union for Conservation of Nature (IUCN). *Eucalyptus urophylla*. The IUCN Red List of Threatened Species [Internet]. 2019 [cited 2021 Dec 21]. Available from: https://doi.org/10.2305/IUCN.UK.2019-3.RLTS. T133377485A133377487.en.

Kaho NPLBR, Marimpan LS. Fire Regime Mapping in Mutis Nature Reserve (Pemetaan Pola Kebakaran Berbasis Fire Regime Di Cagar Alam Gunung Mutis, Timor Barat, Nusa Tenggara Timur). Buletin Leguminosae 2014;19:1-12 (in Indonesian).

Keeley JE, Pausas JG. Evolutionary ecology of fire. Annual Review of Ecology, Evolution, and Systematics 2022; 53(1):203-25.

Leder CV, Calvo DA, Peter G. Seed rain and soil seed bank compensatory roles on *Nassella tenuis* (Phil.) Barkworth seedling recruitment in ungrazed and grazed sites. Journal of Arid Land 2022;14(5):550-60.

Monk KA, de Fretes Y, Reksodiharjo-Lilley G. Ecology of Nusa Tenggara and Maluku. Jakarta: Prenhallindo; 2000 (in Indonesian).

Ottaviani D. Payments for Ecosystem Services and Food Security. Rome: Food and Agriculture Organization of the United Nations; 2011.

Pausas JG. Bark thickness and fire regime. Functional Ecology 2015;29(3):315-27.

Pepe B, Surata K, Purwanto A, Scientific C. Conservation status of natural populations of *Eucalyptus urophylla* in Indonesia and international efforts to protect dwindling. Forest Genetic Resources 2004:31;62-4.

Pivello VR, Vieira I, Christianini AV, Ribeiro DB, Da Silva Menezes L, Berlinck CN, et al. Understanding Brazil's catastrophic fires: Causes, consequences and policy needed to prevent future tragedies. Perspectives in Ecology and Conservation 2021;19(3):233-55.

Procknow D, Rovedder APM, Piaia BB, De Moraes Stefanello M, Camargo B, Felker RM, et al. Seed rain as an ecological indicator of forest restoration in the Pampa biome. Revista Brasileirade Ciencias Agrarias 2020;15(3):e7220.

Putri AVY, Wardhana W, Sadono R. Long-term assessment of historical disturbances in the dry land ecosystems of Mutis Timau Nature Reserve, East Nusa Tenggara, Indonesia. Forest Science and Technology 2024;20:267-78.

Rahmat MU. The change in function of the Mutis Timau protected forest and Mutis Timau Nature Reserve to a National Park does not constitute a downgrade of the forest area [Internet]. 2024 [cited 2015 Mar 25]. Available from: https://ppid.menlhk.go.id/berita/siaran-pers/7900/klhk (in Indonesian).

Rocha JIDS, Menezes GSC, Cazetta E, Dodonov P, Talora DC. Seed rain across fire-created edges in a Neotropical rainforest. 2021. DOI: https://doi.org/10.21203/rs.3.rs-777032/v1.

Sathya M, Jayakumar S. Post-fire regeneration status of tree species in a tropical dry deciduous forest of Southern India. Journal of Tropical Forest Science 2017;29(3):305-17.

Scheper AC, Verweij PA, Van Kuijk M. Post-fire forest restoration in the humid tropics: A synthesis of available strategies and knowledge gaps for effective restoration. Science of the Total Environment 2021;771:Article No. 144647.

Sein CC, Mitlöhner R. *Eucalyptus urophylla* S.T. Blake: Ecology and Silviculture in Vietnam. Bogor, Indonesia: Center for International Forestry Research; 2011.

Shannon CE, Weaver W. The Mathematical Theory of Communication. University of Illinois Press; 1949.

Smith AL, Blanchard W, Blair DP, McBurney L, Banks SC, Driscoll DA, et al. The dynamic regeneration niche of a forest following a rare disturbance event. Diversity and Distributions 2016;22(4):457-67.

Sorenson QM, Young DJN, Latimer AM. Tree planting outcomes after severe wildfire depend on climate, competition, and priority. Forest Ecology and Management 2025;575:Article No. 122346.

Standish RJ, Cramer VA, Wild SL, Hobbs RJ. Seed dispersal and recruitment limitation are barriers to native recolonization of old-fields in western Australia. Journal of Applied Ecology 2007;44:435-45.

Trang PT, Andrew ME, Enright NJ. Burn severity and proximity to undisturbed forest drive post-fire recovery in the tropical montane forests of northern Vietnam. Fire Ecology 2023; 19:Article No. 47.

Tebabal WM, Masresha Kassa G, Anteneh EA. Structural patterns and regeneration status of woody plant species in the forest of Northwest Ethiopia. Sustainable Environment 2024; 10(1):Article No. 2345439.

Verma S, Jayakumar S. Post-fire regeneration dynamics of tree species in a tropical dry deciduous forest, Western Ghats, India. Forest Ecology and Management 2015;341:75-82.

Yang Z, He W, Fan X, Tjahjadi T. PlantNet: transfer learning-based fine-grained network for high-throughput plants recognition. Soft Computing 2022;26:10581-90.

Zivec P, Johnston-Bates J. Seed rain as a propagule source for restoration of semi-arid floodplain old fields. Applied Vegetation Science 2024;27:e70001.

Environment and Natural Resources Journal

Volume 24
Issue 1
2026

Scenario-Based Land Cover and Land Use Change Modeling in Mae Chang Watershed, Lampang Province, Thailand

Sirasit Vongvassana[1,2,3], Sura Pattanakiat[1,2,3], Allan Sriratana Tabucanon[1,3], Theerawut Chiyanon[1,2,3], Pisut Nakmuenwai[1,2,3], Siam Lawawirojwong[4], Warin Boonriam[1], Pathomphot Chinsawadphan[1,2], and Thamarat Phutthai[1,2,3*]

[1]Faculty of Environment and Resource Studies, Mahidol University, Nakhon Pathom 73170, Thailand
[2]Central and Western Regional Centre for Geo-Informatics and Space Technology (GISTMU), Mahidol University, Nakhon Pathom 73170, Thailand
[3]Geo-Informatics in Resource and Environment Research and Training Center (GIREN), Mahidol University, Nakhon Pathom 73170, Thailand
[4]Geo-Informatics and Space Technology Development Agency, GISTDA (Public Organization), Bangkok 10210, Thailand

ARTICLE INFO

Received: 4 Jun 2025
Received in revised: 28 Aug 2025
Accepted: 1 Sep 2025
Published online: 17 Oct 2025
DOI: 10.32526/ennrj/24/20250115

Keywords:
Land use and land cover change/ Land change modeler/ Scenario modeling/ Geoinformatics

*** Corresponding author:**
E-mail:
thamarat.phu@mahidol.ac.th

ABSTRACT

The Mae Chang watershed is part of the headwaters of the Wang River, located in Lampang Province in Northern Thailand. Resource pressures at forest-agriculture-extractive frontiers make this landscape crucial for studying land-habitat conversion and guiding sustainable land-use planning. Thus, this study interpreted LULC (1989, 2005, 2013, 2021) and projected LULC for 2029 and 2037 under BAU, conservation (CON), and development (DEV) scenarios using TerrSet's LCM-MLP with local drivers, isolating intervention effects by contrasting CON/DEV (with constraint and incentive (CI) layers) against BAU (no CI). From 1989 to 2021, deciduous forest declined 23.3% (-249.01 km²), from 1,070.41 to 821.40 km² (65.40→50.18% of the watershed; -15.2 percentage points), while field crops increased by 104.7%, perennial crops by 97.3%, mines/pits by 240.8%, and urban areas by 28.8% based on human activity. Sub-model accuracies ranged 53-92%, and validation achieved Kstandard 0.824, Kno 0.861, Klocation 0.893, exceeding the success threshold. The three future scenarios yielded similar projected areas in both 2029 and 2037 but there were location differences. The deciduous forest area in 2029 and 2037 declined by 22.3% and 31.5%, respectively for all scenarios compared with 2021. The CON scenario outperformed BAU/DEV because strict no-conversion constraints in protected forests and restricted area effectively prevent ongoing deforestation, offering a practical simulation-based tool to support and implement land-use policies at local and regional scales. These findings provide a validated, transferable framework that isolates policy effects and supports evidence-based land-use planning in tropical headwatersheds.

HIGHLIGHTS

- Headwatershed-specific LCM-MLP integrates local drivers and Constraint/Incentive (CI) layers.
- Deciduous forest fell 23.3% (-249 km²) from 1989 to 2021, while evergreen forest remained stable.
- Concerningly, deciduous forests decline while agriculture expands across all future scenarios.
- CON outperformed BAU/DEV via no-conversion constraints in protected areas.
- The model offers a practical tool for land-use policy implementation.

1. INTRODUCTION

Land use and land cover (LULC) change (LULCC) is a key factor driving global biodiversity loss and influencing processes that impact ecosystem services (Tscharntke et al., 2012). Direct and indirect human activities have triggered processes leading to land degradation, impacting the ecological integrity of affected areas (IPCC, 2019). Since 1970, this situation has caused the greatest negative effects on both terrestrial and freshwater ecosystems (IPBES, 2019), with LULCC affecting almost 32% of the global land area between 1960 and 2019 (Winkler et al., 2021).

Citation: Vongvassana S, Pattanakiat S, Tabucanon AS, Chiyanon T, Nakmuenwai P, Lawawirojwong S, Boonriam W, Chinsawadphan P, Phutthai T. Scenario-based land cover and land use change modeling in Mae Chang Watershed, Lampang Province, Thailand. Environ. Nat. Resour. J. 2026;24(1):42-57. (https://doi.org/10.32526/ennrj/24/20250115)

Extensive changes in land conditions are expected to continue due to ongoing land use changes, leading to substantial declines in net primary productivity, reductions in soil carbon levels, and losses of biodiversity (Van der Esch et al., 2017). Quantifying LULCC is therefore essential to address environmental challenges (Winkler et al., 2021). In Southeast Asia, a global biodiversity hotspot, LULCC drivers such as deforestation, increased agricultural intensification, urbanization, mining activity, dam construction, and wetland reduction are already threatening ecosystems (Hughes, 2017), and these losses are projected to persist through to 2050 (Van der Esch et al., 2017). Thailand is one of countries in the region most affected by land conversion (Hughes, 2017) and has experienced rapid economic growth since the 1980s, primarily fueled by agriculture for export (Wang et al., 2022). While this development has been concentrated in urban centers and lowland regions, it has also extended into mountainous areas (Schreinemachers et al., 2013), particularly in Northern Thailand.

According to the Land Development Department of Thailand (LDD) (2023), the forest area in Northern Thailand decreased by 9.66%, from 57.69% to 52.12%, between 2006/2007 and 2019/2021, respectively, while the agricultural area increased by 16.94%, from 34.65% to 40.52%, during the same period, especially in perennial and field crops. The five northern provinces with the greatest relative forest reduction from 2007 to 2018 are Chiang Rai (-19.51%), Nan (-16.03%), Phayao (-8.83%), Lampang (-8.81%), and Phrae (-6.94%). Nevertheless, in northern Thailand, protected areas (PAs) managed by the Department of National Parks Wildlife and Plant Conservation (DNP) more effectively controlled deforestation than in non-protected areas (Lee et al., 2022; Liu et al., 2022), while national reserved forest which is located adjacent and outside PAs, operated by Royal Forest Department (RFD), tend to be severely encroached.

Therefore, to address environmental problems related to LULCC, future LULC should be projected in terms of location and quantity using scenario-based models such as CA, CLUE-S, MCDA, LCM, FLUS, and agent-based models (Alcamo et al., 2006; Gomes et al., 2021).

The Land Change Modeler (LCM) is a tool used to simulate future land use and land cover (LULC) based on past changes. It employs various methods, e.g., the Multi-Layer Perceptron (MLP) Neural Network (NN), Logistic Regression (LR), and SimWeight (SW) (Eastman and Toledano, 2018). The most favorable method is MLP-NN Markov Chain (MC) or MLP-MC due to its effectiveness (Aghababaei et al., 2024; Entahabu et al., 2023) and higher accuracy (Dey et al., 2021; Mishra et al., 2018). Studies in Thailand have also applied the LCM model for prediction. Several studies focused on general simulations or comparative analyses based on historical land use changes and key driving factors, distributed across all regions of the country, both through administrative boundaries and watershed scales (Paiboonvorachat and Oyana, 2011; Suwanlertcharoen et al., 2013; Losiri et al., 2016; Ongsomwang and Boonchoo, 2016; Chuankamnerdkarn, 2020; Hormwichian et al., 2023; Iamchuen et al., 2023; Phonphan et al., 2024). For the northern Thailand context, a study in the Chiang Mai-Lamphun Basin demonstrated the land use projection model's potential for integrating constraint and incentive (CI) factors to produce realistic scenarios, simulating three future scenarios for 2030 and 2050—the business-as-usual (BaU), the ecological protection scenario (EPS), and the baseline development scenario (BDS)—using LCM Markov-CA-MLP (Arunsurat et al., 2023). The results showed that, under strict constraints, the EPS could maintain forest cover at 61.65% in 2021, 2030, and 2050.

The Mae Chang Watershed is located in Lampang Province, Northern Thailand. The watershed is a tributary catchment of the main watershed, Wang, the uppermost part of the Chao Phraya River Watershed. Most of the area is covered by forest, primarily protected by the Royal Forest Department (RFD) of Thailand and the Department of National Parks, Wildlife, and Plant Conservation (DNP) of Thailand (Office of the National Water Resources, 2020). In addition, there are several anthropogenic activities in this watershed, such as forest plantations managed by the Forest Industry Organization (FIO) of Thailand and agricultural areas, such as paddy fields and field crops, and there is some agriculture located in agricultural land reform areas managed by Agricultural Land Reform Office (ALRO) of Thailand. In addition, extractive activity such as coal lignite mining for electricity generation operated by the Electricity Generating Authority of Thailand (EGAT) is found in this watershed, along with some other types of mines. This highlights the importance of the socio-economic dimension of timber, food, energy and ecological aspect. Deforestation and agricultural

expansion has occurred in this watershed (Office of the National Water Resources, 2020), which may continue. These activities in the watershed might act as threats, causing environmental issues related to land use practices, such as soil erosion from agricultural areas (Marine Department, 2023). Therefore, understanding the historical changes in the Mae Chang Watershed, as well as future LULUC and its scenarios through the application of geoinformatics, might lead to more effective spatial planning for decision-makers and governors. The main objectives of the present study are as follows: (1) To quantify LULC changes for the years 1989, 2005, 2013, and 2021 and (2) to predict changes for 2029 and 2037 under three scenarios—business-as-usual (BAU), conservation (CON), and development (DEV)—using GIS-based MLP-MC and incorporating CI layers for scenarios construction, which reflect the real-world situation of the Mae Chang watershed to understand past and future changes for further sustainable planning.

2. METHODOLOGY

2.1 Study area

The Mae Chang watershed is a sub-watershed of the Wang watershed, the main watershed. It is located between latitudes 17°56'3.89" N - 18°33'50.15" N and longitudes 99°22'56.57" E - 99°57'9.43" E (Figure 1) and it covers an area of 1,636.8 km² (Office of the National Water Resources, 2021). The topography of the Mae Chang watershed consists of a mountain range in the western part, followed by hills, valleys, and plains. The elevation ranges from 126 to 1,305 meters above mean sea level (MSL). The main channel is the Nam Mae Chang, which flows from the northeastern part of the watershed through the Mae Chang Reservoir and other barrages in the lower part of watershed, before merging with the Wang River at the outlet located in Koh Kha District, Lampang Province. Most of the area falls under the political boundary of Lampang Province, and mostly in Mae Moh and Mae Ta Districts.

2.2 Material

Geospatial software, including the ArcGIS platform (ArcMap and ArcGIS Pro) (ESRI, Inc., Redlands, CA), QGIS 3.22.10 (QGIS Development Team, 2022), Google Earth Pro, TerrSet (formerly IDRISI) 18.31 (Eastman, 2016), and TerrSet liberaGIS Version 20.0.0 (Eastman, 2024), were utilized to perform the LULC analysis and LULCC prediction. All geospatial data utilized was in the WGS 1984 UTM Zone 47N projected coordinate system. Rasterization was conducted and the resampling method was applied to convert the geospatial data to a 30-meter spatial resolution to harmonize it before further processing in modeling LULCC (Kimario et al., 2024; Kayitesi et al., 2024). The data used in this study is presented in Table S1.

2.3 Land use land cover (LULC) preparation and change analysis

LULC data for the years 1989, 2005, and 2021 was visually interpreted using on-screen digitization based on satellite imagery and supported information provided in Table S1. Only LULC in 2013 retrieved from LDD was directly utilized with some modification. Image interpretation elements, including tone, texture, pattern, shape, association, and site (Campbell et al., 2022), were applied during manual interpretation using the digitizing tools. The LULC nomenclature consists of 14 classes, following LDD's system with some modifications, including: (1) Paddy Field (APAD); (2) Field Crop (AFLD); (3) Perennial (APER); (4) Orchard (AORC); (5) Other Crop (AOTH); (6) Aquaculture (AAQC); (7) Evergreen Forest (FEVG); (8) Deciduous Forest (FDCD); (9) Rangeland and Scrub (MRNS); (10) Swamp (MMSW); (11) Mine and Pit (MINE); (12) Other Miscellaneous (MOTH); (13) Urban and Built-up (URBA); and (14) Water body (WATR).

The verification points in 2021 were collected through a combination of field surveys (during early winter) and very high-resolution imagery via the Google Earth Pro platform (Raja Shekar and Mathew, 2023), using an image zoom level sufficient to distinguish land use types in accordance with the defined nomenclature and through accurate interpretation. The other truthing points were collected from aerial imagery (the main source) as well as from Google Earth Pro imagery, with the reference year selected as close as possible to coincide with the interpreted LULC for 1989 and 2005. The sample size was determined using the cumulative binomial probability distribution (Fitzpatrick-Lins, 1981), as shown in Formula 1.

$$N = \frac{Z^2 pq}{E^2}, \; Z = 2 \text{ (is generalized from 1.96)} \qquad (1)$$

Where; N is the minimum sample size, Z is the Z value of 2, which is an approximation of the standard normal deviate of 1.96, corresponding to a 95% two-tailed confidence level, p is the expected percent

accuracy, q = 100 − p, and E is the allowable error. In this study, more than 204 points were gathered (Ongsomwang, 2011) based on accuracy and allowable error equal to 85% and 5%, respectively.

Finally, the accuracy assessment was performed to determine the overall accuracy (Story and Congalton, 1986; Congalton and Green, 2019). The accepted accuracy value was set to 85% (Anderson et al., 1976) for the final LULC maps.

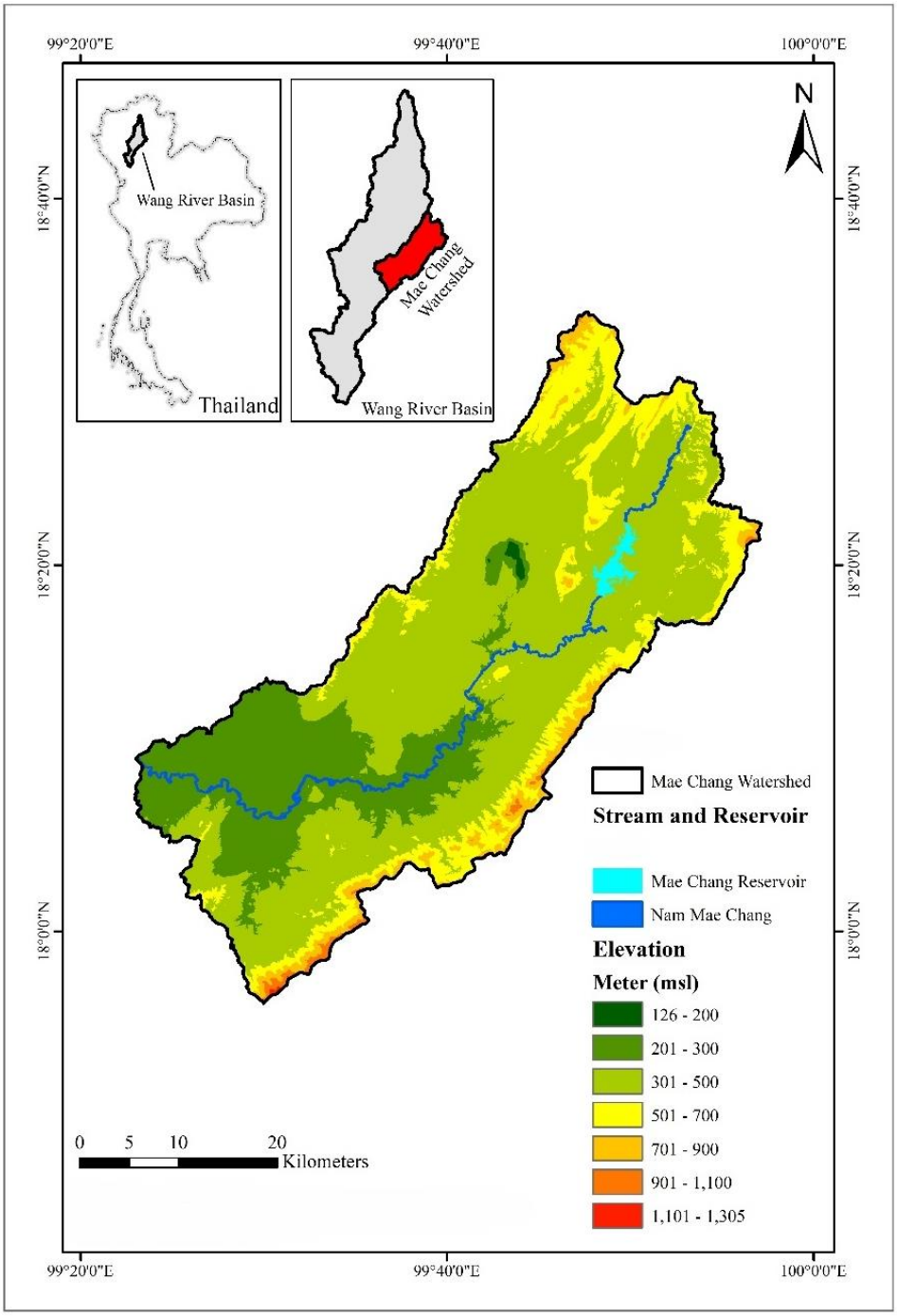

Figure 1. Mae Chang Watershed, Thailand
Data sources:
1) Thailand boundary, Royal Thai Survey Department (RTSD), OCHA HDX, ITOS, CC BY-IGO
2) River basin and watershed boundary, Office of the National Water Resources (ONWR), Thailand
3) Digital Elevation Model (DEM), Land Development Department (LDD), Thailand
4) River and reservoir, NOSTRA

2.4 Scenario construction concept

The theoretical concept and design of the scenario were based on the activation of constraint and incentive layers (Proswitz et al., 2021; Arunsurat, 2022; Gandharum et al., 2024), representing policy or intervention measures. The scenarios are divided into three alternatives as follows:

(1) Business-as-Usual (BAU): This scenario is based on historical LULCC trends without any interventions (Lin et al., 2022; Broquet et al., 2024; Saluja et al., 2024; Gandharum et al., 2024). No enforcement will be applied. No CI layers are activated (Table S2: "✕" for all layers). BAU is used as the policy-neutral baseline.

(2) Conservation (CON): This scenario is based on past LULCC trends, assuming no human activities in protected areas (Proswitz et al., 2021). This design aligns with northern Thai evidence that protected-area enforcement curbs encroachment and limits fragmentation (Lee et al., 2022). The national reserved forest areas, particularly conservation zones (Zone C), and national park will be employed. Additionally, watershed classification class 1 (WSC1), which restricts land use to preserve headwater sources (Tongdeenok, 2023), will also be applied. Operationally, these protected units are enforced as absolute constraints (CI=0) in Table S2, prohibiting land-use conversion within Zone C, National Parks, and WSC1.

(3) Development (DEV): This scenario is similar to BAU, however socio-economic development in the watershed is primarily based on agricultural activities. The agricultural land reform areas managed by the Agricultural Land Reform Office (ALRO) of Thailand will be included, which promotes land use for farmers' livelihoods (Chansawang, 1984; Sreejan, 2024). Furthermore, mining activities, such as coal mining, limestone quarry, and other mineral production, will be implemented in this scenario based on current and future activities. These development fronts are stimulated by incentives (CI=1.1) in ALRO agricultural-reform areas and in recent/future mining footprints, while protected-area constraints remain inactive ("✕") (Table S2).

2.5 LULC change prediction and future scenarios projections

To predict future LULC change (LULCC), the Land Change Modeler (LCM) in TerrSet software was applied following five steps: (1) change analysis; (2) transition potential step and driving variables selection; (3) change prediction; (4) model validation; and (5) future scenarios projections.

2.5.1 Change analysis

Changes between the years 2005 and 2013 were calculated in this panel. The minimum change was set at 600 ha to specify significant changes in the watershed. The LULCC from one category to another was considered and prepared to be selected in the transition potential step.

2.5.2 Transition potential step and driving variables selection

LULC transitions from the change analysis step can be grouped into sub-models based on the same related explanatory drivers of change (Eastman, 2016). A large number of variables may decrease the model's accuracy, while too few variables fail to adequately explain the LULCC (Chen and Yao, 2023).

The initial driving variables (Figure 2) included elevation, slope (degree), distance to roads, distance to streams, distance to agricultural land reform areas, distance to mining (2021), distance to urban and built-up areas (2021), population distribution (2020), and evidence likelihood of LULCC. For the topographic factors, steeper slopes and higher elevations are consistently associated with forest persistence, while low, gentle terrain favors agriculture and settlements (Trisurat et al., 2019). Road expansion increases accessibility, accelerating forest conversion to agricultural and urban and built-up land (Arunsurat et al., 2023). Greater distance from streams stabilizes forest coverage (Trisurat et al., 2019). The ALRO has permitted the area for agricultural activity by the Royal Forest Department, which is responsible for forest zone boundaries in Thailand. Moreover, the ALRO has redistributed state land—largely forest zones—to be used for farming and residential uses (Gine, 2005; Pansak et al., 2024), thus proximity serves as a proxy for policy-driven expansion potential. Additionally, mining activities are the causes of direct LULC change due to the clearing of areas for mining operations. Mining activities induce direct and indirect LULC change and deforestation beyond the immediate site, with those deforestation impacts declining with greater distance from the mining site (Giljum et al., 2022). Urban growth is concentrated near the urban core and along major corridors, with expansion into adjacent zones (Anucharn et al., 2025). The proximity to built-up areas increases conversion likelihood (Arunsurat et

al., 2023). Population factors reflect demographic pressure on land conversion (Trisurat et al., 2019) and are the key driving factors of Thailand's LUCC (Wang et al., 2022). Finally, evidence likelihood (Eastman, 2016) was selected, which is the observed probability of land use and land cover (LULC) category changes occurring between an earlier map and a subsequent one.

The Cramer's V coefficients (CVC), a statistical indicator of the degree of relationship or interdependence between variables, was considered as a guideline for selecting these variables, with a CVC greater than 0.15 indicating usefulness (Eastman, 2016). In this study, the selected variables must have an overall CVC above 0.15.

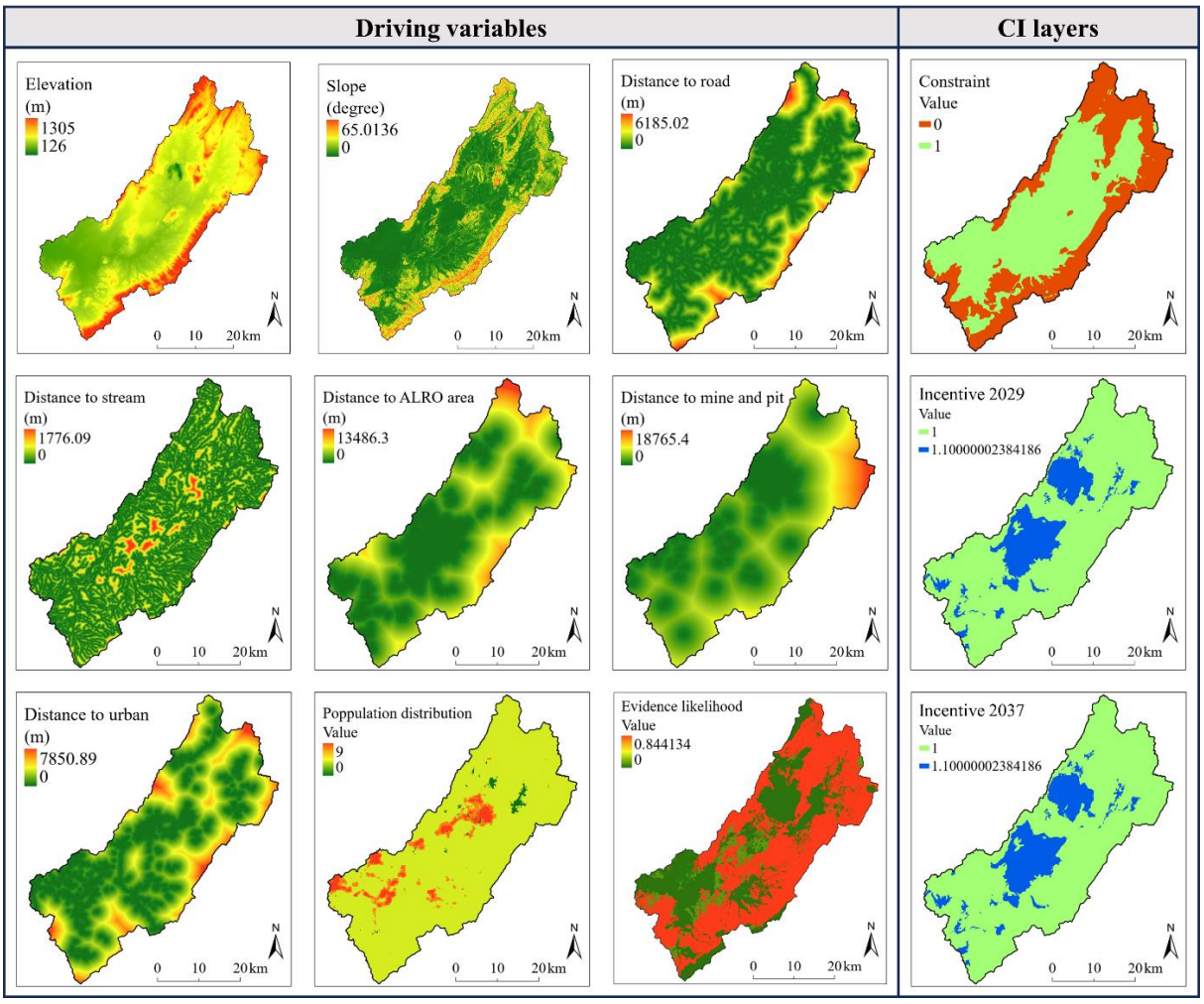

Figure 2. Initial driving variables, and final constraint/incentive layers

The transition potential maps were generated using the multilayer perceptron (MLP) neural network; a feed-forward network with input, hidden, and output layers, trained by back-propagation to learn non-linear relationships between drivers and observed transitions (Hasan et al., 2020; Christensen and Jokar Arsanjani, 2020). In this study, the MLP neural network parameters were set to their default values, utilizing the automatic training and dynamic learning rate. The accuracy rate of each sub-model was set at a minimum of 50%, based on modifications from previous studies (Mishra et al., 2014; Vasanthawada et al., 2023). The skill measure ranges from -1 to 1, with 1 indicating a perfect prediction and -1 indicating worse-than-chance performance (Gharaibeh et al., 2020), with a value between 0 and 1 suggesting the model performed better than random (Christensen and Jokar Arsanjani, 2020).

2.5.3 Change prediction

The predicted 2021 LULC was simulated based on the changes between the actual 2005 and 2013

LULC, using a Markov chain coupled with transition potential maps (Hasan et al., 2020). This step generated two types of predictions: hard and soft prediction models (Eastman, 2016; Gandharum et al., 2024). The hard one refers to predicted LULC where each pixel is assigned to a specific LULC category, which was the approach utilized in this study.

2.5.4 Model validation

The VALIDATE module in TerrSet, which utilizes Kappa statistics was chosen (Saluja et al., 2024). The actual 2021 LULC was selected as the reference source and compared with the projected 2021 LULC, and the results were reported using Kappa indices (Pontius, 2000; Pontius, 2002), such as Kappa Standard (Kstandard), Kappa for No Ability (Kno), and Kappa for Location (Klocation). The Kappa Standard was set at a minimum of 70% (Zadbagher et al., 2018; Leta et al., 2021) for successful validation.

2.5.5 Future scenario projections

After successful calibration and validation, the future scenarios for 2029 and 2037 were predicted. In this step, three scenarios of each future simulation were defined based on the status and value of constraint and incentive layers (CI layer). Values of 0 indicate the area is absolutely constrained (indicating a 'no-change' zone), while values of 1 are unconstrainted and values greater than 1 are treated as incentive (Eastman, 2016). The constraint and incentive values in this study were defined based on Arunsurat (2022). For each scenario, only one CI layer—processed from multiple geospatial datasets—was applied. Table S2 shows the CI layer activation in each scenario.

The overall LULCC modeling based on Land Change Modeler (LCM) is summarized and shown as a flow diagram (Figure 3).

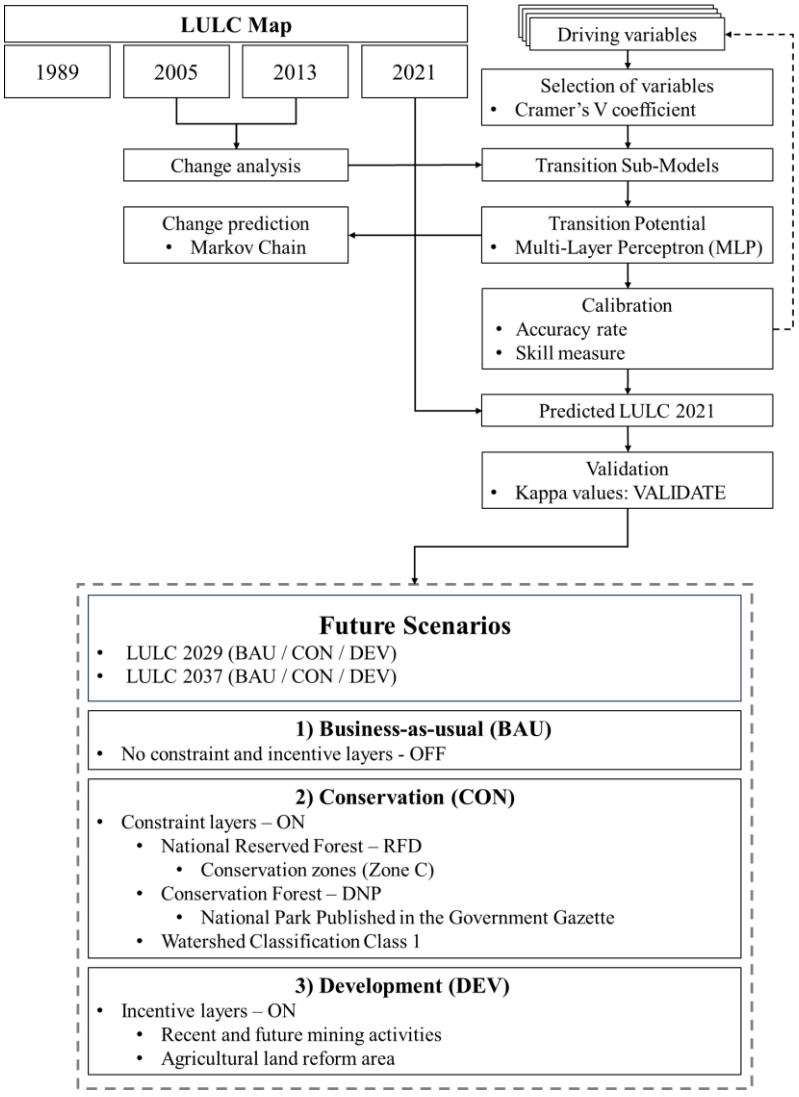

Figure 3. The overall methodology regarding scenario based LULCC prediction

3. RESULTS AND DISCUSSION

After interpretation and classification, the final data yielded overall accuracy of LULC in 1989, 2005, and 2021 of 85.05%, 93.64%, and 91.61%, respectively.

3.1 LULC and change situations in Mae Chang Watershed

The Mae Chang Watershed was primarily covered by forest land, particularly deciduous forest, which covered more than 50% of the total watershed area in 1989 to 2021. Table S3 summarizes the changes in LULC across 1989, 2005, 2013, and 2021. The analysis indicates significant transformations in land use patterns over the 32-year period, driven by a variety of factors such as agricultural expansion, deforestation, and urbanization, as shown in Table S4 and Figure 4.

3.1.1 Agricultural areas

Agriculture represents one of the most dynamic LULC classes. Paddy fields, while starting as one of the largest classes in 1989 at 165.73 km^2 (10.13%), experienced a gradual decline to 160.09 km^2 (9.78%) by 2021. Field crops showed positive trends, increasing slightly from 84.11 km^2 in 1989 to 111.46 km^2 in 2005 (6.81%) and then to 152.65 km^2 in 2013 (9.33%) and 172.21 km^2 (10.52%) in 2021, suggesting a shift toward more intensive agricultural production, mostly consisting of economic crops such as cassava and maize. (Land Development Department, 2015). Similarly, perennial land showed steady growth from 75.47 km^2 (4.61%) in 1989 to 148.93 km^2 (9.10%) in 2021. Orchard areas also saw considerable changes, with an initial small increase from 14.37 km^2 in 1989 to 24.55 km^2 in 2005, followed by a slight decline to 22.34 km^2 by 2021. Other crops remained a minor category throughout the period, with only a modest increase in 2021 to 6.73 km^2 (0.41%). Aquaculture saw a small area of 0.38 km^2 in 2021.

3.1.2 Forest and natural areas

The most significant transformation occurred in deciduous forest, which exhibited a stark decline over time. Starting at 1,070.41 km^2 (65.40%) in 1989, deciduous forests shrank to 821.40 km^2 (50.18%) by 2021. This 15.2% reduction in forest area points to substantial deforestation, likely driven by the expansion of agricultural land, urbanization, and mining activities (Table S4). The evergreen forest class remained relatively stable, covering around 4% of the total area throughout the study period. This might be because the topography and road network are unsuitable for human use, as most of the area belongs to restricted zones such as protected forest areas.

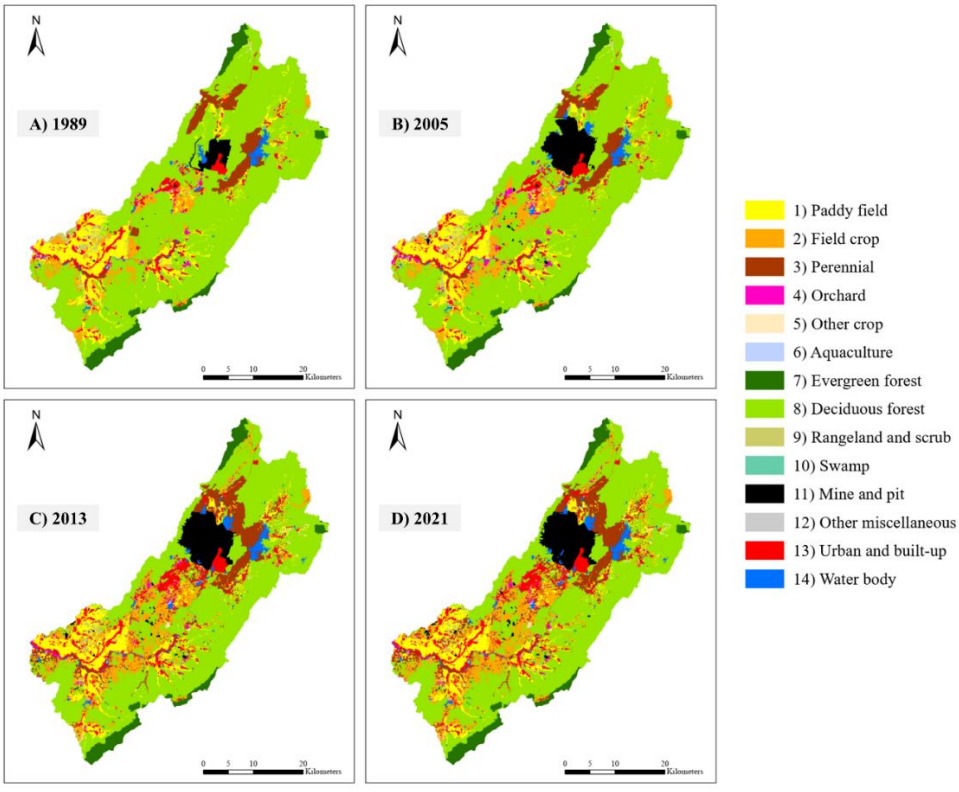

Figure 4. LULC in Mae Chang watershed: A) 1989, B) 2005, C) 2013, and D) 2021

Other natural areas, such as rangeland and scrub, saw a slight decrease from 36.94 km^2 in 1989 to 19.29 km^2 in 2021. Swamp areas, although a very minor component, increased slightly from 0.82 km^2 in 1989 to 2.04 km^2 in 2021.

3.1.3 Mine and pits, and urban areas

Some of the most significant gains were seen in mine and pit areas, which grew from 26.26 km^2 (1.60%) in 1989 to 89.49 km^2 (5.47%) by 2021. This represents a notable expansion in mining and extractive activities, likely contributing to the reduction in forest cover.

Urban and built-up areas also expanded steadily, increasing from 71.95 km^2 (4.40%) in 1989 to 92.67 km^2 (5.66%) in 2021, reflecting the ongoing trend of urbanization. Meanwhile, community relocation is driven by mining companies requiring more space, resulting in new urban areas due to continued mining activities (EGAT, 2022).

3.1.4 Water body

Water bodies also saw a noticeable increase, from 23.00 km^2 (1.41%) in 1989 to 34.90 km^2 (2.13%) in 2021. This is attributed to human activities such as the construction of reservoirs.

3.2 LULCC modeling, calibration, and validation

According to the calibration step, the final five exploratory variables were added to each sub-model, including (1) distance to roads, (2) distance to agricultural land reform areas, (3) distance to mining (2021), (4) distance to urban and built-up areas (2021), and 5) evidence likelihood of LULCC, with the overall CVC more than 0.15 (Table S5).

The four sub-models based on the transition from significant change in the change analysis step were determined, as shown in Table S6. The sub-models were grouped primarily based on the situation occurring in the Mae Chang watershed.

The final sub-model, skill measure, and the accuracy rate of the transition potential process are shown in Table S7. The accuracy rate ranged from 52.87 to 92.40, while the skill measure ranged from 0.3300 to 0.8860. These values coincide with studies in Asia and North America, such as the city of Surat, India (Vasanthawada et al., 2023) and Alabama, United States (Shrestha et al., 2022). The DEF_03 is the highest performing sub-model.

The validation results showed all Kappa variations were greater than 0.8 or 80%. The Kstandard, Kno, and Klocation were 0.8237, 0.8609, and 0.8934, respectively.

3.3 Future scenarios prediction

The LULCC projections reveal significant variations across different future scenarios, Business as usual (BAU), Conservation (CON), and Development (DEV), when compared to the actual LULC in 2021 (Table S8 and Figure 5).

For the BAU scenario, paddy fields increased from 160.09 km² (2021) to 173.69 km² (2029) and 180.42 km² (2037). Field crops expanded to 200.70 km² (2029) and 207.19 km² (2037). Perennial crops showed the strongest growth, rising from 148.93 km² (2021) to 271.13 km² (2029) and 319.06 km² (2037). Evergreen forest remained stable, while deciduous forest declined from 821.40 km² (2021) to 637.87 km² (2029) and 562.46 km² (2037). Mines and pits increased to 102.04 km² (2029) and 107.98 km² (2037). Urban and built-up areas rose to 104.57 km² (2029) and 112.45 km² (2037).

For the CON scenario, paddy fields increased to 173.71 km² (2029) and 180.43 km² (2037). Field crops reached 200.68 km² (2029) and 207.19 km² (2037). Perennial land grew to 271.10 km² (2029) and 319.02 km² (2037). Evergreen forest was stable while deciduous forest fell to 637.87 km² (2029) and 562.49 km² (2037). Mines and pits increased to 102.07 km² (2029) and 107.94 km² (2037). Urban and built-up areas increased to 104.58 km² (2029) and 112.49 km² (2037).

For the DEV scenario, paddy field rose to 173.71 km² (2029) and 180.43 km² (2037). Field crop expanded to 200.68 km^2 (2029) and 207.19 km² (2037). Perennial reached 271.10 km^2 (2029) and 319.02 km² (2037). Evergreen forest was still stable while deciduous forest decreased to 637.87 km² (2029) and 562.49 km^2 (2037). Mines and pits increased 102.07 km² (2029) and 107.94 km² (2037). Urban and built-up areas increased to 104.58 km² (2029) and 112.49 km² (2037).

Across all scenarios, the largest transitions are from deciduous forest to perennial land and from deciduous forest to field crop, increasing from 2029 (≈79-81 km² and ≈78-79 km²) to 2037 (≈115-116 km² and ≈95-96 km²) (Figure 6). Field crop to perennial also rose (≈44-45 to ≈56 km²). Conversions of deciduous forest to paddy field, urban and built-up areas, and mines and pits increased modestly by 2037 (to ≈17, ≈23, and ≈18-20 km², respectively). Some small areas of field crops are transformed to deciduous

forest areas (≈8-11 km²). The projected situations coincide with the studies of Arunsurat et al. (2023) and Saluja et al. (2024), conducted in the northern and northeastern parts of Thailand, whose results show deforestation and agricultural expansion, particularly in the BAU scenarios.

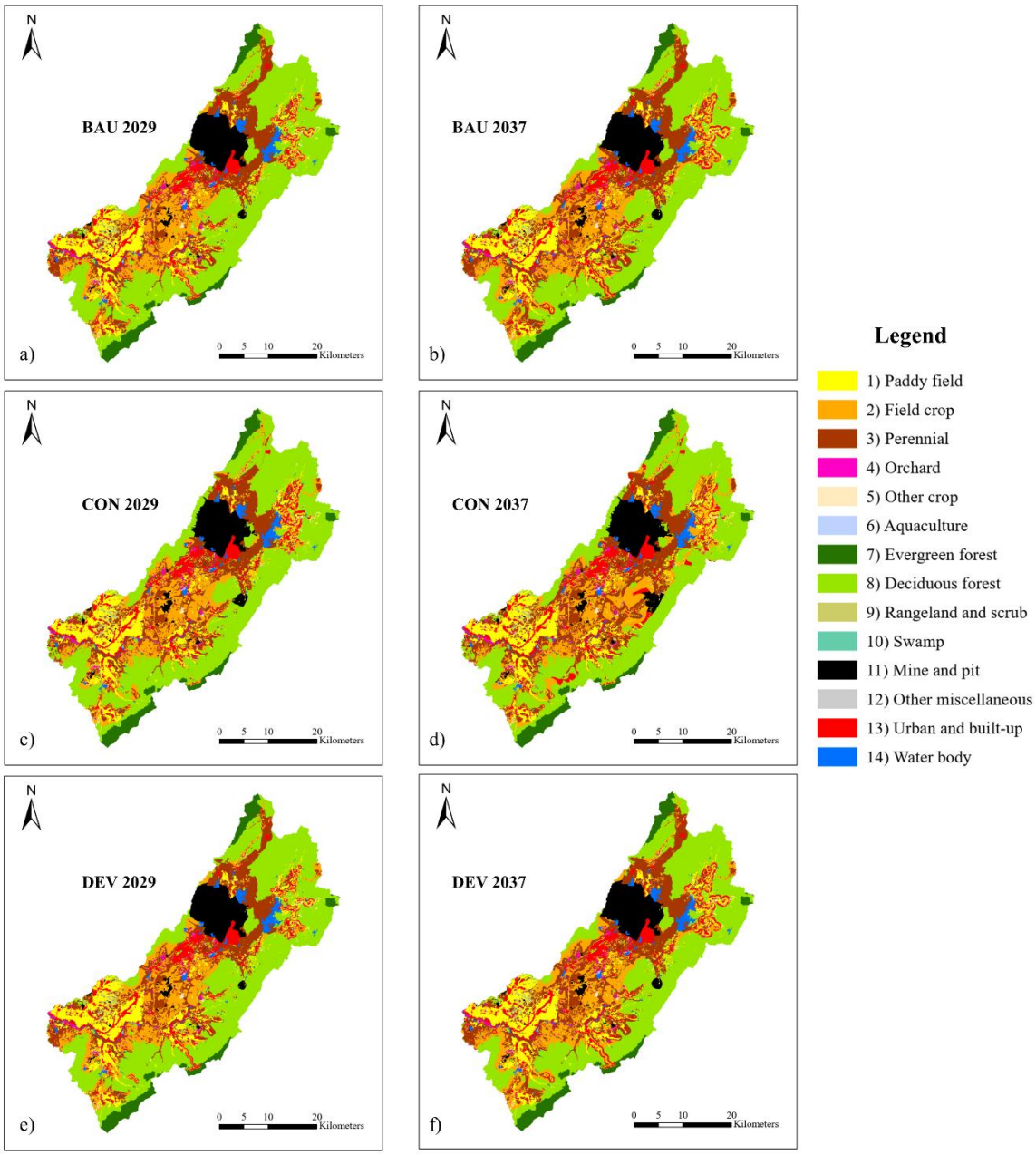

Figure 5. Future scenarios for 2029 and 2037: a), b) BAU scenarios; c), d) CON scenarios; e), f) DEV scenarios

Arunsurat et al. (2023), which studied in Chiang Mai-Lamphun basin in Chiang Mai and Lamphun Provinces, located near the Mae Chang Watershed, demonstrates scenario-dependent quantities of change. Under the Ecological Protection Scenario (EPS), forest cover is maintained at approximately 61.65% in both periods, whereas the Business-as-Usual (BaU) and Baseline Development Scenario (BDS) pathways decline to about 54% by 2050, with greater allocation to agricultural and built-up uses. In the Mae Chang watershed projections, the dominant transitions are likewise from deciduous forest to perennial land and to field crops; however, total areas by class are essentially indistinguishable across BAU, CON, and DEV in 2029 and 2037 (Table S8), indicating that scenario effects are negligible in quantity and act primarily by spatially reallocating change rather than altering overall amounts. This might happen because this study did not adjust the Markov demand but mainly relied on CI layers, so the

total area can be similar across all scenarios. The results from this study also coincide with Abbasnezhad et al. (2023), which used the same Markov matrix for several scenarios.

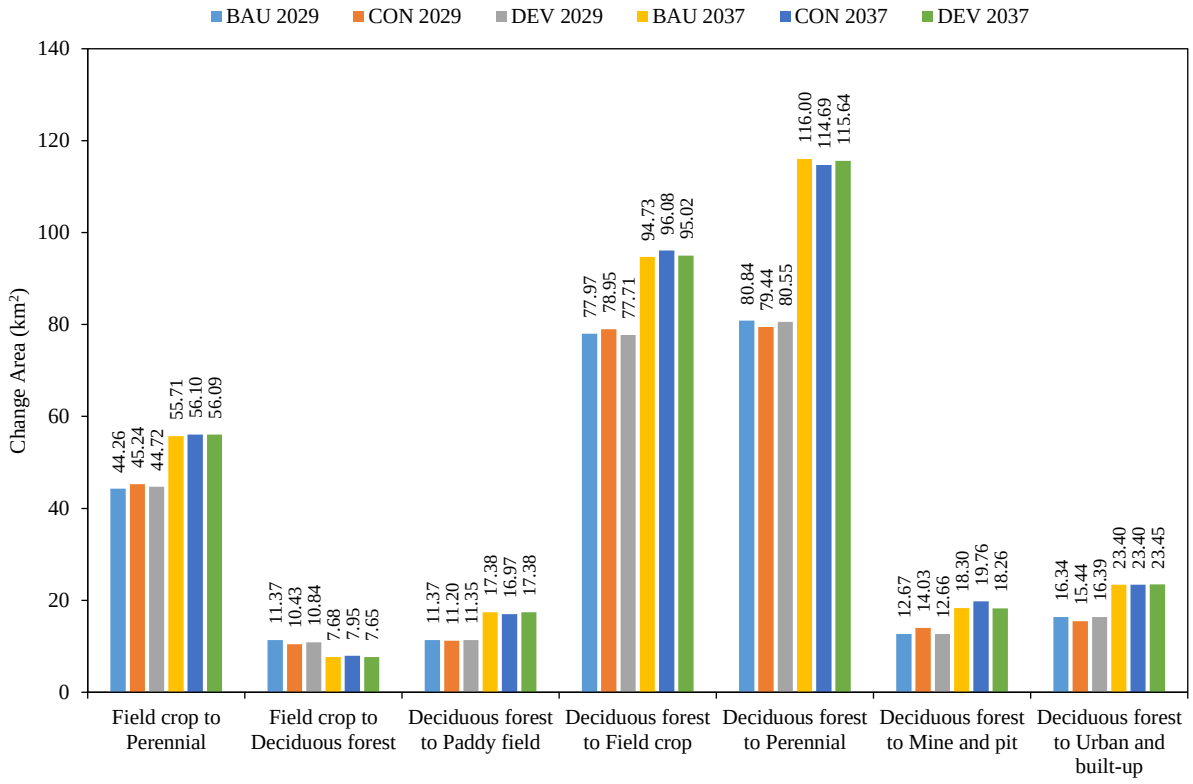

Figure 6. LULCC primary transition from actual LULC 2021 of each scenario

Even though the results in terms of the quantity of change showed a similar pattern across all scenarios (Table S8 and Figure 6), there are significant differences when considering the spatial distribution of the projected LULCC (Figure 7). In the BAU and DEV scenarios, where constraints (protected and restricted areas) are not enforced, deforestation may continue in those areas.

The LULCC, particularly forest loss and agricultural expansion, can exacerbate soil erosion (Paiboonvorachat and Oyana, 2011), increasing sediment yield and nutrient export, which in turn degrade water quality (Chotpantarat and Boonkaewwan, 2018). Mining activities similarly contribute to water quality deterioration (Woon et al., 2021). While such developments may enhance human well-being, they also impose significant environmental costs.

Under the CON scenario, the predominance of evergreen and deciduous forests in the headwatershed supports preservation. Evidence from Northern Thailand indicates that protected areas mitigate forest loss and fragmentation, whereas unprotected landscapes near urban-agricultural frontiers are more susceptible to degradation—reinforcing the role of the CON scenario in safeguarding core habitats (Lee et al., 2022). This underscores the importance of protected and restricted zones, which not only conserve headwater sources but also sustain ecosystem services such as water provision (Chotikasathira, 1988).

3.4 Uncertainties and limitations

LULCC modeling is constrained by the inherent complexity of environmental systems, uncertainties in data, and the difficulty of anticipating human decision-making that shapes land transformation (Bachri et al., 2024). Our results may carry uncertainty from both data and modeling factors. First, although the land use nomenclature was defined with more detail, satellite imagery alone cannot always capture this level of precision. Therefore, we incorporated very high-resolution imagery from both aerial and satellite sources to ensure the highest possible accuracy of the LULC data input into the model. Second, by analyzing only the dominant transitions for this watershed, some minor or dispersed LULC changes were omitted and may underestimate localized impacts while leaving landscape-scale totals broadly unchanged. Third, scenario construction relied on activating constraint and incentive layers; we did not vary land-demand

(class quantities) by scenario. Consequently, BAU/CON/DEV differences should be interpreted primarily as spatial reallocation of change rather than as large shifts in total area by class. Finally, some drivers (e.g., gridded population distribution) were sourced from global products with an effective resolution coarser than 30 m, which can misalign with local patterns and misallocate future changes near settlements. Mining also induces rapid, localized changes in topography (elevation/slope). However, these driving variables were excluded because their Cramer's V values did not meet our selection threshold, which may result in underrepresentation of future LULC change. Therefore, given the inevitable uncertainties in land-use change modeling, outputs from the Land Change Modeler must be treated as approximations and interpreted alongside local context and variations in land-use processes (Bachri et al., 2024).

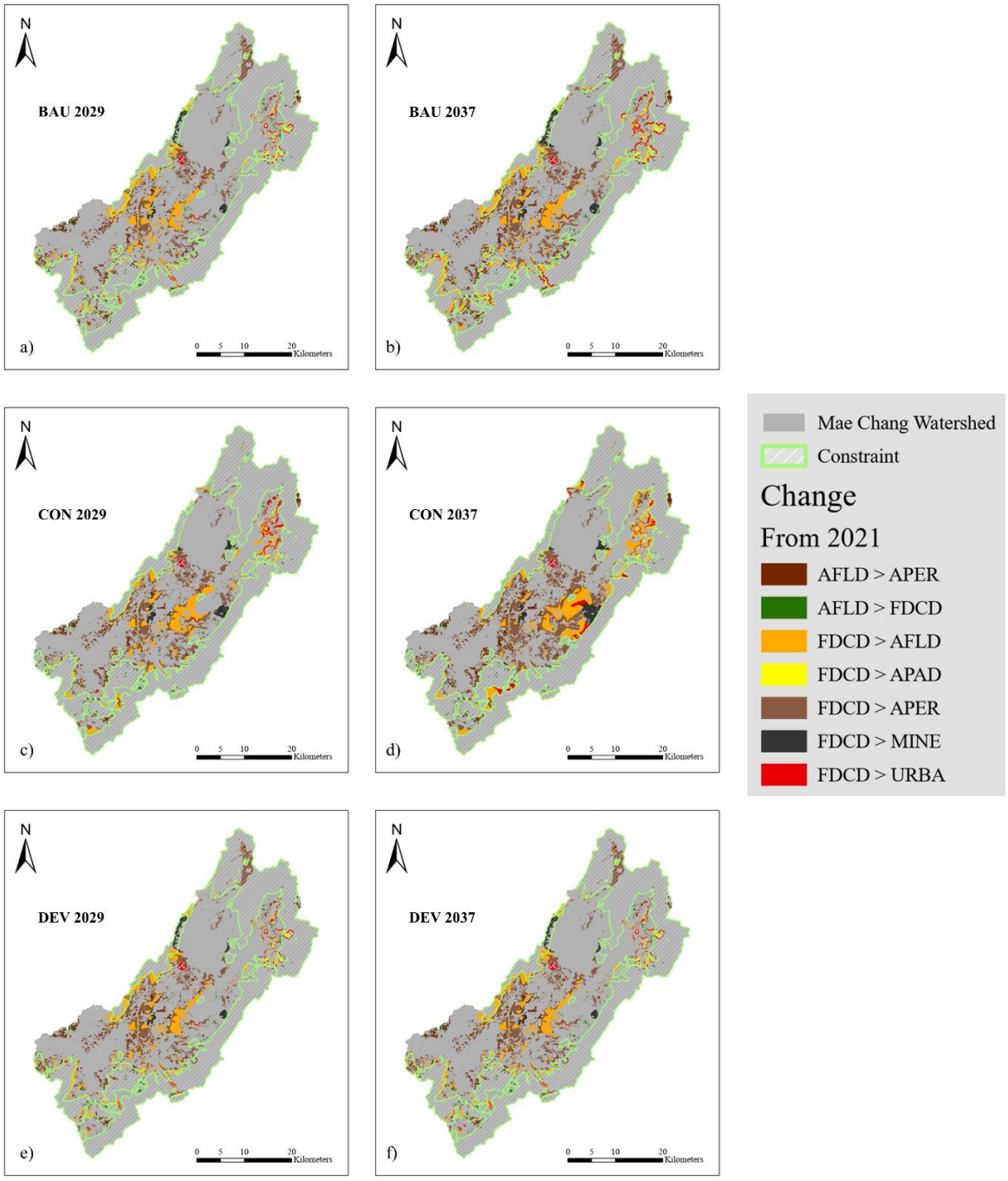

Figure 7. Primary LULC changes from 2021 for each scenario: a) BAU 2029, b) BAU 2037, c) CON 2029, d) CON 2037, e) DEV 2029, and f) DEV 2037.

4. CONCLUSION

The data highlights significant trends in land use change over the period from 1989 to 2021, with the deciduous forest cover in the watershed having declined substantially by 23.3%. Over the same period, field crops expanded by 104.7%, perennial crops by 97.3%, mines and pits by 240.8%, and urban areas by 28.8%, reflecting significant shifts in land use dynamics. Meanwhile, the stability of evergreen forests points to some level of environmental conservation. These LULC changes suggest both development-driven land conversions and efforts to sustain agricultural productivity.

Moreover, this study employed Multilayer Perceptron (MLP) Neural Network, Markov Chain modeling, coupled with transition potential maps and CI layers establishment, to simulate future LULC scenarios for 2029 and 2037 under Business-As-Usual (BAU), Conservation (CON), and Development (DEV). The findings underscore the importance of sustainable land management policies to mitigate the impact of human activities on natural ecosystems, particularly with the growing demand for land resources, with CON able to constrain deforestation, particularly in protected, conserved, and restricted area. This is crucial to ensure the well-being of both human and ecological systems in the future. Since Thailand has also has the National Biodiversity Action Plan 2023-2027, the targeted and recommended actions are to expand and strengthen protected areas and OECMs (Other Effective Area-Based Conservation Measures), prioritize high-biodiversity and ecosystem-service sites, ensure effective, resource management and monitoring, connect areas via ecological corridors, uphold participatory governance and rights, implement continuous, outcome-tracked restoration, and focus management on ecosystem integrity, connectivity, and sustainable benefits (Office of Natural Resources and Environmental Policy and Planning, 2024). It is crucial that these actions are followed.

Due to the unavoidable uncertainties in land-use change modeling, the results from the Land Change Modeler are best treated as approximations. Future studies should integrate finer-resolution datasets and local socio-environmental factors to improve predictive reliability, for example, population income, agricultural land suitability, local bias correction from global to local correct climatic factors (historical and future scenarios).

ACKNOWLEDGEMENTS

This study is part of the degree of Doctor of Philosophy (Environment and Resource Studies), Faculty of Graduate Studies, Mahidol University. This study obtained partial data from research projects supported by The Agricultural Research Development Agency (Public Organization), including the drought impact assessment on agricultural security in Mae Chang watershed Lampang Province (grant number POP6405032350), and food security assessment based on land cover and land use change situation in Mae Chang watershed, Lampang Province (grant number POP6505030390). We would also like to extend our thanks to all organizations in Lampang Province and other organizations for their collaboration in providing valuable data.

AUTHOR CONTRIBUTIONS

Conceptualization, Methodology, Software, Validation, Formal Analysis, Investigation, Resources, Data Curation, Writing-Original Draft Preparation, Writing-Review and Editing, Visualization: Vongvassana S.; Conceptualization, Resources, Data Curation, Supervision, Project administration, funding acquisition: Pattanakiat S.; Supervision: Tabucanon AS.; Supervision, Data Curation: Chiyanon T.; Supervision: Nakmuenwai P.; Supervision: Lawawirojwong S.; Investigation, Resources: Boonriam W.; Data Curation, Resources: Chinsawadphan P.; Conceptualization, Writing-Review and Editing, Supervision: Phutthai T.

DECLARATION OF CONFLICT OF INTEREST

The authors declare that they have no known competing financial interests or personal relationships that could have appeared to influence the work reported in this paper.

REFERENCES

Abbasnezhad B, Abrams JB, Hepinstall-Cymerman J. Incorporating social and policy drivers into land-use and land-cover projection. Sustainability 2023;15:Article No. 14270.

Aghababaei M, Ebrahimi A, Naghipour AA, Asadi E, Verrelst J. Monitoring of plant ecological units cover dynamics in a semiarid landscape from past to future using multi-Layer Perceptron and Markov chain model. Remote Sensing 2024;16(9):Article No. 1612.

Alcamo J, Kok K, Busch G, Priess JA, Eickhout B, Rounsevell M, et al. Searching for the future of land: Scenarios from the local to the global scale. In: Lambin EF, Geist H, editors. Land-Use and Land-Cover Change: Local Processes and Global Impacts. Global Change-The IGBP Series. Berlin, Heidelberg: Springer; 2006. p. 137-56.

Anderson JR, Hardy EE, Roach JT, Witmer RE. A Land Use and Land Cover Classification System for Use with Remote Sensor Data. (US Geological Survey Professional Paper; 964). Washington D.C.: US Government Printing Office; 1976.

Anucharn T, Hongpradit P, Iamchuen N, Puttinaovarat S. Spatial analysis of urban expansion and energy consumption using

nighttime light data: A comparative study of Google Earth Engine and traditional methods for improved living spaces. ISPRS International Journal of Geo-Information 2025; 14:Article No. 178.

Arunsurat R. Analyzing Future Land Cover Change in Chiang Mai-Lamphun Basin Using GIS and Multi-Scenarios Modeling [dissertation]. Graduate School, Chiang Mai University; 2022.

Arunsurat R, Wangpakapattanawong P, Sharp A, Khokthong W. Multi-scenario simulations of future forest cover changes influenced by Socio-economic development: A case study in the Chiang Mai-lamphun basin. EnvironmentAsia 2023; 16(1):1-15.

Bachri S, Shrestha RP, Sumarmi, Irawan LY, Masruroh H, Prastiwi MRH, et al. Land use change simulation model using a land change modeler in anticipation of the impact of the Semeru volcano eruption disaster in Indonesia. Environmental Challenges 2024;14:Article No. 100862.

Broquet M, Campos FS, Cabral P, David J. Habitat quality on the edge of anthropogenic pressures: Predicting the impact of land use changes in the Brazilian Upper Paraguay River Basin. Journal of Cleaner Production 2024;459:Article No. 142546.

Campbell JB, Wynne RH, Thomas VA. Introduction to Remote Sensing. 6th ed. New York: Guilford Press. 2022.

Chansawang A. Land and land reform. Kasetsart Journal of Social Sciences 1984,5:62-8 (in Thai).

Chen S, Yao S. Identifying the drivers of land expansion and evaluating multi-scenario simulation of land use: A case study of Mashan County, China. Ecological Informatics 2023;77:Article No. 102201.

Chotikasathira S. The Role of Watershed Classes in Water Flow and Its Characteristics of Ping-Wang River Basins [dissertation]. Graduate School, Kasetsart University; 1988 (in Thai).

Chotpantarat S, Boonkaewwan S. Impacts of land-use changes on watershed discharge and water quality in a large intensive agricultural area in Thailand. Hydrological Sciences Journal 2018;63:1386-407.

Christensen M, Arsanjani J. Stimulating implementation of sustainable development goals and conservation action: Predicting future land use/cover change in Virunga National Park, Congo. Sustainability 2020;12(4):Article No. 1570.

Chuankamnerdkarn N. Land Use Change Projection in 2050 for Eastern Thailand using Land Change Modeler. Bangkok, Thailand: Faculty of Liberal Arts, Thammasat University; 2020 (in Thai).

Congalton RG, Green K. Assessing the Accuracy of Remotely Sensed Data: Principles and Practices. 3rd ed. Boca Raton, Florida: CRC Press; 2019.

Dey NN, Al Rakib A, Kafy A-A, Raikwar V. Geospatial modelling of changes in land use/land cover dynamics using Multi-layer Perceptron Markov chain model in Rajshahi City, Bangladesh. Environmental Challenges 2021;4:Article No. 100148.

Eastman JR. Terrset Geospatial Monitoring and Modeling System Manual. Massachusetts: Clark Labs, Clark University; 2016.

Eastman JR. TerrSet liberaGIS Geospatial Monitoring and Modeling System Manual. Massachusetts: Clark Clark Labs, Clark University; 2024.

Eastman JR, Toledano J. A short presentation of the land change modeler (LCM). In: Camacho Olmedo M, Paegelow M, Mas JF, Escobar F, editors. Geomatic Approaches for Modeling Land Change Scenarios. Lecture Notes in Geoinformation and Cartography. Cham, Switzerland: Springer International Publishing; 2018. p. 499-505.

Electricity Generating Authority of Thailand (EGAT). Progress of the evacuation of people in Ban Dong Subdistrict. Electricity Generating Authority of Thailand [Internet]. 2022 [cited 2024 Oct 10]. Available from: https://mpp.egat.co.th/hellomaemoh/index.php?option=com_content&view=article&id=853:2022-02-01-08-10-09&catid=10&Itemid=101 (in Thai).

Entahabu HH, Minale AS, Birhane E. Modeling and predicting land use/land cover change using the land change modeler in the Suluh River Basin, northern highlands of Ethiopia. Sustainability 2023;15(10):Article No. 8202.

Fitzpatrick-Lins K. Comparison of sampling procedures and data analysis for a land-use and land-cover map. Photogrammetric Engineering and Remote Sensing 1981;47(3):343-51.

Gandharum L, Hartono DM, Karsidi A, Ahmad M, Prihanto Y, Mulyono S, et al. Past and future land use change dynamics: Assessing the impact of urban development on agricultural land in the Pantura Jabar Region, Indonesia. Environmental Monitoring and Assessment 2024;196:Article No. 645.

Gharaibeh A, Shaamala A, Obeidat R, Al-Kofahi S. Improving land-use change modeling by integrating ANN with Cellular Automata-Markov Chain model. Heliyon 2020;6(9):Article No. 05092.

Giljum S, Maus V, Kuschnig N, Luckeneder S, Tost M, Sonter LJ, et al. A pantropical assessment of deforestation caused by industrial mining. Proceedings of the National Academy of Sciences of the United States of America 2022;119: e2118273119.

Gine X. Land Security in Rural Thailand: Evidence from Property Rights Reform. World Bank Policy Research. Vol. 3734. Washington (DC): World Bank; 2005.

Gomes E, Inácio M, Bogdzevič K, Kalinauskas M, Karnauskaitė D, Pereira P. Future land-use changes and its impacts on terrestrial ecosystem services: A review. Science of the Total Environment 2021;781:Article No. 146716.

Hasan S, Shi W, Zhu X, Abbas S, Khan HUA. Future simulation of land use changes in rapidly urbanizing South China based on Land Change Modeler and remote sensing data. Sustainability 2020;12(11):Article No. 4350.

Hormwichian R, Kaewplang S, Kangrang A, Supakosol J, Boonrawd K, Sriworamat K, et al. Understanding the interactions of climate and land use changes with runoff components in spatial-temporal dimensions in the Upper Chi Basin, Thailand. Water 2023;15(19):Article No. 3345.

Hughes AC. Understanding the drivers of Southeast Asian biodiversity loss. Ecosphere 2017;8:e01624.

Iamchuen N, Lamlet P, Anucharn T, Wongsagoon T. A comparison of future simulation of land use models in urbanization: A case study of Buriram District, Buriram Province. The Journal of Spatial Innovation Development 2023;4(1):60-75 (in Thai).

Intergovernmental Science-Policy Platform on Biodiversity and Ecosystem Services (IPBES). Summary for Policymakers of the Global Assessment Report on Biodiversity and Ecosystem Services of the Intergovernmental Science-Policy Platform on Biodiversity and Ecosystem Services. Bonn, Germany: IPBES Secretariat; 2019. p. 56.

Intergovernmental Panel on Climate Change (IPCC). Summary for Policymakers. In: Climate Change and Land: An IPCC Special Report on Climate Change, Desertification, Land Degradation,

Sustainable Land Management, Food Security, and Greenhouse Gas Fluxes in Terrestrial Ecosystem. Cambridge University Press; 2019.

Kayitesi NM, Guzha AC, Tonini M, Mariethoz G. Land use land cover change in the African Great Lakes Region: A spatial-temporal analysis and future predictions. Environmental Monitoring and Assessment 2024;196(9):Article No. 852.

Kimario EP, Mbilinyi B, Hieronimo P. To evaluate future wetland degradation at Wami Ruvu River Basin from 2020 to 2050 using remote sensing imagery and hybrid ca-markov model. African Journal on Land Policy and Geospatial Sciences 2024;7(1):15-38.

Land Development Department. State of Soil and Land Resources of Thailand [Internet]. 2015 [cited 2024 Oct 10]. Available from: https://e-library.ldd.go.th/library/Ebook/bib9456.pdf (in Thai).

Land Development Department. Land use in Thailand [Internet]. 2023 [cited 2024 Sep 13]. Available from: http://www1.ldd.go.th/web_OLP/index.html (in Thai).

Lee K, Wangpakapattanawong P, Khokthong W. Evaluating forest cover changes in protected areas using geospatial analysis in Chiang Mai, Thailand. Chiang Mai University Journal of Natural Sciences 2022;21(2):e2022030.

Leta MK, Demissie TA, Tränckner J. Modeling and prediction of land use land cover change dynamics based on Land Change Modeler (LCM) in Nashe watershed, Upper Blue Nile basin, Ethiopia. Sustainability 2021;13(7):Article No. 3740.

Lin X, Zhang S, Hou X, Xu Z. Impact of land use change on watershed soil erosion under different development scenarios. Environmental Engineering Science 2022;39(4): 379-92.

Liu Y, Ziegler AD, Wu J, Liang S, Wang D, Xu R, et al. Effectiveness of protected areas in preventing forest loss in a tropical mountain region. Ecological Indicators 2022;136: Article No. 108697.

Losiri C, Nagai M, Ninsawat S, Shrestha R. Modeling urban expansion in Bangkok Metropolitan Region using demographic-economic data through Cellular Automata-Markov Chain and Multi-Layer Perceptron-Markov Chain models. Sustainability 2016;8(7):Article No. 686.

Marine Department. Guideline for Dredging and Restoring Mae Jang River, Lampang Province. Ministry of Transport [Internet]. 2023 [cited 2024 Sep 17]. Available from: https://www.oic.go.th/FILEWEB/CABINFOCENTER23/DRAWER004/GENERAL/DATA0001/00001239.PDF (in Thai).

Mishra VN, Rai PK, Mohan K. Prediction of land use changes based on land change modeler (LCM) using remote sensing: A case study of Muzaffarpur (Bihar), India. Journal of the Geographical Institute Jovan Cvijic SASA 2014;64(1):111-27.

Mishra VN, Rai PK, Prasad R, Punia M, Nistor M-M. Prediction of spatio-temporal land use/land cover dynamics in rapidly developing Varanasi District of Uttar Pradesh, India, using geospatial approach: A comparison of hybrid models. Applied Geomatics 2018;10:257-76.

Office of Natural Resources and Environmental Policy and Planning. Thailand's National Biodiversity Action Plan 2023-2027. Bangkok: Ministry of Natural Resources and Environment; 2024. p. 224.

Office of the National Water Resources. Summary Report of Basic Information on the Wang River Basin: Project for Developing Basic Databases of 22 River Basins. Kasetsart University; 2020.

Office of the National Water Resources. Download data for the 22 watershed areas [Internet]. 2021 [cited 2024 Sep 18]. Available from: http://www.onwr.go.th/?page_id=9893 (in Thai).

Ongsomwang S. Principles of Remote Sensing and Digital Image Processing. Nakhon Ratchasima, Thailand: School of Remote Sensing, Institute of Science, Suranaree University of Technology; 2011. p. 466 (in Thai).

Ongsomwang S, Boonchoo K. Integration of geospatial models for the allocation of deforestation hotspots and forest protection units. Suranaree Journal of Science and Technology 2016;23(3):283-307.

Paiboonvorachat C, Oyana TJ. Land-cover changes and potential impacts on soil erosion in the Nan Watershed, Thailand. International Journal of Remote Sensing 2011; 32(21):6587-609.

Pansak W, Takrattanasaran N, Nongharnpitak N, Khongdee N. Soil-related laws in Thailand: International Yearbook of Soil Law and Policy 2022. Cham: Springer International Publishing; 2024. p. 243-62.

Phonphan W, Arunplod C, Wongsongja N, Utarasakul T, Niemmanee T, Kayee P, et al. Evaluating spatiotemporal dynamics: A comparative study of predictive efficacy in land use land cover change Models-Markov Chain, CA-ANN, and PLUS. International Journal of Geoinformatics 2024;20(6):13-25.

Pontius RG. Quantification error versus location error in comparison of categorical maps. Photogrammetric Engineering and Remote Sensing 2000;66(8):1011-6.

Pontius RG. Statistical methods to partition effects of quantity and location during comparison of categorical maps at multiple resolutions. Photogrammetric Engineering and Remote Sensing 2002;68(10):1041-9.

Proswitz K, Edward MC, Evers M, Mombo F, Mpwaga A, Näschen K, et al. Complex socio-ecological systems: Translating narratives into future land use and land cover scenarios in the Kilombero catchment, Tanzania. Sustainability 2021;13(12): Article No. 6552.

QGIS Development Team. QGIS Geographic Information System. Version 3.22.10. QGIS Association; 2022.

Raja Shekar P, Mathew A. Detection of land use/land cover changes in a watershed: A case study of the Murredu watershed in Telangana state, India. Watershed Ecology and the Environment 2023;5:46-55.

Saluja R, Maung TM, Piman T, Loc HH. Land use transitions in the lower Songkhram River Basin in Mekong and its impact on carbon sequestration potential. ACS ES&T Water 2024;4(7):2918-31.

Schreinemachers P, Fröhlich HL, Clemens G, Stahr K. From challenges to sustainable solutions for upland agriculture in Southeast Asia. In: Fröhlich HL, Schreinemachers P, Stahr K, Clemens G, editors. Sustainable Land Use and Rural Development in Southeast Asia: Innovations and Policies for Mountainous Areas. Berlin Heidelberg, Germany: Springer; 2013.

Shrestha M, Mitra C, Rahman M, Marzen L. Mapping and predicting land cover changes of small and medium size cities in Alabama using machine learning techniques. Remote Sensing 2022;15:Article No. 106.

Sreejan C. Legal measures for agricultural land reform and national reserved forest protection. Graduate Law TU Journal 2024;17(3):417-41 (in Thai).

Story M, Congalton R. Accuracy assessment: A user's perspective. Photogrammetric Engineering and Remote Sensing 1986;52(3):397-9.

Suwanlertcharoen T, Prukpitikul S, Buakaew V, Kaewpoo N. Land use and land cover prediction and change detection using Geo-informatics in Khlong Kui Watershed, Prachuap Khiri Khan Province. Proceedings of the Geoinfotech; 2013 Dec 25-27; Geo-Informatics and Space Technology Development Agency (Public Organization), IMPACT Forum Muang Thong Thani, Bangkok: Thailand; 2013 (in Thai).

Tongdeenok P. Watershed management and classification in Thailand. BIO Web of Conferences 2023;80:Article No. 03024.

Trisurat Y, Shirakawa H, Johnston JM. Land-use/land-cover change from Socio-economic drivers and their impact on biodiversity in Nan Province, Thailand. Sustainability 2019;11:Article No. 649.

Tscharntke T, Batáry P, Clough Y, Kleijn D, Scherber C, Thies C, et al. Combining biodiversity conservation with agricultural intensification. In: Cunningham S, Young A, Lindenmayer D, editors. Land Use Intensification: Effects on Agriculture, Biodiversity and Ecological Processes. Australia: CSIRO Publishing; 2012. p. 7-15.

Van der Esch S, ten Brink B, Stehfest E, Bakkenes M, Sewell A, Bouwman A, et al. Exploring Future Changes in Land Use and Land Condition and the Impacts on Food, Water, Climate Change and Biodiversity: Scenarios for the Global Land Outlook. Hague, Netherlands: PBL Netherlands Environmental Assessment Agency; 2017.

Vasanthawada SRS, Puppala H, Prasad PRC. Assessing impact of land-use changes on land surface temperature and modelling future scenarios of Surat, India. International Journal of Environmental Science and Technology 2023;20(7):7657-70.

Wang Y, Hu Y, Niu X, Yan H, Zhen L. Land use/cover change and its driving mechanism in Thailand from 2000 to 2020. Land 2022;11(12):Article No. 2253.

Winkler K, Fuchs R, Rounsevell M, Herold M. Global land use changes are four times greater than previously estimated. Nature Communications 2021;12(1):Article No. 2501.

Woon SHJ, Srinuansom K, Chuah CJ, Ramchunder SJ, Promya J, Ziegler AD. Pre-closure assessment of elevated arsenic and other potential environmental constraints to developing aquaculture and fisheries: The case of the Mae Moh mine and power plant, Lampang, Thailand. Chemosphere 2021;269: Article No. 128682.

Zadbagher E, Becek K, Berberoglu S. Modeling land use/land cover change using remote sensing and geographic information systems: case study of the Seyhan Basin, Turkey. Environmental Monitoring and Assessment 2018; 190(8):Article No. 494.

Environment and Natural Resources Journal

Volume 24
Issue 1
2026

Assessment of Wood Properties of *Hevea brasiliensis* Clones Grown in Zamboanga Sibugay Philippines for their Potential Applications

Oliver S. Marasigan* **and Marina A. Alipon**

Physics and Mechanics Section, Material Science Division, Forest Products Research and Development Institute (FPRDI), Department of Science and Technology (DOST), College, Los Baños, Laguna 4031 Philippines

ARTICLE INFO

Received: 7 Mar 2025
Received in revised: 28 Aug2025
Accepted: 3 Sep 2025
Published online: 20 Oct 2025
DOI: 10.32526/ennrj/24/20250060

Keywords:
Anatomical properties/ Mechanical properties/ *Hevea brasiliensis*/ Physical properties/ Rubberwood

*** Corresponding author:**
E-mail:
oliver.marasigan@fprdi.dost.gov.ph

ABSTRACT

The potential utilization of 25 year old rubber tree (*Hevea brasiliensis* [Wild. ex A.Juss.] Müll. Arg.) clones (PB 260 and RRIM 600) were assessed based on their anatomical, physical, and mechanical properties. Anatomical features were evaluated using IAWA standards, while physical and mechanical properties were determined following ASTM D143-2019. Five trees per clone were collected from Naga, Zamboanga Sibugay. Results showed that PB 260 exhibited fiber dimensions significantly greater than RRIM 600, with 6.42% longer fibers, 9.42% larger fiber diameters, and 22.47% wider lumens. However, PB 260 had thinner cell walls by 13.33%. Vessel dimensions of PB 260 were also significantly higher, with 14.05% longer and 11.83% wider vessels. For physical properties, RRIM 600 showed higher basic relative density (0.53), tangential shrinkage (4.91%), and volumetric shrinkage (7.58%) compared to PB 260 (0.48, 4.52, and 7.21%, respectively). However, PB 260 had higher green moisture content (126.14%) than RRIM 600 (102.15%). Mechanical testing revealed RRIM 600 had higher strength, attributed to its higher basic relative density and thicker cell wall thickness. RRIM 600 is recommended for construction, flooring, and cabinetry, while PB 260 is suitable for medium grade furniture, carving, and pallets. The study highlights the potential of *H. brasiliensis* clones as alternative raw materials for the Philippine wood industry.

HIGHLIGHTS

- Full wood property test of PB 260 and RRIM 600 clones in the Philippines.
- *Hevea brasiliensis* clones show strong potential for local timber use.
- Significant variation observed in wood properties between the two clones.

1. INTRODUCTION

The rubber tree [*Hevea brasiliensis* (Wild. ex A.Juss.) Müll. Arg.] is native to regions in South America including Bolivia, northern, southern, and west-central Brazil, Colombia, French Guiana, Peru, and Venezuela. It has also been introduced to various Asian countries such as India, Bangladesh, Cambodia, Malaysia, Taiwan, and the Philippines (POWO, 2024). In the Philippines, *H. brasiliensis* is a vital agro-industrial crop, predominantly grown on Mindanao Island, with smaller cultivation areas in Luzon and Visayas. The top-producing regions in Mindanao include the Zamboanga Peninsula, SOCCSKSARGEN (South Cotabato, Cotabato, Sultan Kudarat, Sarangani, and General Santos), ARMM (Autonomous Region in Muslim Mindanao), the Davao Region, and the Caraga Region (PSA, 2021).

As of 2021, approximately 229,431 ha were planted with *H. brasiliensis*, with Zamboanga Peninsula, SOCCSKSARGEN, and ARMM contributing 85% of the country's production (PSA, 2021). The Zamboanga Peninsula is the largest producer, accounting for 41.7% of the total yield. Of the 111,845 ha of mature plantation, 43,592 ha are in Zamboanga (PSA, 2021). If policies on *H. brasiliensis* wood utilization are expanded, nearly 6 million m^3 of logs could be processed (PSA, 2021). Sustainable management strategies, including balancing latex production with wood processing, could optimize its potential as an alternative raw material for wood-

Citation: Marasigan OS, Alipon MA. Assessment of wood properties of *Hevea brasiliensis* clones grown in Zamboanga Sibugay Philippines for their potential applications. Environ. Nat. Resour. J. 2026;24(1):58-76. (https://doi.org/10.32526/ennrj/24/20250060)

based products such as furniture, panel boards, and construction materials (De Lima et al., 2023; Allwi et al., 2021).

Despite its abundance, a limited number of studies have been carried out to evaluate the wood properties of *H. brasiliensis* in the Philippines (Alipon and Bondad, 2008). In contrary, other countries utilize the *H. brasiliensis* wood for production of furniture and composite panels like particleboard and MDF (Ayrilmis et al., 2017).

The growing demand for sustainable wood sources has also led to research on genetically improved clones, which influence wood properties (Naji et al., 2014). Studies in Malaysia, Brazil, and Thailand have examined how different *H. brasiliensis* clones affect wood characteristics (Allwi et al., 2021; de Lima et al., 2023; Riyaphan et al., 2015). These studies highlight significant variations in anatomical, physical, and mechanical properties. For example, de Lima et al. (2023) found differences in relative density, shrinkage, fiber length, and vessel characteristics across five clones. Allwi et al. (2021) reported variations in moisture content, density, and shrinkage, while Riyaphan et al. (2015) observed differences in mechanical properties such as modulus of rupture, modulus of elasticity, hardness, and tensile strength.

In the Philippines, particularly in Zamboanga Sibugay, RRIM 600 and PB 260 are the most commonly planted *H. brasiliensis* clones. RRIM 600 has been extensively studied in other countries, with reported properties including a relative basic density of 0.59-0.63, 49.89% moisture content, and shrinkage values of 3.58% (radial), 4.70% (tangential), and 9.69% (volumetric) (Allwi et al., 2021). Its mechanical properties have been reported as a modulus of rupture (MOR) of 108.0 MPa, modulus of elasticity (MOE) of 9.40 GPa, tensile strength of 1.60 MPa, and surface hardness of 6.6 kN (Riyaphan et al., 2015). However, these values are based on studies conducted outside the Philippines. There is limited information on the wood properties of RRIM 600 grown under Philippine conditions, where climatic and site factors may influence its performance. PB 260, on the other hand, remains largely undocumented in literature. Including RRIM 600 in this study provides a reference clone for site-specific comparison and supports a better evaluation of PB 260's wood properties under local growing conditions.

Despite the availability of different clones of *H. brasiliensis* trees, research on their wood properties in the Philippines remains scarce. Since raw material quality influences final product performance, evaluating *H. brasiliensis* clones at different stem heights is essential for determining their suitability for specific applications. Therefore, this study aims to characterize and compare the anatomical, physical, and mechanical properties of two widely cultivated clones in the Philippines (i.e., RRIM 600 and PB 260) at different height levels. The findings are intended to guide the selection and utilization of suitable clones for various processing and products industry sectors.

2. METHODOLOGY

2.1 Collection and preparation of samples

Five 25 year old trees of *H. brasiliensis* clones (RRIM 600 and PB 260), with diameters greater than 25 cm, were selected from the Tambanan Agrarian Reform Beneficiaries Cooperative (TARBEMCO) in Barangay Tambanan, Naga, Zamboanga Sibugay. The description of the collection sites and trees is presented in Table 1. The average diameter and merchantable height of the logs used were 30.35 cm and 8.58 m for PB 260, and 28.95 cm and 8.55 m for RRIM 600, respectively (Table 1). Each tree trunk was divided into two portions-namely butt (2.4 m) and middle (4.8 m) from the base of the trunk. A total of 20 disks, each 152 mm thick, and 20 billets measuring 2.4 m were cut. The disks were assigned for the determination of the anatomical and physical properties, and billets were used for the testing and evaluation of mechanical properties. Figure 1 shows the sample scheme used.

2.2 Fiber and vessel measurement

From the disc, match-sized splits (25 mm long) were cut and submerged in test tubes containing a macerating solution of equal volumes of hydrogen peroxide and glacial acetic acid. Following the modified Franklin's (1945) method as applied by Alipon et al. (2021), the test tubes were placed in a hot water bath for an hour or until the samples became whitish and soft.

Once softened, the samples were thoroughly rinsed with distilled water to remove any residual acid. To separate the fibers and vessels, the samples were shaken in distilled water, and the resulting macerated material was stained with safranine to enhance visibility under the microscope. Using a Zeiss Primo Star microscope and Zen Lite software, fiber length, vessel length, and vessel width were measured at 10x magnification, while fiber diameter and lumen diameter were measured at 40x magnification (Figure 2). Fiber and vessel measurements followed the

guidelines by the International Association of Wood Anatomists (IAWA) (Wheeler et al., 1989). Cell wall thickness was calculated as the difference between the fiber diameter and lumen diameter. A total of 250 individual fibers and 250 vessels were measured for each clone.

Table 1. Characteristics of the collection site and *H. brasiliensis* clones

Characteristics		Description
Region		9
Province		Zamboanga Sibugay
Municipality		Naga
Barangay		Tambanan
Latitude		7°48'59.3"N
Longitude		122°40'30.9"E
Climatic type		3 and 4
Elevation (m.a.s.l.)		49.3
Temperature (°C)		27.10 (1.5)
Average humidity (%)		77.99 (7.8)
Average precipitation (mm)		179.07 (7.06)
Estimated age of both clones (year old)		25
Average diameter (cm)	PB 260	30.35 (9.26)
	RRIM 600	28.95 (11.00)
Average merchantable height (m)	PB 260	8.58 (2.23)
	RRIM 600	8.55 (2.05)

Note: Inside the parenthesis is the standard deviation.

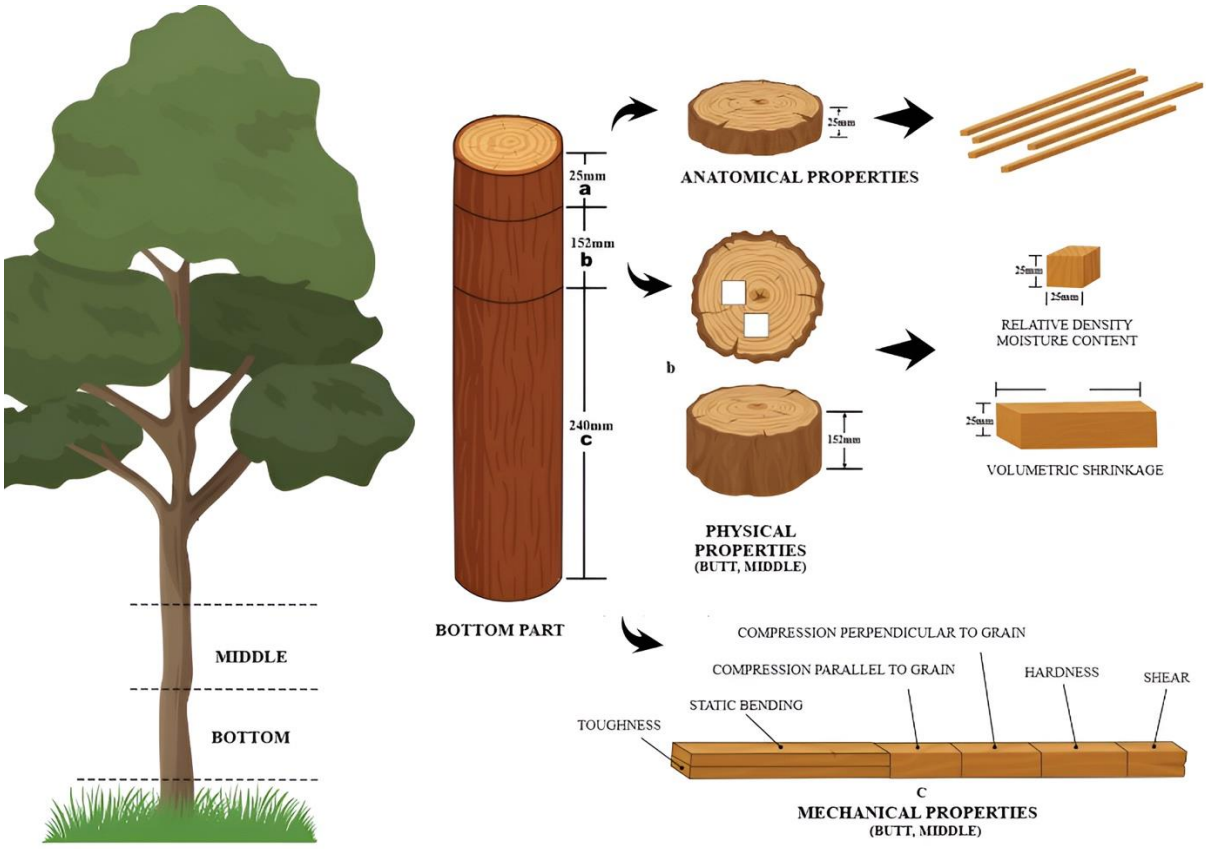

Figure 1. Sampling scheme used in the study (Marasigan and Mundin, 2024)

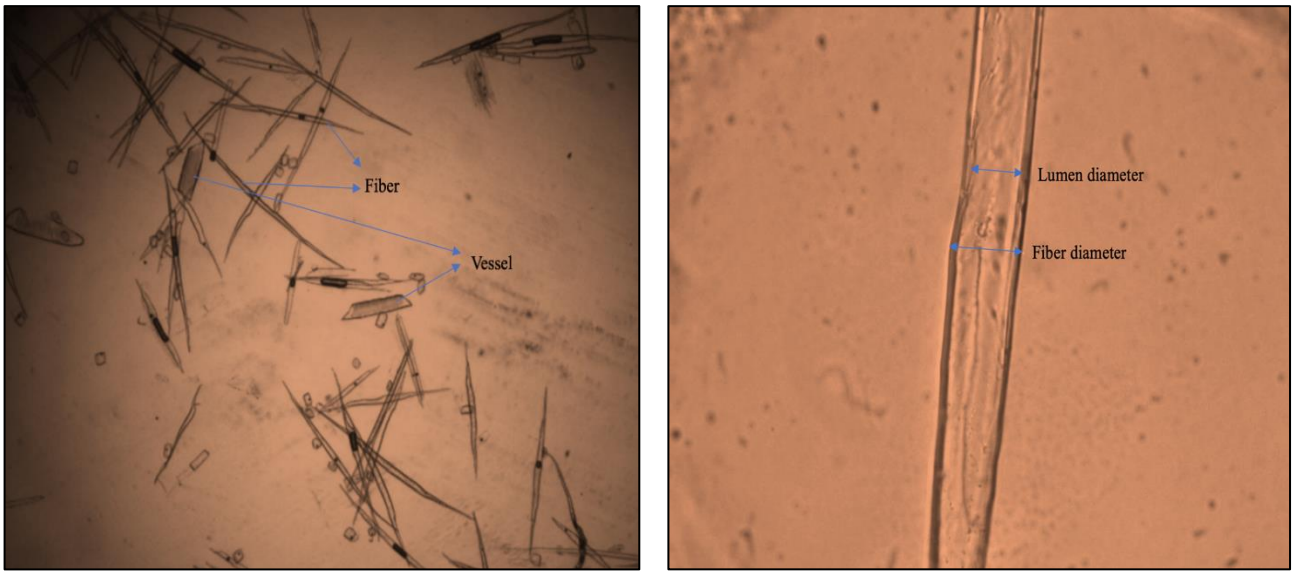

Figure 2. Sample photograph depict the fiber and vessel of the *H. brasiliensis* clones

2.3 Derived values

Based on the fiber morphology data, the derived values such as Runkel ratio (1), Slenderness ratio (2), and Mulhsteph ratio (3) were computed using the equation below:

$$\text{Runkel ratio} = \frac{2 \times \text{cell wall thickness}}{\text{Lumen diameter}} \quad (1)$$

$$\text{Slenderness ratio} = \frac{\text{Fiber length}}{\text{Fiber diameter}} \quad (2)$$

$$\text{Mulhsteph ratio (\%)} = \frac{\text{Fiber diameter}^2 - \text{lumen diameter}^2}{\text{Fiber diameter}^2} \times 100 \quad (3)$$

2.4 Physical properties determination

The physical properties were assessed following the ASTM D143-52 standard (ASTM 2019). A 25 mm × 25 mm × 25 mm sample was extracted from the disc for analyzing green moisture content (MC) and basic relative density (RD). The initial mass of the samples was measured, and their volume was determined using the water displacement method. The samples were then oven-dried at 103±2°C until a constant weight was reached, and their oven-dry mass was recorded. The green MC was calculated as the percentage reduction in mass relative to the oven-dry weight, while the basic RD was obtained as the ratio of the oven-dry weight to the green volume of the sample. One hundred samples from each clone were analyzed to determine green MC and basic RD. The calculations were based on the following equations:

$$\text{MC (\%)} = \frac{W_i - W_o}{W_o} \times 100 \quad (4)$$

$$\text{RD} = \frac{W_o}{V_g} \quad (5)$$

Where; MC represents green moisture content, RD represents basic relative density, W_i represents initial weight (g), W_o represents oven-dry weight (g), and V_g represents green (wet) volume from displaced water (g).

The shrinkage values from green to oven-dry conditions were determined using blocks measuring 25 mm (R) × 25 mm (T) × 102 mm (L). The radial (R), tangential (T), and longitudinal (L) directions of each sample were marked and measured with a dial gauge with a precision of 0.0254 mm. For each clone, a total of 100 samples were used. The directional shrinkage values were calculated using the following equations:

$$S_a\ (\%) = \frac{D_i - D_o}{D_i} \times 100 \quad (6)$$

Where; S_a represents shrinkage from green to oven-dry conditions, D_i represents initial dimension (mm), and D_o represents oven-dry dimension (mm).

Volumetric shrinkage (VS) was calculated using the change in specimen volume between green and oven-dry conditions, using the formula:

$$V_s\ (\%) = \frac{V_i - V_o}{V_i} \times 100 \quad (7)$$

Where; V_i is the initial green volume (mm^3), and V_o is the oven-dry volume (mm^3).

2.5 Determination of mechanical properties

The mechanical properties of the samples were determined according to ASTM D143-52 (ASTM, 2019). For each clone, two sets of samples (green and 12% MC) were prepared, with each clone consisting of 20 samples. These samples were tested for various mechanical properties, including static bending (stress at the proportional limit, modulus of rupture, modulus of elasticity), compression strength (parallel and perpendicular to the grain), hardness (side and end), shear strength, and toughness. The specimen dimensions for each mechanical test are summarized in Table 2, following the specifications of ASTM D143-52 (2019). All tests were conducted using an Universal Testing Machine (Shimadzu UH-300kNx series), except for the toughness test, which was performed using the U.S. Forest Products Laboratory's Product Testing Machine, developed by Sonntag Scientific Corporation (Serial No. 872286). The loading rates for the tests were as follows: 1.3 mm/min for static bending, 0.30 mm/min for compression tests (both parallel and perpendicular), 0.6 mm/min for shear tests, and 6.0 mm/min for hardness testing.

Table 2. Dimensions of test-specimens for the various tests

Mechanical test	Dimensions (L × W × H) (mm)
Static bending	400 × 25 × 25
Compression parallel to grain	100 × 25 × 25
Compression perpendicular to grain	150 × 50 × 50
Shear strength	60 × 50 × 50
Hardness	150 × 50 × 50
Toughness	280 × 20 × 20

2.5 Statistical analysis

Statistical analysis was carried out using R Studio version 4.2.1 (R Core Team, 2020). The data were analyzed using a Factorial Completely Randomized Design (Factorial CRD) with two factors: clone and height level. Before conducting the analysis of variance (ANOVA), the Kolmogorov-Smirnov test for normality showed no significant deviation ($p>0.05$), indicating that the data followed a normal distribution. ANOVA was then applied to evaluate the significance of mean differences across clones, height levels, and their interaction. To identify which specific means were significantly different, Tukey's honestly significant difference (HSD) test was performed.

3. RESULTS AND DISCUSSION

3.1 Anatomical properties

The results of the ANOVA and Tukey's HSD for the anatomical properties between clones of *H. brasiliensis* wood were shown in Table 3. The average fiber characteristics of clone PB 260, including fiber length (1.28 mm), fiber diameter (2.97 µm), and lumen diameter (2.18 µm), were significantly higher, being 6.42% longer and 9.42% and 22.47% larger, respectively, compared to the RRIM 600 clone, which had averages of 1.20 mm, 2.69 µm, and 1.78 µm, respectively. Conversely, the cell wall thickness (CWT) of PB 260 (3.9 µm) was significantly smaller, showing a 13.33% lower compared to RRIM 600 (4.50 µm). Furthermore, PB 260 displayed a significantly higher vessel characteristics, with a vessel length of 0.75 mm and width of 0.26 mm, which were 14.05% longer and 11.83% larger, respectively, than those of RRIM 600 (0.66 mm and 0.23 mm, respectively).

Table 4 presents a comparison of the anatomical properties obtained in the present study with values reported in previous studies. Compared to the 33 year old *H. brasiliensis* clones studied by de Lima et al. (2023) in Brazil, the fiber length of *H. brasiliensis* clones in the present study was longer than RRIM 600 (1.18 mm) and IAN 873 (1.17 mm) but shorter than LCB510 (1.25 mm) and GT1 (1.34 mm). Additionally, the fiber length of PB 260 exceeded that of IAN 717 (1.23 mm). Regarding CWT, PB 260 exhibited a smaller value compared to the clones examined by de Lima et al. (2023). In contrary, RRIM 600 in the present study showed a larger CWT compared to IAN 873 (4.05 µm) and GT 1 (4.31 µm) and was comparable to IAN 717 (4.50 µm).

Table 3. Anatomical and physical properties of *H. brasiliensis* clones

Wood properties	Clones			
	PB 260		RRIM 600	
Anatomical properties				
Fiber length (mm)	1.27[a]	(0.02)	1.20[b]	(0.04)
Fiber diameter (µm)	29.70[a]	(0.02)	26.90[b]	(0.04)
Lumen diameter (µm)	21.80[a]	(1.54)	17.80[b]	(0.61)
Cell wall thickness (µm)	3.90[b]	(0.22)	4.50[a]	(0.18)
Vessel length (mm)	0.75[a]	(0.02)	0.66[b]	(0.03)
Vessel width (mm)	0.26[a]	(0.01)	0.22[b]	(0.00)
Physical properties				
Moisture content (%)	126.14[a]	(7.13)	102.15[b]	(7.69)
Basic relative density	0.48[b]	(0.04)	0.53[a]	(0.02)
Radial shrinkage (%)	2.81[a]	(0.79)	2.81[a]	(0.88)
Tangential shrinkage (%)	4.52[b]	(0.83)	4.91[a]	(1.08)
Longitudinal shrinkage (%)	0.50[a]	(0.55)	0.41[a]	(0.32)
Volumetric shrinkage (%)	7.21[b]	(0.72)	7.58[a]	(0.93)

Note: Values with different superscripts in the same row are significantly different (p=0.05). Values inside the parenthesis indicate standard deviation.

Table 4. Anatomical properties of *Hevea brasiliensis* clones compared with other reported values

Clones	Fiber length (mm)	Fiber diameter (µm)	Lumen diameter (µm)	Cell wall thickness (µm)	Vessel length (mm)	Vessel diameter (mm)
PB 260[*]	1.27	29.70	21.80	3.90	0.75	0.26
RRIM 600[*]	1.20	26.90	17.80	4.50	0.66	0.22
LCB 510[a]	1.25	-	-	4.89	0.76	0.17
RRIM 600[a]	1.19	-	-	4.65	0.73	0.18
IAN 873[a]	1.17	-	-	4.05	0.69	0.16
IAN 717[a]	1.24	-	-	4.50	0.74	0.18
GT1[a]	1.37	-	-	4.31	0.85	0.19
RRIM 2020[b]	1.24	29.63	20.28	4.88	-	0.177
RRIM 2025[b]	1.34	28.54	18.92	4.71	-	0.186

Source: * - present study; a - De Lima et al. (2023); b - Naji et al. (2014)

Furthermore, the fiber lengths observed in the present study (1.27 mm for PB 260 and 1.20 mm for RRIM 600) were shorter compared to the 1.50 mm reported by Onakpoma et al. (2023) for 25-year-old *H. brasiliensis* trees in Nigeria. The CWT of RRIM 600 (4.50 µm) closely aligned with their reported value of 4.85 µm, while PB 260 exhibited a thinner CWT of 3.90 µm. These differences may also reflect genetic variation among clones or the influence of local growing conditions (Panshin and de Zeeuw, 1980).

In terms of fiber diameter, the present study (26.90-29.70 µm) observed a wider value compared to the 24.86 µm reported by Onakpoma et al. (2023) for 15-year-old *H. brasiliensis*, but thinner than the 27.23 µm reported for 25-year-old trees. The observed fiber diameter was narrower than the ranges reported by Teoh et al. (2011) and Naji et al. (2014), who found values between 26.0 to 30.0 µm and 26.33 to 32.84 µm, respectively, but thicker than the values reported by Izani and Sahri (2008), which ranged from 23.5 to 24.9 µm.

The lumen diameter in the present study (17.80-21.80 µm) was thicker than the range of 12.93 to 21.31 µm reported by Onakpoma et al. (2023). Additionally, it was thicker than the lumen width values reported by Izani and Sahri (2008), ranging from 10.0 to 12.0 µm, and Naji et al. (2014), who reported a higher range of 16.43 to 26.56 µm.

In terms of vessel characteristics, the vessel length of PB 260 (0.75 mm) was longer than that of the clones studied by de Lima et al. (2023), such as RRIM 600 (0.73 mm), IAN 873 (0.699 mm), and IAN 717 (0.74 mm), but shorter compared to LCB 510 (0.76 mm) and GT 1 (0.85 mm) (Table 4). However, the vessel length of PB 260 (0.66 mm) was shorter than the values reported for the clones studied by de Lima et al. (2023). Regarding vessel diameter, the

results of the present study (0.23-0.25 mm) were wider than the values reported by de Lima et al. (2023), which ranged from 0.16 to 0.19 mm.

Significant variations in anatomical properties were observed across the height levels (p=<0.05). Fiber length and CWT increased significantly toward the middle portion in both clones (Figure 3). For RRIM 600, fiber length and CWT increased by 4.27% and 4.44%, respectively, while for PB 260, the increases were more pronounced at 11.79% and 13.51%, respectively. In contrast, fiber and lumen diameter decreased significantly toward the middle portion (Figure 3). In RRIM 600, fiber and lumen diameter decreased slightly by 1.10% and 3.84%, respectively, whereas in PB 260, the reductions were 1.00% and 15.44%, respectively (Figure 3).

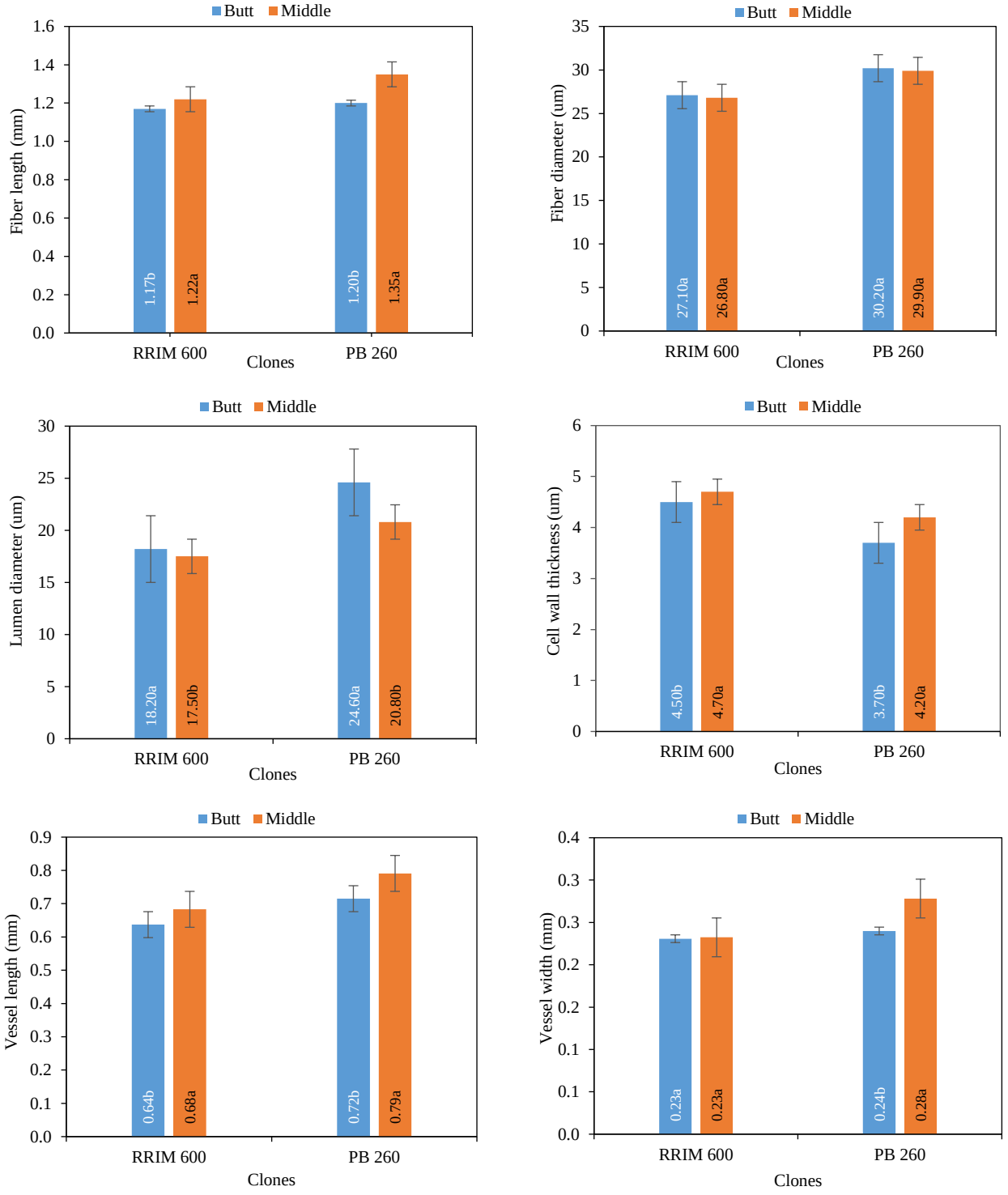

Figure 3. Anatomical properties of *H. brasiliensis* clones at different height levels. Within each clone, bars with different superscripts (a, b) are significantly different (p≤0.05)

The trends observed in the present study contrast with the findings of Onakpoma et al. (2023), who reported longer fibers, as well as thicker fiber, lumen diameter, and CWT at the butt portion of *H. brasiliensis* grown in Nigeria. This discrepancy could likely be attributed to inherent differences in wood properties among trees, as well as the influence of environmental factors, such as climate, soil conditions, and growing practices, on wood development (Dinwoodie, 2000).

Vessel characteristics also exhibited significant variation along the height levels (Figure 3) ($p=<0.05$). Vessel length increased notably toward the middle portion, with increments of 7.06% in RRIM 600 and 10.78% in PB 260. Vessel width also increased in both clones, despite to varying extents. For RRIM 600, the increase was insignificant at 0.69%, while for PB 260, it was significant at 15.95%.

The fiber length of the clones in this study fell under Class II based on the Indonesian Timber Assessment Criteria as Raw Materials for Pulp and Paper (Hartono et al., 2022), which categorizes fiber length between 1.00-2.00 mm as moderately suitable for pulp and paper production. In this classification, Class I (>2.00 mm) indicates high suitability, Class II (1.00-2.00 mm) indicates moderate suitability, and Class III (<1.00 mm) indicates low suitability. Suansa and Al-Mefarrej (2020) emphasized that fibers with an average length greater than 0.4 mm are suitable for papermaking, a claim supported by the low Runkel and Muhlsteph ratios of the clones. RRIM 600 exhibited averages of 0.51 and 56.05, while PB 260 had 0.36 and 42.63, respectively (Table 5). According to Runkel and Muhlsteph ratios classification of DOST-FPRDI (2007), these values categorized the clones as very promising raw material for papermaking, as long fibers with thin cell walls improve tearing, tensile, bursting strength, and folding endurance (Sharma et al., 2011).

Table 5. Derived ratio of *H. brasiliensis* clones

Clone	Slenderness ratio	Runkel ratio	Muhlsteph ratio
RRIM 600	44.52	0.51	56.05
PB 260	43.07	0.36	45.62

In addition to their potential for papermaking, the fiber dimensions of the two clones also align with criteria suitable for composite materials with in plane isotropic properties, which typically require fiber lengths between 1 and 5 mm (Madsen et al., 2013). Although the processing and performance requirements differ from those of papermaking, the high slenderness ratios observed: 44.52 for RRIM 600 and 43.07 for PB 260, are considered advantageous for composite applications, as they contribute to improved fiber bonding and bending strength in wood based panels (Ayrilmis et al., 2017).

Onakpoma et al. (2023) and Amorim et al. (2021) highlighted the suitability of *H. brasiliensis* fibers for composite board production. Longer fibers are particularly advantageous in composite boards as they are less likely to deviate from the horizontal plane, leading to a larger contact area between fibers (Onakpoma et al., 2023). This reduces thickness swelling and enhances dimensional stability under loading. Additionally, longer fibers offer higher resin content per unit surface area compared to shorter fibers, resulting in panels with superior mechanical properties. Composite board produced from longer fibers also exhibit higher internal bond strength than those made from shorter fibers (Ayrilmis et al., 2017).

Fiber diameter significantly influences the mechanical properties of wood and composite materials. A large fiber diameter can weaken inter-fiber bonding due to a smaller surface area compared to volume, reducing stress transfer efficiency. On the other hand, lumen diameter, also plays a vital role in pulp and paper manufacturing and composite production. A larger lumen improves pulp beating by allowing liquids to penetrate fiber voids (Riki et al., 2019) and can lower wood's specific gravity (Izani and Sahri, 2008), which may affect the mechanical properties of composite board.

Regarding CWT, thick fibers are undesirable for pulp and paper production, as well as composite board applications, because they are less flexible, resistant to collapse, and difficult to pulp (Onakpoma et al., 2023). This hinders effective inter-fiber bonding, whereas thin-walled fibers promote better bonding (Sharma et al., 2011). Pulps made from thin-walled fibers are smoother and more suitable for producing a variety of paper grades (Riki et al., 2019). On the other hand, thick-walled fibers result in paper with poor printing

surfaces, higher bulk weight, lower tensile strength, poor burst strength, high tearing strength, and low folding endurance (Pulkkinen et al., 2008). However, for composite board, lumber, and furniture production, thick-walled fibers are beneficial as they enhance load-carrying capacity. Thick-walled fibers tend to have fewer voids and pores, making them better at resisting applied external loads compared to thin-walled fibers (NagarajaGanesh and Rekha, 2020).

3.2 Physical properties

The descriptive statistics and analysis of variance (ANOVA) results for the physical properties between clones of *H. brasiliensis* are presented in Table 3. Significant variations were observed between clones in basic relative density (RD), green moisture content (MC), tangential shrinkage (TS), and volumetric shrinkage (VS) ($p=<0.05$). The RRIM 600 clones exhibited significantly higher basic RD, TS, and VS compared to the PB 260 clones, while the PB 260 clones displayed significantly higher green MC than the RRIM 600 clones. On the other hand, significant variation along the height was only observed in green MC (Figure 4).

The basic RD of RRIM 600 (0.53) was significantly higher than that of PB 260 (0.48). Conversely, the green MC of RRIM 600 (102.15%) was significantly lower compared to PB 260 (126.14%). Similar significant variations in the basic RD of *H. brasiliensis* clones were reported by Allwi et al. (2021) and de Lima et al. (2023). However, the average basic RD observed in the present study was lower than the values reported by these studies (Table 6).

Table 6. Physical and mechanical properties of *Hevea brasiliensis* clones compared with other reported values

Clones	Physical properties					Mechanical properties				
	RD	RS	TS	LS	VS	$C_{//}$	C_L	SS	MOR	MOE
PB 260*	0.48	2.81	4.52	0.50	7.21	25.97	6.01	6.10	56.00	6.54
RRIM 600*	0.53	2.81	4.91	0.41	7.58	29.65	6.00	6.91	62.93	8.12
LCB 510[a]	0.60	-	-	-	8.11	-	-	-	-	-
RRIM 600[a]	0.59	-	-	-	9.69	-	-	-	-	-
IAN 873[a]	0.57	-	-	-	9.18	-	-	-	-	-
IAN 717[a]	0.57	-	-	-	7.54	-	-	-	-	-
GT1[a]	0.56	-	-	-	7.07	-	-	-	-	-
GT1[b]	0.63	1.82	4.00	0.76	-	48.74	15.69	-	85.26	8.05
RRIM 600[b]	0.62	2.98	4.86	0.72	-	48.90	18.18	-	79.84	8.29
RRIT 251[c]	-	-	-	-	-	-	-	-	100.00	9.40
RRIM 600[c]	-	-	-	-	-	-	-	-	108.00	10.40
R59[c]	-	-	-	-	-	-	-	-	103.00	10.50
R650[c]	-	-	-	-	-	-	-	-	91.00	8.80
R1397[c]	-	-	-	-	-	-	-	-	101.00	9.70
R1757[c]	-	-	-	-	-	-	-	-	111.00	10.40
R2086[c]	-	-	-	-	-	-	-	-	109.00	10.30
GT1[d]	0.54	-	-	-	-	48.83	11.24	9.43	-	-
RRIM 600[d]	0.55	-	-	-	-	43.53	11.38	9.60	-	-

Source: * - present study; a - De Lima et al. (2023); b - Allwi et al. 2021; c - Riyaphan et al. (2015); d - Eufrade et al. (2015).
Note: RD - Basic relative density; RS - Radial shrinkage (%); TS - Tangential shrinkage (%); LS - Longitudinal shrinkage (%); VS - Volumetric shrinkage; $C_{//}$ - Compression parallel to the grain (MPa); C_L - Compression perpendicular to the grain (MPa); SS - Shear strength (MPa); MOR - Modulus of rupture (MPa); MOE - Modulus of elasticity (GPa)

The significantly higher RD in RRIM 600 can likely be attributed to its thicker cell wall and narrower vessel diameter compared to PB 260. As shown in Table 7, basic RD exhibited a positive correlation with CWT and a negative correlation with vessel diameter. This aligns with findings by Van Duong et al. (2021), who reported that RD is positively correlated with CWT but negatively correlated with vessel diameter. Similarly, Hamdan et al. (2020) found that CWT is directly related to RD, and de Lima et al. (2023) observed the highest RD in *H. brasiliensis* clones with thicker cell walls and narrower vessel diameters.

Table 7. Correlation matrix of wood properties of *H. brasiliensis* clones

Properties	FL	FD	LD	CWT	VL	VW	RD	MC	TS	RS	LS	VS	MOR	SPL	MOE	Comp Par	Comp Per	SS	HS	HE
FD	0.99*	—																		
LD	0.67*	0.69*	—																	
CWT	-0.55ns	-0.56ns	-0.91*	—																
VL	0.73*	0.70*	0.84*	-0.79*	—															
VW	0.92*	0.89*	0.78*	-0.60ns	0.89*	—														
RD	-0.50ns	-0.52ns	-0.90*	0.86*	-0.61*	-0.57ns	—													
MC	0.61ns	0.63ns	0.92*	-0.88*	0.67*	0.65*	-0.99*	—												
TS	-0.64*	-0.60ns	-0.34ns	0.31ns	-0.38ns	-0.55ns	0.38ns	-0.48ns	—											
RS	0.21ns	0.24ns	-0.09ns	-0.09ns	-0.28ns	-0.14ns	-0.06ns	0.14ns	-0.34ns	—										
LS	0.61ns	0.53ns	-0.05ns	0.07ns	0.18ns	0.45ns	0.03ns	0.08ns	-0.65*	0.33ns	—									
VS	-0.50ns	-0.44ns	-0.40ns	0.25ns	-0.58ns	-0.65*	0.33ns	-0.39ns	0.76*	0.36ns	-0.42ns	—								
MOR	-0.69*	-0.61ns	-0.51ns	0.46ns	-0.62ns	-0.74*	0.57ns	-0.62ns	0.73*	0.02ns	-0.70*	0.74*	—							
SPL	-0.72*	-0.68*	-0.73*	0.69*	-0.80*	-0.80*	0.71*	-0.76*	0.65*	0.03ns	-0.48ns	0.67*	0.84*	—						
MOE	-0.61ns	-0.56ns	-0.54ns	0.67*	-0.63*	-0.59ns	0.53ns	-0.63ns	0.81*	-0.22ns	-0.46ns	0.64*	0.76*	0.70*	—					
Comp Par	-0.90*	-0.90*	-0.84*	0.77*	-0.79*	-0.88*	0.75*	-0.84*	0.60ns	-0.19ns	-0.47ns	0.46ns	0.74*	0.85*	0.69*	—				
Comp Per	-0.88*	-0.90*	-0.79*	0.69*	-0.68*	-0.81*	0.70*	-0.77*	0.52ns	-0.15ns	-0.37ns	0.41ns	0.65*	0.64*	0.62ns	0.90*	—			
SS	-0.66*	-0.66*	-0.79*	0.85*	-0.73*	-0.64*	0.68*	-0.76*	0.41ns	-0.09ns	-0.19ns	0.34ns	0.55ns	0.67*	0.73*	0.85*	0.84*	—		
HS	-0.74*	-0.70*	-0.62ns	0.49ns	-0.72*	-0.83*	0.59ns	-0.63ns	0.47ns	0.19ns	-0.60ns	0.60ns	0.89*	0.85*	0.53ns	0.81*	0.73*	0.61ns	—	
HE	-0.70*	-0.67*	-0.75*	0.67*	-0.73*	-0.77*	0.77*	-0.81*	0.54ns	0.00ns	-0.47ns	0.55ns	0.83*	0.96*	0.58ns	0.87*	0.68*	0.65*	0.90*	—
T	-0.44ns	-0.45ns	-0.20ns	-0.08ns	-0.25ns	-0.47ns	0.03ns	-0.04ns	-0.21ns	0.25ns	-0.28ns	-0.03ns	0.15ns	0.18ns	-0.34ns	0.34ns	0.34ns	0.07ns	0.51ns	0.33ns

Note: ***** - significant at the 95% confidence level; ns - not significant. FL - Fiber length; FD - Fiber diameter; LD - Lumen diameter; CWT - Cell wall thickness; VL - Vessel length; VW - Vessel width; RD - Basic relative density; MC - Moisture content; TS - Tangential shrinkage; RS - Radial shrinkage; LS - Longitudinal shrinkage; VS - Volumetric shrinkage; MOR - Modulus of rupture; SPL - Stress at the proportional limit; MOE - Modulus of elasticity; Comp Par - Compression parallel to the grain; Comp Per - Compression perpendicular to the grain; SS - Shear strength; HS - Hardness: Side; HE - Hardness: End; T - Toughness.

According to the RD classification of Alipon and Bondad (2008), the *H. brasiliensis* clones in this study fall under the moderately high classification, with basic RD ranging from 0.46 to 0.54. The RD of the clones were comparable to species such as *Parashorea malaanonan*, *Rubroshorea negrosensis*, *Pentacme contorta*, *Rubroshorea polysperma*, *Swietenia macrophylla*, *Gmelina arborea*, and *Acacia mangium*. However, it was higher than the RD of *Rubroshorea almon*, *Rubroshorea palosapis*, and *Eucalyptus deglupta*, classified as moderately low, and *Rubroshorea ovata* and *Falcataria moluccana*, classified as low (Alipon and Bondad, 2008). Notably, the RD classification for *H. brasiliensis* by Alipon and Bondad (2008) was under moderately low. The findings of the present study can serve as a basis for updating the RD classification of *H. brasiliensis* grown in Philippines.

The significant variation in green MC between clones is likely due to differences in anatomical properties. As shown in Table 7, green MC was positively correlated with lumen diameter and negatively correlated with CWT. This observation is consistent with Aiso et al. (2016), who found that MC is positively correlated with lumen diameter and negatively correlated with CWT. Larger lumen diameters enable wood to retain more water. In this study, the PB 260 clone had larger lumen diameters compared to RRIM 600, while RRIM 600 exhibited thicker cell walls than PB 260 (Table 3). Additionally, the results of this study can aid the industry in estimating transportation, sawmilling, and drying costs (Shmulsky and Jones, 2019).

No significant variation in basic RD was observed along the height levels (Figure 4). This finding is consistent with the results of Allwi et al. (2021), who reported no significant variation in basic RD in the RRIM 600. However, significant variation in green MC was observed along the height of the stem, with the butt portion exhibiting the higher MC (Figure 4). A similar pattern in MC variation along the height of *H. brasiliensis* clones was also noted by Allwi et al. (2021). Anatomical characteristics may have contributed to this moisture distribution. The butt portion showed thinner CWT and wider LD compared to the middle portion (Figure 3). These characteristics are consistent with the observed correlations, where MC decreased with increasing CWT and increased with larger LD (Table 7). This indicates that the butt portion of *H. brasiliensis* clones in the present study may require a longer drying time compared to the middle portion.

In terms of shrinkage properties, no significant difference was observed in RS and LS of both species (Table 3). This indicates that both RRIM 600 and PB 260 may respond similarly to the changes in MC in terms of RS and LS. On the other hand, RRIM 600 clones recorded significantly higher TS and VS with an average of 4.91% and 7.58%, respectively, than PB 260 (4.52% and 7.21%, respectively) (Table 3).

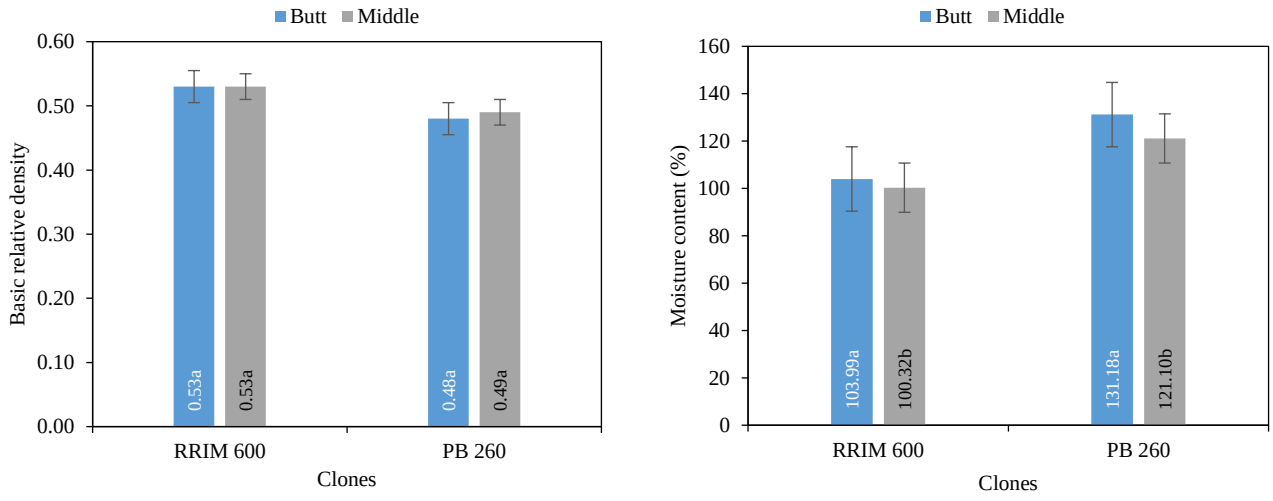

Figure 4. Physical properties of *H. brasiliensis* clones at different height levels. Within each clone, bars with different superscripts (a, b) are significantly different ($p \leq 0.05$)

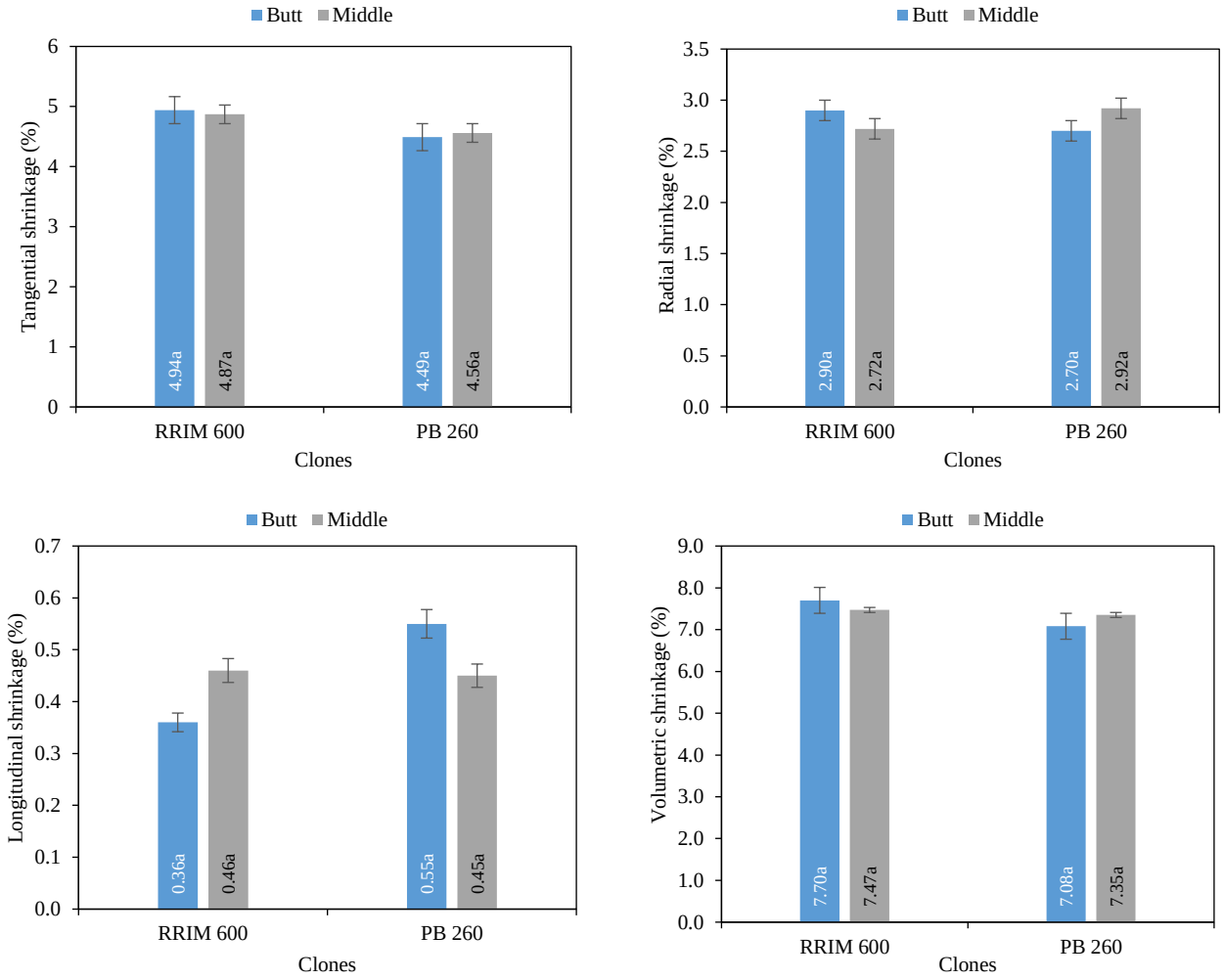

Figure 4. Physical properties of *H. brasiliensis* clones at different height levels. Within each clone, bars with different superscripts (a, b) are significantly different ($p \leq 0.05$) (cont.)

Table 6 present a comparison of the physical properties obtained in the present study with values reported in previous studies. Compared to the *H. brasiliensis* clones studied by Allwi et al. (2021), the present study observed a RS of 2.81%, which was higher than the 1.82% reported for the GT 1 clones but slightly lower than the 2.98% for RRIM 600. In terms of TS, RRIM 600 in present study exhibited a higher value of 4.91% compared to 4.0% for GT 1 and 4.68% for RRIM 600, while PB 260 had a lower TS of 4.52% than RRIM 600. Regarding LS, the present study recorded LS values of 0.50% for PB 260 and 0.41% for RRIM 600, although non-significant, both of which were lower than the LS values for GT 1 (0.76%) and RRIM 600 (0.72%) clones. On the other hand, compared to the five clones studied by de Lima et al. (2023), the VS of the present study was lower except for GT 1 (7.07%).

The significantly higher TS and VS observed in RRIM 600 are likely attributed to their higher basic RD and thicker cell wall as the significant positive correlations between TS and VS with RD and CWT is observed (Table 7). The results of the present study suggest that shrinkage properties are strongly influenced by RD and CWT, with wood of higher RD and thicker cell wall exhibiting greater shrinkage. Hamdan et al. (2020) and Okon (2014) also noted that shrinkage properties are positively correlated with CWT. Other factors, such as high microfibril angle (MFA) and low extractive content, may also contribute to the wood's increased shrinkage (Shmulsky and Jones, 2019).

The VS of the *H. brasiliensis* clones in the present study was assessed using the classification of Alipon et al. (2005), placing the clones in the low shrinkage category. The results suggest that the clones may be suitable for applications where shrinkage is critical, such as in furniture, cabinetry, moldings, flooring and musical instruments. However, the suitability for specific applications may still depend on

their mechanical properties. Notably, the shrinkage behavior of these clones is better to that of the Philippine mahogany group and other commercially used timber species (Alipon et al., 2005).

3.3 Mechanical properties

The mean values and analysis of variance for the mechanical properties of *H. brasiliensis* clones at both green and 12% MC conditions, as well as along different height levels, are presented in Table 8. At the 12% MC condition, significant differences between clones were observed in modulus of elasticity (MOE), compression parallel-to-grain, and shear strength. At the green condition, significant differences were recorded in all mechanical properties except toughness. However, significant variations along the height were observed only in shear strength at green condition and in hardness (side) at 12% MC condition.

At both green and 12% MC conditions, the mechanical properties of RRIM 600 were higher than those of PB 260. At the 12% MC condition, RRIM 600 exhibited a 21.55% higher MOE (8.12 GPa), 13.23 % higher compression parallel-to-grain (29.65 MPa) compared to PB 260 (6.54 GPa and 25.97 MPa). In terms of shear strength, RRIM 600 (6.91 MPa) was 12.45% stronger than PB 260 (6.10 MPa).

At the green condition, RRIM 600 showed a significant higher modulus of rupture (MOR) (42.73 MPa), MOE (5.49 GPa), and stress at the proportional limit (SPL) (20.07 MPa), which were 17.53%, 22.49%, and 39.78% higher, respectively, compared to PB 260 (35.85 MPa, 4.38 GPa, and 13.41 MPa). Additionally, RRIM 600 displayed greater compression strength, with values 41.11% higher for compression parallel-to-grain (18.24 MPa) and 53.49% higher for compression perpendicular-to-grain (3.72 MPa) compared to PB 260 (12.02 MPa and 2.15 MPa, respectively). RRIM 600 also exhibited a 30.46% higher shear strength (5.22 MPa), 29.31% greater hardness: side (2.66 kN), and 24.44% higher hardness: end (3.03 kN) compared to PB 260 (3.84 MPa, 1.98 kN, and 2.37 kN, respectively).

Table 6 presents a comparison of the mechanical properties obtained in this study with those reported in previous research. The MOE of RRIM 600 (8.12 GPa) at 12% MC was higher than that of the GT 1 clone (8.05 GPa) of *H. brasiliensis* but lower than RRIM 600 (8.28 GPa) (Allwi et al., 2021). Additionally, the MOE values of both clones in the present study at 12% MC were lower than those of the seven *H. brasiliensis* clones (Riyaphan et al., 2015). In contrast to above, the MOR at 12% MC for both RRIM 600 and PB 260 was lower than the values reported for the clones studied by Allwi et al. (2021) and Riyaphan et al. (2015).

The compression parallel-to-grain at 12% MC for RRIM 600 (29.65 MPa) and PB 260 (25.97 MPa) was lower than GT 1 and RRIM 600 clones, reported by Allwi et al. (2021) (48.74 MPa and 48.91 MPa) and Eufrade et al. (2015) (49.83 MPa and 43.53 MPa) (Table 6). Similarly, the compression perpendicular-to-grain for RRIM 600 (6.00 MPa) and PB 260 (6.01 MPa) was lower than GT 1 and RRIM 600 clones, reported by Allwi et al. (2021) (15.69 MPa and 18.18 MPa) and Eufrade et al. (2015) (11.24 MPa and 11.38 MPa). Moreover, shear strength at 12% MC of the present study (RRIM 600: 6.91 MPa, PB 260: 6.10 MPa) was lower compared to the shear strength observed by Eufrade et al. (2015) for GT 1 (9.43 MPa) and RRIM 600 (9.60 MPa) clones.

The high mechanical properties of RRIM 600 compared to PB 260, observed in both green and 12% MC conditions, are likely associated to its higher basic RD and anatomical characteristics. As shown in Table 7, all mechanical properties exhibited a positive correlation with RD and CWT, but a negative correlation with fiber diameter, lumen diameter, and vessel diameter. These findings align with previous studies by Eufrade et al. (2015) and Allwi et al. (2021), who reported a positive relationship between RD and mechanical properties of *H. brasiliensis*. Additionally, Nordahlia et al. (2014) found a positive correlation between mechanical properties and fiber diameter and CWT. Other studies have also highlighted the significant effect of fiber cell wall thickness, and vessel diameter on the mechanical properties of wood (Hamdan et al., 2020; Nordahlia et al., 2014).

At 12% MC, the mechanical properties of RRIM 600 and PB 260 clones improved, except for toughness. This improvement is likely due to the shortening and strengthening of hydrogen bonds between microfibrils, which enhance the wood's mechanical properties (Shmulsky and Jones, 2019). However, the reduction in toughness can be attributed to the lower MC, which increases the wood's brittleness (Shmulsky and Jones, 2019). Conditioning the wood of *H. brasiliensis* to 12% MC is therefore recommended to optimize its strength properties.

Table 8. Mechanical properties at green and 12% MC condition of *H. brasiliensis* clones at different height levels

Properties	Unit	MC Condition	Clone and height levels				Overall Mean	
			PB 260		RRIM 600		PB 260	RRIM 600
			Butt	Middle	Butt	Middle		
Modulus of rupture	MPa	Green	37.55[a] (5.44)	34.16[a] (4.38)	45.48[a] (11.74)	40.00[a] (7.28)	35.85[b] (5.11)	42.74[a] (9.92)
		12%	54.08[a] (19.18)	57.92[a] (11.86)	56.98[a] (25.77)	68.88[a] (15.61)	56.00[a] (15.65)	62.93[a] (21.62)
Modulus of elasticity	GPa	Green	4.39[a] (0.82)	4.37[a] (0.41)	5.59[a] (1.27)	5.39[a] (1.48)	4.38[b] (0.63)	5.49[a] (1.35)
		12%	6.10[a] (1.64)	6.99[a] (0.93)	7.39[a] (2.80)	8.84[a] (0.75)	6.54[b] (1.37)	8.12[a] (2.13)
Stress at the proportional limit	MPa	Green	13.28[a] (2.67)	13.54[a] (4.96)	20.73[a] (2.14)	19.41[a] (1.87)	13.41[b] (3.88)	20.07[a] (2.07)
		12%	24.68[a] (6.98)	22.26[a] (3.43)	21.95[a] (6.71)	27.87[a] (4.11)	23.47[a] (5.49)	24.91[a] (6.21)
Compression parallel to the grain	MPa	Green	11.71[a] (1.79)	12.34[a] (2.40)	18.25[a] (3.29)	18.22[a] (3.52)	12.02[b] (2.09)	18.24[a] (3.32)
		12%	25.32[a] (5.06)	26.62[a] (5.48)	28.25[a] (7.75)	31.05[a] (2.84)	25.97[b] (5.17)	29.65[a] (5.86)
Compression perpendicular to the grain	MPa	Green	2.61[a] (0.57)	1.70[a] (1.04)	3.41[a] (0.99)	4.02[a] (1.19)	2.15[b] (0.94)	3.72[a] (1.11)
		12%	6.23[a] (0.95)	5.80[a] (1.49)	6.64[a] (2.05)	5.35[a] (1.26)	6.01[a] (1.23)	6.00[a] (1.78)
Shear strength	MPa	Green	3.61[b] (0.44)	4.06[a] (0.96)	4.58[b] (0.33)	5.87[a] (0.97)	3.84[b] (0.76)	5.22[a] (0.97)
		12%	6.13[a] (0.79)	6.07[a] (0.82)	7.14[a] (2.04)	6.67[a] (0.95)	6.10[b] (0.79)	6.91[a] (1.57)
Hardness: side	kN	Green	2.13[a] (0.33)	1.84[a] (0.43)	2.66[a] (0.54)	2.66[a] (0.62)	1.98[b] (0.40)	2.66[a] (0.57)
		12%	3.25[a] (0.86)	2.84[b] (0.49)	3.59[a] (0.81)	3.03[b] (0.59)	3.05[a] (0.71)	3.31[a] (0.75)
Hardness: end	kN	Green	2.37[a] (0.56)	2.36[a] (0.38)	2.82[a] (0.46)	3.24[a] (0.42)	2.37[b] (0.47)	3.03[a] (0.48)
		12%	4.40[a] (0.79)	4.70[a] (0.73)	4.79[a] (0.70)	4.47[a] (0.72)	4.55[a] (0.75)	4.63[a] (0.71)
Toughness	J/spec	Green	12.85[a] (3.87)	9.39[a] (3.46)	10.06[a] (3.53)	14.26[a] (5.92)	11.12[a] (3.99)	12.16[a] (5.21)
		12%	12.39[a] (5.62)	12.81[a] (4.27)	12.58[a] (3.34)	10.14[a] (1.70)	12.60[a] (4.86)	11.36[a] (2.87)

Note: Within each clone and across height levels, as well as for the overall mean, values with different superscripts in the same row are significantly different ($p<0.05$). Values inside the parenthesis indicate standard deviation.

Across height levels, significant differences were observed in shear strength under green condition and side hardness at 12% MC (Table 8). For shear strength, values increased from 3.61 to 4.06 MPa in PB 260 and from 4.58 to 5.87 MPa in RRIM 600, indicating consistently higher strength in the middle portion. In contrast, side hardness at 12% MC slightly decreased from 3.25 to 2.84 kN in PB 260 and from 3.59 to 3.03 kN in RRIM 600. Similar trends of increased strength properties in the middle portion have also been reported for other species, including *Falcataria falcata* (Marasigan et al., 2022), and Eucalyptus species such as *E. gomphocephala*, *E. cladocalyx*, and *E. grandis* × *camaldulensis* (Wessels et al., 2016).

The observed differences in strength properties along the height levels can be attributed to variations in RD and anatomical characteristics, as indicated by the correlations in Table 7. Dinwoodie (2000) also reported a positive correlation between RD and strength properties across height levels. Furthermore, anatomical factors such as cell wall thickness, vessel frequency, and vessel diameter contribute to the differences in strength properties along the axial heights (Sseremba et al., 2016).

Based on the strength classification by Alipon and Bondad (2008), RRIM 600 and PB 260 are classified under medium and moderately low strength, respectively, in both green and 12% MC conditions (Table 9). The classification of PB 260 aligns with Alipon and Bondad's (2008) findings, but the classification of RRIM 600 differs from their classification. This suggests that factors such as clone type may influence the properties of *H. brasiliensis*. Other factors, such as age and location, could also contribute to variations in the wood's strength, a concept that can be explored in future studies.

On the basis of above-mentioned strength classification, RRIM 600 clones were ranked similarly to *S. macrophylla*, *G. arborea*, *A. mangium*, *P. malaanonan*, *R. negrosensis*, *P. contorta*, and *R. polysperma* while PB 260 was ranked similarly to *R. almon*, *R. palosapis*, and *E. deglupta*. Both clones were rated higher than *R. ovata* and *F. falcata*, which is classified as low strength (Table 9). Recommended uses for each clone based on their classification are provided in Table 9. Additionally, sample furniture made from RRIM 600 and PB 260 wood, including a center table, shelves, cabinets, and a picnic table, is shown in Figure 5. Given the current Philippine wood market, RRIM 600 has the potential to replace *S. macrophylla*, *G. arborea*, and *A. mangium*. Similarly, PB 260 could serve as a substitute for *E. deglupta*, and both species can be viable alternatives to *F. falcata*.

Figure 5. Different furniture made from the combination RRIM 600 and PB 260 rubber wood clones. (a) Coffee table, (b) shelves, (c) cabinet, and (d) picnic table.

Table 9. Strength classification of the *Havea brasiliensis* clones, Philippine mahogany group, and commercially used timber species and their recommended uses (Alipon and Bondad, 2008).

Strength classification	*Havea brasiliensis* clones	Philippine mahogany group	Commercially used timber species in the Philippines	Recommended Uses
Medium	RRIM 600	Bagtikan (*Parashorea malaanonan*)	Mahogany (*Swietenia macrophylla*)	General construction, doors, framing, paneling, flooring, planking, medium-grade furniture, cabinet, veneer, and plywood (face and core).
		Red lauan (*Rubroshorea negrosensis*)	Yemane/Gmelina (*Gmelina arborea*)	
		White lauan (*Pentacme contorta*)	Mangium (*Acacia mangium*)	
		Tanguile (*Rubroshorea polysperma*)		
Moderately low	PB 260	Almon (*Rubroshorea almon*)	Bagrass (*Eucalyptus deglupta*)	For pulp and paper production, wood carving and sculpture, conventional furniture, drafting boards, toys, venetian blinds, crates, pallets, form wood, and shingles.
		Mayapis (*Rubroshorea palosapis*)		
Low		Tiaong (*Rubroshorea ovata*)	Falcata (*Falcataria falcata*)	Light construction where strength hardness and durability are not critical requirements such as door and panel cores, moldings, ceiling, pulp and paper, and core veneer. It can also be used for interior construction, cheap types of furniture, window frames (treated), flooring, planking, and packing cases.

Zamboanga Sibugay is recognized as one of the leading regions for *H. brasiliensis* plantations in the Philippines (Mag-aso and Garcia, 2021). Utilizing the senile clones cultivated in this area could help meet the growing demand for wood resources in Mindanao and other regions across the country. According to DENR-FMB (2023), the average retail price of *H. brasiliensis* lumber (2" × 4" × 8') is PHP 28.14 (USD 0.48) per bd ft. Based on the diameter and height measurements of the clones in the present study (Table 1), each tree is estimated to yield approximately 501.61 bd ft of lumber, generating an estimated income of PHP 14,113.23 (USD 239.74) per tree.

To ensure the effective utilization of this tree, appropriate prophylactic treatments are generally recommended after cutting to prevent attacks by xylophagous organisms, which are often attracted to the high carbohydrate content typically reported in rubberwood (Teoh et al., 2011). Although this study focuses solely on the anatomical, physical, and mechanical properties of *H. brasiliensis* clones, future research may evaluate their chemical composition and resistance to biological degradation. The application of conventional preservatives (e.g., propiconazole, deltamethrin, tebuconazole, permethrin, disodium octaborate tetrahydrate, and copper azole) or alternative heat-based treatments could also be explored to enhance durability.

4. CONCLUSION

The Philippine wood industry, along with plantation developers and farmers, could explore the use of senile *Hevea brasiliensis* clones as a source of additional raw materials for composite boards, furniture, cabinetry, flooring, paneling, construction materials, veneers, plywood, and door panels. This species, which is abundant in Mindanao, offers significant potential to provide farmers with additional income, reduce waste, and address the increasing wood demand in the country. The present study revealed notable differences in the wood properties of *H. brasiliensis* clones as well as along different stem height levels. Anatomically, PB 260 exhibited longer fibers and larger fiber diameter, lumen diameter, vessel length, and vessel diameter, whereas RRIM 600 had a thicker cell wall. Physically, RRIM 600 displayed higher basic relative density, tangential shrinkage, and volumetric shrinkage, while PB 260 recorded the highest green moisture content. Mechanically, at 12% MC, significant differences were observed between clones in MOE, compression parallel-to-grain, and shear strength, while in the green condition, all mechanical properties except toughness differed significantly. Variations along the height of the tree were also noted but were less pronounced in mechanical properties. Future studies should include chemical characterization (e.g., lignin, cellulose, and holocellulose content) and durability testing to further optimize the utilization of these clones for industrial applications.

ACKNOWLEDGEMENTS

The authors express their gratitude to the Department of Science and Technology-Forest Products Research and Development Institute (DOST-FPRDI) for funding this study and and to the Tambanan Agrarian Reform Beneficiaries Cooperative (TARBEMCO) for providing the research tree samples. The authors also acknowledge the Physical Plant and Sawmilling and Furniture Testing Section of DOST-FPRDI for their support in the transportation and sawmilling of the logs. The authors also acknowledge the Wood Anatomy and Wood Physics and Mechanics Sections for their assistance in sample preparation and testing. The authors also thank Barile E. of the Communication Materials Production and Library Services for her assistance in proofreading and editing the manuscript.

AUTHOR CONTRIBUTIONS

Conception and design of study: Marasigan OS, Alipon MA; Acquisition of data: Marasigan OS, Alipon MA; Analysis and/or interpretation of data: Marasigan OS, Alipon MA; Drafting the manuscript: Marasigan OS, Alipon MA; Revising the manuscript for significant intellectual content: Marasigan OS, Alipon MA; Approval of the version of the manuscript to be published: Marasigan OS, Alipon MA.

DECLARATION OF CONFLICT OF INTEREST

The authors declare no conflict of interest.

REFERENCES

Aiso H, Ishiguri F, Toyoizumi T, Ohshima J, Iizuka K, Priadi D, et al. Anatomical, chemical, and physical characteristics of tension wood in two tropical fast-growing species, *Falcataria moluccana* and *Acacia auriculiformis*. Tropics 2016;25(1):33-41.

Alipon MA, Bondad EO, Cayabyab PC. Relative Density of Philippine Woods. College, Laguna, Philippines: Forest Products Research and Development Institute; 2005.

Alipon MA, Bondad EO, Gilbero DM, Jimenez JP, Emmanuel PD, Marasigan OS. Anatomical properties and utilization of 3-, 5-, and 7-yr-old Falcata (*Falcataria moluccana* Miq. Barneby and J.W. Grimes) from CARAGA Region, Mindanao, Philippines. Philippine Journal of Science 2021;150(5):1307-19.

Alipon MA, Bondad EO. Strength Grouping of Philippine Timbers for Various Uses. College, Laguna, Philippines: Forest Products Research and Development Institute; 2008.

Allwi NZ, Abdul Halip J, Sabtu NS. Assessment of rubberwood (*Hevea brasiliensis*) clones properties for the Malaysian furniture industry. The Malaysian Forester 2021;84(1):94-113.

American Society for Testing Materials (ASTM). Standard Methods of Testing Small Clear Specimens of Timber (ASTM Designation: D143-52: Part 16:30). Philadelphia, PA.: ASTM; 2019.

Amorim EP, Menucelli JR, Germano AD, Freitas RFP, Barbosa JA, Paula FA, et al. Technological potential of fibers from 20 *Hevea brasiliensis* clones for use as pulp, paper, and composite materials. Research, Society and Development 2021; 10(10):e549101019102.

Ayrilmis N, Akbulut T, Yurtta SE. Effects of core layer fiber size and face-to-face core layer ratio on the properties of three-layered fiberboard. BioResources 2017;12:7964-74.

De Lima IL, Moreira IV, Ranzini M, Longui EL, Cambuim J, Moraes MLT, et al. Physical and anatomical properties of *Hevea brasiliensis* clones. Ciencia y Tecnologia 2023; 25(20):1-12.

Department of Environment and Natural Resources-Forest Management Bureau (DENR-FMB). Philippine Forestry Statistics. Diliman, Quezon City: DENR; 2023.

Department of Science and Technology-Forest Products Research and Development Institute (DOST-FPRDI). Monograph on Production and Utilization of Philippine Bamboos. Los Baños, Philippines: DOST-FPRDI; 2007.

Dinwoodie JM. Timber: Its Nature and Behavior. 2nd ed. London: Taylor and Francis Group; 2000. p. 272.

Eufrade HJ Jr, Ohto JM, da Silva LL, Palma HAL, Ballarin AW. Potential of rubberwood (*Hevea brasiliensis*) for structural use after the period of latex extraction: A case study in Brazil. Journal of Wood Science 2015;61:384-90.

Franklin GL. Preparation of thin sections of synthetic resins and woody resin composites and a new method for wood. Nature 1945;155:51-7.

Hamdan H, Nordahlia AS, Anwar UMK, Iskandar MM, Omar MKM, Tumirah K. Anatomical, physical, and mechanical properties of four pioneer species in Malaysia. Journal of Wood Science 2020;66:Article No. 59.

Hartono R, Purba FVA, Iswanto A, Priadi T, Sutiawan J. Fiber quality of yellow bamboo (*Bambusa vulgaris* vitata) from forest area with special purpose Pondok, Buluh, Simalungun Regency, North Sumatera Province. IOP Conference Series: Earth and Environmental Science 2022;1115:Article No. 012084.

Izani MAN, Sahri MH. Wood and cellular properties of four new *Hevea* species. Proceedings of the FORTROP II International Conference; 2008 Nov 17-20; Bangkok, Thailand; 2008.

Madsen B, Brondsted P, Andersen TL. Biobased composites: Materials and potential applications as wind turbine blade materials. In: Advances in Wind Turbine Blade Design and Materials. Amazon; 2013. p. 363-86.

Mag-Aso J, Garcia FG. Productivity from the different rubber-based farming system models in Cotabato Province, Philippines. IOP Conference Series: Earth and Environmental Science 2021;892:Article No. 012019.

Marasigan OS, Mundin MMA. Physico-mechanical properties and potential utilization of *Melia azedarach* L. grown in Quezon Province, the Philippines. Philippine Journal of Science 2024;153(4):1429-41.

Marasigan OS, Razal RA, Carandang WM, Alipon MA. Physical and mechanical properties of stems and branches of Falcata (*Falcataria moluccana* (Miq.) Barneby and J.W. Grimes) grown in Caraga, Philippines. Philippine Journal of Science 2022;151(2):575-86.

Nagarajaganesh B, Rekha B. Intrinsic cellulosic fiber architecture and their effect on the mechanical properties of hybrid composites. Archives of Civil and Mechanical Engineering 2020;20:Article No. 125.

Naji HR, Bakar ES, Sahri MH, Soltani M, Abdul Hamid H, Ebadi SE. Variation in mechanical properties of two rubberwood clones in relation to planting density. Journal of Tropical Forest Science 2014;26(4):503-12.

Nordahlia AS, Anwar UMK, Hamdan H, Zaidon A, Mohd Omar MK. Mechanical properties of 10-year-old sentang (*Azadirachta excelsa*) grown from vegetative propagation. Journal of Tropical Forest Science 2014;26(2):240-8.

Okon KE. Relationship between fibre dimensional characteristics and shrinkage behavior in a 25-year-old *Gmelina arborea* in Oluwa Forest Reserve, South West Nigeria. Applied Science Research 2014;6:50-7.

Onakpoma I, Ogunsanwo OY, Ohwo OA, Raut S, Aguma Q, Schimleck LR, et al. Rubberwood-Potential for pulp and composite board utilization. Forests 2023;14(9):Article No. 1722.

Panshin A, De Zeeuw C. Textbook of Wood Technology. 4th ed. New York, USA: McGraw-Hill Book Company; 1980. p. 722.

Philippine Statistics Authority (PSA). Other Crops: Area Planted/Harvested, by Region and by Province, 1990-2019 [Internet]. 2021 [cited 2024 Dec 27]. Available from: https://openstat.psa.gov.ph/.

Plants of the World Online (POWO). Facilitated by the Royal Botanic Garden, Kew [Internet]. 2024 [cited 2024 Dec 27]. Available from: http://www.plantsoftheworldonline.org/.

Pulkkinen I, Alopaeus V, Fiskari J, Joutsimo O. The use of fibre wall thickness data to predict handsheet properties of eucalypt pulp fibres. O Papel 2008;69:71-85.

R Core Team. R: A Language and Environment for Statistical Computing [Internet]. 2020 [cited 2024 Dec 27]. Available from: https://www.R-project.org/.

Riki JTB, Sotandde OA, Oluwadare AO. Anatomical and chemical properties of wood and their practical implications in pulp and paper production: A review. Journal of Research in Forestry, Wildlife and Environment 2019;11:358-68.

Riyaphan J, Phumchai T, Neimsuwan T, Witayakran S, Sungsing K, Kaveeta R, et al. Variability in chemical and mechanical properties of Para rubber (*Hevea brasiliensis*) trees. Science Asia 2015;41:251-8.

Sharma AK, Dutt D, Upadhyaya JS, Roy TK. Anatomical, morphological, and chemical characterization of *Bambusa tulda*, *Dendrocalamus hamiltonii*, *Bambusa balcooa*, *Malocana baccifera*, *Bambusa arundinaceae*, and *Eucalyptus tereticornis*. BioResources 2011;6(4):5062-73.

Shmulsky R, Jones PD. Forest Products and Wood Science: An Introduction. 7th ed. Hoboken, NJ: John Wiley and Sons, Inc.; 2019.

Sseremba OE, Mugabi P, Banana AY. Within-tree and tree-age variation of selected anatomical properties of the wood of Uganda-grown *Eucalyptus grandis*. Forest Products Journal 2016;66:433-42.

Suansa NI, Al-Mefarrej HA. Branch wood properties and potential utilization of this variable resource. BioResources 2020;15(1):479-91.

Teoh YP, Don MM, Ujang S. Assessment of properties, utilization, and preservation of rubberwood (*Hevea brasiliensis*): A case study in Malaysia. Journal of Wood Science 2011;57:255-66.

Van Duong D, Schimleck L, Tai Tien D, Chu Van T. Radial variation in cell morphology of *Melia azedarach* planted in Northern Vietnam. *Maderas.* Ciencia y Tecnología 2021;23(7):1-10.

Wessels CB, Crafford PL, Du Toit B, Grahn T, Johansson M, Lundqvist SO, et al. Variation in physical and lumber properties from three drought-tolerant *Eucalyptus* species grown on the dry west coast of Southern Africa. European Journal of Wood and Wood Products 2016;74:563-75.

Wheeler EA, Baas P, Gasson PE. IAWA list of microscopic features for hardwood identification. IAWA Bulletin 1989;10(3):219-332.

Environment and Natural Resources Journal

Volume 24
Issue 1
2026

Innovation Compact System Usage for Household Water Treatment: A Case Study on Water Quality in Coastal Central Java

Sulistiyani Sulistiyani*, Tri Joko, Onny Setiani, Yusniar Hanani Darundiati, and Muhammad Auliya Rahman

Faculty of Public Health, Universitas Diponegoro, Prof. Jacub Rais, Tembalang, Semarang, Central Java, Indonesia

ARTICLE INFO

Received: 29 Apr 2025
Received in revised: 3 Sep 2025
Accepted: 8 Sep 2025
Published online: 14 Nov 2025
DOI: 10.32526/ennrj/24/20250110

Keywords:
Drinking Water Quality Index/ Household water treatment/ Ultraviolet disinfection/ Coastal groundwater/ Indonesia

*** Corresponding author:**
E-mail:
sulistiyani@live.undip.ac.id

ABSTRACT

In many coastal regions of Central Java, Indonesia, access to safe drinking water remains limited owing to often contaminated groundwater sources. This study evaluated the performance of a compact household water treatment system integrating aeration, filtration, adsorption, and ultraviolet (UV) disinfection. Water samples from 15 wells across Kendal, Semarang, and Demak were tested for 13 parameters, including turbidity, total dissolved solids (TDS), color, ammonia, iron, manganese, dissolved oxygen (DO), and total coliforms, analyzed by ISO/IEC 17025-accredited laboratories. The treatment significantly improved water quality, reducing turbidity from 14.00 to 4.96 NTU (65%), TDS from 738.6 to 336.35 mg/L (54%), color from 21.93 to 9.15 TCU (58%), and ammonia from 1.82 to 1.02 mg/L (44%); meanwhile, DO increased from 5.48 to 8.24 mg/L (33%). The Drinking Water Quality Index scores of samples from 80% of the sites improved from "very poor" (>200) to "good" (<100), indicating untreated water transformation from non-potable to potable. However, microbiological safety remained a limitation, with total coliforms reduced by 52% (from 230 to 110 CFU/100 mL) but failing to meet the 0 CFU/100 mL standard. Therefore, additional heat treatment or UV contact time extension from 3 to 6 h is recommended to achieve full microbial compliance. This study demonstrates the effectiveness of the treatment system in significantly improving physical and chemical quality, while highlighting the need to optimize its microbial disinfection capacity. Its affordability and simplicity make it a promising decentralized solution for underserved communities.

HIGHLIGHTS

- Compact system integrates aeration, filtration, adsorption, and UV.
- Turbidity, TDS, and ammonia reduced by over 40-60% across samples.
- Simple, affordable system fits household use in coastal communities.

1. INTRODUCTION

Access to clean water is fundamental to human health, well-being, and socioeconomic development (Amorocho-Daza et al., 2023). The basic water requirement per person ranges from several to tens of liters per day (Annobil, 2021). According to the World Health Organization (2022), a minimum of 20 L/capita/day is required to meet drinking, cooking, and hygiene requirements. Although survival-level drinking water needs are estimated at approximately 2.5 to 3 L/person/day, the WHO recommends an intermediate access threshold of approximately 50 L/person/day to adequately support public health and sanitation. These benchmarks highlight the importance of ensuring sufficient water quantity and quality for human use, especially in areas with limited infrastructure.

In Indonesia, the national water supply system is heavily dependent on non-piped sources. Although approximately 90% of the population has access to some form of improved water source, only about 19% of households are connected to municipal piped networks (PDAM) (Firdaus et al., 2024). Many households still rely on groundwater from wells and

Citation: Sulistiyani S, Joko T, Setiani O, Darundiati YH, Rahman MA. Innovation compact system usage for household water treatment: A case study on water quality in Coastal Central Java. Environ. Nat. Resour. J. 2026;24(1):77-87. (https://doi.org/10.32526/ennrj/24/20250110)

springs, harvested rainwater, or commercially packaged water. Bottled and refill station water consumption has increased significantly in recent years, with forecasts suggesting that by 2026, nearly half of Indonesia's population will rely on packaged drinking water (Zikrina et al., 2024). Conversely, only approximately 9% of the population uses PDAM water for drinking, despite system coverage reaching approximately 35% of the national territory. This discrepancy is largely attributed to concerns about service reliability, water safety, and infrastructure limitations, particularly in rural and peri-urban areas (Cronin et al., 2017; Firdaus et al., 2024).

Historically, groundwater and spring water sources in Indonesia have been considered safe. However, rapid environmental degradation, pollution, and adverse geochemical conditions have contributed to the contamination of many sources (Basuki et al., 2024). In particular, coastal aquifers in northern Java are frequently affected by saline intrusion and reductive conditions that mobilize metals such as iron and manganese. In Indramayu, groundwater commonly exhibits elevated levels of these metals, surpassing the national drinking water standards. Indonesian regulations require drinking water to meet stringent physical, chemical, microbiological, and radiological quality requirements (Rusydi et al., 2021). Failure to comply with these standards due to the presence of pathogens, excessive metals, or high turbidity poses serious health risks in practice. Households that lack access to safe piped water often resort to boiling or purchasing refill water as a mitigation strategy (Bashir et al., 2020).

Water quality degradation is particularly severe in the coastal regions of Central Java. For example, Semarang has experienced ongoing groundwater salinization and increased pollution pressures (Rahmawati and Marfai, 2013). Despite being a provincial capital, only approximately 8% of the residents consume PDAM water directly, with a larger proportion (approximately 26%) depending on water from refill stations, which are treated but often not subject to the same level of regulatory oversight. Piped services are often nonexistent in rural and peri-urban areas (USAID, 2023). The widespread reliance on packaged water has also created substantial environmental burdens. Recent sustainability assessments have estimated that packaged water consumption in Java contributes to the annual production of millions of tons of plastic waste.

The combination of saline and contaminated groundwater, limited piped-water infrastructure, and increasing dependence on expensive packaged water present a complex challenge for coastal Central Java, which needs affordable, household-level water treatment technologies that can improve water quality at the point of use. This study introduces the Innovation Compact System, a small-scale integrated treatment solution that combines multiple purification processes to transform well water and groundwater into potable water compliant with Indonesian national standards, removing the need for boiling. By enabling the local treatment of non-piped sources, this technology offers a cost-effective alternative to packaged water, potentially reducing household expenses, minimizing environmental waste, and improving health outcomes in underserved communities.

2. METHODOLOGY

2.1 Materials and tools

This study used gravel, silica sand, white sponges, biofoams, and tools such as glass and stainless steel casings, separators, connectors, pumps, burrs, drills, and ultraviolet (UV) lamps. Sterile bottles were used for microbiological sampling, and a 5 L high-density polyethylene (HDPE) jerry can was employed as a sterile container to preserve the integrity of collected samples. All physicochemical and microbiological analyses were performed using standardized ISO methods in ISO/IEC 17025-accredited laboratories.

2.2 Research design

The Innovation Compact System for water treatment (Figure 1) was engineered by incorporating key mechanisms, specifically aeration, filtration, adsorption, and disinfection. Aeration enhances the dissolved oxygen (DO) concentration and eliminates dissolved gases, including hydrogen sulfide. Filtering is conducted using media such as activated carbon to eliminate solid particles and diminish turbidity, color, and odor. Adsorption promotes the binding of both organic and inorganic contaminants to the adsorbent surface. UV light disinfection can effectively eliminate harmful microorganisms and simultaneously maintain the essential mineral content of water. Integrating these four processes into a single system is a practical and efficient solution for improving drinking water quality.

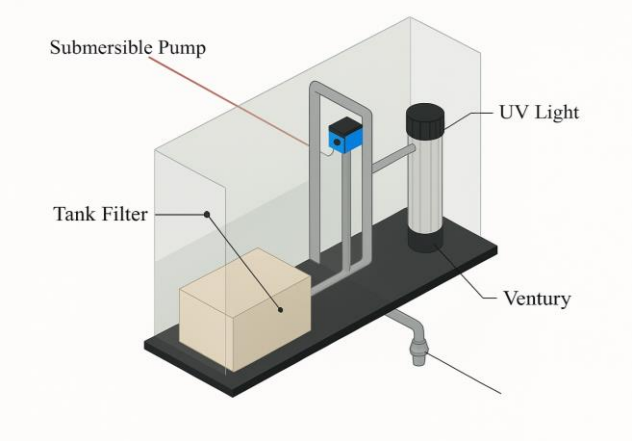

Figure 1. Compact drinking water treatment system design

The treatment system, with a capacity of 5 L, was carefully developed to prioritize users and operational efficiency. Untreated water was inserted into the system by a physical filter unit comprising various layered materials, such as silicon dandals and other selected media, specifically developed to remove suspended solids and reduce haze. The water was then moved by pumps built through the system to initiate a ventilation process to improve the DO content and remove volatile compounds. Subsequently, the treated water was exposed to UV rays for 3 h to remove pathogenic bacteria and ensure thorough disinfection. This comprehensive process ensured that the resulting water met the strict quality standards and was safe and suitable for drinking.

2.3 Sampling

The samples were collected using grab sampling. Sterile equipment was employed for microbiological examination, and physical and chemical analyses were performed on water samples gathered in a 5 L jerry can. Careful handling was performed to prevent oxygen bubbles from entering the container. The number of samples collected was calculated using Equation 1:

$$(t-1)(r-1) \geq 15 \quad (1)$$

Where; t refers to number of treatments, which is 2 (1 control and 1 device), and r is the number of replications, which was determined to be 15 using the formula.

Water quality sampling was conducted across three coastal regions in Central Java: Kendal City, Semarang City, and Demak Regency. Fifteen sampling sites were selected to capture a range of environmental and residential conditions: Peggagayam (Neighborhood Unit 3 / Community Unit 9), Gayaman (Neighborhood Units 1, 2, and 3 / Community Unit 2), East Tugurejo (Neighborhood Units 4, 5, and 6 / Community Unit 5), Jrakah (Neighborhood Units 1 and 4 / Community Unit 3), Dempel (Neighborhood Unit 2 / Community Unit 2), with three samples taken from different points, Jati Utara (Neighborhood Unit 2 / Community Unit 3), and Krajan (Neighborhood Unit 3 / Community Unit 4) (Figure 2).

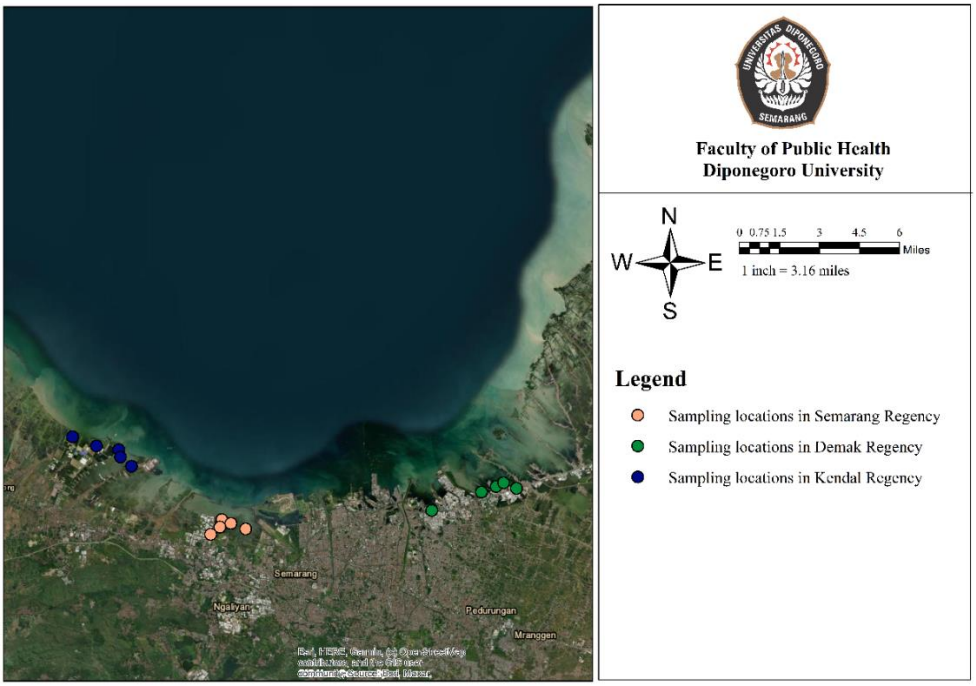

Figure 2. Sampling locations in the selected coastal regions

2.4 Water quality assessment

The Drinking Water Quality Index (DWQI) was assessed using the weighted arithmetic index method, which remains a widely adopted approach for quantifying the overall water quality suitability for human consumption. Each physicochemical and microbiological parameter was assigned a unit weight (Wi), reflecting its relative importance to public health and environmental risks. The weight values were determined with reference to the WHO Guidelines for Drinking Water Quality (4th edition, 2008) and adjusted to align with the national standards stipulated in the Regulation No. 492/Menkes/Per/IV/2010 (Ministry of Health of the Republic of Indonesia, 2010; World Health Organization, 2022).

Parameters with high toxicological and pathogenic significance such as lead, nitrite (NO_2^-), and total coliform bacteria, were assigned higher Wi values (≥0.08) to acknowledge their potential to cause acute and chronic health effects even at low concentrations. Conversely, parameters considered mainly aesthetic or non-toxic, such as color, temperature, and alkalinity, were assigned lower Wi (≤0.03). This weighting approach follows established protocols adopted in water quality studies diverse geographical settings (Table 1) (Şener et al., 2017; Solangi et al., 2020; Yilikal et al., 2018).

The DWQI computation involved four steps. First, a quality rating (qi) for each parameter was calculated using Equation 2:

$$qi = (\frac{C_i}{S_i}) \times 100 \quad (2)$$

Where; CiC_iCi is the measured concentration of the iii-th parameter and SiS_iSi is the corresponding permissible limit according to WHO or Permenkes 492. Second, the sub-index (SIi) was derived as follows:

$$SI_i = W_i \times q_I \quad (3)$$

Finally, the DWQI value for each sample was obtained by summing the sub-indices:

$$DWQI = \sum_{i=1}^{n} SI_i \quad (4)$$

Table 1. DWQI parameter weights (Wi) and standard values (Si)

Parameter	Unit	Standard value (S_i)*	Weight (W_i)	Justification**
Turbidity	NTU	<5	0.05	Aesthetic concern, may indicate pathogens
Temperature	°C	±25	0.03	Minimal health impact
TDS	mg/L	<500	0.05	Affects palatability
Color	TCU	<15	0.04	Aesthetic parameter
Alkalinity	mg/L	-	0.02	No direct toxicity
Ammonia	mg/L	<1.5	0.08	Indicates pollution, toxic at high levels
Iron	mg/L	<0.3	0.08	Can affect organs, high levels dangerous
Hardness	mg/L	<500	0.05	Related to Ca and Mg, not toxic
Manganese	mg/L	<0.4	0.05	Affects nervous system at high doses
DO	mg/L	-	0.1	Indicates water freshness, aquatic life
pH	-	6.5-8.5	0.1	Influences solubility of toxic elements
Lead	mg/L	<0.01	0.15	Highly toxic, neurotoxin
Organic substances	mg/L	<10	0.05	Reflects organic pollution load
Total coliform	CFU/100 mL	0	0.15	Indicator of fecal contamination

*Si values (Ministry of Health of the Republic of Indonesia, 2010; World Health Organization, 2022).
**Justifications (Şener et al., 2017; Solangi et al., 2020; Yilikal et al., 2018).

The final DWQI values obtained for each water sample were interpreted using a standard classification scheme (Şener et al., 2017; Solangi et al., 2020; Yilikal et al., 2018) that categorizes water quality into five distinct levels ranging from “excellent” to “unsuitable for drinking purposes” based on the cumulative score derived from all analyzed parameters. The interpretation framework used in this study is summarized in Table 2.

2.5 Data analysis

Statistical analysis was conducted using IBM SPSS Statistics version 23 to evaluate the household water treatment system effectiveness based on DWQI changes. Descriptive analysis was performed to summarize the DWQI scores before and after treatment. The Shapiro-Wilk test was used to assess data normality. Depending on the distribution, either a paired sample t-test or Wilcoxon signed-rank test was

used to determine whether the post-treatment DWQI differed significantly from the pre-treatment values. A p-value <0.05 was considered statistically significant. This study aims to assess the overall improvement in drinking water quality resulting from the application of the compact treatment system.

Table 2. Interpretation of the DWQI results

DWQI range	Water quality category	Interpretation
<50	Excellent	Suitable for drinking without treatment
50-100	Good	Acceptable, may need minor treatment
100-200	Poor	Not recommended without treatment
200-300	Very poor	Strong treatment required before consumption
>300	Unsuitable	Not fit for drinking under any circumstance

Adapted from: (Mohammad et al., 2024; Şener et al., 2017; World Health Organization, 2022)

3. RESULTS AND DISCUSSION

3.1 Comparative water quality assessment

Table 3 shows the average water quality parameter values before and after using the compact filter device to clean the water a long with how well the system meets the Ministry of Health (MoH) standards and how much the percentage decreases. The treatment improved the overall water quality, with most tests showing large decreases that met the regulatory standards.

Following treatment, most water quality parameters exhibited substantial improvement, whereas a few remained relatively stable, yet within acceptable regulatory limits. Turbidity decreased by 65%, with values decreasing from 14.00 to 4.96. Similarly, total dissolved solids (TDS) showed a 54% reduction from 738.6 to 336.35 mg/L. Color also improved significantly, dropping by 58% from 21.93 to 9.15 TCU. These changes indicate the system's effectiveness in removing suspended particles and dissolved contaminants, thereby enhancing the treated water aesthetic and sensory qualities. Chemical parameters also showed significant reductions. Alkalinity declined by 49% from 40.12 to 20.36 mg/L. Hardness was reduced by 47% from 266.27 to 141.69 mg/L, and the ammonia concentration decreased by 44% from 1.82 to 1.02 mg/L. All post-treatment values complied with the quality thresholds established by the MoH, indicating that the treated water achieved chemical stability suitable for domestic consumption.

Table 3. Comparison of water quality parameters before and after treatment

Parameter	Before	After	MoH Regulation	Reduction (%)
	Mean	Mean		
Turbidity (NTU)	14	4.96	<5	65
Temperature (°C)	21.79	22.5	±25	3
TDS (mg/L)	738.6	336.35	<500	54
Color (TCU)	21.93	9.15	<15	58
Alkalinity (mg/L)	40.12	20.36	<200	49
Ammonia (mg/L)	1.82	1.02	<1.5	44
Iron (mg/L)	0.05	0.04	<0.3	20
Hardness (mg/L)	266.27	141.69	<500	47
Manganese (mg/L)	4.68	2.77	<0.4	41
DO (mg/L)	5.48	8.24	≥5	33
pH	8.13	7.77	6.5-8.5	4
Lead (mg/L)	0.01	0.01	<0.01	0
Organic substances (mg/L)	9.80	5.44	<10	44
Total coliform (CFU/100 mL)	230	110	0	52

Note: TDS (total dissolved solids); DO (dissolved oxygen); MoH (Ministry of Health)

The manganese concentration decreased by 41% from 4.68 to 2.77 mg/L; however, this value remained above the regulatory maximum of 0.4 mg/L, highlighting the need for additional treatment to ensure complete contaminant removal. In contrast with these reductions, the DO concentration increased

by 33% from 5.48 to 8.24 mg/L, reflecting enhanced oxygenation and support for aerobic biological processes. The water temperature minimally increased by 3% from 21.79 to 22.50°C, whereas the pH decreased slightly by 4% from 8.13 to 7.77. Both these parameters remained within the acceptable range by the MoH, demonstrating that the process did not significantly alter the thermal or buffering characteristics of the water. The iron concentration was reduced by 20% from 0.05 to 0.04 mg/L. The lead concentration remained constant at 0.01 mg/L. Thus, both parameters were also within regulatory limits. Organic matter concentrations declined by 44% from 9.80 to 5.44 mg/L, meeting the MoH standard of <10 mg/L. Microbiological analysis revealed a 52% decrease in total coliforms from 230 to 110 CFU per 100 mL, indicating partial microbial removal. These collective findings confirm that the compact filtration system effectively enhanced both the physicochemical and microbiological qualities of groundwater. However, persistent exceedances in parameters such as manganese and moderate levels of coliforms suggest the need for supplementary treatment processes to ensure full compliance with national drinking water quality standards.

Table 4 shows that all sampling locations initially exhibited DWQI scores within the "poor" (100-200) to "very poor" (200-300) categories, indicating that untreated groundwater from household dug wells was unsuitable for direct consumption due to elevated levels of turbidity, TDS, ammonia, and microbial contaminants. Following system implementation, the DWQI values substantially improved at most sites, with post-treatment scores predominantly falling within the "good" category (50-100). This shift demonstrates a significant enhancement in the overall water quality, rendering the treated water generally acceptable for drinking, although minor additional treatments are potentially beneficial in specific cases. The most notable improvements were recorded in Kendal and Semarang, where all sampling points improved from "poor" or "very poor" to "good." Conversely, some locations in the Demak Regency retained "poor" values even after treatment, suggesting localized limitations possibly linked to higher initial contaminant loads or reduced filtration efficacy due to system saturation. These findings highlight the effectiveness of the compact system as a decentralized water treatment solution while emphasizing the need for site-specific adjustments or supplementary treatment components to ensure consistent performance across variable groundwater conditions.

Table 4. DWQI scores before and after treatment by location

Location	DWQI Before	Interpretation	DWQI After	Interpretation
Kendal Regency				
Site 1	135.56	Poor	96.23	Good
Site 2	119.62	Poor	99.42	Good
Site 3	108.49	Poor	88.65	Good
Site 4	147.27	Poor	92.66	Good
Site 5	129.91	Poor	104.1	Good
Semarang City				
Site 1	155.38	Poor	102.77	Good
Site 2	200.91	Very poor	111.03	Good
Site 3	150.63	Poor	78.45	Good
Site 4	153.75	Poor	83.48	Good
Site 5	133.68	Poor	97.07	Good
Demak Regency				
Site 1	223.8	Very poor	108.96	Poor
Site 2	165.65	Poor	90.35	Good
Site 3	151.52	Poor	100.84	Poor
Site 4	126.23	Poor	97.48	Good
Site 5	130.53	Poor	97.88	Good

These results reaffirm the well-documented efficacy of compact filtration systems in improving physicochemical water quality, particularly parameters such as turbidity, TDS, color, and ammonia. The efficient removal of suspended solids and dissolved inorganic matter by the proposed system is consistent with previous findings that demonstrated comparable performance of both ultrafiltration and activated carbon systems used in rural and decentralized contexts (Apea et al., 2023). Similarly, the filtration system significantly reduced the hardness, alkalinity, and ammonia within acceptable regulatory limits, mirroring the findings of (Ghonimy et al., 2025) where ultrafiltration reduced the total suspended solids and organic compounds by >80% in wastewater reuse applications. The increased DO levels were consistent with those in previous studies, suggesting that enhanced aeration and organic load removal contribute to improved DO levels post-treatment. The manganese concentrations remained above the permissible threshold set by the MoH, which is consistent with challenges noted in earlier filtration studies reporting limited efficacy in metal removal without specialized adsorption media or additional chemical treatments (Molelekwa et al., 2014).

Microbiologically, the reduction in total coliforms by the system underscores its partial effectiveness in removing pathogens. This is broadly comparable to decentralized membrane filtration studies, which reported log reductions of 0.86 to 1.14 for total and fecal coliforms under field conditions (Francis et al., 2016). Although meaningful, these reductions were insufficient to fully comply with international microbial safety standards, highlighting the necessity for complementary disinfection methods, such as chlorination or UV treatment. Similar patterns were noted by (Molelekwa et al., 2014), where ultrafiltration alone achieved partial microbial removal but required integration with secondary barriers for full compliance. Furthermore, the negligible temperature and pH changes reinforce the existing literature that such parameters are typically unaffected by passive filtration systems, especially those that do not involve chemical dosing or biological processing. These findings support the general consensus that compact and decentralized filtration units are viable for improving chemical and aesthetic water quality in low-resource settings; however, further enhancements, especially for microbial safety, remain critical for comprehensive health protection.

3.2 Treatment efficiency

Table 5 shows a statistically significant improvement in DWQI after treatment ($p<0.001$). The mean difference was 51.67 with a standard deviation of 28.45, indicating that the drinking water quality improved substantially following treatment with the system.

Table 5. Paired sample t-test DWQI before and after filtration

Parameter	Mean difference	SD	p-value (2-tailed)	Interpretation
DWQI before - after treatment	51.67	28.45	0.001	Significant difference

Note: SD=standard deviation

Figure 3 presents the DWQI values before and after treatment across the five sites in the Kendal Regency, Semarang City, and Demak Regency. A consistent decrease in DWQI scores was observed after system implementation. In Kendal and Semarang, the pre-treatment DWQI values ranged from approximately 120 to >200, categorizing the water as “very poor” to “unsuitable for drinking,” whereas the post-treatment values decreased to <110 within the “moderate” quality range. Demak Regency, which recorded the highest initial DWQI values (>220 at Site 1), also showed significant improvement, with post-treatment values reduced to <120. These findings confirm that the household-scale treatment system effectively enhanced water quality in all tested locations, including those with high initial contamination levels, aligning with the statistical evidence in Table 5 and demonstrating its potential as a viable solution for improving access to safe drinking water in coastal Central Java.

The multistage purifier evaluated in this study consistently converted raw water from “poor” to “good” at all sites. This dramatic quality shift is consistent with the global evidence that well-designed point-of-use (POU) systems can greatly enhance drinking water quality. Household water treatment is widely used to improve water safety (Rao et al., 2025). Typical POU configurations combine sediment filtration, activated carbon adsorption, membranes, and UV disinfection to remove contaminants (Wu et

al., 2021). Our system incorporates these elements by adding an initial aeration stage to oxidize iron and sulfide before sequential filtration and a final UV chamber, thereby targeting turbidity, organic adsorbates, and microorganisms.

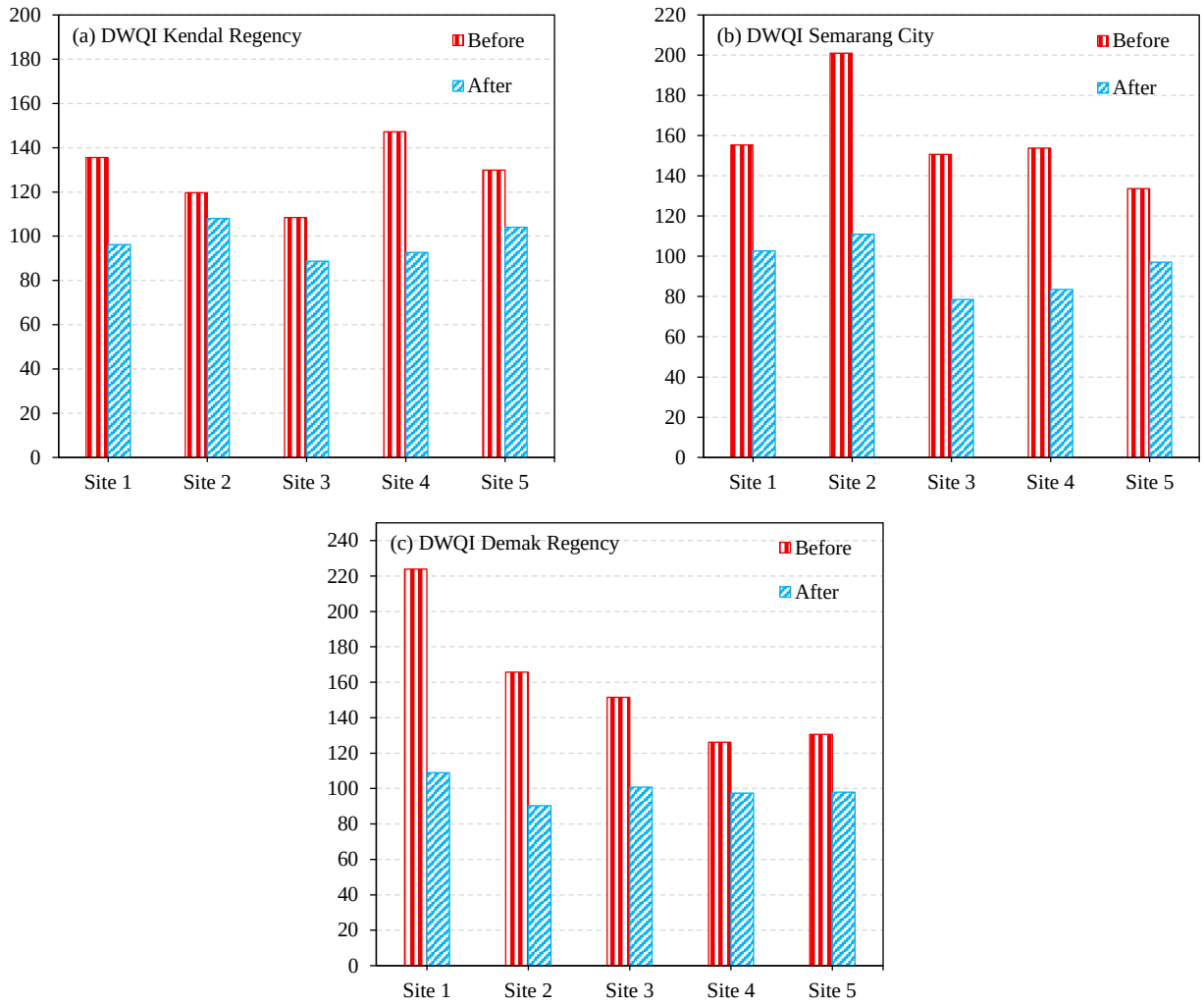

Figure 3. Comparative DWQI values before and after treatment

Field data showed that the system removal performance matched or exceeded those of benchmarks from recent studies. For example, Hincapié et al. (2025) tested household units (sedimentation + pre-filtration + UVC) in rural Colombia and Mexico and found >97% of treated samples achieved turbidity <5 NTU, with *Escherichia coli* driven to potable (non-detect) levels in every case. Hassan et al. (2024) reported that a layered nonwoven and cotton filtration unit achieved ~96% turbidity removal and 99.6% *E. coli* removal before chlorination/disinfection. Our compact unit produced treated water that met the WHO and Indonesian standards,which agrees with the high-efficiency outcomes. Similarly, a recent plateau region study in China found that installing RO-based POU systems "improved" compliance with drinking water standards compared with raw water (Zhang et al., 2020). In our study, the DWQI improvement from "poor" to "good" reflected a similar degree of contaminant reduction.

The novelty of the evaluated system lies in its tailored integration of processes in low-infrastructure contexts. Unlike many consumer POU filters often reliant on commodity cartridges and lack monitoring, this design is rugged and easily operable. By combining aeration, granular/adsorptive media, and UV light into one compact unit, multiple pollutant classes can be addressed synergistically. This multistage strategy parallels the "combined" treatment approach identified as most effective in recent reviews. For instance, Rao et al. (2025) noted that

HWT systems using combined coagulant-disinfectant steps achieved the highest microbial log removal. Although our unit uses physical oxidation instead of chemical coagulation, the analogous multibarrier structure yielded excellent purification across diverse source waters.

The compact purifier demonstrated data-driven performance on par with that of state-of-the-art POU technologies. The "good" DWQI score after treatment is quantitatively consistent with the >95% removal efficiencies reported in the literature. By achieving potable-quality water without centralized infrastructure, this system uniquely contributes to the field of household water treatment. Its innovation lies not in an untested theory but in applying proven physical, adsorptive, and UV processes in a novel configuration optimally suited to high-contamination, low-resource settings. These comparative insights confirm that the performance of the treatment unit is state-of-the-art and can be distinctly adapted to local challenges.

3.3 System performance limitations and process optimization strategies

Notably, when examined based on the microbiological parameters, the water did not meet the safe consumption standard of 0 CFU/L. This limitation aligns with previous studies indicating that microbial removal in decentralized or compact treatment systems is highly sensitive to operational parameters, particularly UV intensity and exposure duration. Adeniyi and Jimoh (2024) found that UV-C irradiation with sufficient dose (≥40 mJ/cm²) can remove up to 99.9% of bacterial contaminants, but suboptimal configurations may only inactivate some pathogens. Extending UV exposure time is a practical optimization approach capable of achieving higher disinfection levels with increased contact time, particularly at temperatures supporting microbial susceptibility (20-28 °C) (Lu et al., 2022).

Alternative, post-disinfection heat treatment can serve as an effective secondary barrier. Heat-based disinfection through boiling or controlled heating is widely recognized for its microbial effectiveness, particularly for inactivating resistant bacteria and viruses. Although this approach may increase the energy consumption, it ensures full compliance with Regulation No. 492/Menkes/Per/IV/2010, which requires the complete absence of coliform bacteria in 100 mL of drinking water. Other studies e.g., (Reed et al., 2022; Ruas et al., 2022) emphasize that the efficiency of filtration and disinfection processes is significantly influenced by the hydraulic retention time. Longer contact times allow for more complete adsorption, oxidative degradation, and microbial inactivation, particularly of persistent or slow-reacting contaminants.

To optimize the current system, two strategies are proposed: (1) UV contact time extension from 3 to 6 h to enhance microbial exposure and disinfection efficacy and (2) thermal disinfection stage integration to ensure complete microbiological safety. Although relatively minor in terms of system redesign, such adjustments can significantly improve system compliance with health standards and expand their applications to areas with high microbiological loads. Future prototypes could also benefit from the real-time monitoring of disinfection parameters and automatic flow rate adjustment to dynamically adjust the exposure based on initial contamination levels.

4. CONCLUSION

This study demonstrated the effectiveness of a compact household drinking water treatment system that integrates filtration, adsorption, aeration, and UV disinfection in significantly improving water quality by reducing color and total coliform counts while increasing DO. Aeration enhances the oxygen levels to support biological processes, and UV disinfection results in notable microbial reduction without side effects. However, the system showed limited effectiveness for turbidity, iron, manganese, ammonia, and lead concentrations, indicating the need for further optimization. Overall, this system presents a sustainable and decentralized solution for improving drinking water quality in coastal and resource-limited areas. Future studies should explore its broader pollutant removal and long-term performance.

ACKNOWLEDGEMENTS

The authors express their sincere gratitude to all parties that contributed to the completion of this research, including the laboratory staff, field assistants, and individuals who provided support during the study.

AUTHOR CONTRIBUTIONS

Sulistiyani S and Joko T contributed to the study design and literature review. Setiani O and Darundiati YH were responsible for data collection and software analysis. Rahman MA interpreted the results and drafted the manuscript. All the authors critically reviewed, edited, and approved the final version of the manuscript.

DECLARATION OF CONFLICT OF INTEREST

The authors declare that they have no known competing financial interests or personal relationships that could have influenced the work reported in this study.

REFERENCES

Adeniyi AO, Jimoh MO. Decontamination potential of ultraviolet type C radiation in water treatment systems: Targeting microbial inactivation. Water (Switzerland) 2024;16(19):5-6.

Amorocho-Daza H, van der Zaag P, Sušnik J. Access to water-related services strongly modulates human development. Earth's Future 2023;11(4):e2022EF003364.

Annobil E. Chapter 25 - Water: how much should be consumed and what are its health benefits? In: Short E, editor. A Prescription for Healthy Living: A Guide to Lifestyle Medicine, Academic Press; 2021. p. 281-6.

Apea OB, Akorley EB, Oyelude EO, Ampadu B. Chemical analysis and filtration efficiency of ceramic point-of-use water filters. Heliyon 2023;9(7):e18343.

Bashir I, Lone FA, Bhat RA, Mir SA, Dar ZA, Dar SA. Concerns and threats of contamination on aquatic ecosystems. In: Hakeem KR, Bhat RA, Qadri H, editors. Bioremediation and Biotechnology: Sustainable Approaches to Pollution Degradation. Cham, Switzerland: Springer International Publishing; 2020. p. 1-26.

Basuki TM, Indrawati DR, Nugroho HYSH, Pramono IB, Setiawan O, Nugroho NP, et al. Water pollution of some major rivers in Indonesia: The status, institution, regulation, and recommendation for its mitigation. Polish Journal of Environmental Studies 2024;33(4):3515-30.

Cronin AA, Odagiri M, Arsyad B, Nuryetty MT, Amannullah G, Santoso H, et al. Piloting water quality testing coupled with a national socioeconomic survey in Yogyakarta Province, Indonesia, towards tracking of Sustainable Development Goal 6. International Journal of Hygiene and Environmental Health 2017;220(7):1141-51.

Firdaus A, Marsya DP, Khalidah NA, Dwi LL. Strategy analysis for the fulfilment of clean water needs through piped-water service in Metropolitan City during the COVID-19 Pandemic. International Journal of Technology 2024;15(5):291-319.

Francis MR, Sarkar R, Roy S, Jaffar S, Mohan VR, Kang G, et al. Effectiveness of membrane filtration to improve drinking water: A quasi-experimental study from rural southern India. American Journal of Tropical Medicine and Hygiene 2016;95(5):1192-200.

Ghonimy M, Alharbi A, Saad SAH, Hussein NS. Improving wastewater quality using ultrafiltration technology for sustainable irrigation reuse. Water (Switzerland) 2025; 17(6):Article No. 870.

Hassan K, Alzahrani A, Alotaibi NM, Helmy M. Performance of an integrated household greywater treatment system for water optimization and reuse. Applied Water Science 2024;14(11): Article No. 242.

Hincapié M, Galdós-Balzategui A, Freitas BLS, Reygadas F, Sabogal-Paz LP, Pichel N, et al. Automated household-based water disinfection system for rural communities: Field trials and community appropriation. Water Research 2025;284: Article No. 123888.

Lu H, Wang X, Li X, Zhang X. Study on the disinfection efficiency of the combined process of ultraviolet and sodium hypochlorite on the secondary effluent of the sewage treatment plant. Processes 2022;10(1622):13-7.

Ministry of Health of the Republic of Indonesia. Regulation of the Ministry of Health of the Republic of Indonesia Number 492/Menkes/Per/IV/2010 Concerning Drinking Water Quality Requirements. Jakarta, Indonesia: 2010.

Mohammad A, Asgedom AG, Mokenen KN, Tesfay AH, Gebretsadik TT, Van der Bruggen B. Evaluation of groundwater quality for drinking water using a quality index in Abyi Adi, Tigrai, Northern Ethiopia. Heliyon 2024;10(16):e36173.

Molelekwa GF, Mukhola MS, Van Der Bruggen B, Luis P. Preliminary studies on membrane filtration for the production of potable water: A case of Tshaanda rural village in South Africa. PLoS ONE 2014;9(8):1-10.

Rahmawati N, Marfai MA. Salinity pattern in Semarang Coastal City: An overview. Indonesian Journal on Geoscience 2013;8(2):107-18.

Rao G, Wells E, Reynolds C, Yoo R, Kowalsky E, DeFrance J, et al. Systematic review of the microbiological performance of household water treatment technologies. Environmental Science and Technology 2025;59(41):Article No. 2809.

Reed MH, Strope EK, Cremona F, Myers JA, Newell SE, Mccarthy MJ. Effects of filtration timing and pore size on measured nutrient concentrations in environmental water samples Effects of fi ltration timing and pore size on measured nutrient concentrations in environmental water samples. Limnology and Oceanography: Methods 2022;21(1):1-12.

Ruas G, López-Serna R, Scarcelli PG, Serejo ML, Boncz MÁ, Muñoz R. Influence of the hydraulic retention time on the removal of emerging contaminants in an anoxic-aerobic algal-bacterial photobioreactor coupled with anaerobic digestion. Science of the Total Environment 2022;827:Article No. 154262.

Rusydi AF, Onodera SI, Saito M, Ioka S, Maria R, Ridwansyah I, et al. Vulnerability of groundwater to iron and manganese contamination in the coastal alluvial plain of a developing Indonesian city. SN Applied Sciences 2021;3(4):1-12.

Şener Ş, Şener E, Davraz A. Evaluation of water quality using water quality index (WQI) method and GIS in Aksu River (SW-Turkey). Science of the Total Environment 2017;(584-585):131-44.

Solangi GS, Siyal AA, Babar MM, Siyal P. Groundwater quality evaluation using the water quality index (WQI), the synthetic pollution index (SPI), and geospatial tools: A case study of Sujawal District, Pakistan. Human and Ecological Risk Assessment: An International Journal 2020;26(6):1529-49.

United States Agency for International Development (USAID). IUWASH Tangguh Baseline Report. Jakarta, Indonesia: USAID Indonesia; 2023.

World Health Organization. Guidelines for Drinking-Water Quality: Fourth Edition Incorporating the First and Second Addenda. Geneva, Switzerland: World Health Organization; 2022.

Wu J, Cao M, Tong D, Finkelstein Z, Hoek EMV. A critical review of point-of-use drinking water treatment in the United States. npj Clean Water 2021;4(1):Article No. 40.

Yilikal A, Zeleke G, Gebremariam E. Assessment of surface water quality in Legedadie and Dire catchments, Central Ethiopia, using multivariate statistical analysis. Acta Ecologica Sinica 2018;38(2):81-95.

Zhang Z, Zhang W, Hu X, Li K, Luo P, Li X, et al. Evaluating the efficacy of point-of-use water treatment systems using the water quality index in Rural Southwest China. Water 2020;12(3):Article No. 867.

Zikrina MN, Kazama S, Sawangjang B, Takizawa S. Filling discrepancies between consumer perception and actual piped water quality to promote the potable use of the municipal water supply in Indonesia. Sustainability 2024;16(16):Article No. 7082.

Environment and Natural Resources Journal

Volume 24
Issue 1
2026

Forecasting Dengue Fever Incidence in Thailand Using ARIMA: Implications for Public Health Planning

Punpaphatporn Bunprom[1], Issara Siramaneerat[2*], and Pimnapat Bhumkittipich[2]

[1]Environmental Social Sciences and Sustainable Development, Department of Social Science, Faculty of Liberal Arts, Rajamangala University of Technology Thanyaburi (RMUTT), Pathum Thani 12110, Thailand
[2]Department of Social Sciences, Faculty of Liberal Arts, Rajamangala University of Technology Thanyaburi (RMUTT), Pathum Thani 12110, Thailand

ARTICLE INFO

Received: 19 Mar 2025
Received in revised: 5 Sep 2025
Accepted: 8 Sep 2025
Published online: 30 Oct 2025
DOI: 10.32526/ennrj/24/20250069

Keywords:
Dengue fever/ ARIMA
Forecasting/ Time series analysis/
Public health/ Climatic factors

*** Corresponding author:**
E-mail: issara_s@rmutt.ac.th

ABSTRACT

Dengue fever remains a significant public health concern in Thailand, characterized by recurrent outbreaks and considerable morbidity. Understanding and forecasting temporal patterns of dengue incidence are essential for effective prevention and control strategies. This study analyzed monthly dengue fever incidence in Thailand from 2013 to 2024 and forecasted trends for 2025-2026 using the Autoregressive Integrated Moving Average (ARIMA) model. Data were obtained from the Bureau of Epidemiology, Department of Disease Control, and Ministry of Public Health. The optimal ARIMA (1,0,1) model was selected based on diagnostic criteria including the Autocorrelation Function (ACF), Partial Autocorrelation Function (PACF), and the Ljung-Box test. Model performance was evaluated using the Mean Absolute Percentage Error (MAPE), yielding 43.40%, and indicating moderately accurate predictions for planning purposes. The model successfully captured seasonal trends, with dengue incidence typically peaking mid-year. Forecasts for 2025-2026 indicate periodic fluctuations, with December 2026 projected to have the highest incidence (7,336 cases) and January 2025 the lowest (2,401 cases). While the ARIMA model demonstrated utility in forecasting general trends, its limitations include the inability to incorporate external variables such as climate, vector control programs, vector control efforts, or viral serotype shifts. Despite this, the findings provide actionable insights for public health planning and resource allocation aimed at mitigating future dengue outbreaks in Thailand.

HIGHLIGHTS

ARIMA (1, 0, 1) was applied to forecast dengue incidence in Thailand. Twelve years of climate and case data enhanced the model accuracy. Seasonal peaks were detected, with December 2026 as the highest. Forecasts support timely dengue prevention and public health planning.

1. INTRODUCTION

Climate change has emerged as a critical global challenge, influencing all aspects of human life, including public health (Semenza et al., 2022; Wu and Huang, 2022) One of the most significant health consequences is the rise in vector-borne diseases, which have caused recurrent outbreaks across multiple regions (Delrieu et al., 2023). Among these, dengue virus (DENV) remains the most prevalent vector-borne viral infection worldwide, with the majority of cases concentrated in South America, Southeast Asia, and the Western Pacific (Guo et al., 2017). According to the World Health Organization (WHO, 2024), more than 12.7 million dengue cases were reported globally between January and September 2024 almost double the 6.5 million cases recorded in 2023. During this same period, dengue-related deaths totaled 8,791. Dengue is transmitted primarily by mosquitoes of the Aedes genus, notably *Aedes aegypti* and *Aedes albopictus*, which thrive in tropical and subtropical climates (Russo et al., 2020). These vectors are capable of spreading the virus even in the absence of clearly defined outbreak patterns, complicating control and prevention efforts.

Citation: Bunprom P, Siramaneerat I, Bhumkittipich P. Forecasting dengue fever incidence in Thailand using ARIMA: Implications for public health planning. Environ. Nat. Resour. J. 2026;24(1):88-97. (https://doi.org/10.32526/ennrj/24/20250069)

Thailand is among the countries most affected by dengue fever in Southeast Asia. Retrospective data from 2019 to 2024 indicate fluctuating but persistent disease transmission, with the most severe outbreak occurring in 2023, during which 158,620 cases and 181 deaths were reported (Thai PBS, 2023). Although the incidence declined to 105,250 cases and 90 deaths in 2024, the first quarter of 2025 still recorded 3,550 cases, a 4.8-fold decrease from the same period in 2024. Nevertheless, fatalities continue at an average rate of one death per week, indicating that dengue remains a persistent public health threat, particularly for children, the elderly, and individuals with obesity. Currently, no specific antiviral treatment or universally available vaccine exists for dengue infection. Patient management relies on immune system response and supportive care (WHO, 2025). This issue places a significant burden on the national healthcare system, particularly during epidemic periods (Wongkoon et al., 2012). Time series analysis is a critical methodological approach in public health and infectious disease surveillance, offering valuable insights into disease trends and outbreak dynamics (Sutriyawan et al., 2024). The Autoregressive Integrated Moving Average (ARIMA) model (Bayu et al., 2024) is a widely utilized time series forecasting technique for seasonal patterns and has been proven effective in modeling and predicting dengue fever incidence by identifying temporal patterns and forecasting future trends. With its high flexibility, the ARIMA model can be applied in various ways to prevent and control dengue fever, such as identifying temporal patterns to determine mosquito control measures during high-risk periods and aiding in the development of an early warning system for dengue outbreaks, thereby enhancing the efficiency and accuracy of vector control plans. Furthermore, time series analysis provides insights into dengue transmission patterns and the impact of environmental factors on disease incidence (Aung et al., 2024). The application of the ARIMA model has demonstrated success in various countries (Sutriyawan et al., 2024; Riley et al., 2020), underscoring its effectiveness in strengthening outbreak preparedness and public health interventions. Thus, this research aims to apply the Autoregressive Integrated Moving Average (ARIMA) time series model to forecast the incidence of dengue fever in Thailand. The ARIMA model was selected because it can effectively handle non-stationary time series data while providing transparent and interpretable results. Its practical applicability makes it well suited for public health decision-making, and previous studies in tropical settings have demonstrated its effectiveness in forecasting infectious disease incidence where seasonal patterns are dominant (Aung et al., 2024; Sutriyawan et al., 2024). The study focuses on identifying temporal patterns and predicting future trends, which will aid in the development of an early warning system and enhance mosquito control planning during high-risk periods. Furthermore, the findings will contribute to a deeper understanding of the transmission dynamics of dengue fever and the factors influencing disease outbreaks. The results of this study are expected to provide valuable insights for more effective prevention and control strategies for dengue fever in the future.

2. METHODOLOGY

2.1 Study design

This retrospective observational study was conducted using historical data from 2013 to 2024. The dataset included monthly time-series data on rainfall, relative humidity, minimum and maximum temperatures, and the number of rainy days, obtained from the Thai Meteorological Department. Corresponding dengue fever case data for the same period were sourced from the Bureau of Epidemiology, Department of Disease Control, Ministry of Public Health.

2.2 Study area

Thailand covers an area of 513,120 square kilometers and is located between latitudes 5°37′N and 20°27′N and longitudes 97°22′E and 105°37′E (Government of Thailand, 2025). It is situated in the center of Southeast Asia, bordered by the Andaman Sea and the Gulf of Thailand (Figure 1) (Freepik, 2024). To the east, Thailand shares borders with Laos and Cambodia; to the north and west, it is bordered by Myanmar; and to the south, it borders Malaysia. The country is divided into six regions: Northern, Northeastern, Central, Eastern, Western, and Southern

Thailand, comprising 77 provinces with a total population of approximately 69 million people (Thai Meteorological Department, 2025). Thailand has a tropical climate, characterized by high temperatures and humidity. In general, the northern and northeastern regions experience lower temperatures than Bangkok in winter and higher temperatures in summer. The hottest months of the year are April and May. The rainy season extends from June to late October, while the period from November to late February is cooler and less

humid. Thailand's climate is significantly influenced by monsoons, including the southwest monsoon, which brings moisture from the Indian Ocean during the rainy season, and the northeast monsoon, which carries cold, dry air from China during the winter season, as reported by the Digital Government Development Agency (DGA, 2025).

Figure 1. Map of Thailand

2.3 Statistical analysis

Data analysis was conducted using Gretl version 2023d, an open-source econometric software. The temporal pattern of dengue incidence in Thailand was analyzed using the Autoregressive Integrated Moving Average (ARIMA) model, following the Box-Jenkins methodology (Abhinandithe and Vaishnavi, 2019). Monthly dengue incidence data from 2013 to 2024 were used to build the time series model.

To verify stationarity, both the Augmented Dickey-Fuller (ADF) and KPSS tests were applied to the original series. The ADF test failed to reject the null hypothesis of non-stationarity, while the KPSS test indicated non-stationarity as well. Consequently, first-order differencing (d=1) was applied, after which the series achieved stationarity. Candidate autoregressive (p) and moving average (q) terms were then identified by examining the autocorrelation function (ACF) and partial autocorrelation function (PACF) plots, supplemented by Gretl's automatic model selection procedure with a periodicity of 12.

Several ARIMA specifications were estimated and compared using the Akaike Information Criterion (AIC), where lower values indicate a superior fit. Among the candidate models tested, including ARIMA (1,0,0), ARIMA (1,0,1), and ARIMA (13,0,0) the ARIMA (1,0,1) model achieved the lowest AIC value, representing the best balance between explanatory power and parsimony. Table 1 shows the comparison of ARIMA model specifications, including log-likelihood and AIC values. Among the candidate models, ARIMA (1,0,1) achieved the lowest AIC, confirming its suitability as the best-fitting model.

Table 1. Comparison of candidate ARIMA models for dengue incidence forecasting in Thailand (2013-2024)

Candidate model	p	d	q	Log-lik(L)	AIC
ARIMA (1,0,1) (selected)	1	0	1	-1,355.031	2,718.062
ARIMA (1,0,0)	1	0	0	-1,375.651	2,719.727
ARIMA (13,0,0)	13	0	0	-1,375.651	2,757.301

Residual diagnostics confirmed the adequacy of the selected model. The residual ACF and PACF remained within the 95% confidence bounds, the Ljung-Box test showed no evidence of serial correlation, and the stationary R2R^2R2 value indicated a strong fit. Residuals were normally distributed, independent, and homoscedastic, thereby meeting the assumptions of the ARIMA framework.

Finally, the ARIMA (1,0,1) model was used to generate 24-month forecasts of dengue incidence for 2025-2026. Forecast accuracy was evaluated using the Mean Absolute Percentage Error (MAPE), and 95% prediction intervals were constructed to reflect forecast uncertainty.

2.4 Ethical consideration

Ethical approval for the study protocol was obtained from the Ethics Committee of Sirindhorn College of Public Health, Yala having the approval number SCPHYLIRB-2567/452 period. All the information obtained was anonymized, and data privacy and confidentiality were ensured (IRB/16 Dec/2024).

3. RESULTS

Figure 2 presents a map of Thailand along with a spatial representation of the dengue incidence rate from 2013 to 2024. This map illustrates the spread of dengue fever across all 77 provinces, revealing a cyclical pattern of outbreaks. Based on monthly dengue case data in Thailand from 2013 to 2024 (a total of 144 months), the findings indicate that dengue outbreaks exhibit a recurring cycle, with cases typically peaking in the mid-year period (May-September) and declining towards the end of the year (November-February). This pattern aligns with the rainy season and temperature fluctuations that influence the breeding of Aedes mosquitoes. The highest number of monthly cases recorded was 31,132, particularly during severe outbreak years such as 2015, 2019, and 2022. In contrast, the lowest number of cases observed was 391, which occurred during the winter months. This decrease may have been influenced by disease control measures, particularly during 2020-2021, when COVID-19 lockdown policies were implemented (Liyanage et al., 2021). Additionally, the data reflect an epidemic cycle occurring every 3-4 years, a distinctive characteristic of dengue outbreaks in Thailand. This study utilizes a dataset comprising monthly dengue case records in Thailand from January 2013 to December 2024, revealing that the data exhibit a random or non-seasonal pattern. The time series of dengue cases observed demonstrates a stationary pattern, as depicted in Figure 3(a).

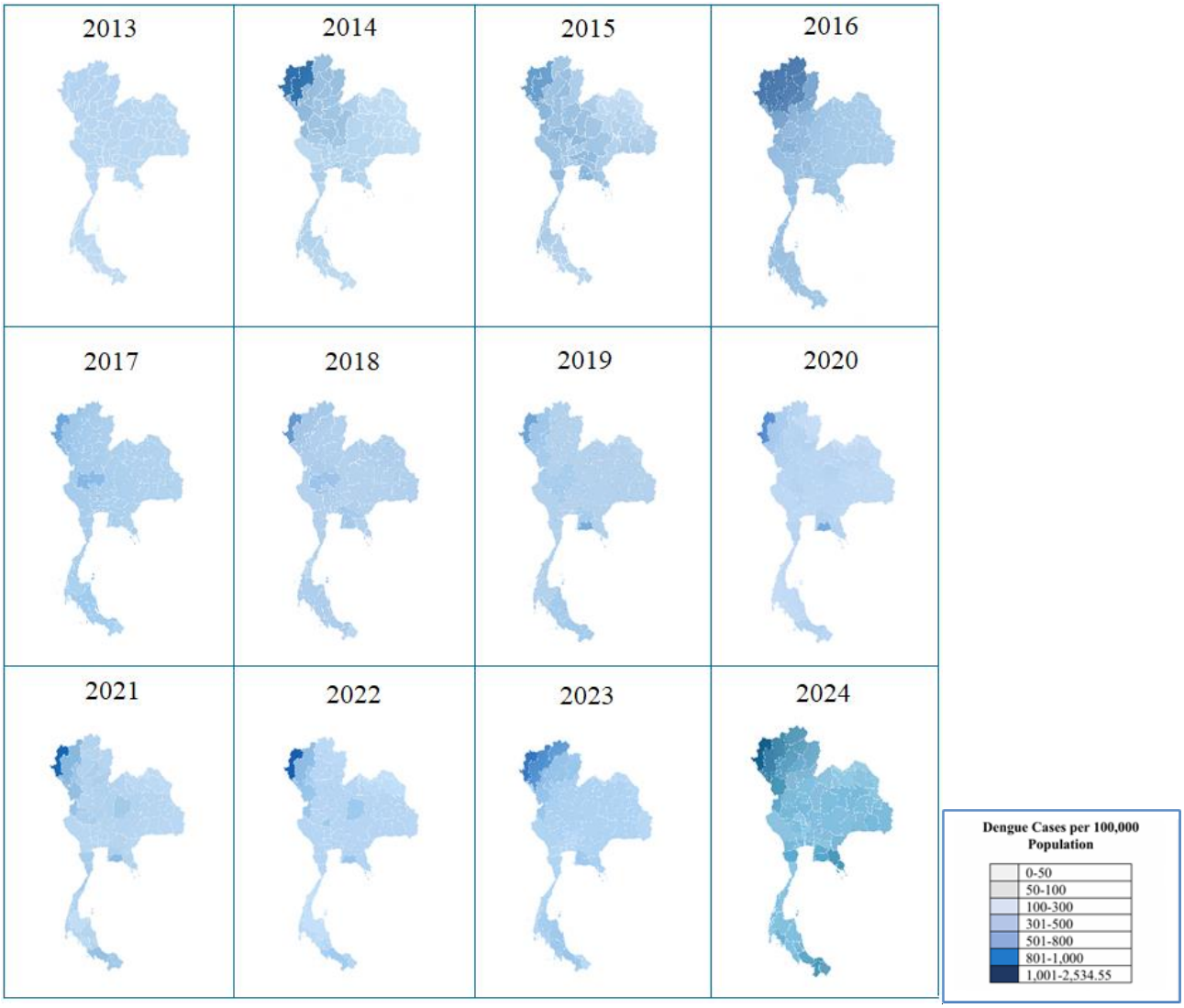

Figure 2. Dengue incidence in Thailand in 2013-2024

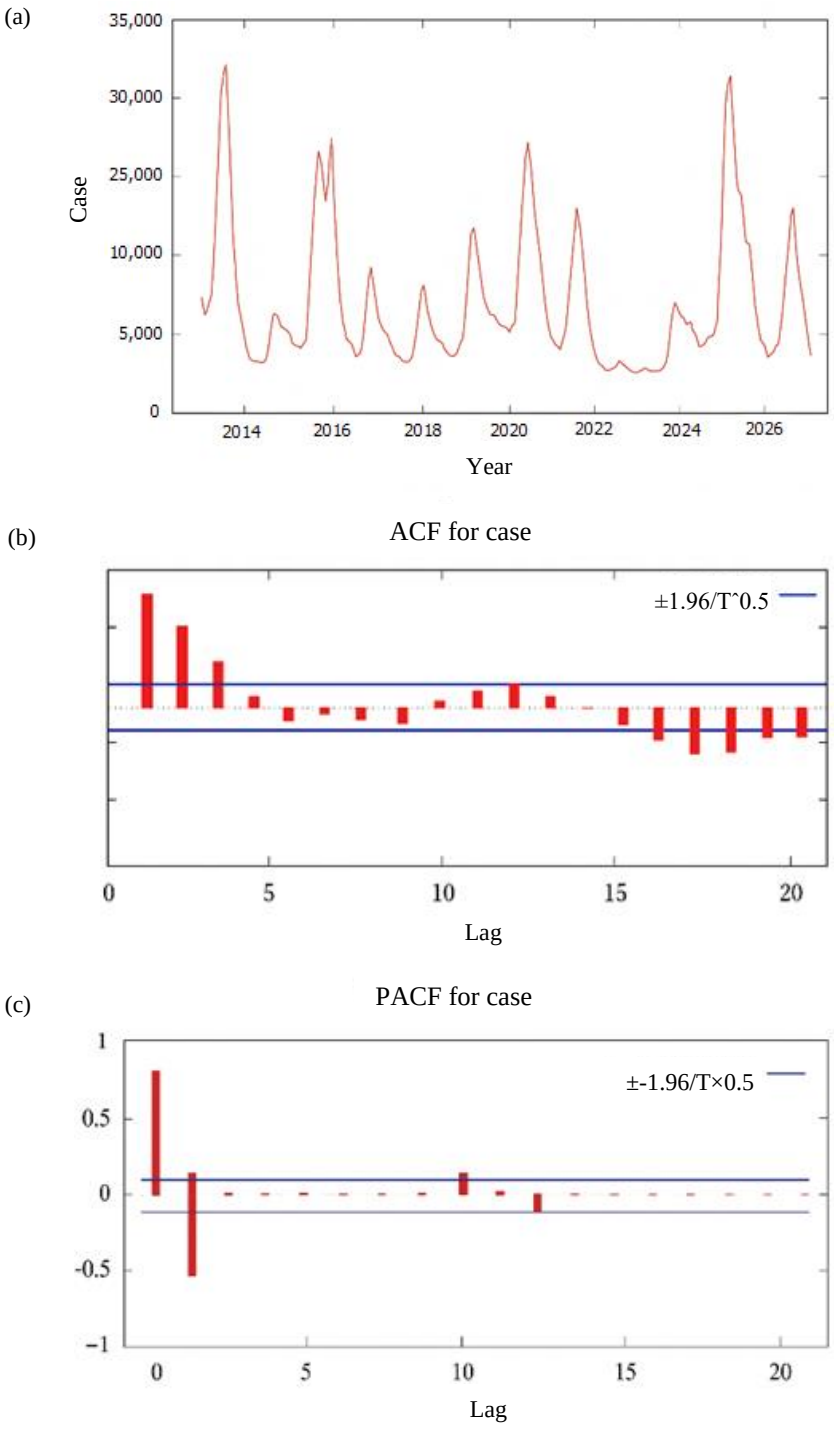

Figure 3. Dengue incidence from January 2013 to December 2024 in Thailand (a), autocorrelation function (b), partial autocorrelation function (c).

The automatic model selection in Gretl identified periodicity of 12 for the selected data. The ARIMA (1,0,1) model was identified as the best fitting model for the given data, providing predictive values for a 12-month forecast from January 2013 to December 2024. The difference between the observed value and the predictive value for each month was referred to as the residual of the model. The Autocorrelation factor (ACF) and The Partial autocorrelation factor (PACF) were tested for residuals to observe the pattern of residuals. Residuals should not show any significant pattern, only then will the selected model be considered as best fitting model.

As shown in Figure 3, the auto correlation and the Partial auto correlation of predicted cases at different lag times are depicted. Two lines in the graph indicate the 95% confidence limits of the residual ACF and residual PACF. At any lag time, the residual ACF

and residual PACF did not exceed the 95% confidence limits indicating that there were no significant autocorrelation patterns between the residuals across different lag times. This suggests that the residuals exhibited no significant pattern and were discrete, independent and identically distributed following a white noise pattern. Table 1 presents the model fit statistics and Ljung-Box test for residuals of the selected predictive model (seasonal ARIMA (1,0,1)). The model yielded a stationary R-squared value of 0.8576. The Ljung-Box test statistic was 11.271, with a p-value of 0.792, indicating that the residuals were not significantly autocorrelated and confirming the adequacy of the selected model.

Moreover, the findings of this study reveal a seasonal trend that is generally consistent with historical dengue incidence, although the projected peak month differs, indicating that the model is sufficiently suitable for forecasting dengue incidence rates for 2025-2026. The ARIMA (1,0,1) model was applied to predict the incidence rate of dengue fever from January 2025 to December 2026, yielding a Mean Absolute Percentage Error (MAPE) of 43.40%. The forecasted incidence rates for dengue fever in 2025-2026 are presented in Figure 4, which illustrates that the trend of dengue cases in Thailand from January to December 2025-2026 shows periodic increases, along with fluctuations in case numbers and a 95% confidence interval (95% CI) surrounding the projections.

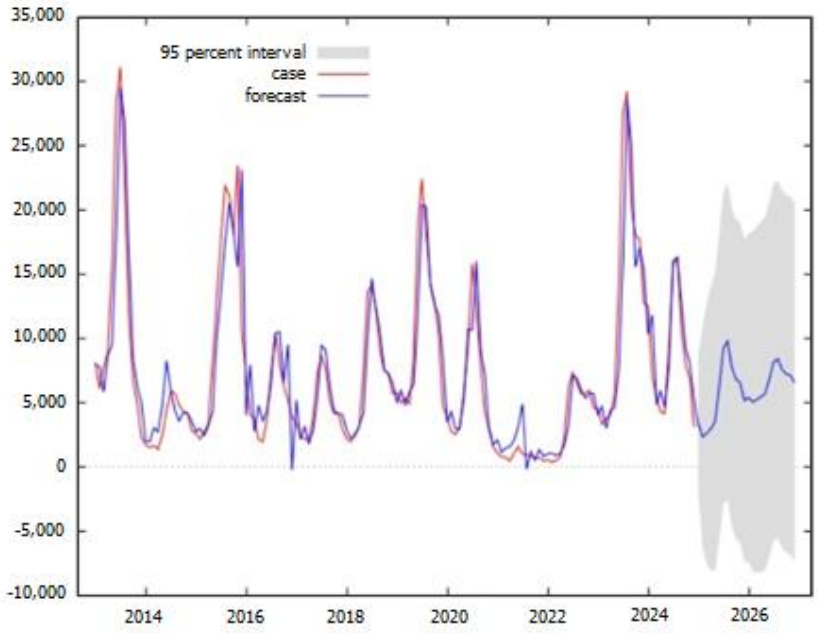

Figure 4. Observed and predicted dengue incidence from ARIMA model (1, 0, 1) in 2025-2026 in Thailand

Furthermore, the forecasted incidence of dengue fever in Thailand during 2025-2026, as presented in Table 2 and Figure 4, indicates clear seasonal patterns. The model projects that December 2026 will record the highest number of cases (7,336 cases), while January 2025 is expected to have the lowest incidence (2,401 cases). These findings were generated using the ARIMA (1,0,1) model, which successfully captured temporal fluctuations in dengue transmission. Notably, the predicted monthly values show a consistent upward trend throughout the forecast period, with case numbers rising steadily across consecutive months. This suggests an intensification in disease transmission, warranting enhanced vector-control and preparedness efforts.

4. DISCUSSION

Over the past decade, dengue fever has continued to pose a complex public health challenge in Thailand, with seasonal outbreaks and varying intensities across regions. By employing the ARIMA (1,0,1) model to forecast dengue incidence from 2025 to 2026, this study offers a valuable analytical lens into future trends based on historical disease patterns. The model, built upon 12 years of surveillance data, captured cyclical fluctuations consistent with monsoon-driven mosquito breeding and

revealed a projected case peak in December 2026, suggesting a possible extension of transmission beyond the traditional rainy season. These findings align with prior work in similar tropical settings, such as Indonesia and Vietnam, where ARIMA models have informed early detection systems and resource allocation strategies (Olowe et al., 2023; Zaw et al., 2023).

Table 2. Monthly predicted dengue fever cases in Thailand during 2025-2026 based on the ARIMA (1, 0, 1) model

Month (2025)	Cases	Month (2025)	Cases
January	2,401	January	7,152
February	3,570	February	7,198
March	4,462	March	7,233
April	5,144	April	7,260
May	5,665	May	7,280
June	6,062	June	7,296
July	6,366	July	7,308
August	6,598	August	7,317
September	6,775	September	7,324
October	6,910	October	7,329
November	7,013	November	7,333
December	7,092	December	7,336

One of the study's notable contributions lies in its integration of long-term national data, which enhances forecasting reliability and policy relevance. In practical terms, identifying periods of heightened risk supports the development of more timely, targeted vector-control operations. The potential shift in seasonal peaks underscores the need to reevaluate current prevention strategies, which have historically concentrated on mid-year interventions. Strengthening surveillance efforts in the months leading to the projected December spike could mitigate the burden of outbreaks, particularly in densely populated or resource-constrained settings. These insights are not merely statistical; they provide actionable guidance for operational planning, health worker mobilization, and community engagement.

Despite these contributions, the ARIMA model's simplicity, while a strength in terms of transparency and accessibility, also introduces notable limitations. The exclusion of exogenous variables such as precipitation, temperature, or other socio-environmental conditions restricts the model's ability to fully capture the multifactorial nature of dengue transmission. By applying ARIMA (1, 0, 1), however, the model captures cyclical trends that may reflect monsoon-driven mosquito dynamics, thereby offering partial insights into seasonal patterns despite its restricted scope. Moreover, unaccounted factors such as vector-control effort, virus serotype shifts, and changes in human mobility patterns may influence outbreak dynamics in ways not reflected in historical case data. While the model's mean absolute percentage error (MAPE) was moderate, the absence of external inputs may hinder its responsiveness to atypical outbreak scenarios. To address these limitations, future research should explore ARIMAX or SARIMAX models that integrate climatic variables, as well as nonlinear approaches such as long short-term memory (LSTM) networks and ensemble machine learning models for greater precision (Ouattara et al., 2022; Wibawa et al., 2024).

This study's findings are also situated within the broader context of climate-sensitive disease surveillance. As climate patterns become more erratic, disease forecasting must evolve beyond historical extrapolation. The increasing unpredictability of dengue trends reinforces the need for adaptive, multi-sectoral strategies. Framing these results within the social-ecological systems (SES) framework helps underscore the interdependence between human behavior, ecological changes, and vector dynamics (Watts et al., 2020). Furthermore, this research contributes to global health agendas by aligning with Sustainable Development Goal (SDG) 3 on ensuring healthy lives, and SDG 13 on climate action. By advocating for climate-informed vector control and data-driven early warning systems, the study offers both scientific and strategic value.

In summary, while the ARIMA (1,0,1) model has clear limitations in isolating the drivers of dengue outbreaks, it remains a practical tool for trend estimation and risk anticipation. Its utility lies not only in what it predicts but in how those predictions can shape preparedness. Building upon these results with more integrative models will allow public health authorities to respond more effectively to a changing epidemiological landscape. In the long term, embedding predictive analytics into routine disease surveillance can serve as a cornerstone of Thailand's broader climate resilience and public health readiness. This aligns directly with the study's objectives, as outlined in the introduction, which emphasize identifying temporal patterns and predicting future trends. By achieving these aims, the research provides a foundation for developing an early warning system and strengthening mosquito control planning during high-risk periods.

4.1 Interpretation of key findings

This study reveals a recurring pattern in dengue fever outbreaks in Thailand, with the highest incidence observed during the rainy season (May-September), driven by climatic conditions such as rainfall and temperature fluctuations that favor mosquito breeding. The cyclical nature of the outbreaks, with peaks every 3-4 years, highlights the influence of environmental factors on dengue transmission. Notably, the ARIMA model identified significant seasonal fluctuations, providing a strong foundation for forecasting future outbreaks. Furthermore, the ability of the ARIMA model to capture recurrent seasonal peaks demonstrates its utility as a practical forecasting tool for dengue fever in Thailand. Unlike simple trend analysis, ARIMA accounts for both short-term autocorrelations and long-term seasonal cycles, providing reliable short-term forecasts that are critical for planning vector control operations. This adaptability to historical surveillance data, combined with its relatively low data requirements, makes ARIMA particularly advantageous in resource-limited settings where more sophisticated models may not be feasible. For example, Mustaffa and Zahari (2024) found that seasonal ARIMA models performed competitively against more complex models in forecasting dengue incidence in Malaysia, reinforcing ARIMA's practical utility in tropical public health contexts. However, while the model performed well in capturing the trends, the study's relatively low explanatory power suggests that factors beyond climate, such as socio-economic conditions, vector control measures, and urbanization, also play significant roles in the transmission dynamics.

4.2 Public health implications

The study's findings have important implications for public health strategies in Thailand. First, the predictable seasonal pattern of dengue outbreaks provides an opportunity for targeted interventions during peak transmission periods. This includes intensified vector-control efforts, such as mosquito spraying and habitat elimination, particularly during the rainy season. Additionally, early warning systems that integrate real-time weather data can help health authorities take proactive measures before an outbreak reaches its peak, potentially reducing the burden on healthcare systems. Furthermore, the study's emphasis on the cyclical nature of outbreaks calls for sustained and long-term planning rather than reactive, short-term responses. Strengthening surveillance systems, especially in rural and peri-urban areas, will also be crucial in detecting and responding to early signs of dengue resurgence.

4.3 Novel contributions of the study

This study makes several novel contributions to the field of dengue epidemiology. First, it offers a detailed, long-term analysis (2013-2024) of dengue incidence in Thailand, using a comprehensive dataset that includes both climatic and disease data. The study's integration of the ARIMA model for forecasting dengue outbreaks based on climatic variables provides a robust statistical approach to understanding dengue dynamics. The research also identifies the specific climatic factors (temperature and rainfall) most strongly associated with dengue transmission in Thailand, which can inform localized prevention strategies. Additionally, the study's focus on seasonal fluctuations in disease incidence contributes to understanding how climate variability influences the frequency and severity of outbreaks across regions.

Rather than reiterating the results, the discussion has been restructured to emphasize the insights drawn from the findings. While the ARIMA model's effectiveness is acknowledged, the key takeaway is the broader public health implications, particularly the importance of integrating climate-sensitive approaches into dengue control programs. More directly, these findings highlight how evidence-based forecasting can guide targeted interventions and shape policy decisions to improve dengue preparedness and prevention. The novel contribution lies in linking climatic variability with seasonal outbreaks, which can now be used to inform early warning systems and strengthen disease surveillance. The limitations section highlights areas for further research, including the need to account for additional variables such as socio-economic and environmental factors, which will enhance the predictive capacity of future models.

5. CONCLUSION

This study presents an ARIMA model for forecasting the incidence of dengue fever in Thailand, utilizing monthly confirmed dengue case data from 2013 to 2024. The analysis indicates that the ARIMA (1,0,1) model was identified as the best-fit model, as it accurately described the data and demonstrated the ability to forecast dengue incidence. The evaluation of the forecast revealed a Mean Absolute Percentage

Error (MAPE) of 43.40%, indicating that the model provided reasonably accurate predictions. The forecast for 2025-2026 shows that December 2026 is expected to have the highest number of dengue cases, reaching 7,336, while January 2025 is predicted to have the lowest at 2,401 cases. These findings provide valuable insights for future dengue control and prevention efforts.

While the findings of this study provide valuable insights into the seasonal trends of dengue fever in Thailand, further research is needed to address the limitations outlined above. Public health authorities can benefit from this study by using the model's forecast to prepare for expected outbreaks, particularly in the high-risk months. However, incorporating additional variables and exploring more advanced forecasting techniques will allow for more accurate predictions, ultimately improving response strategies. Future research should focus on the integration of diverse data sources, including socio-economic and environmental factors, and adopting machine learning methods to enhance the precision and adaptability of dengue forecasting models.

6. LIMITATIONS

This study has several limitations that must be considered when interpreting the findings. First, the exclusion of exogenous variables, such as climatic and environmental factors beyond temperature, humidity, and rainfall, may have impacted the model's predictive power. Factors like urbanization, land use changes, and public health interventions (e.g., vector control measures) are known to influence dengue transmission dynamics and should be incorporated into future studies for a more comprehensive understanding. Additionally, underreporting or misclassification of dengue cases, particularly in rural or resource-limited settings, could lead to inaccuracies in the data, potentially skewing the results. This issue is particularly relevant in regions with limited access to healthcare or surveillance infrastructure, where dengue cases may not be accurately recorded.

Furthermore, the reliance solely on the ARIMA model presents another limitation. While effective in modeling linear trends, the ARIMA model may not fully capture the complex, non-linear dynamics of dengue outbreaks, particularly during periods of sudden surges or atypical conditions. As a result, the model's ability to predict extreme outbreak conditions is constrained. Future studies should consider integrating climatic data into more robust multivariate models, such as ARIMAX or SARIMAX, which can incorporate additional exogenous variables for more accurate forecasting. Additionally, alternative or complementary forecasting methods, such as machine learning techniques (e.g., random forests, gradient boosting, and Long Short-Term Memory (LSTM) neural networks), could offer improved modeling of non-linear relationships and better handle complex patterns. Hybrid models that combine statistical methods with machine learning techniques may also enhance forecast accuracy and reliability, particularly during atypical outbreak conditions.

ACKNOWLEDGEMENTS

The authors would like to express their sincere gratitude to the faculty members of the Environmental Social Sciences and Sustainable Development Program, Faculty of Liberal Arts, Rajamangala University of Technology Thanyaburi (RMUTT), for their invaluable guidance, encouragement, and academic support throughout this research.

AUTHOR CONTRIBUTIONS

Punpaphat Bunprom conceptualized and drafted the manuscript, as well as interpreted the analyses; Issara Siramaneerat provided guidance on the data analysis, reviewed and approved it; Pimnapat Bhumkittipich assisted in studying the qualitative results. All authors have reviewed and approved the manuscript.

DECLARATION OF CONFLICT OF INTEREST

The authors have no conflict of interest to declare.

REFERENCES

Abhinandithe S, Vaishnavi CP. Time series analysis on admission rates of dengue in medical college hospital. International Journal of Scientific Research and Reviews 2019;8(2): 2504-11.

Aung SH, Kyaw AMM, Phuanukoonnon S, Jittamala P, Soonthornworasiri N. A SARIMA time series forecasting for dengue cases for reporting to Yangon Region, Myanmar. Journal of Public Health and Development 2024;22(1):184-96.

Bayu T, Soeprobowati TR, Adissu S. Analyzing climate change status through evaluating trend of temperature and rainfall and predicting future climate change status at Lake Tana Basin. Applied Environmental Research 2024;46(1):Article No. 003.

Delrieu M, Martinet JP, Menkes C, O'Connor O, Burtet-Sarramegna V, Viennet E, et al. Temperature and transmission of chikungunya, dengue, and Zika viruses: A systematic review of experimental studies on *Aedes aegypti* and *Aedes albopictus*. Current Research in Parasitology and Vector-Borne Diseases 2023;4:Article No. 100139.

Digital Government Development Agency (DGA). Province and region dataset of Thailand [dataset]. Digital Government Open Data Catalog [Internet]. 2025 [cited 2025 Aug 7]. Available from: https://catalog-dga.data.go.th/sv/dataset/di-open1-02 (in Thai).

Freepik. Map Thailand Blue Geometric Polygon Map [Internet]. 2024 [cited 2025 Sep 1]. Available from: https://www.freepik.com/premium-vector/map-thailand-blue-geometric-polygon-map_24694186.htm.

Government of Thailand. Climate of Thailand [Internet]. 2025 [cited 2025 Aug 7]. Available from: https://thailand.go.th/useful-information-detail/009_141?hl=th (in Thai).

Guo C, Zhou Z, Wen Z, Liu Y, Zeng C, Xiao D, et al. Global epidemiology of dengue outbreaks in 1990-2015: A systematic review and meta-analysis. Frontiers in Cellular and Infection Microbiology 2017;7:Article No. 317.

Liyanage P, Rocklöv J, Tissera HA. The impact of COVID-19 lockdown on dengue transmission in Sri Lanka: A natural experiment for understanding the influence of human mobility. PLOS Neglected Tropical Diseases 2021;15(6):e0009420.

Mustaffa NA, Zahari SM, Nasir N, Azil AH. Forecasting the incidence of dengue fever in Malaysia: A comparative analysis of seasonal ARIMA, dynamic harmonic regression, and neural network models. International Journal of Advanced and Applied Sciences 2024;11(1):20-31.

Olowe OS, Jacinto HS, Limbago JS, Folorunso EA, Sarfo I, Brown C. Assessing social vulnerability to climate change in a fishery-dependent village in South Central Vietnam. Environment and Natural Resources Journal 2023;21(5):390-401.

Ouattara CA, Traore TI, Traore S, Sangare I, Meda CZ, Savadogo LGB. Climate factors and dengue fever in Burkina Faso from 2017 to 2019. Journal of Public Health in Africa 2022;13(1):Article No. 2145.

Riley P, Ben-Nun M, Turtle J, Bacon D, Riley S. SARIMA forecasts of dengue incidence in Brazil, Mexico, Singapore, Sri Lanka, and Thailand: Model performance and the significance of reporting delays. medRxiv 2020. DOI: 10.1101/2020.06.26.20141093.

Russo G, Cuesta JG, Bondarenko I, Delacollette C, Nkengasong JN, Kieny MP, et al. Chikungunya fever in Africa: A systematic review. Pathogens and Global Health 2020; 114(3):136-44.

Semenza JC, Rocklöv J, Ebi KL. Climate change and cascading risks from infectious disease. Infectious Diseases and Therapy 2022;11:1371-90.

Sutriyawan A, Martini M, Sutiningsih D, Agushybana F, Wahyuningsih NE, Adamu VE, et al. Time series analysis of dengue incidence in Bandung City, Indonesia using an ARIMA model. Journal of Microbiology, Epidemiology and Immunobiology 2024;101(5):803-11.

Thai Public Broadcasting Service (Thai PBS). Dengue fever situation in 2023, Department of Disease Control. The Visual Thai PBS [Internet]. 2023 [cited 2023 Oct 7]. Available from: https://thevisual.thaipbs.or.th/green/mosquito/รายการข่าวเจาะย่อโลก (in Thai).

Thai Meteorological Department. Climate of Thailand [Internet]. 2025 [cited 2025 Mar 11]. Available from: https://www.tmd.go.th (in Thai).

Watts MJ, Kotsila P, Mortyn PG, Monteys VS, Brancati CU. Influence of socio-economic, demographic, and climate factors on the regional distribution of dengue in the United States and Mexico. International Journal of Health Geographics 2020;19:Article No. 44.

Wibawa BSS, Wang YC, Andhikaputra G, Lin YK, Chiang Hsieh LH, Tsai KH. The impact of climate variability on dengue fever risk in Central Java, Indonesia. Climate Services 2024;33:Article No. 100433.

Wongkoon S, Jaroensutasinee M, Jaroensutasinee K. Development of temporal modeling for prediction of dengue infection in Northeastern Thailand. Asian Pacific Journal of Tropical Medicine 2012;5(3):249-52.

World Health Organization (WHO). WHO launches global strategic plan to fight rising dengue and other Aedes-borne arboviral diseases [Internet]. 2024 [cited 2024 Oct 3]. Available from: https://www.who.int/news/item/03-10-2024-who-launches-global-strategic-plan-to-fight-rising-dengue-and-other-aedes-borne-arboviral-diseases.

World Health Organization (WHO). Vaccines and immunization: Dengue [Internet]. 2025 [cited 2025 Aug 7]. Available from: https://www.who.int/news-room/questions-and-answers/item/dengue-vaccines.

Wu Y, Huang C. Climate change and vector-borne diseases in China: A review of evidence and implications for risk management. Biology (Basel) 2022;11(3):Article No. 370.

Zaw W, Lin Z, Ko Ko J, Rotejanaprasert C, Pantanilla N, Ebener S, et al. Dengue in Myanmar: Spatiotemporal epidemiology, association with climate and short-term prediction. PLOS Neglected Tropical Diseases 2023;17(6):e0011331.

Environment and Natural Resources Journal

Volume 24
Issue 1
2026

Spatiotemporal Trends in Temperature and Rainfall in Northwestern Vietnam (2009-2024)

Xuan-Duc Do*

Department of Climate Change and Sustainability Science, VNU School of Interdisciplinary Sciences and Arts, Vietnam National University, Hanoi, Vietnam

ARTICLE INFO

Received: 21 Feb 2025
Received in revised: 8 Sep 2025
Accepted: 15 Sep 2025
Published online: 17 Nov 2025
DOI: 10.32526/ennrj/24/20250046

Keywords:
Temporal and spatial/ Temperature and rainfall/ Meteorology and weather/ Weather fluctuations/ Climate change/ Northwestern Vietnam

*** Corresponding author:**
E-mail: ducxd@vnu.edu.vn

ABSTRACT

The present study sought to optimize the data from eleven Regional Hydro-Meteorological Station in the Northwestern Vietnam. The study results indicated that that the average temperature has tended to increase, which is lower than the average global surface temperature. Still, the maximum temperature, and lowest temperature are higher than the global average (values 0.6, 0.3, and 3.0°C, respectively). The rainy season (23.7°C) generally exhibits warmer temperatures than the dry season (16.9°C). There is a positive correlation between temperatures in consecutive months during both the dry and rainy seasons (r values): 0.75 (September, October), 0.53 (October, December), 0.51 (May, June) 0.46 (August, October), 0.45 (November, December), and 0.38 (April, May), respectively. There is negative correlation between the temperatures of months that are in the same season but far apart, R-values -0.61 (February, December), -0.58 (February, November), -0.56 (April, September), -0.31 (April, October), respectively. The total rainfall and total minimum rainfall showed decreasing trend were 127 mm, and 2.8 mm, respectively. By contrast, total rainfall max tends to increase by 230 mm. The highest rainfall was concentrated from May to October (1,219 mm). Higher correlation values for rainfall were observed in winter (January to March, and October to December), at 0.65, 0.78, 0.85, 0.93, 0.94, and 0.99 compared to summer (April to September), with r values of 0.29, 0.36, 0.57, 0.42, and 0.45, respectively. In a year, positive correlations between temperature and rainfall predominate most months of spring (January, February, and March), autumn (July, August, and September), and winter (October, November, and December), R-values: 0.59, 0.36, 0.44, 0.53, respectively, while negative correlations are more common in April, May, and June (summer) with the r values of -0.33, -0.16, and -0.25, respectively. The present study may provide a valuable and future climate, and rainfall projections.

HIGHLIGHTS

- Monitoring data of temperature and rainfall variation were used with the method for standardizing temperature and rainfall numeric data.
- The average temperature has tended to increase, and the total rainfall showed decreasing, and there is a positive correlation between temperatures in consecutive months during both the dry and rainy seasons.
- There is negative correlation between the temperatures of months that are in the same season but far apart.
- Positive correlations between temperature and rainfall predominate most months of spring, autumn while negative correlations are more common in summer.

1. INTRODUCTION

The spatiotemporal analysis of temperature and rainfall is crucial for understanding climate patterns and their impacts on agriculture and water resources. Studies across different regions, including Karnataka, India (Chowhan et al., 2023), and Kashmir Valley Ghana (Abbam et al., 2018) have consistently found significant trends in temperature and rainfall over time, with some regions experiencing increasing temperatures and others showing changes in rainfall patterns. The impacts of these variations are particularly important for agriculture-dependent areas, potentially affecting crop yields and food security (Abbam et al., 2018; Chowhan et al., 2023). The research highlights

Citation: Do X-D. Spatiotemporal trends in temperature and rainfall in Northwestern Vietnam (2009-2024). Environ. Nat. Resour. J. 2026;24(1):98-114. (https://doi.org/10.32526/ennrj/24/20250046)

the importance of location-specific analyses, as climate patterns can vary significantly across different regions. These findings can inform water resource management strategies and help develop targeted interventions to address the consequences of extreme climate events (Chowhan et al., 2023).

The importance of analyzing spatiotemporal variations in temperature and rainfall lies in their role in agricultural planning and climate change adaptation. Research across Ethiopia, Iran, and other regions reveals significant warming trends, with annual minimum and maximum temperatures increasing by 0.11°C and 0.08°C per decade, respectively (Meseret and Belay, 2019). Rainfall patterns show high variability and irregular distribution, classified as erratic in some areas (Worku et al., 2019). These climatic changes affect agriculture, potentially affecting crop production, disease proliferation, and household resilience (Getnet et al., 2023). To address these challenges, researchers recommend developing context-specific climate change adaptation strategies and implementing climate-smart agriculture technologies, such as small-scale irrigation, improved crop varieties, and efficient fertilizer use (Getnet et al., 2023; Meseret and Belay, 2019).

Analyzed spatial and temporal variations in temperature across different regions. In Ethiopia, annual minimum and maximum temperatures increased significantly by 0.11°C and 0.08°C per decade, respectively, from 1983 to 2014 (Meseret and Belay, 2019). Similarly, the Cauvery River Delta in India showed upward trends in annual and seasonal temperatures from 1960-2018, with warming accelerating after the 1980s (Ganeshkumar et al., 2020). In China's Hengduan Mountains, temperatures increased significantly from 1960-2008, with greater warming at higher altitudes (Zongxing et al., 2012). In China's Qinling- Huaihe demarcation zone, warming trends were observed from 1961 to 2018, particularly pronounced since the 1990s, with minimum temperatures showing the most notable increase (He and Hao, 2024). Within-city temperature variations were also examined in Shenzhen, China, revealing significant spatial heterogeneity and nocturnal and seasonal variability, with temperature differences between locations reaching up to 8.7°C during extreme heat days (Cao et al., 2021). These studies highlight the importance of understanding regional and local temperature variations in the context of global warming.

The spatial and temporal variability of rainfall is crucial for agricultural planning and understanding environmental processes. Studies across different regions have shown significant variations in rainfall patterns. In Bangladesh, moderate inter-annual and high intra-annual rainfall variability was observed, with increasing trends in coastal and northern areas (Shahid, 2009). Similarly, in India's Nagaland state, annual rainfall varied from 859 mm to 2,123 mm, with higher rainfall in the northern part (Kaur et al, 2021). The Parambikulam Aliyar Palar basin in Tamil Nadu exhibited wide rainfall variations, ranging from 445.2 mm to 4,364 mm annually (Balathandayutham et al., 2014). These studies emphasize the importance of analyzing spatial and temporal rainfall variability for effective agricultural and environmental management.

Research indicates a complex relationship between temperature and rainfall, with both positive and negative correlations observed depending on location and season. Studies in Malawi and Sweden found positive correlations between daily rainfall and temperature (Dzupire et al., 2020; Cong et al., 2012). However, in Sweden, negative correlations were observed from April to July and in September (Cong et al., 2012). A study across the contiguous United States found both positive and negative correlations, with most areas showing negative correlations in summer, particularly in the central and southern Great Plains (Zhao and Mak, 1993). The eastern Corn Belt was the only major area with a significant positive correlation in winter. These findings highlight the geographical and seasonal variability in temperature-rainfall relationships.

This study analyses temporal and spatial variations in temperature and rainfall using over 10 years of observational data. Previous studies utilized long-term observational data, ranging from 10 to 50 years, (Meseret and Belay, 2019; Worku et al., 2019). In Vietnam, significant climate changes were revealed. The average temperature rise of 0.26°C per decade since the 1970s is approximately twice the global rate, and decreasing rainfall trendsin northern Vietnam (Nguyen et al., 2018).

All studies employed various statistical techniques, such as trend analysis, correlation analysis, and geostatistical methods. Findings consistently revealed significant spatial and temporal variations in both temperature and rainfall patterns. However, studies on the development of analyzing temporal and spatial variation in temperature and rainfall are lacking. Therefore, it is important to fill this gap in knowledge

regarding the combined temporal and spatial variations of temperature and rainfall.

Northwest Vietnam is highly vulnerable to climate change impacts, particularly natural disasters like droughts, floods, and landslides. In this study, our primary objective was to analyze temporal and spatial variations in temperature and rainfall. We explored three specific objectives in this study: (1) to introduce the temporal and spatial (seasonal) variation of temperature in analyzing the relationship between temperature variables; (2) to combine the analysis of temporal and spatial trend rainfall trends using data monitoring, network, and; (3) to analyze the correlation between temperature and total rainfall each month in every season and over the year in the Northwest Vietnam.

2. METHODOLOGY

2.1 Research area

This case study was conducted in Northwestern Vietnam, located in Hoa Binh, Son La, Dien Bien, and Lai Chau provinces, Northwest Vietnam. It covers 38,000 km^2, accounting for 11.4% of Vietnam's total area. The region is characterized by mountainous terrain, with over 94% of the land classified as sloping (Hoang et al., 2017). The region faces environmental challenges due to agricultural expansion on steep slopes, leading to forest degradation and soil erosion (Hoang et al., 2017). Figure 1 shows the temperature and rainfall monitoring points. These 11 (coded as S1-S11) points monitored the temperature and rainfall of the region through two parameters: temperature and rainfall. Historical mean values of these parameters for the stations were used for 15 years (2009-2024).

2.2 Data collection

Eleven monitoring stations have been fully operated by the Northwestern Vietnam Regional Hydro-Meteorological Station in the study area since 2009 (Figure 1), including S1 (Tam Duong), S2 (Than Uyen), S3 (Sin Ho), S4 (Muong Lay), S5 (Tuan Giao), S6 (Pha Din), S7 (Phieng Lanh), S8 (Dien Bien), S9 (Song Ma), S10 (Bac Yen), and S11 (Son La). Figure 1 shows that these Meteorological stations S1, S2, S3, S4, S5, S6, S7, S8, S9, S10, and S11 monitored the temperature and rainfall of Northwestern Vietnam. The monitoring frequency is continuous hourly, daily, monthly, and yearly, with temporal variation recorded in all the months from January to December. Monitoring data of temperature and rainfall variation from April to September were used for the rainy season, and data from January, February, March to October, November, and December were used for the dry season. Spatial variation at 11 stations (S1-S11) during 2009-2024 was collected.

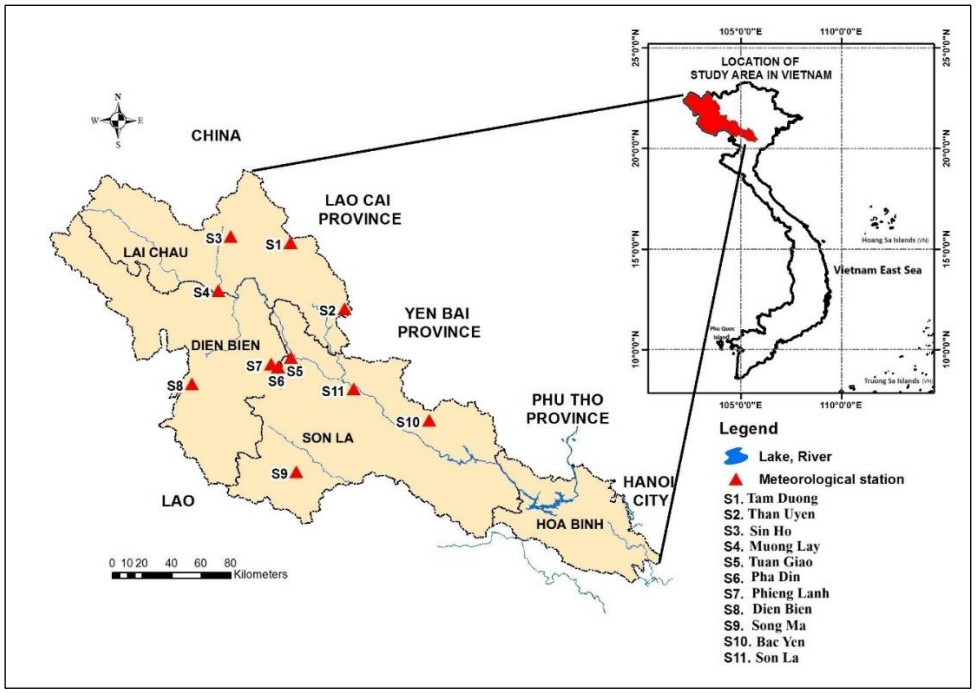

Figure 1. Location of monitoring points temperature and rainfall in Northwestern Vietnam

2.3 Methods

The equation to calculate the mean (algebraic measure) of sample temperature and rainfall is sensitive to outliers (Han and Kamber, 2012). Therefore, a trimmed mean (which removes extreme values) is recommended when analyzing data from the monitoring network over a year, treating variables equally by Equation (1).

$$\bar{x} = \frac{\sum_{i=1}^{n} w_i x_i}{\sum_{i=1}^{n} w_i} \quad (1)$$

According to (Han and Kamber, 2012), the method for standardizing temperature and rainfall numeric data is given by Equation (2).

$$\text{Z-score: } x = \frac{x-\mu}{\sigma} \quad (2)$$

Where; X: raw data, μ: is the mean of the temperature and rainfall, σ: is the standard deviation. The distance between the raw score and the temperature and rainfall mean in units of the standard deviation, <0 when the raw score is below the mean, >0 when above (Han and Kamber, 2012). Along with that an equation to variance and standard deviation (sample: s, population: σ): Standard deviation s (or σ) is the square root of variance by Equations (3), and (4).

$$s^2 = \frac{1}{n}\sum_{i=1}^{n}(x_i - \bar{x})^2 = \frac{1}{n}[\sum_{i=1}^{n} x_i{}^2 - \frac{1}{n}(\sum_{i=1}^{n} x_i)^2] \quad (3)$$

$$\sigma = \frac{1}{N}\sum_{i=1}^{n}(x_i - \mu)^2 = \frac{1}{n}\sum_{i=1}^{n} x_i{}^2 - \mu^2 \quad (4)$$

Multivariate correlation analysis method: Pearson (1909), argued that came up with an equation (5) to estimate the correlation coefficient (r), This is a statistical index that measures the correlation between two variables, in this study, between temperature (x) and rainfall (y). The correlation coefficient has values from -1 to 1. The correlation coefficient is equal to 0, or close to 0 means the two variables have no relationship with each other. If the value of the correlation coefficient is negative (r<0) That means when x increases, y decreases and vice versa, when x decreases, y increases; if the correlation coefficient value is positive (r>0) This means that when x increases, y also increases, and when x decreases, y also decreases by Equation (5).

$$r = \frac{\sum_{i=1}^{n}(x_i - \bar{x})(y_i - \bar{y})}{\sqrt{\sum_{i=1}^{n}(x_i - \bar{x})^2 \sum_{i=1}^{n}(y_i - \bar{y})^2}} \quad (5)$$

Where; (r) is the correlation coefficient Pearson, is the average value of the temperature variable (x) and rainfall (y), and xi, yi is the average value of the variables (x) and (y) at the meteorological station i, n is the number of variables by Equation (5).

2.4 Statistical analysis

Tested for statistical significance and normal distribution, the R-Studio package was used for statistical analysis of the monitoring data. Surface temperature and rainfall data were log-transformed for homogeneity and tested to fit a statistical significance and normal distribution using the Cor. test (Table 1, and Table 2). Significant differences and correlations among variations were determined using one-way analysis to analyze variance (ANOVA) checks whether there are statistically significant differences between more than two variables, and Pearson coefficients (r) with the help of correlation analysis, the linear relationship between variables can be examined, to strength of the correlation is indicated by the correlation coefficient, which ranges from -1 to +1. Significant differences in data between the temperature, rainfall, and between month dry and rainy seasons were analyzed using the Independent-Samples T-Test. Figures were drawn using Origin Pro 2018 v9.5.0 and R-Studio. With probability <0.05, the average data during 2009-2024 (Table 1, and Table 2) of temperature, and rainfall values are considered statistically significant. These values can be used to forecast change trends and quality correlations over temporal and spatial variations. Pearson correlation test in R use the Cor. test function to check the statistical significance of temperature and rainfall monitoring data.

3. RESULTS AND DISCUSSIONS

3.1 Temporal variation in temperature

Figures 2(a), 2(b), and 2(c) show the temperature variation trend in the northwestern of Vietnam in the period from 2009 to 2024, specifically:

The mean temperature (±standard deviation) for each year were as follows, specifically:

2009 (21.1±2.1), 2010 (21.4±2.0), 2011 (21.1±2.3), 2012 (20.6±2.1), 2013 (21.4±2.1), 2014 (21.7±2.3), 2015 (20.6±2.1), 2016 (21.6±2.2), 2017 (21±2.1), 2018 (21.3±2.2), 2019 (21.7±3.4), 2020 (23.0±1.9), 2021 (21.8±2.2), 2022 (20.8±1.9), 2023 (22.1±2.3), 2024 (21.7±2.3).

Table 1. Check the statistical significance of temperature monitoring data using the correlation test (Cor. test) for the period 2009-2024

Months of the year	Test statistic value	Probability value
January	t = 2.56	p-value < 0.01
February	t = 6.61	p-value < 0.01
March	t = 2.94	p-value < 0.05
April	t = 2.27	p-value < 0.05
May	t = 2.73	p-value < 0.05
June	t = 2.41	p-value < 0.05
July	t = 2.98	p-value < 0.05
August	t = 2.28	p-value < 0.05
September	t = 2.02	p-value < 0.05
October	t = 2.58	p-value < 0.05
November	t = 3.56	p-value < 0.01
December	t = 2.68	p-value < 0.01

Table 2. Check the statistical significance of rainfall monitoring data using the correlation test (Cor. test) for the period 2009-2024

Months of the year	Test statistic value	Probability value
January	t = 3.19	p-value < 0.01
February	t = 3.62	p-value < 0.01
March	t = 3.94	p-value < 0.01
April	t = 3.79	p-value < 0.01
May	t = 3.68	p-value < 0.05
June	t = 3.87	p-value < 0.05
July	t = 3.73	p-value < 0.05
August	t = 3.04	p-value < 0.05
September	t = 2.29	p-value < 0.05
October	t = 10.2	p-value < 0.01
November	t = 3.27	p-value < 0.05
December	t = 5.79	p-value < 0.01

(a)

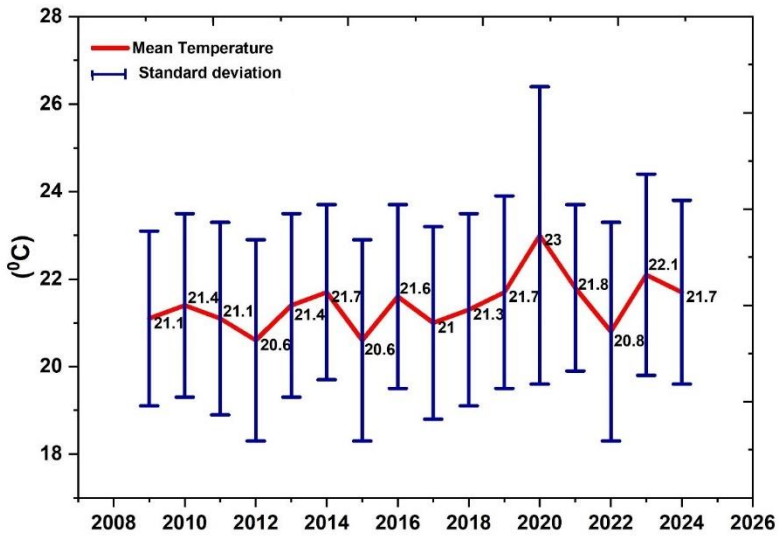

Figure 2. Changes in temperature in the Northwestern of Vietnam during 2009 to 2024

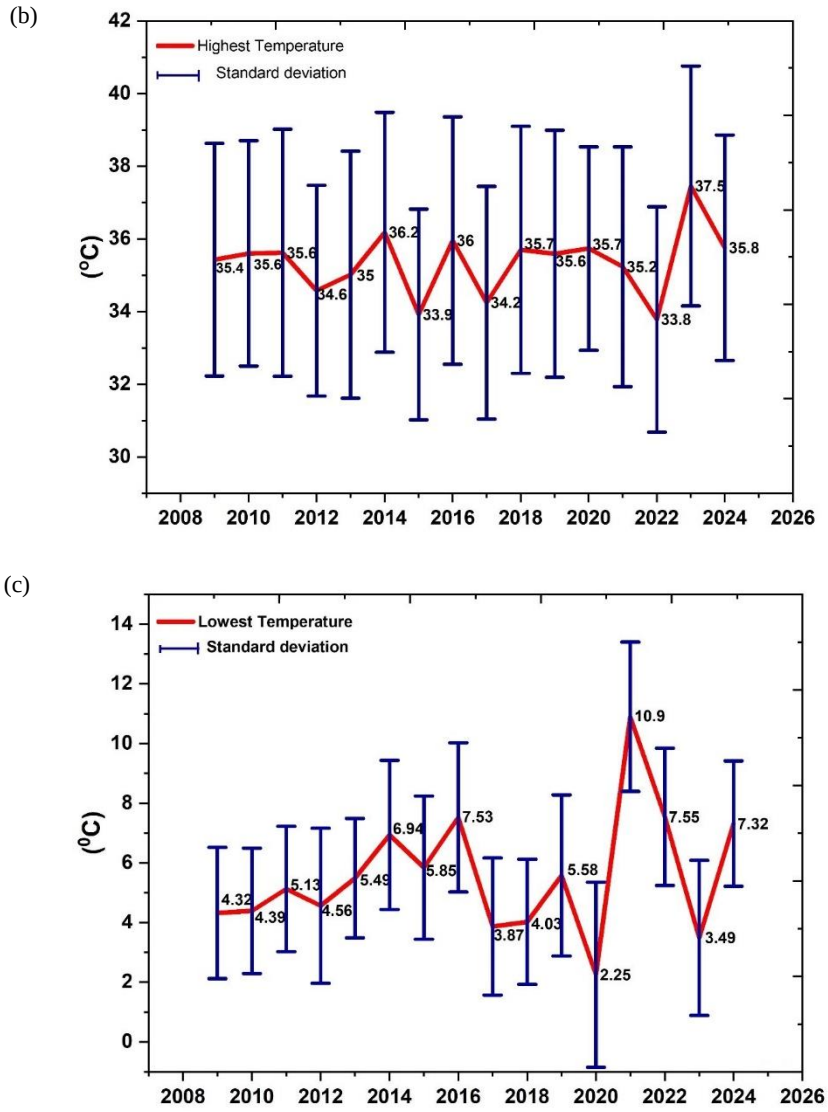

Figure 2. Changes in temperature in the Northwestern of Vietnam during 2009 to 2024 (cont.)

The highest temperatures recorded each year were, specifically: 2009 (35.4±3.2), 2010 (35.6±3.1), 2011 (35.6±3.4), 2012 (34.6±2.9), 2013 (35.0±3.4), 2014 (36.2±3.3), 2015 (33.9±2.9), 2016 (36.0±3.4), 2017 (34.2±3.2), 2018 (35.7±3.4), 2019 (35.6±3.4), 2020 (35.7±2.8), 2021 (35.2±3.3), 2022 (33.8±3.1), 2023 (37.5±3.3), 2024 (35.8±3.1).

The lowest temperatures recorded each year were, specifically: 2009 (4.32±2.2), 2010 (4.39±2.1), 2011 (5.13±2.1), 2012 (4.56±2.6), 2013 (5.49±2.0), 2014 (6.94±2.5), 2015 (5.85±2.4), 2016 (7.53±2.5), 2017 (3.87±2.3), 2018 (4.03±2.1), 2019 (5.58±2.7), 2020 (2.25±3.1), 2021 (10.9±2.5), 2022 (7.55±2.3), 2023 (3.49±2.6), 2024 (7.42±2.1).

An increasing trend in temperature values in the period 2009-2024 was found for the mean temperature ($r=0.4$, $p<0.001$). The corresponding temprature increases were 0.6°C for the mean temperature (Figure 2(a)), 0.3°C for the highest temperature (Figure 2(b)), and 3.0°C for the lowest temperature (Figure 2(c)).

3.2 Spatial variation in temperature

Figure 3 shows the monthly mean temperature values, specifically: January (11.8-16.2), February (13.1-19.0°C), March (19.4-21.7°C), April (21.4-24.0°C), May (23.1-24.9°C), June (24.6-25.0°C), July (24.2-24.8°C), August (23.9-24.7°C), September (22.9-24.3°C), October (20.2-23.1°C), November (17.6-20.2°C), December (12.6-16.8°C).

The variation in average monthly temperature between the years 2009-2024 was recorded with mean values highest from April to September each year corresponding to 22.7°C (April, $p<0.05$), 24.2°C (May, $p<0.05$), 24.7°C (June, $p<0.05$), 24.4°C (July, $p<0.05$), 24.2°C (August, $p<0.05$), and 23.8°C

(September, p<0.05) during the rainy season. The dry season lasts from January to March. From October to December each year the average monthly temperature is lower than in the rainy season, with corresponding values of 14.9°C (January, p<0.01) 15.5°C (February, p<0.01), 20.1°C (March, p<0.05), 21.6°C (October, p<0.05), 19.1°C (November, p<0.01), and 15.1°C (December, p<0.01), respectively (Figure 3, and Figure 4).

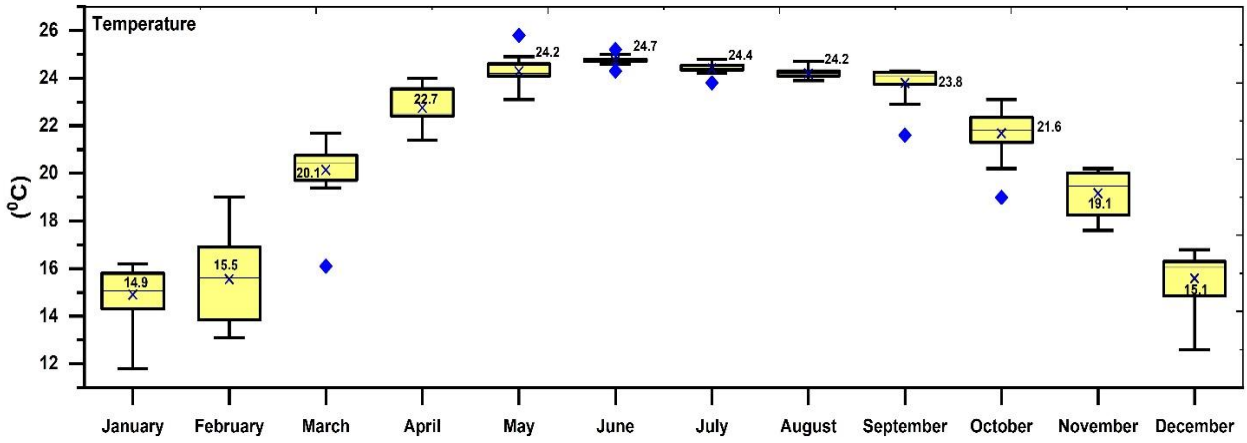

Figure 3. Change temperature in months from 2009 to 2024

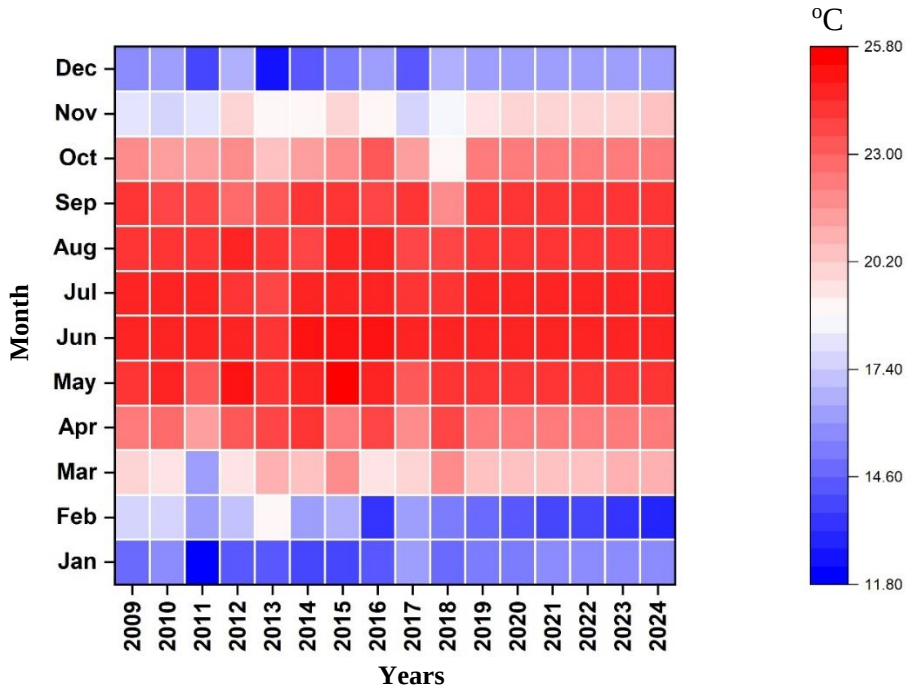

Figure 4. The monthly temperature concentration levels temperatures

Figure 5 shows the correlation (r) between the average temperatures of each month over the period from 2009 to 2024. A strong and moderate positive correlation was found between January and March, as well as between January and December (r=0.60, p<0.01; r=0.44, p<0.01). The between March and April, May, and November (r=0.45, p<0.05; r=0.49, p<0.01; r=0.45, p<0.05). The between April and May (r=0.38, p<0.05). The between May and June, August, November, and December (r=0.51, p<0.05; r=0.43, p<0.05; r=0.37, p<0.05; r=0.41, p<0.05). The between August and October (r=0.46, p<0.01), between September and October (r=0.75, p<0.01), and between October and November, as well as between October and December (r=0.53, p<0.01; r=0.41, p<0.01; r=0.45, p<0.01). Figure 4 also shows a strong negative correlation between the temperatures of February and October, November, and December (r=-0.58, p<0.01;

r=-0.61, p<0.01). The and between April and September (r=-0.56, p<0.05). Figure 4 indicates a relatively clear correlation between the average temperatures of some months in the dry season and certain months in the rainy season. Additionally, it shows a weak and unclear positive or negative correlation between the months of the dry and rainy seasons. Monthly temperature correlations are influenced by various factors.

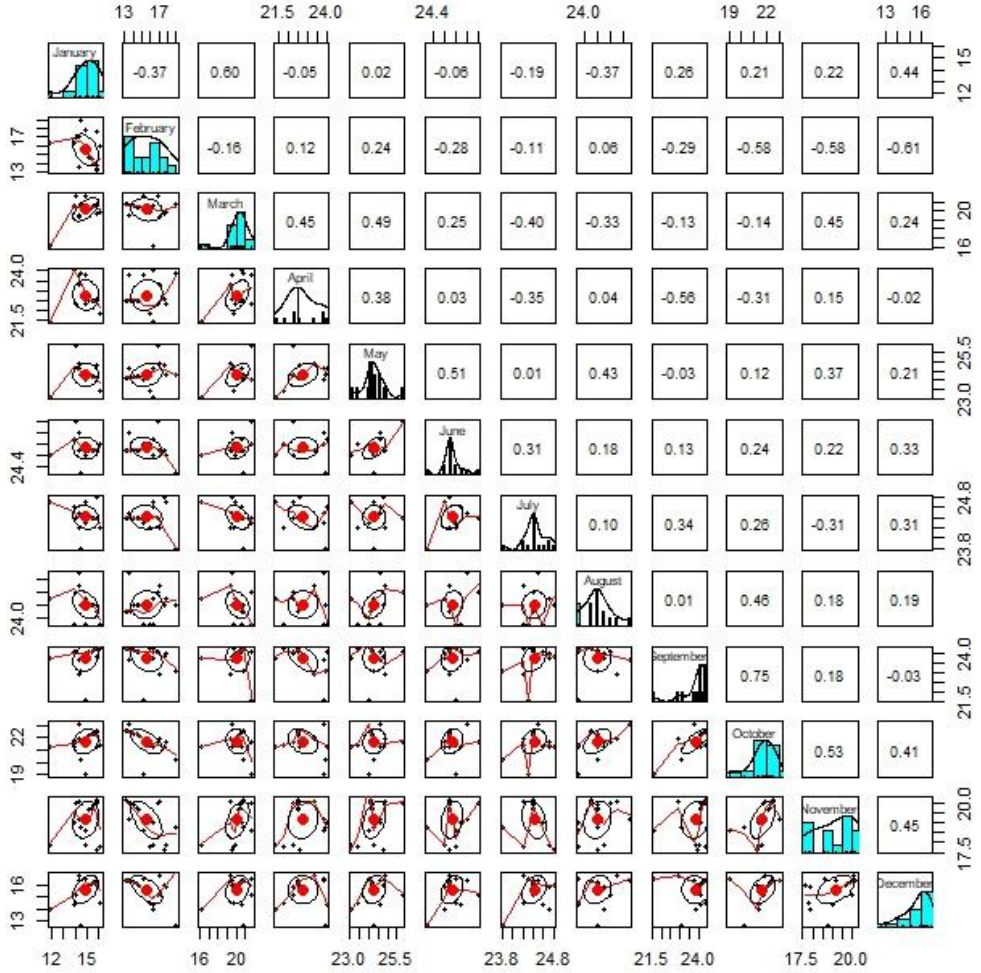

Figure 5. The correlation coefficient (r) between monthly temperatures

3.3 Temporal variation in rainfall

The total rainfall values recorded at the eleven monitoring stations are shown in Figure 6. The annual rainfall (in mm) across the years is as follows: 2009 (1,810±465), 2010 (1,449±440), 2011 (1,787±453), 2012 (2,315±528), 2013 (1,580±426), 2014 (1,628±481), 2015 (1,462±417), 2016 (1,968±501), 2017 (1,997±462), 2018 (1,830±505), 2019 (2,029±405), 2020 (1,609±350), 2021 (2,083±636), 2022 (1,979±571), 2023 (1,540±589), 2024 (1,683±587).

The decreasing trend of total rainfall and total rainfall min (in mm) was observed during 2009-2024, respectively: 127 mm (r=-0.71, p<0.05), 2.8 mm (r=-0.83, p<0.01). By contrast, the total rainfall max (in mm) tends to increase during 2009-2024, was 230 mm (r=0.82, p<0.01). The values of rainfall in the years were different amongst the total rainfall, total rainfall max, and total rainfall min (in mm). The rainfall trend in Northwestern, Vietnam, highlights the regional variability in rainfall trends and the importance of local-scale analysis for climate adaptation strategies.

3.4 Spatial variation in rainfall

The comparative data on the values of rainfall (in mm) in month during 2009-2024 were, specifically: January (134-706 mm), February (41-299 mm), March (347-549 mm), April (471-843 mm), May (624-1,931 mm), June (464-2,055 mm), July (336-2,068 mm), August (928-2,275 mm), September (883-2,106 mm), October (273-1,964 mm), November (114-379 mm),

December (81-390 mm), (Figure 7). The mean month values of rainfall were, specifically: with January (374±346), February (175±247), March (437±456), April (600±910), May (1,141±1,399), June (1,082±1,316), July (1,161±1,232), August (1,543±1,864), September (1,442±1,688), October (945±1,277), November (245±233), December (221±247) (Figure 7).

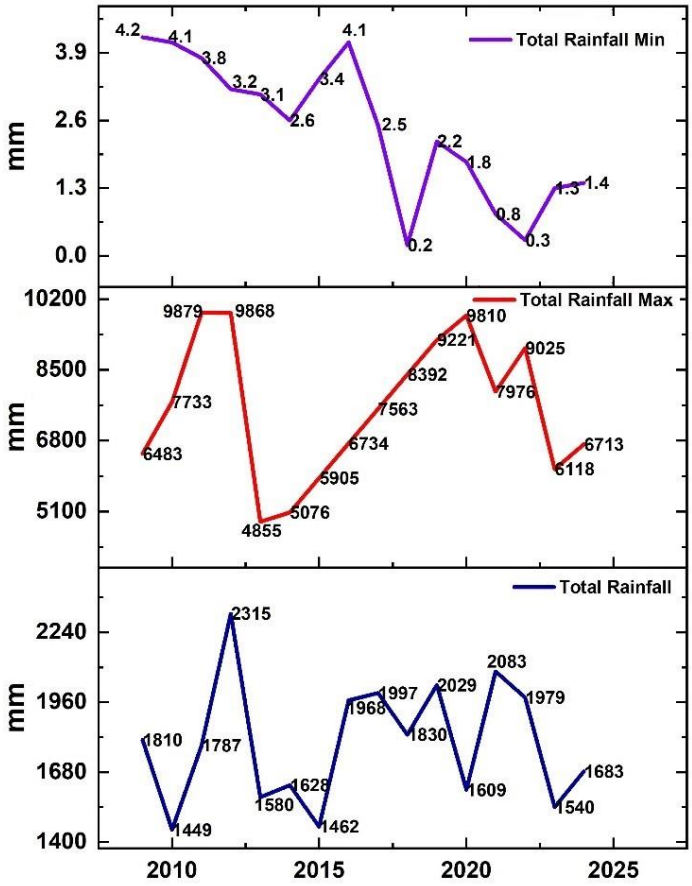

Figure 6. The rainfall in Northwestern, Vietnam during 2009-2024

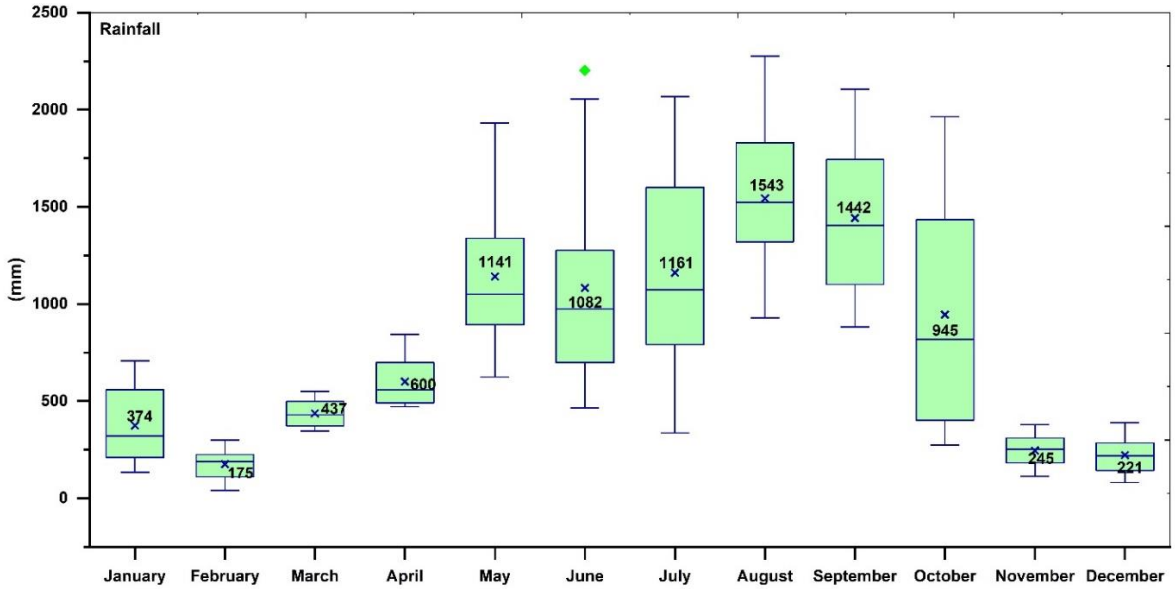

Figure 7. Change of rainfall in months from 2009 to 2024

Figures 8 and 9 show Northwestern Vietnam experiences alternating wet and dry and dry seasons. The highest total rainfall is consistently concentrated in the rainy season, which lasts from May to October. The dry season, occurring in January, February, March, April, November, and December, has a lower average total rainfall. Thus, the intensity and distribution of rainfall vary between seasons, with the dry season generally having lower total rainfall. These seasonal rainfall patterns strongly affect hydrology, vegetation, and sediment transport, particularly in mountainous Northwestern, Vietnam.

The total rainfall correlation levels by month are determined and shown in Figure 8 Strong correlations were observed, such as January with April (r=0.99, p<0.01) and January with March (r=0.94, p<0.01); April with October (r=0.90, p<0.01), October with December (r=0.93, p<0.01) as most important month correlation in Northwestern Vietnam (in 12 monitored month). The correlation of month total rainfall variables in the rainy is determined and shown in Figure 9. The total rainfall correlation between July and August, June and July, and May and August is the most important month correlation in the rain of Northwestern Vietnam. The correlation of the month were r=0.45 (p<0.05), r=0.42 (p<0.05), r=0.35 (p<0.05), r=0.22 (p<0.05), respectively. The relationship between dry and rainy season rainfall should be considered carefully to improve monitoring and understanding of total rainfall trends.

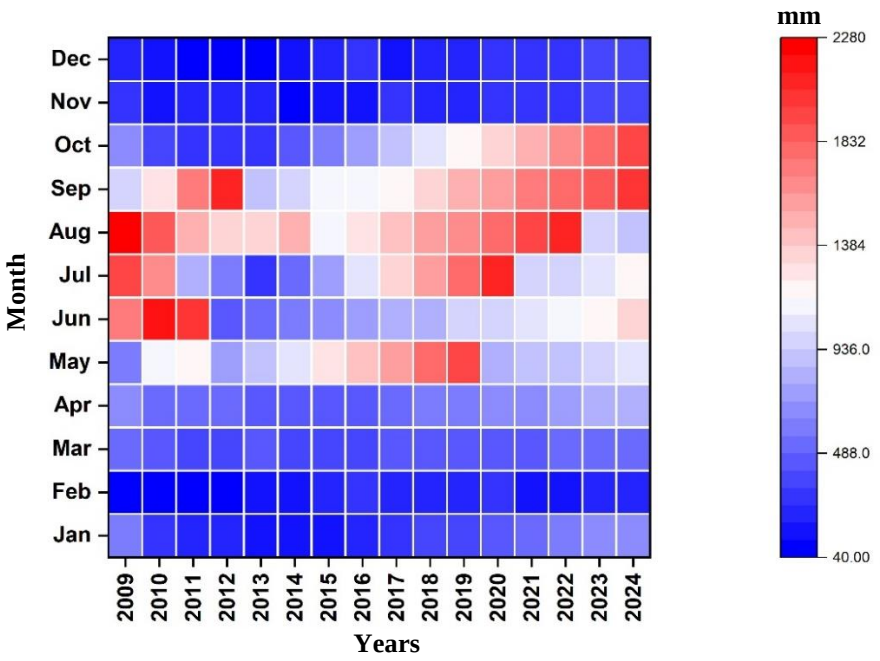

Figure 8. The monthly rainfall concentration levels

The total rainfall correlation levels by month are determined and shown in Figure 8 Strong correlations were observed, such as January with April (r=0.99, p<0.01) and January with March (r=0.94, p<0.01); April with October (r=0.90, p<0.01), October with December (r=0.93, p<0.01) as most important month correlation in Northwestern Vietnam (in 12 monitored month). The correlation of month total rainfall variables in the rainy is determined and shown in Figure 9. The total rainfall correlation between July and August, June and July, and May and August is the most important month correlation in the rain of Northwestern Vietnam. The correlation of the month were r=0.45 (p<0.05), r=0.42 (p<0.05), r=0.35 (p<0.05), r=0.22 (p<0.05), respectively. The relationship between dry and rainy season rainfall should be considered carefully to improve monitoring and understanding of total rainfall trends.

3.5 The correlation between temperature and total rainfall

Figure 10 shows the correlation between temperature and total monthly rainfall in the Northwest region of Vietnam during the period 2009-2024. January and December are identified as the two months of the dry season with the strongest positive correlation among the 12 months of the year. The correlation coefficients between temperature and total rainfall in January and December were (r=0.59, p<0.01; r=0.53, p<0.05), respectively. In addition,

during the dry season, a moderate positive correlation between temperature and total rainfall is observed in March, October, and November. The correlation coefficients between temperature and total rainfall for March, October, and November were ($r=0.36$, $p<0.05$; $r=0.44$, $p<0.05$; $r=0.36$, $p<0.05$), respectively. However, a strong negative correlation between temperature and total precipitation is found in February (dry season), with a correlation coefficient were ($r=-0.65$). Thus, the positive correlation between temperature and total rainfall is generally observed during the dry season (in with winter), except for February.

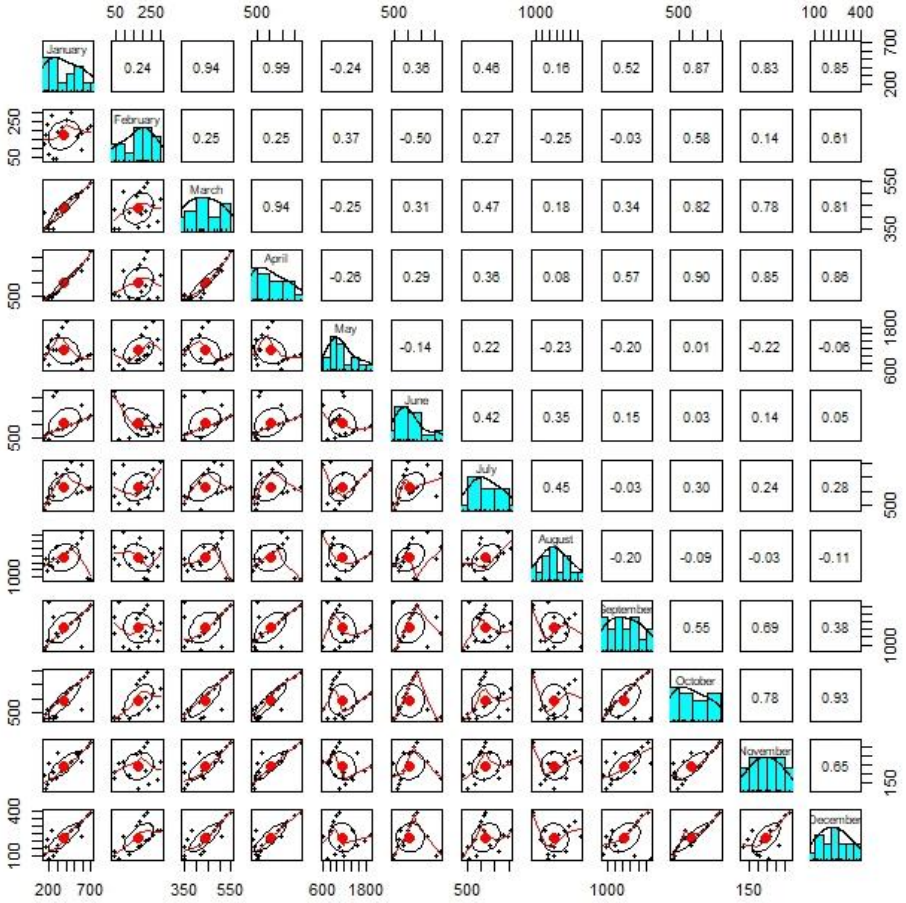

Figure 9. The correlation coefficient (r) between monthly rainfall

Figure 10 shows the correlation between temperature and rainfall during the summer (corresponding to the rainy season) with contrasting results in the Northwest region of Vietnam. Rainfall and summer temperature typically have a low negative average correlation (4 out of 6 summer months). The correlation coefficients between temperature and rainfall for April, May, June, and August are ($r=-0.33$, $p<0.05$; $r=-0.16$, $p<0.05$; $r=-0.25$, $p<0.05$; $r=-0.07$, $p<0.05$), respectively. However, for July and September, a low positive correlation between temperature and rainfall was identified, with coefficients of ($r=0.39$, $p<0.05$; $r=0.10$, $p<0.05$), respectively. These varied findings suggest that the relationship between temperature and rainfall is complex and region-specific.

4. DISCUSSIONS

4.1 The increasing trend of temperature and temporal and spatial

Over the past 15 years (2009-2024), the average temperature in the Northwest region of Vietnam increased by 0.6°C. This is lower than the global average surface temperature increase of 1.09°C recorded between 2010 and 2020 (Shukla et al., 2022). According to the IPCC's Sixth Assessment Report (AR6), the decade from 2011 to 2020 was approximately 1.09°C warmer than pre-industrial levels (Zhou, 2021). The maximum temperature increase in the Northwest of Vietnam during the period 2010-2020 was 0.3°C, which is higher than the global average maximum temperature increase. Analysis of the highest temperature of the year reveals

a global increase of 0.19-0.25°C per decade in the last 30 years (Papalexiou et al., 2018). The lowest temperature in the Northwest region of Vietnam has increased by an average of 3°C, which is higher than the lowest temperature increase globally. The findings indicate a positive correlation between temperature and precipitation during most months of spring, autumn, and winter (Vose et al., 2005). The consistent increase in minimum temperatures, particularly evident after 2010, aligns with global trends and serves as an indicator of the global warming trend with a notable rise in the rate of warming observed in recent decades.

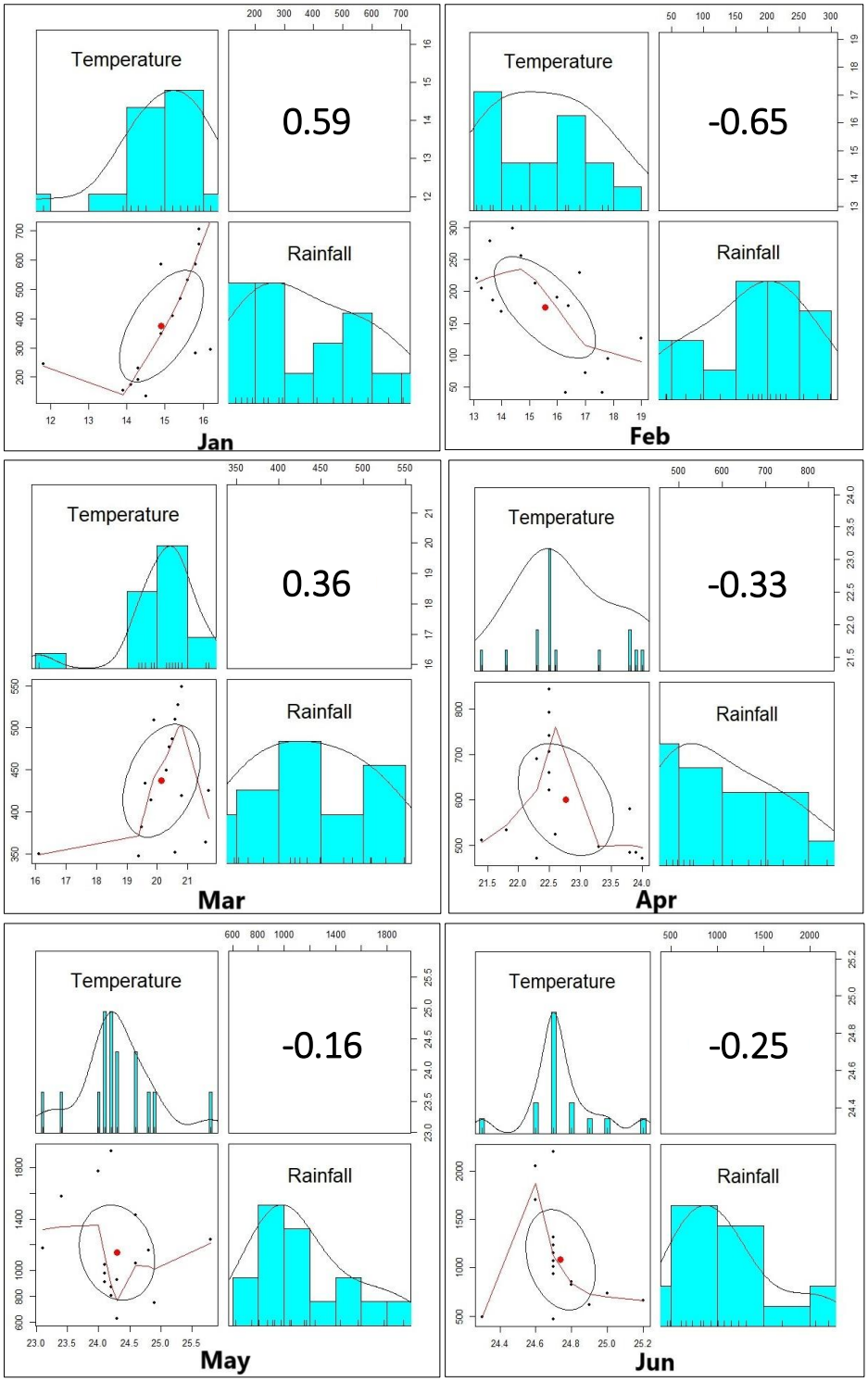

Figure 10. The correlation between temperature and total rainfall by month

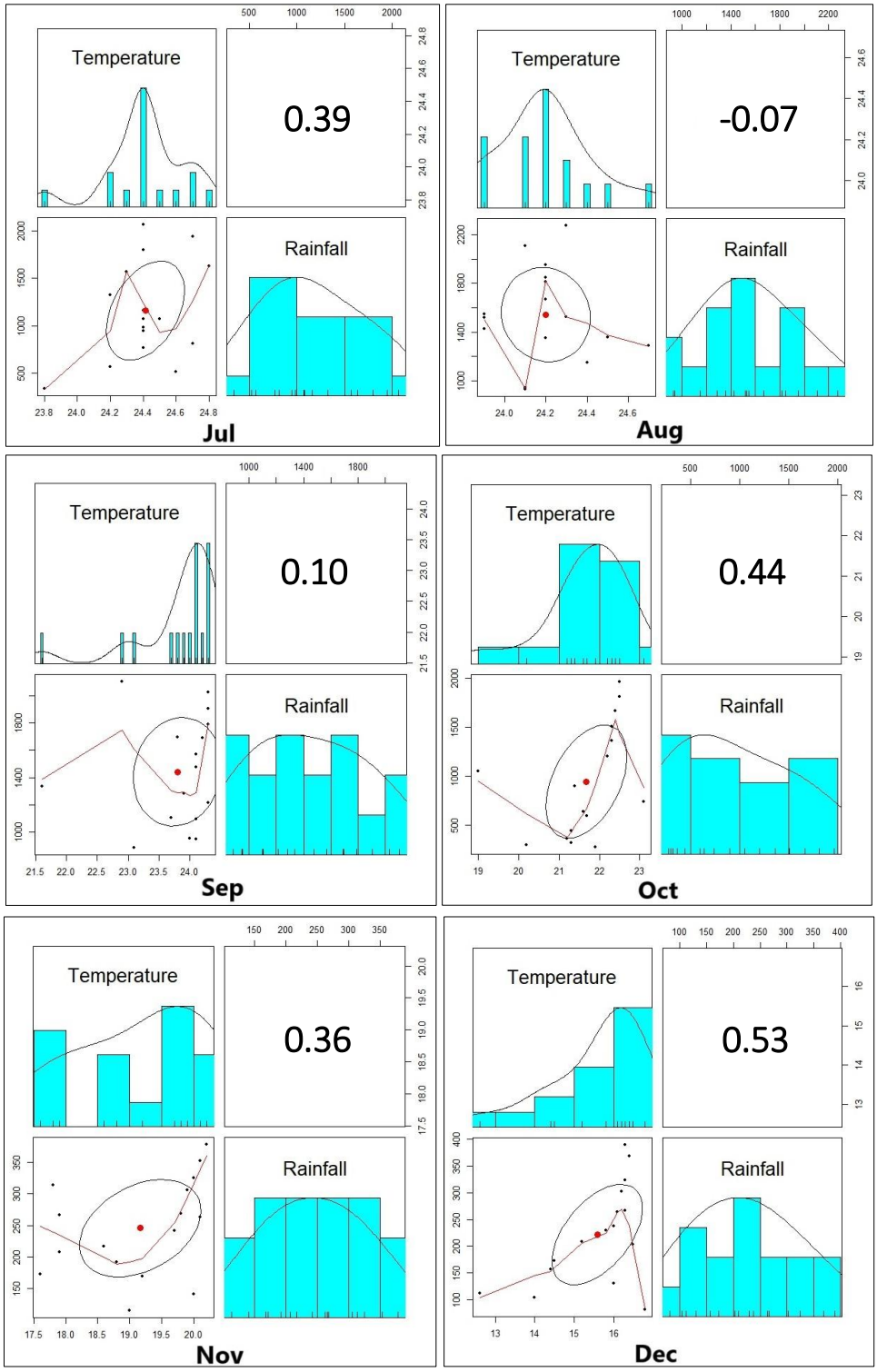

Figure 10. The correlation between temperature and total rainfall by month (cont.)

The research results show that the summer in the Northwest of Vietnam, corresponding to the rainy season from April to September each year, has the temperature average highest in the year. The research findings are consistent with other following studies. Research indicates that the rainy season generally exhibits warmer temperatures than the dry season in tropical regions. Similarly, East Java, Indonesia has experienced temperature increases of more than 1°C over 34 years, with the rainy season exhibiting warmer temperatures than the dry season (Natayu et al., 2021). This phenomenon could be attributed to the increased cloud cover and reduced solar radiation during the rainy season, leading to a greenhouse effect that traps

heat and results in higher temperatures. Research has shown significant positive correlations between temperatures of successive months seasons. In Iceland, extremely high correlations (r>0.8) were observed, especially in areas during summer (Degenhardt et al., 2019).

The research results indicate that there is a positive correlation between the temperatures of consecutive months in both the dry and rainy seasons and a negative correlation between the temperatures of months that are in the same season but far apart, particularly in northern Japan between April and August since 1998 (Kanno, 2013), Similar observed across North America and Europe, especially during summers (Madden and Williams, 1978).

The research results indicate a positive correlation between the temperatures of consecutive months during both the dry and rainy seasons. For example, there is a positive correlation between January, February, and March (dry season, and a positive correlation between April, May, June, July, August, and September (rainy season). The study identified a positive correlation between the temperatures of consecutive months within both the dry (e.g., January to March) and rainy seasons (e.g., April to September). This result is consistent with previous studies when research on temperature correlations across seasons reveals complex patterns. Studies indicate positive correlations between temperatures of consecutive months within both dry and rainy seasons (Emekwuru et al., 2023). However, negative correlations are observed between temperatures of months in the same season but a long (Madden and Williams, 1978). These findings highlight the intricate relationships between temperature and seasonal variations in different geographical contexts. Northern Vietnam has seen a substantial increase in hot days and a decrease in cold days, with the Northwest region showing a decline of 3.5 to 4.5 cold days per decade (Ngo and Bui, 2023). These temperature changes have implications for public health.

4.2 The rainfall tends to decrease and temporal and spatial variation

The average total rainfall in the study area tends to decrease after 15 years, corresponding to 127 mm may be influenced by deforestation with larger deforested areas associated with decreased rainfall, and changes and topography, climate models predict that continued deforestation could lead to further decreases in precipitation (Bonini et al., 2014; Ramos da Silva et al., 2008).This finding is consistent with long-term trends observed in other regions, such as the Yarra River catchment in Australia, which has experienced significant declines in monthly and annual precipitation over the past 50 years (Barua et al., 2013), and Punjab, India, where both total rainfall and the number of rainy days declined from 2001-2015 compared to 1986-2000 (Kaur et al., 2021). The Kathmandu Valley in Nepal experienced a significant reduction in rainfall after 2000, with mountain stations showing decreasing trends in all seasons (Prajapati et al., 2021). While no significant temporal trends were found in basin-scale precipitation in southeast Arizona, spatial variability of cumulative precipitation decreased exponentially over time, becoming uniform after 20 years. These findings suggest a consistent reduction in rainfall across different regions, which may have important implications for water resource management and ecosystem dynamics. These changes necessitate adaptive water resource management strategies, including supply-demand adaptations, capacity building, public participation, and regional cooperation.

The total average rainfall value in the study area shows a clear seasonal variation, with the highest rainfall concentrated from May to October (summer), while during the winter season (from October to December and until April of the following year), the rainfall is significantly lower compared to summer. This result is consistent with recent studies that collectively highlight significant seasonal variations in rainfall patterns across different regions. For example, in Costa Rica's Reventazón River basin, two distinct seasonal periods were identified: December-April with predominantly orographic rain, and May-November with convective showers (Chacón et al., 1985). In monsoon systems, summer typically brings higher rainfall due to thermal contrasts between land and ocean, causing low-level moist air convergence over land. These findings highlight the complex interactions between various climatic factors in determining precipitation regimes.

This result is the correlation of rainfall in Northwestern, Vietnam in have highlighted significant patterns in rainfall trends and their correlations with global climate phenomena. A general downward trend in rainfall in in South Africa’s, region of Africa, Australia to global warming (Nenwiini et al., 2013). The correlation coefficient (r) between the rainfall amounts of the months in winter is higher than in

summer, with the highest r values between winter months ranging from (r=0.65 to r=0.99), whereas the highest correlation coefficient for summer months ranges from (r=0.55 to r=0.95). This result is consistent with recent studies shows the spatial variability of rainfall differs between seasons, with higher correlations observed in winter compared to summer (Chacón et al., 1985). The winter rainfall is more strongly correlated with the rainfall than in the summer, possibly due to the high latitude of Northwestern Vietnam. Research in California revealed positive precipitation correlation trends in winter with strong correlations to ENSO (The alternation of warm El Nino and cold La Nina conditions, referred to as the El Nino-Southern Oscillation (ENSO, AAO (The Antarctic Oscillation), and NAO (North Atlantic Oscillation) (González et al., 2022). In High Mountain Asia, winter precipitation showed positive correlations with various global modes of variability, while summer precipitation exhibited negative correlations, particularly with the Eurasian teleconnection (Massoud et al., 2024).

These findings collectively suggest that seasonal rainfall patterns are dynamic and closely linked to large-scale climate oscillations. These studies highlight the complex and regionally-specific nature of seasonal rainfall correlations, emphasizing the importance of considering local climate patterns in rainfall predictions, forecasting landslides and debris flows in mountainous regions, and understanding rainfall patterns for effective disaster prevention in mountainous areas, and reduce impacting crop yields and farming strategies. Besides understanding rainfall distribution is essential for addressing environmental to mitigate these challenges, can adopted various management strategies.

4.3 Temperature and rainfall trend fluctuate seasonally

The research results show there is a positive correlation between temperature and rainfall in most months of spring, autumn, and winter. However, in summer, a negative correlation between temperature and rainfall predominates in Northwestern, Vietnam. Correlation between the variables studied indicates a significant relationship between the two factors. Research worldwide shows similar results in regions on a global scale, For example, In Europe, specifically Scania, Sweden, negative correlations between rainfall and temperature were found from April to July (Cong et al., 2012). Similarly in Europe, positive correlations between temperature and rainfall predominate in walinter, while negative correlations are more common in summer (Lhotka et al., 2022; Rodrigo, 2022). In summer, a negative correlation between temperature and rainfall predominates in most areas, particularly in the central and southern Great Plains of the United States (Zhao and Mak, 1993; Madden and Williams, 1978). In Southern South America, the correlation between temperature and precipitation varies by season and region, with some areas showing positive correlations in winter and negative correlations in summer (Rusticucci and Penalba, 2000). These studies highlight the importance of understanding regional variations in temperature-precipitation relationships and their connection to large-scale atmospheric circulation for better water management and future climate projections.

Climate projections for Vietnam indicate significant warming trends, with average temperatures expected to rise by 1.3-4.3°C by the end of the 21st century, the Northwestern region is projected to experience the most substantial temperature increase (Nguyen et al., 2018).

5. CONCLUSION

The study, we analyzed the temporal and spatial variations and the relationship between temperature and precipitation, using data from 11 monitoring stations over a 15 years. The case study is in the Northwest Vietnam revealed that:

- The average temperature increase in the Northwest of Vietnam is lower than the global average, but,increases in both maximum and minimum temperatures exceeding the global average.
- The highest average temperature in the year is concentrated in the rainy season corresponding to summer, there is a positive correlation between consecutive months within the same season, and a negative correlation is observed between months in the same season that are far apart.
- There is a significant decreasing trend in both annual and monthly precipitation over the past 15 years in the study area. The highest precipitation is concentrated in the summer months, and significantly lower precipitation in winter.
- The value of the strong positive correlation coefficient of rainfall is higher during winter months and lower duringsummer months, indicating that the spatial variation of rainfall differs between seasons.

- Something like, temperature and rainfall during spring, autumn, and winter months exhibit a common positive correlation; however, a dominant negative correlation is observed in summer.

The findings suggest the need for improved water conservation strategies and climate-resilient agricultural practices in Northwestern Vietnam. Adaptive water resources management can address climate change-induced droughts, and reservoir expansion can serve as a critical infrastructural intervention to augment water storage capacity, thereby enhancing the resilience of local communities to hydrological variability.

ACKNOWLEDGEMENTS

The author would like to express gratitude to the Meteorological and Hydrological Station of the Northwestern Vietnam for their generosity in supporting this study. All data and information are retrieved and used with the permission of the Meteorological and Hydrological Station of the Northwestern Vietnam for scientific purposes.

AUTHOR CONTRIBUTIONS

Writing Review, Data Curation, Statistical analysis, Writing-Original draft, Writing-Review and Editing: Xuan-Duc Do.

DECLARATION OF CONFLICT OF INTEREST

The author declare no conflict of interest could have appeared to influence the work reported in this paper.

REFERENCES

Abbam T, Johnson FA, Dash J, Padmadas SS. Spatiotemporal variations in rainfall and temperature in Ghana over the twentieth century, 1900-2014. Earth and Space Science 2018;5(4):120-32.

Balathandayutham K, Mayilswami C. Evaluation of spatial and temporal characteristics of rainfall variability on Parambikulam Aliyar Palar (Pap) Basin, Tamil Nadu, India. Trends in Biosciences 2014;7(3):183-90.

Barua S, Muttil N, Ng AWM, Perera BJC. Rainfall trend and its implications for water resource management within the Yarra River catchment, Australia. Hydrological Processes 2013;27(12):1727-38.

Bonini I, Rodrigues C, Dallacort R, Marimon Junior BH, Carvalho MAC. Rainfall and deforestation in the municipality of Colíder, southern Amazon. Revista Brasileira de Meteorologia 2014;29:483-93.

Cao J, Zhou W, Zheng Z, Ren T, Wang W. Within-city spatial and temporal heterogeneity of air temperature and its relationship with land surface temperature. Landscape and Urban Planning 2021;206:Article No. 103979.

Cong RG, Brady M. The interdependence between rainfall and temperature: Copula analyses. The Scientific World Journal 2012;(1):Article No. 405675.

Chacón RE, Fernandez W. Temporal and spatial rainfall variability in the mountainous region of the Reventazón river basin, Costa Rica. Journal of Climatology 1985;5(2):175-88.

Chowhan V, Chandargi DM, Goudappa SB, Kammar SK, Koppalakar BG, Lokesh GB. Assessing farmer vulnerability to climate change in Karnataka: A focus on index development. International Journal of Environment and Climate Change 2023;13(11):130-42.

Degenhardt L, Ólafsson H. Persistence of observed air temperatures in Iceland. International Journal of Climatology 2019;39(3);1262-75.

Dzupire NC, Ngare P, Odongo L. A copula based bi-variate model for temperature and rainfall processes. Scientific African 2020;8:Article No. 00365.

Emekwuru N, Ejohwomu O. Temperature, humidity and air pollution relationships during a period of rainy and dry seasons in Lagos, West Africa. Climate 2023;11(5):Article No. 113.

Ganeshkumar B, Krishna GG. Spatiotemporal variability of temperature and its extremes over an agro-ecological region of Tamil Nadu, India. Polish Journal of Environmental Studies 2020;29(5):3561-8.

Getnet GT, Dagnew AB, Ayal DY. Spatiotemporal variability and trends of rainfall and temperature in the tropical moist montane ecosystem: Implications to climate-smart agriculture in Geshy watershed, Southwest Ethiopia. Climate Services 2023;30:Article No. 100384.

González-Pérez A, Álvarez-Esteban R, Penas A, del Río S. Analysis of recent rainfall trends and links to teleconnection patterns in California (US). Journal of Hydrology 2022;612:Article No. 128211.

Han JM, Kamber JP. Data Mining - Concepts and Techniques. 3rd ed. USA: Elsevier Inc; 2012.

He S, Hao C. Analysis on spatial-temporal variation characteristics of climate in Qinling-Huaihe demarcation zone since 1961. Ecological Indicators 2024;158:Article No. 111345

Hoang LT, Roshetko JM, Huu TP, Pagella T, Mai PN. Agroforestry-the most resilient farming system for the hilly Northwest of Vietnam. International Journal of Agriculture System 2017;5(1):1-23.

Kanno H. Strongly negative correlation between monthly mean temperatures in April and August since 1998 in northern Japan. Journal of the Meteorological Society of Japan 2013;91(3);355-73.

Kaur N, Yousuf A, Singh MJ. Long term rainfall variability and trend analysis in lower Shivaliks of Punjab, India. Mausam 2021;72(3):571-82.

Lhotka O, Kyselý J. Precipitation-temperature relationships over Europe in CORDEX regional climate models. International Journal of Climatology 2022;42(9):4868-80.

Madden RA, Williams J. The correlation between temperature and precipitation in the United States and Europe. Monthly Weather Review 1978;106(1):142-7.

Massoud EC, Lim YK, Andrews LC, Girotto M. Connecting global modes of variability to climate in High Mountain Asia. Atmosphere 2024;15(2):Article No. 142.

Meseret Z, Belay S. Spatial and temporal variability in temperature and rainfall over Mecha Area, Ethiopia. International Journal of Scientific Research in Multidisciplinary Studies 2019;5(12):56-65.

Natayu A, Kamila FT, Dananjaya IBGG, Reflin RR, Fikri MR. Understanding the climate behavior through data interpretation: Java-Bali-Nusa Tenggara case. Indonesian

Journal of Computing, Engineering, and Design 2021; 3(2):130-45.

Nenwiini S, Kabanda TA. Trends and variability assessment in rainfall of Vhembe District South Africa. Proceedings of the Society of South African Geographers (SSAG) Conference; 2012 Jun 20-22; Department of Environmental and Geographical Science, University of Cape Town: 2012. p. 171-6.

Ngo DT, Bui TKH, Trends and return frequencies of hot and cold extreme events in Northern Vietnam from 1961-2018. VNU Journal of Science 2023;39(2):31-42.

Nguyen-Dang M, Nguyen-Minh T, Sasaki h, Takayabu I. A study of seasonal rainfall in Vietnam at the end of 21st century according to the Non-Hydrostatic Regional Climate Model. Vietnam Journal of Science, Technology and Engineering 2018;60(3):89-96.

Papalexiou SM, AghaKouchak A, Trenberth KE, Foufoula-Georgiou E. Global, regional, and megacity trends in the highest temperature of the year: Diagnostics and evidence for accelerating trends. Earth's Future 2018;6(1):71-9.

Pearson K. Determination of the coefficient of correlation. Science 1909;30(757):23-5.

Prajapati R, Talchabhadel R, Silwal P, Upadhyay S, Ertis B, Thapa BR, et al. Less rain and rainy days-lessons from 45 years of rainfall data (1971-2015) in the Kathmandu Valley, Nepal. Theoretical and Applied Climatology 2021;145(3):1369-83.

Ramos da Silva R, Werth D, Avissar R. Regional impacts of future land-cover changes on the Amazon basin wet-season climate. Journal of Climate 2008;21(6):1153-70.

Rodrigo FS. A simple approach for the study of the relationship between temperature and precipitation. Theoretical and Applied Climatology 2022;150(1):215-28.

Rusticucci M, Penalb O. Interdecadal changes in the precipitation seasonal cycle over Southern South America and their relationship with surface temperature. Climate Research 2000;16(1):1-15.

Shahid S. Spatio-temporal variability of rainfall over Bangladesh during the time period 1969-2003. Asia-Pacific Journal of Atmospheric Science 2009;45(3):375-89.

Shukla PR, Skea J, Slade R, Khourdajie Al A, van Diemen R, McCollum D, et al. Climate Change 2022: Mitigation of Climate Change. Contribution of working group III to the sixth assessment report of the Intergovernmental Panel on Climate Change 2022. Cambridge University Press; 2022.

Vose R, Easterling DR, Gleason BE. Maximum and minimum temperature trends for the globe: An update through 2004. Geophysical Research Letters 2005;32:Article No. L23822.

Worku T, Khare D, Tripathi SK. Spatiotemporal trend analysis of rainfall and temperature, and its implications for crop production. Journal of Water and Climate Change 2019;10(4):799-817.

Zhao W, Mak K. The relationship between precipitation and temperature over the contiguous United States. Journal of Climate 1993;6(6):1232-6.

Zhou T. New physical science behind climate change: What does IPCC AR6 tell us? The Innovation (Camb) 2021;2(4):Article No. 100173.

Zongxing L, He Y, Wang P, Theakstone WH, An W, Wang X, et al. Changes of daily climate extremes in southwestern China during 1961-2008. Global and Planetary Change 2012;80: 255-72.

Environment and Natural Resources Journal

Volume 24
Issue 1
2026

Decolorization of Treated Municipal Wastewater for Non-Potable Reuse Using a Household UV/H_2O_2 Process

Chanoknan Phumphuang[1], Kwannate Manoonpong[2], and Pijit Jiemvarangkul[1*]

[1]Department of Civil Engineering, King Mongkut's University of Technology North Bangkok, Bangkok 10800, Thailand
[2]Department of Civil and Environmental Engineering Technology, College of Industrial Technology, King Mongkut's University of Technology North Bangkok, Bangkok 10800, Thailand

ARTICLE INFO

Received: 22 Jun 2025
Received in revised: 4 Sep 2025
Accepted: 19 Sep 2025
Published online: 29 Oct 2025
DOI: 10.32526/ennrj/24/20250159

Keywords:
UV/ H_2O_2 process/ Color removal/ Treated municipal wastewater/ Pseudo-second-order kinetics/ Water reuse

*** Corresponding author:**
E-mail: pijit.j@eng.kmutnb.ac.th

ABSTRACT

Color remaining in treated municipal wastewater can limit its acceptance for non-potable reuse. This study evaluated a simple UV/H_2O_2 step for decolorization of secondary effluent from three Bangkok Metropolitan Administration (BMA) wastewater treatment plants. Experiments were performed in a 0.75 L batch reactor equipped with a single low-pressure UV lamp (254 nm, 16 W); H_2O_2 doses of 33, 100, 167, and 333 mg/L were tested at ambient 25-30°C and unadjusted pH. Reaction times were 0-10 minutes with sampling at 0, 3, 5, and 10 min. Color (ADMI) decreased rapidly in the first minutes: >65% removal at 5 min for 100 mg/L H_2O_2, and a maximum of 76% at 10 min for 333 mg/L H_2O_2. Linearized kinetic fits showed that a pseudo-second-order model ($R^2 \approx 0.953$-0.966) described the data better than pseudo-first-order ($R^2 \approx 0.909$-0.921), indicating apparent bimolecular behavior under the tested conditions. A screening-level reagent cost based on commercial 50% w/w H_2O_2 pricing was 5.8 THB/m^3 at 100 mg/L (≈0.179 USD/m^3 using 32.4 THB: USD). These results demonstrate that a household-scale UV/H_2O_2 configuration can provide fast decolorization of municipal secondary effluent under short contact times, with a simple kinetic descriptor and an initial cost benchmark relevant to building-level non-potable reuse.

HIGHLIGHTS

- A household UV/H_2O_2 system removed over 65% of wastewater color in 5 minutes.
- Maximum decolorization of 76% was achieved with 333 mg/L H_2O_2 after 10 minutes.
- Reaction followed pseudo-second-order kinetics, indicating a bimolecular mechanism.
- Treatment cost at 100 mg/L H_2O_2 was approximately 5.8 THB/m^3—economically feasible.
- The system is suitable for non-potable reuse in large buildings (e.g., toilet flushing, cleaning).

1. INTRODUCTION

Water reuse is a practical strategy for addressing water scarcity, particularly for non-potable applications. In Bangkok, more than 2.6 million cubic meters of domestic wastewater are generated daily, of which only about 60-70% is treated before discharge (BMA, 2022). However, less than 1% of treated wastewater is reused, indicating substantial potential for reclamation. Given growing water demand and urban expansion, promoting the reuse of treated effluent in non-potable applications has become increasingly important. Treated domestic wastewater is a significant resource with potential for non-potable reuse, offering an environmentally sustainable solution and supporting applications like agricultural irrigation, street cleaning, and environmental restoration, commonly referred to as "water reclamation" (Institute for Environment and Sustainability, 2014; Duckett et al., 2024). The idea of using treated wastewater is to reduce potable water consumption in buildings, especially large-scale buildings, such as shopping malls, office buildings, universities, government offices. Many activities such as floor washing, toilet flushing, and garden irrigation do not need high quality water, so the use of treated wastewater is a practical solution. However, treated

Citation: Phumphuang C, Manoonpong K, Jiemvarangkul P. Decolorization of treated municipal wastewater for non-potable reuse using a household UV/H_2O_2 process. Environ. Nat. Resour. J. 2026;24(1):115-126. (https://doi.org/10.32526/ennrj/24/20250159)

wastewater contains color consisting of organic compounds, particularly humic and fulvic substances which are generated by microorganisms in the biological wastewater treatment processes (Park et al., 2005; Puspita et al., 2011). These soluble organic compounds are resistant to biological degradation and cause a light yellow to brown coloration in the effluent. This color creates an unpleasant impression on users and causes staining on sanitary fixtures.

Various advanced treatment methods have been applied to remove residual color from wastewater. Among them, the UV/H_2O_2 process—a type of Advanced Oxidation Process (AOP)—has shown promising decolorization performance. Several studies have reported high efficiency of this method. For instance, Caretti and Lubello (2010) achieved up to 90% and 80% color removal within 10 minutes when treating wastewater treatment effluent using a 150 W-medium pressure UV lamp and a 15W-low pressure UV lamp, respectively. Sugha and Bhatti (2022) observed 86% dye degradation and 78% COD reduction after 120 minutes of UV/H_2O_2 treatment (50 mg/L dye, initial pH 4). More recently, Son et al. (2024) demonstrated over 99% color removal in actual textile wastewater using UV/H_2O_2 with 5 mM H_2O_2, 26.6 W/m² UV intensity, and 180 minutes of irradiation, identifying H_2O_2 concentration as the most critical operating variable. Moreover, Jennifer et al. (2024) showed that UV/H_2O_2 effectively removed anionic surfactants from tertiary treated effluent, achieving over 90% removal. These findings highlight the consistent performance of the UV/H_2O_2 process across different wastewater types and emphasize its potential for practical application.

The UV/H_2O_2 process generates powerful oxidizing hydroxyl radicals. Hydrogen peroxide (H_2O_2) reacts with UV to create OH· as the following reaction: $H_2O_2 + hv \rightarrow 2OH$. The UV/$H_2O_2$ process has been applied in various fields, including drinking water, water treatment, wastewater treatment, organic contamination removal, and groundwater remediation (Puspita et al., 2011; Lhotský et al., 2017; Pamuła et al., 2022; Sugha and Bhatti, 2022). It can improve the wastewater quality by removing micropollutants, which are difficult to treat by conventional treatments including pharmaceuticals in domestic wastewater and pesticides (Kim et al., 2009; Luo et al., 2014; Afonso-Olivares et al., 2016; Pamuła et al., 2022; Mukherjee et al., 2023). This process can reduce chemical oxygen demand (COD) and promote disinfection in water reuse applications (Pamuła et al., 2022; Yang et al., 2024). Several studies have reported the application of the UV/H_2O_2 process to remove color from wastewater including dye and textile industries (Papić et al., 2006; Zawadzki and Deska, 2021; Sugha and Bhatti, 2022). Moreover, several studies have applied this process for decolorization of treated wastewater from activated sludge wastewater treatment (Park et al., 2005; Puspita et al., 2011). However, most of studies have not explored key engineering aspects, such as the optimal sizing of UV systems, comparative operational and installation costs with other water reuse technologies, and the cost of water supply.

Beyond UV/H_2O_2, several post-treatment options have been used to reduce residual color in treated effluents, including coagulation-flocculation, granular activated carbon (GAC) adsorption, ultrafiltration (UF), ozonation, Fenton/photo-Fenton oxidation, and TiO_2 photocatalysis. Coagulation and GAC can remove humic-like chromophores cost-effectively but generate sludge or require media regeneration and breakthrough management (Barloková et al., 2023; Knap-Bałdyga and Żubrowska-Sudoł, 2023). UF provides consistent decolorization but entails higher capital/operating costs and membrane fouling that necessitate chemical cleaning (Zhang et al., 2023). Ozonation is effective for color and other chromophores but can form bromate in bromide-containing waters, requiring careful control or downstream mitigation (Morrison et al., 2023). Fenton/photo-Fenton processes often achieve high decolorization but typically require acidic condition (pH~3), produce iron sludge, and have higher reagent demand (Ziembowicz and Kida, 2022). TiO_2 photocatalysis shows high laboratory performance but faces catalyst recovery and scale-up challenges in full-scale applications (Kumari et al., 2023).

Recent work has advanced UV/H_2O_2 for challenging effluents and tertiary polishing—for example, actual textile wastewater achieving very high decolorization under optimized UV fluence and peroxide dose (Son et al., 2024), and hybrid tertiary sequences that couple UV or UV/H_2O_2 with nature-based units for effluent polishing (Miguel et al., 2024), alongside costed UV/H_2O_2 applications in high-strength industrial streams (Kim et al., 2023). Building on these advances, our study operationalizes UV/H_2O_2 for building-scale reuse by deploying a household UV device on municipal secondary effluent at neutral pH, demonstrating rapid visible-color reduction, and developing a bottom-up treatment cost appropriate for

building or campus applications. In terms of sustainability, the design avoids sludge-forming coagulants and relies on modular, readily available UV equipment. It also reduces the need for potable water in non-potable applications, as shown in recent decentralized/tertiary studies of compact UV-AOP systems (Jennifer et al., 2024).

2. METHODOLOGY

2.1 Treated municipal wastewater

Treated municipal wastewater samples were collected from three wastewater treatment plants operated by the Bangkok Metropolitan Administration (BMA). The characteristics of the treated wastewater are summarized in Table 1. Turbidity levels ranged from 1.30 to 6.54 NTU, with an average of 5.03 NTU, while the pH averaged 7.56. The five-day biochemical oxygen demand (BOD_5) ranged from 1.67 to 4.50 mg/L, with a mean value of 2.69 mg/L. Chemical oxygen demand (COD) ranged from 19.8 to 29.3 mg/L, averaging 23.2 mg/L. After filtration through 20-micron filter paper, the average color value was 25 ADMI. All parameters complied with Thailand's effluent discharge standards for buildings and factories within typical ranges for secondary effluents (Royal Gazette, 2017; Royal Gazette, 2018).

Table 1. Baseline characteristics of secondary-effluent grab samples from three BMA WWTPs

Source of sample	Turbidity (NTU)	pH	BOD_5 (mg/L)	COD (mg/L)	Color (ADMI)
Plant A	6.54	7.60	1.67	19.8	24.0
Plant B	7.24	7.49	4.50	29.3	29.0
Plant C	1.30	7.60	1.90	20.3	22.0
Range (min-max)	1.3-7.24	7.49-7.60	1.67-4.50	19.8-29.3	22.0-29.0

Note: Single grab per plant; SD is not reported to avoid conflating inter-plant variability with replicate precision. Inter-plant variability is shown as the range (min-max).

2.2 Chemicals and materials

Treated municipal wastewater (secondary effluent) was obtained as grab samples from three wastewater treatment plants operated by the Bangkok Metropolitan Administration (BMA). The oxidant used was hydrogen peroxide (H_2O_2, 30% w/w, CAS 7722-84-1; CARLO ERBA Reagents), from which working solutions in the range 33-333 mg/ L were prepared. H_2O_2 30% w/w was used for laboratory dosing and kinetic experiments. For cost estimation, unit prices refer to commercial-grade H_2O_2 50% w/w commonly sold in the local market; costs are normalized to the pure H_2O_2 dose and then converted to the equivalent mass of 50% stock for pricing. For sample pre-filtration, qualitative ashless filter paper (Whatman No. 41, GE Healthcare Life Sciences; nominal particle retention≈20 µm) was employed. Ultraviolet irradiation was provided by a low-pressure 16-W household UV unit (commercial supplier) equipped with a quartz sleeve; the manufacturer's rated flow is 453 L/h. Samples from the three wastewater treatment plants were analyzed and treated separately; no compositing was performed.

2.3 Pre-treatment and filtration

Secondary effluent samples were passed through a 20-micron filter paper prior to UV/H_2O_2 testing. This step was introduced to emulate the simple pre-filtration commonly used upstream of small UV systems to limit lamp sleeve fouling and reduce light shielding by suspended solids and standardize the optical conditions for kinetic evaluation by focusing on the dissolved/colloidal chromophore fraction. No coagulants or adsorbents were added, and pH was not adjusted. Filtration was performed immediately before each experiment. (Note: this pre-filtration is equivalent to the role typically served by cartridge/sand filters in building-scale reuse systems.) Dissolved organic carbon (DOC) was not measured in this study; kinetics therefore emphasize the dissolved color fraction under a fixed UV setting.

2.4 Reactor and operating conditions

2.4.1 Selection of H_2O_2 dose and experimental plan

To define a usable range for small, building-scale systems, four H_2O_2 concentrations were selected: 33, 100, 167, and 333 mg/L, corresponding to approximately 0.97, 2.94, 4.91, and 9.79 mM (MW(H_2O_2)=34 g/mol). This 1-10 mM range encompasses doses commonly reported for UV/H_2O_2 decolorization in tertiary polishing and dye-laden wastewaters, with 5 mM frequently identified as effective under optimized UV fluence (Son et al.,

2024). Experiments followed a one-factor-at-a-time plan at a fixed low-pressure UV setting (254 nm, 16 W), varying H_2O_2 dose and contact time (0, 3, 5, 10 min). All tests were performed in triplicate (n=3), and concentration-time data were analyzed using kinetic models (pseudo-first- and pseudo-second-order) to support design-level sizing. We did not conduct a formal design of experiments (e.g., factorial/response-surface varying UV fluence, H_2O_2 dose, and contact time); this will be undertaken in future work to optimize performance and cost for scale-up.

2.4.2 Operating conditions

Experiments were conducted in a batch reactor (working volume=0.75 L) equipped with a single low-pressure 254 nm, 16 W UV lamp in a quartz sleeve (household UV device). After dosing H_2O_2 (30% w/w stock) to the target concentration, samples were mixed (~300 rpm, 30 s) before UV exposure. Contact times were 0-10 min (0, 3, 5, 10 min sampling). Tests were run at ambient temperature (~25-30°C) and neutral pH characteristic of the effluent (no pH adjustment). All tests were performed in triplicate (n=3). Irradiance at the liquid surface was not measured; experiments used a single low-pressure 254 nm, 16 W lamp in a fixed geometry for all tests, so comparisons across H_2O_2 doses and contact times were made at the same UV setting. Color (ADMI) and turbidity (NTU) were measured by standard methods; glassware was rinsed with deionized water between runs as see Figure 1. Residual H_2O_2 was not measured in this screening study. In practical non-potable reuse configurations, a short post-UV holding period is provided to allow decay of H_2O_2 prior to distribution.

2.5 Color measurements

The American Dye Manufacturers Institute (ADMI) method was used to measure the color of water samples in this study, in accordance with U.S. EPA Method 110.1 (USEPA, 1978). The principle of ADMI color measurement involves the use of a spectrophotometer to determine absorbance at multiple wavelengths, specifically 436, 525, and 620 nanometers, which correspond to key regions of the visible light spectrum as perceived by the human eye. These absorbance values are mathematically combined to yield a single ADMI value, providing a standardized and quantitative representation of color intensity in wastewater samples. In this study, color measurements were performed using a HACH DR6000 UV-Vis spectrophotometer.

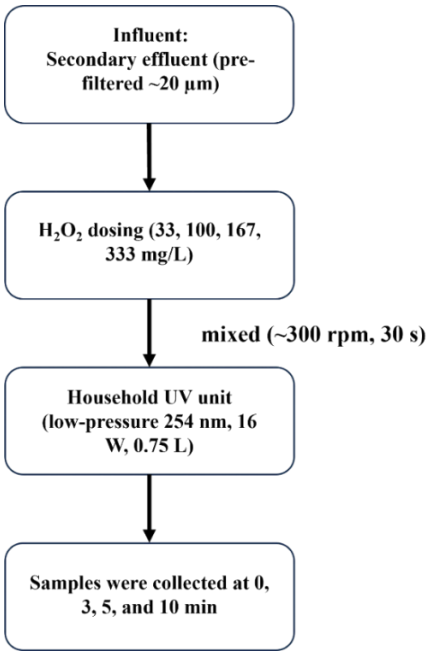

Figure 1. Experimental process and conditions for UV/H_2O_2 tests

2.6 Chemical kinetics of color removal

The kinetics of the color removal reaction were investigated to evaluate the potential application of the UV/H_2O_2 process. Two kinetic models, namely pseudo-first order and pseudo-second order, were applied to describe the degradation behavior, using the following rate equations:

$$\text{Pseudo-First-order model: } \frac{dC}{dt} = -k'C \quad (1)$$

$$\text{Intregated from: } \ln\left(\frac{C}{C_0}\right) = -k't \quad (2)$$

$$\text{Pseudo-Second-order model: } \frac{dC}{dt} = -k''C^2 \quad (3)$$

$$\text{Intregated from: } \frac{1}{C_0} - \frac{1}{C} = -k''t \quad (4)$$

Where; C is the color concentration (ADMI), t is the reaction time (minutes), k' is the pseudo-first-order rate constant (min^{-1}), and k" is the pseudo-second-order rate constant ($ADMI^{-1} \cdot min^{-1}$).

Because samples were filtered prior to treatment, the reported kinetics emphasize the dissolved/colloidal color fraction under reduced light-scattering conditions. At full scale, pre-filtration is typically included upstream of UV to protect lamps and improve UV transmittance; nevertheless, performance on unfiltered effluent may be lower due to shielding by suspended solids. Accordingly, design for building-scale reuse should include a basic 1-5 µm pre-filter ahead of the UV/H_2O_2 unit, and site-specific performance testing is recommended.

2.7 Cost calculation (reagent-only)

The reported cost covers H_2O_2 only. Doses are expressed as mg/L of pure H_2O_2. For pricing with 50% w/w commercial stock, the required stock mass per cubic meter is:

$$m_{stock,50\%} = \frac{D \times 10^{-3}}{0.50} \left(kg/m^3\right) \quad (5)$$

And the reagent cost is:

$$C_{H_2O_2} = m_{stock,\ 50\%} \times P_{50\%} \left(THB/m^3\right) \quad (6)$$

Where; D is the pure- H_2O_2 dose (mg/L) and $P_{50\%}$ is the market price of 50% w/w H_2O_2 (THB/kg). If a different stock strength is procured on site, replace 0.50 by the corresponding mass fraction p. Calculations were performed in Microsoft Excel and reported to three significant figures. All THB values were converted to USD using an exchange rate of 32.4 THB=1 USD on 16 June 2025.

2.8 Data analysis

All data processing and plotting were performed in Microsoft Excel (Home edition). Replicate measurements are reported as mean±standard deviation (SD) with n=3. Fits were performed by ordinary least squares in Excel on the linearized kinetic models. Model selection used R^2 and residual patterns. Numerical results are rounded to three significant figures.

3. RESULTS AND DISCUSSION

3.1 Characteristic of color reduction

Color dropped quickly in the first 3-5 min at all H_2O_2 doses. At 5 min, 100 mg/L removed >65% of color, and the best case was 76% at 10 min with 333 mg/L (Figure 2). The fast early drop likely occurs because hydroxyl radicals quickly attack the color-forming compounds. After that, removal slows as the easiest compounds are used up and other substances in the water compete for radicals. Raising H_2O_2 from 33 to 167 mg/L clearly improves removal at 3-5 min but increasing to 333 mg/L gives only a small extra benefit by 10 min, indicating diminishing returns at higher dose.

These trends are consistent with previous UV/H_2O_2 reports on secondary effluents and dye-laden wastewaters, which often show fast initial decolorization followed by slower tails (Park et al., 2005; Puspita et al., 2011; Sugha and Bhatti, 2022; Son et al., 2024). Here, a household low-pressure UV unit still achieved operationally relevant decolorization within minutes, supporting building-scale non-potable reuse where short retention and simple equipment are preferred. The time-course data in Figure 2 were subsequently used for kinetic fitting in Section 3.2, which quantifies the observed behavior. In contrast, the H_2O_2-only control (without UV irradiation) showed no measurable color loss at any dose (results not shown).

In addition, visible color disappearance was observed in the water samples, consistent with the study's objectives (Figure 3). For example, at 100 mg/L H_2O_2, the water sample appeared colorless after just 3 minutes of UV irradiation, corresponding to a color value of 11 ADMI or 54% removal (Figure 3(a)).

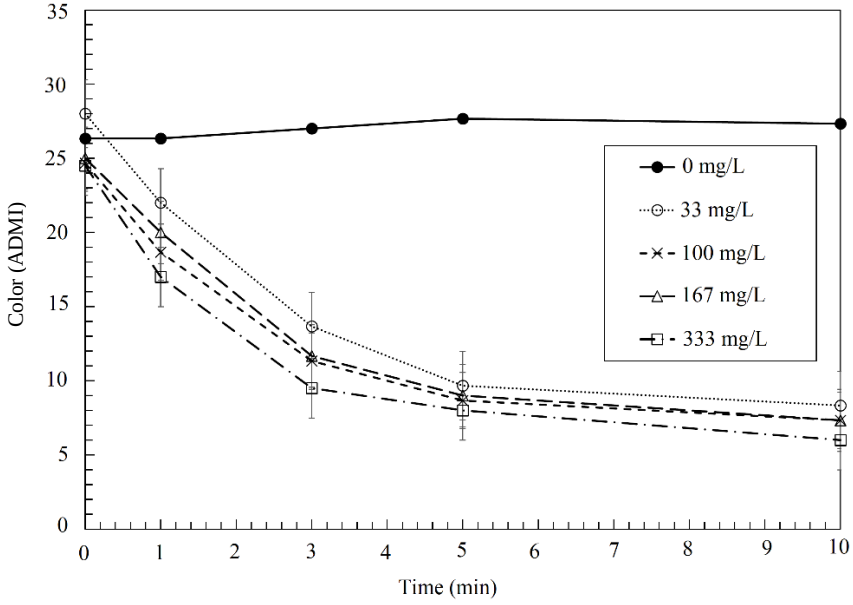

Figure 2. Color of the treated wastewater samples using UV/H_2O_2. Error bars show±SD (n=3). (Data shown as ADMI; initial values differ by plant (as shown in Table 1).

In practical terms, it is important to note that typical UV systems for water and wastewater disinfection are designed with retention times of approximately 30 to 60 seconds to effectively inactivate viruses (Tchobanoglous et al., 2003). Based on the experimental results, the decolorization reaction showed minimal changes after 5 minutes. Furthermore, the combination of H_2O_2 and UV irradiation for just 3 to 5 minutes was sufficient to render the water visibly colorless (Figure 3). Therefore, an irradiation time of 3 to 5 minutes (equivalent to 6-10 times the typical UV disinfection retention time) may be considered a practical design choice for UV systems targeting color removal, balancing efficiency with energy consumption and operational cost. No significant changes were observed in other parameters, including pH, conductivity, and turbidity, across all samples after irradiation. The visual panels (Figure 3(a-b)) emphasize that low H_2O_2 doses (33-100 mg/L) are sufficient to remove visible color within 3-5 min; the 333 mg/L performance is shown quantitatively in Figure 2.

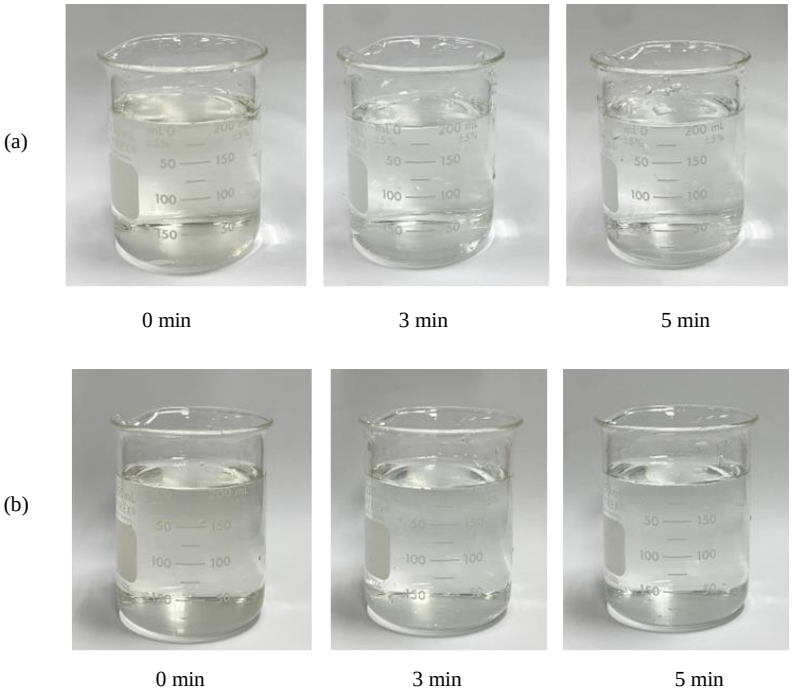

Figure 3. Comparison of the color of treated wastewater and color removal using H_2O_2 in combination with UV irradiation a) 100 mg/L of H_2O_2 and b) 33 mg/L of H_2O_2.

3.2 Chemical kinetics

Experiments were conducted under fixed conditions (Low-pressure lamp UV 254 nm, 16 W; neutral pH; ambient temperature at 25-30°C). Within this setting, we assess peroxide effects as observed trends rather than statistical claims. Time-course data are presented as absolute ADMI. Kinetic fits were obtained from the linearized forms $\ln(C/C_0)$ vs time for pseudo-first order model and $(1/C-1/C_0)$ vs time pseudo-second order model using the run-specific C_0 as mentioned in section 2.6. Linearized plots of $\ln(C/C_0)$ versus time and $(1/C_0-1/C)$ versus time are shown in Figure 4(a) and Figure 4(b), respectively. Across all H_2O_2 doses, the pseudo-second order model provided consistently higher R^2 (0.953-0.966) than pseudo-first order (0.909-0.921) with more uniform residuals; therefore, pseudo-second order was selected for reporting and interpreted as apparent bimolecular control under our conditions (Park et al., 2005; Puspita et al., 2011; Sugha and Bhatti, 2022; Son et al., 2024). Linear regression analysis was conducted for both kinetic models, and the calculated rate constants are presented in Table 2. To maintain readability, R^2 of all fitted models are reported in Table 2 rather than overlaid on Figure 4; the figure displays the fitted lines, while Table 2 lists the numerical parameters. Across the tested range, increasing H_2O_2 from 33 to 167 mg/L was associated with higher fitted pseudo-Second order rate constants, while the increment to 333 mg/L gave only modest additional gain (Table 2). We therefore describe a positive dose-response trend under the fixed UV setting; formal significance testing

was not performed in this screening study. A limitation of this study is that lamp irradiance was not measured; while this does not affect the within-study kinetic comparisons at a fixed setting, inter-laboratory reproducibility will benefit from reporting irradiance/fluence in future pilots.

Higher lamp power/UV fluence generally accelerates decolorization at fixed contact time, as reported for treated effluents and dye-rich matrices (Caretti and Lubello, 2010; Puspita et al., 2011; Sugha and Bhatti, 2022; Son et al., 2024). At neutral pH, bicarbonate or carbonate and natural organic matter can scavenge ·OH, moderating apparent kinetics (Park et al., 2005; Puspita et al., 2011). Tests here were at 25-30°C; temperature can modestly enhance rates but was not isolated. A future design-of-experiments study will explicitly vary UV fluence (lamp power), H_2O_2 dose, pH, and temperature to quantify main/interaction effects and optimize performance.

Table 2. Kinetic constants of pseudo-first order and pseudo-second order

H_2O_2 (mg/L)	Pseudo-First order constant		Pseudo-Second order constant	
	k' (min^{-1})	R^2	k'' ($ADMI^{-1}·min^{-1}$)	R^2
33	0.147	0.918	0.010	0.954
100	0.148	0.910	0.011	0.953
167	0.147	0.921	0.011	0.963
333	0.169	0.909	0.014	0.966

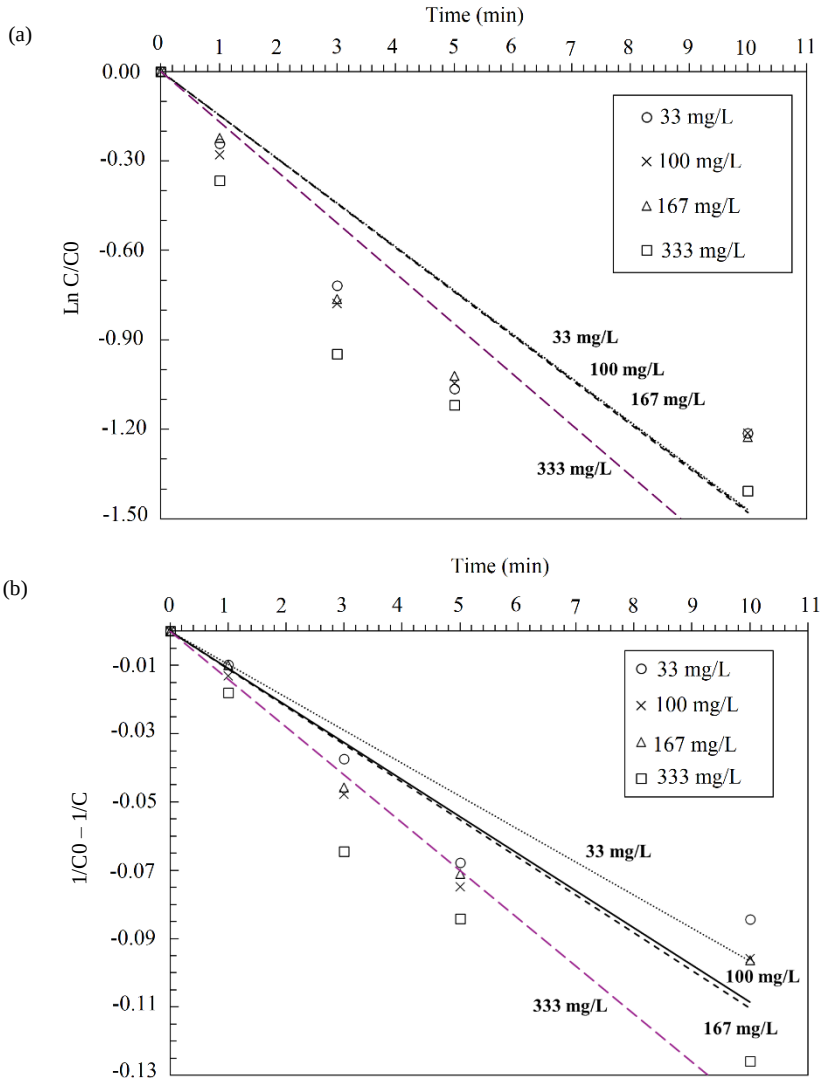

Figure 4. Reaction kinetic models (a) Pseudo-First order reaction and (b) Pseudo-Second order reaction. Rate constants and R^2 for all fits are provided in Table 2

The high coefficient of determination (R^2>0.95) indicates that the reaction kinetics in this study closely follow the pseudo-second-order model, consistent with findings from previous research (Zawadzki and Deska, 2021). This model suggests that the rate of color removal is influenced by both the concentration of hydroxyl radicals and the concentration of color, implying a bimolecular reaction mechanism, which indicates the involving of both concentration on hydroxyl radical and color. Such behavior typically occurs when the concentration of hydroxyl radical changes throughout the reaction. Hydroxyl radicals in this process are primarily generated through the photolysis of H_2O_2 under UV irradiation. The strong fits to the pseudo-second order model (Table 2) indicate apparent bimolecular behavior, where the observed rate reflects both chromophore concentration and the effective ·OH exposure (Park et al., 2005; Puspita et al., 2011). Under our fixed UV condition, the positive dose-response is consistent with increased radical availability (Caretti and Lubello, 2010; Sugha and Bhatti, 2022). However, other variables—not varied here—also influence rates, including UV fluence/lamp power (Son et al., 2024), pH and radical scavenging by carbonate and natural organic matter (Sugha and Bhatti, 2022), and temperature (Park et al., 2005). We therefore interpret the peroxide effect as a trend specific to these operating conditions. Despite these complexities, the primary aim of this study is to evaluate the effectiveness of the UV/H_2O_2 process in eliminating residual color from treated wastewater. The results presented in the previous section demonstrate that this widely available UV equipment exhibits sufficient performance to achieve this objective. Moreover, the proposed kinetic model offers a practical foundation for future engineering applications in water reused processes. However, matrix constituents (e.g., NOM/DOC) can scavenge radicals and reduce UV transmittance, moderating apparent rates under otherwise identical conditions.

3.3 Comparison with previous studies

Under a fixed Low pressure UV setting (254 nm, 16 W; neutral pH; ambient 25-30°C), this study achieved >65% color removal at 5 min with 100 mg/L H_2O_2 and around 76% at 10 min with 333 mg/L. The pattern—rapid early decolorization followed by diminishing gains at longer contact/higher dose—is consistent with UV/H_2O_2 behavior reported for municipal secondary effluents and dye-laden matrices, where fast radical attack on chromophores is followed by slower tails due to scavenging and depletion of the most reactive moieties (Park et al., 2005; Caretti and Lubello, 2010; Puspita et al., 2011; Sugha and Bhatti, 2022). Recent work on actual textile wastewater under optimized fluence and higher peroxide has shown very high ultimate decolorization (Son et al., 2024); by contrast, our household-UV configuration emphasizes short retention and simple hardware for building-scale effluent reuse, yielding practically meaningful removal within minutes. Table 3 compares UV/H_2O_2 color-removal performance reported in prior studies with the results of the present study. The reviewed studies vary in wastewater type, H_2O_2 concentration, UV exposure conditions, and irradiation time. Reported decolorization efficiencies range from approximately 78% to over 99%, depending on experimental setups (Park et al., 2005; Caretti and Lubello, 2010; Puspita et al., 2011; Sugha and Bhatti, 2022; Son et al., 2024).

In this study, approximately 65% color removal was achieved within 5 minutes using 100 mg/L H_2O_2 and a household-scale low-pressure UV system treating municipal wastewater. This performance is comparable to other studies on treated municipal or domestic effluents—for example, Caretti and Lubello (2010) reported 80-90% removal within 10 minutes at 50 mg/L H_2O_2, while Puspita et al. (2011) and Park et al. (2005) achieved >90% removal after 20-30 minutes of treatment at high-energy lamp. Despite the relatively simple and low-energy setup used in this work, the efficiency falls within the reported range, highlighting the practicality of the UV/H_2O_2 process for decentralized color removal in non-potable water reuse. In comparison, studies using industrial wastewaters—such as textile effluents—report higher color removal (>99% removal) but typically require longer treatment times, higher H_2O_2 doses. These differences emphasize the importance of using the UV/H_2O_2 process with wastewater characteristics and reuse goals. A brief cost perspective for this dose-time window is provided in Section 3.4, where reagent costs are reported in THB and USD (conversion per Section 2.7). For building-scale reuse, a basic pre-filter is typically installed upstream of UV (as used here). A downstream, low-cost polishing step (e.g., granular activated carbon) could target residual chromophores and potentially increase overall color removal and enabling lower H_2O_2 doses with minimal added complexity. Evaluation of such UV/H_2O_2 + GAC trains will be included in future pilot testing.

Table 3. Summary of UV/H_2O_2 color removal performance from previous studies and this work

Study	Sample type	UV lamp	H_2O_2 (mg/L)	Irradiation time (min)	Color removal (%)
Park et al. (2005)	Municipal secondary effluent	75 W	44	20	>90%
Caretti and Lubello (2010)	Municipal secondary effluent	15 W	50	10	80-90%
Puspita et al. (2011)	Municipal secondary effluent	40 W	32	30	>90%
Sugha and Bhatti (2022)	Synthetic dye wastewater	11 W	425	10	65%
Son et al. (2024)	Actual textile wastewater	4 W	170	180	91%
This study	Municipal secondary effluent	16 W	100	5	65%

3.4 Reagent cost (H_2O_2)

Based on the commercial-grade price of H_2O_2 at 50% w/w, the estimated chemical costs for the UV/H_2O_2 process are summarized in Table 4. In this study, the cost of H_2O_2 usage ranged from 1.93 to 19.31 baht per cubic meter of treated wastewater, depending on the applied concentration. The total operational cost of the UV/H_2O_2 process includes the cost of the UV system, electricity consumption, and the H_2O_2 reagent. According to Metropolitan Waterworks Authority (MWA) of Thailand, the starting price of water supplied to large commercial buildings or industrial users is 9.5 baht per cubic meter (Thailand Metropolitan Waterworks Authority (MWA), 2022). In comparison, using 100 mg/L of H_2O_2—identified as an effective concentration in this study—acquires an approximate cost of 5.8 baht per cubic meter, which is considered economically feasible. As discussed in the previous section regarding system sizing, a 3-minute UV retention time, achieving 52-58% color removal (Figure 2), may serve as a reasonable operational target. This design would allow the combined cost of system installation and chemical usage to remain competitive with the price of municipal water supply, supporting practical implementation of the UV/H_2O_2 process for wastewater treatment.

Table 4. Reagent cost of H_2O_2 per m^3 of treated wastewater (priced with 50% w/w stock). Values shown in THB and USD (conversion per Section 2.7)

H_2O_2 concentration (mg/L)	Cost per m^3 of wastewater (THB/m^3)	Cost (USD/m^3)
33	1.9	0.059
100	5.8	0.179
167	9.7	0.300
333	19.3	0.596

Note: Experimental dosing used 30% w/w H_2O_2, but costs are normalized to pure H_2O_2 and priced using 50% w/w commercial stock (conversion via mass fraction). Reported values represent reagent cost only; electricity and UV capital are excluded.

A recent study by Cai et al. (2020) evaluated various advanced oxidation processes (AOPs) for treating reverse osmosis concentrate from industrial wastewater and reported that the UV/H_2O_2 process had comparatively higher operational costs (1.44 USD/m^3 as 0.30 USD/m^3 for chemical cost) than alternatives like the Fenton process (0.519 USD/m^3), primarily due to energy-intensive UV systems and higher reagent consumption. While such costs may be acceptable in large-scale industrial treatment, they can be prohibitive in small-scale or building-scale applications. In contrast, this study demonstrates that using a simple, low-pressure household UV system and 100 mg/L of H_2O_2 achieves 65% color removal within 5 minutes at a cost of approximately 5.8 THB/m^3 (USD ~0.179/m^3) for chemical cost. These results emphasize the economic feasibility of the UV/H_2O_2 process for decentralized municipal wastewater reuse, especially in urban buildings where cost-efficiency and operational simplicity are essential.

In Thailand, treated wastewater is typically discharged into public sewer systems. However, increasing environmental concerns and growing water scarcity have heightened public awareness and interest in sustainable practices, such as water reclamation, water reuse, and green building initiatives. Over the past several years, recycling treated wastewater has gained significant attention. Many large buildings equipped with on-site wastewater treatment systems—such as condominiums, shopping malls, and government buildings—are now exploring the reuse of treated wastewater to reduce dependence on the public water supply. The initial strategy focuses on utilizing reclaimed water for non-potable purposes, such as landscape irrigation, floor washing, toilet flushing, and other activities where direct human contact is minimal. Nevertheless, the light-yellow coloration often present in treated wastewater raises concerns regarding its acceptability for reuse. Conventional post-treatment methods, including sand filtration,

activated carbon filtration, and chlorine disinfection, are frequently insufficient to effectively remove this residual color. To resolve this issue, advanced treatment methods, such as ultrafiltration (UF), have been recommended. Although UF is highly effective in color removal, it involves high capital investment and requires intensive maintenance, which creates wastewater during washing the membrane. An alternative approach involves the application of the UV/H_2O_2 advanced oxidation process. While this method requires scaling up the UV system to approximately six times its standard size, the overall capital cost remains lower than that of ultrafiltration. Furthermore, unlike UF, which still requires a separate disinfection step, the UV/H_2O_2 process simultaneously achieves both color removal and effective disinfection. Therefore, the UV/H_2O_2 process represents a practical, efficient, and cost-effective solution for color removal, making it a promising option for the reuse of treated municipal wastewater in large buildings. Furthermore, its modularity, low maintenance requirements, and absence of waste residuals offer practical advantages over conventional technologies, especially in urban settings promoting sustainable and decentralized water reuse.

To contextualize costs relative to common reuse trains, recent technology-economic assessments report operating expenditures (OPEX) for tertiary ultrafiltration (UF) polishing of \$0.129-\$0.152/m^3 (converted from 0.11-0.13 €/m^3), whereas full-scale ozonation-based tertiary treatment is \$1.01-\$2.85/m^3 (converted from 0.86-2.44 €/m^3) (Clem and Mendonça, 2022; Echevarría et al., 2022). These ranges reflect the higher capital intensity and energy/oxidant demand characteristic of membrane and ozone systems. By comparison, the household-scale UV/H_2O_2 configuration evaluated here—achieving ≈65% color removal in 5 min with 100 mg/L H_2O_2—yields an estimated treatment cost of ≈\$0.179/m^3 (converted from 5.8 THB/m^3), which is competitive for building- or campus-level non-potable reuse where simplicity, modularity, and low maintenance are priorities.

While our analysis centers on reagent-only cost for a compact UV/H_2O_2 step, literature indicates that membrane polishing (e.g., UF) and ozonation-based trains generally carry higher capital intensity and/or energy/oxidant demand at full scale; see cited studies for comparative ranges and drivers (Caretti and Lubello, 2010; Cai et al., 2020). Our screening window (≤167 mg/L H_2O_2; 3-5 min) is therefore intended as a low-complexity option for building-level reuse, with full TEA (energy + lamp replacement) to be developed in future work.

3.5 Regulatory context for non-potable reuse

Non-potable reuse for building or district applications (e.g., toilet/urinal flushing, laundry, street cleaning) is typically governed by "fit-for-purpose" specifications that target microbiological safety, clarity, and operational reliability. Representative criteria compiled by the USEPA and state programs include (USEPA, 2024):

- Microbiological: Total coliform ≤2.2 MPN·100 m/L (7-day median) with 23 MPN·100 m/L single-sample maximum for Class A reclaimed water; demonstration of ≥4-log virus removal/inactivation via treatment and disinfection.
- Clarity (Turbidity): For coagulation/ filtration treatment, 2 NTU monthly average (5 NTU max); for membrane filtration, 0.2 NTU monthly average (0.5 NTU max).
- Disinfection operation: Free chlorine ≥1 mg/L with ≥30 min contact at peak flow or validated UV disinfection dose meeting target log-credits.

For onsite (single-building) non-potable reuse, USEPA resources emphasize end-use specific controls and, in some local authorities, conformance with product standards such as NSF/ANSI 350 for graywater systems; similar "fit-for-purpose" principles guide centralized non-potable reuse categories summarized in the EPA's REUSExplorer (USEPA, 2024). For irrigation-type end uses, ISO 16075 provides international guidance on project design and monitoring for the safe use of treated wastewater, complementing WHO risk-based approaches (International Organization for Standardization, 2020). While Thailand's reclaimed-water specifications are evolving, recent reviews indicate growing interest and pilots in municipal reuse. Therefore, we present the above criteria as representative targets for Thai urban/building contexts, consistent with non-potable reuse benchmarks discussed in previous studies in Thailand (Chiemchaisri et al., 2015; Kanchanapiya and Tantisattayakul, 2022).

Residual H_2O_2 naturally decomposes to H_2O and O_2 in typical effluents. In practice, several treatment systems include a short post-UV residence time, so the residual is non-detectable before distribution. Because lamp-based UV/H_2O_2 provides

no disinfectant residual—and this study did not measure residual H_2O_2 or microbiological indicators—regrowth control is treated as an operational matter (e.g., storage turnover, light-blocking storage tanks, routine sanitation) in line with non-potable reuse practice. These controls, together with residual/microbial monitoring, will be verified in future pilot testing.

4. CONCLUSION

This study evaluated color removal from treated municipal wastewater using a household low-pressure UV unit (254 nm, 16 W) combined with H_2O_2 under neutral pH and ambient temperature (25-30°C). Color decreased rapidly within the first 3-5 min across doses, with >65% removal at 5 min for 100 mg/L H_2O_2 and a maximum of ~76.0% at 10 min for 333 mg/L. Linearized kinetic fitting showed that the pseudo-second-order model (R^2≈0.953-0.966) described the data better than the pseudo-first-order model (R^2≈0.909-0.921), indicating apparent bimolecular behavior under the tested conditions.

A screening-level cost calculation (reagent-only, priced using 50% w/w commercial H_2O_2) yielded 1.90, 5.80, 9.70, and 19.3 THB/m^3 at 33, 100, 167, and 333 mg/L, respectively; using 32.4 THB=1 USD (Section 2.7), these correspond to 0.059, 0.179, 0.300, and 0.596 USD/m^3. These values reflect chemical reagent cost only; electricity and UV capital were not included.

Results were obtained at a fixed lamp power with pre-filtration, neutral pH, and ambient temperature. Microbiological indicators were not measured, and the cost analysis excluded energy and capital. Accordingly, conclusions are limited to color removal performance, kinetic description, and reagent cost under the reported conditions. Residual H_2O_2 was not measured; future pilot work will apply a post-UV holding step and verify non-detectable residual prior to reuse. No microbiological enumeration or regrowth assessment was performed; these will be included in future pilot studies.

ACKNOWLEDGEMENTS

The authors would like to express their sincere gratitude to the Department of Civil Engineering and the Department of Civil and Environmental Engineering Technology, King Mongkut's University of Technology North Bangkok, for providing laboratory facilities and academic support throughout this study. Special thanks are extended to the Drainage and Sewerage Department, Bangkok Metropolitan Administration (BMA), for providing the treated wastewater samples and relevant data used in this research. The collaboration and support from all institutions involved are deeply appreciated.

AUTHOR CONTRIBUTIONS

Conceptualization, Manoonpong K, Jiemvarangkul P; Methodology, Phumphuang C, Jiemvarangkul P; Writing-Original Draft Preparation, Phumphuang C, Jiemvarangkul P; Writing-Review and Editing, Manoonpong K, Jiemvarangkul P; Project Administration, Jiemvarangkul P.

DECLARATION OF CONFLICT OF INTEREST

The authors declare that they have no known competing financial interests or personal relationships that could have appeared to influence the work reported in this paper.

REFERENCES

Afonso-Olivares C, Fernández-Rodríguez C, Ojeda-González RJ, Sosa-Ferrera Z, Santana-Rodríguez JJ, Rodríguez JMD. Estimation of kinetic parameters and UV doses necessary to remove twenty-three pharmaceuticals from pre-treated urban wastewater by UV/H_2O_2. Journal of Photochemistry and Photobiology A: Chemistry 2016;329:130-8.

Barloková D, Ilavský J, Sedláková J, Matis A. Removal of Humic Substances from Water with Granular Activated Carbons. Engineering Proceedings; 2023.

Bangkok Master Plan (BMA). Bangkok State of the Environment Report 2022. Bangkok: Department of Environment, Bangkok Metropolitan Administration; 2022.

Cai QQ, Wu MY, Li R, Deng SH, Lee BCY, Ong SL, et al. Potential of combined advanced oxidation - Biological process for cost-effective organic matters removal in reverse osmosis concentrate produced from industrial wastewater reclamation: Screening of AOP pre-treatment technologies. Chemical Engineering Journal 2020;389:Article No. 123419.

Caretti C, Lubello C. Experimental study on colour removal from textile wastewaters using the H_2O_2/UV process with low- and medium-pressure lamps. Water Science and Technology: Water Supply 2010;10(4):Article No. 638.

Chiemchaisri C, Chiemchaisri W, Prasertkulsak S, Hamjinda NS, Kootatep T, Itonaga T, et al. Evaluation of treated sewage reuse potential and membrane-based water reuse technology for the Bangkok Metropolitan area. Water Science and Technology 2015;72(11):1954-61.

Clem V, Mendonça HV. Ozone reactor combined with ultrafiltration membrane: A new tertiary wastewater treatment system for reuse purpose. Journal of Environmental Management 2022;315:Article No. 115166.

Duckett D, Troldborg M, Hendry S, Cousin H. Making waves: Promoting municipal water reuse without a prevailing scarcity driver. Water Research 2024;249:Article No. 120965.

Echevarría C, Pastur M, Valderrama C, Cortina JL, Vega A, Mesa C, et al. Techno-economic assessment of decentralized polishing schemes for municipal water reclamation and reuse in the industrial sector in costal semiarid regions: The case of Barcelona (Spain). Science of the Total Environment 2022;815:Article No. 152842.

Institute for Environment and Sustainability. Water Reuse in Europe-Relevant Guidelines, Needs for and Barriers to Innovation. Luxembourg: Publications Office of the European Union; 2014.

International Organization for Standardization. ISO 16075-1:2020 Guidelines for Treated Wastewater Use for Irrigation Projects-Part 1: The basis of a reuse project for irrigation. Geneva: ISO; 2020.

Jennifer Z-A, Sonia A-D, Francesca E-B, Nadia F-M, Suanny M-R. Advanced oxidation processes by UV/H_2O_2 for the removal of anionic surfactants in a decentralized wastewater treatment plant in Ecuador. Water Science and Technology 2024;90(8):2340-51.

Kanchanapiya P, Tantisattayakul T. Wastewater reclamation trends in Thailand. Water Science and Technology 2022;86(11):2878-911.

Kim BJ, Choi J-Y, Lee H-J, Lee C. Elimination of DOC in RO concentrate from a wastewater reclamation plant: Cost comparison of different AOPs. Environmental Engineering Research 2023;28(4):Article No. 220598.

Kim I, Yamashita N, Tanaka H. Photodegradation of pharmaceuticals and personal care products during UV and UV/H2O2 treatments. Chemosphere 2009;77(4):518-25.

Knap-Bałdyga A, Żubrowska-Sudoł M. Natural organic matter removal in surface water treatment via coagulation—Current issues, potential solutions, and new findings. Sustainability 2023;15(18):Article No. 13853.

Kumari H, Sonia, Suman, Ranga R, Chahal S, Devi S, et al. A Review on Photocatalysis Used For Wastewater Treatment: Dye Degradation. Water, Air, and Soil Pollution 2023;234(6):Article No. 349.

Lhotský O, Krákorová E, Mašín P, Žebrák R, Linhartová L, Křesinová Z, et al. Pharmaceuticals, benzene, toluene and chlorobenzene removal from contaminated groundwater by combined UV/H_2O_2 photo-oxidation and aeration. Water Research 2017;120:245-55.

Luo Y, Guo W, Ngo HH, Nghiem LD, Hai FI, Zhang J, et al. A review on the occurrence of micropollutants in the aquatic environment and their fate and removal during wastewater treatment. Science of the Total Environment 2014;473-474:619-41.

Tchobanoglous G, Burton FL, Stensel HD. Wastewater Engineering: Treatment and Reuse. 4th ed. Boston McGraw-Hill; 2003.

Miguel EdSC, Machado BS, Teles APS, da Silva TF, Magalhães Filho FJC, Cavalheri PS. Optimizing sewage treatment by UV/H_2O_2 process and vertical flow constructed wetland integration. Journal of Water Process Engineering 2024;64:Article No. 105580.

Morrison CM, Hogard S, Pearce R, Mohan A, Pisarenko AN, Dickenson ERV, et al. Critical review on bromate formation during ozonation and control options for its minimization. Environmental Science and Technology 2023;57(47):18393-409.

Mukherjee J, Lodh BK, Sharma R, Mahata N, Shah MP, Mandal S, et al. Advanced oxidation process for the treatment of industrial wastewater: A review on strategies, mechanisms, bottlenecks and prospects. Chemosphere 2023;345:Article No. 140473.

Pamuła J, Karnas M, Paluch A, Styszko K. Comparative study on classical and modified UV/H_2O_2 and Fenton reaction based methods for the removal of chemical pollutants in water treatment. Desalination and Water Treatment 2022;275:92-102.

Papić S, Koprivanac N, Bozić AL, Vujević D, Dragicević SK, Kusić H, et al. Advanced oxidation processes in azo dye wastewater treatment. Water Environment Research 2006;78(6):572-9.

Park K-Y, Ahn K-H, Kim K-P, Kweon JH,Maeng S-K. Characteristics and treatability of persistent colors in biologically treated wastewater effluents. Environmental Engineering Science 2005;22(5):557-66.

Puspita P, Roddick FA, Porter NA. Decolourisation of secondary effluent by UV-mediated processes. Chemical Engineering Journal 2011;171(2):464-73.

Royal Gazette. Notification of the Ministry of Industry Re: Effluent Discharge Standards from Factories B.E. 2560. Volume 134. Bangkok, Thailand: Ministry of Industry; 2017 (in Thai).

Royal Gazette. Notification of the Ministry of Natural Resources and Environment Re: Effluent Discharge Standards for Certain Types and Sizes of Buildings B.E. 2535. Volume 135. Bangkok, Thailand: Ministry of Natural Resources and Environment; 2018 (in Thai).

Son C-Y, Kang J-K, Lee Y-J, Lee C-G, Kim J, Park S-J, et al. Degradation of residual dyes in actual textile wastewater using UV/H_2O_2: Evaluation of the impact of operating variables through multi-layer perceptron analysis. Environmental Engineering Research 2024;29(5):Article No. 230716.

Sugha A, Bhatti MS. Degradation of methylene blue dye by UV/H_2O_2 advanced oxidation process: Reaction kinetics, residual H_2O_2 and specific energy consumption evaluation. Desalination and Water Treatment 2022;274:297-307.

Thailand Metropolitan Waterworks Authority (MWA). Service-rate [Internet]. 2022 [cited 26 June 2025]. Available from: https://www.mwa.co.th/services/users-should-know/users-service-rate/service-rate/.

United States Environmental Protection Agency (USEPA). Method 110.1: Color by Spectrophotometry. L. National Exposure Research. Cincinnati, OH: U.S. Environmental Protection Agency; 1978.

United States Environmental Protection Agency (USEPA). REUSExplorer: Summary of Washington's Water Reuse Guideline/Regulation for Centralized Non-Potable Reuse [Internet]. 2024 [cited 26 June 2025]. Available from: https://www.epa.gov/reuse/reusexplorer.

Yang K, Abu-Reesh IM, He Z. Domestic wastewater treatment towards reuse by "self-supplied" microbial electrochemical system assisted UV/H_2O_2 process. Water Research 2024;267:Article No. 122504.

Zawadzki P, Deska M. Degradation efficiency and kinetics analysis of an advanced oxidation process utilizing ozone, hydrogen peroxide and persulfate to degrade the dye Rhodamine B. Catalysts 2021;11(8):Article No. 974.

Zhang J, Li G, Yuan X, Li P, Yu Y, Yang W, et al. Reduction of ultrafiltration membrane fouling by the pretreatment removal of emerging pollutants: A review. Membranes (Basel) 2023;13(1):Aticle No. 77.

Ziembowicz S, Kida M. Limitations and future directions of application of the Fenton-like process in micropollutants degradation in water and wastewater treatment: A critical review. Chemosphere 2022;296:Article No. 134041.

Environment and Natural Resources Journal

Volume 24
Issue 1
2026

Population Density Estimation of Hornbills in the Eastern Part of Huai Kha Khaeng Wildlife Sanctuary, Thailand

Thanapong Fueakong[1], Warong Suksavate[1], Anak Pattanavibool[2], Pornkamol Jornburom[3], Kwanchai Waitanyakarn[3], Apinya Saisamorn[3], Pannita Neepai[1], and Ronglarp Sukmasuang[1*]

[1]Department of Forest Biology, Faculty of Forestry, Kasetsart University, Chatuchak, Bangkok 10900, Thailand
[2]Department of Conservation, Faculty of Forestry, Kasetsart University, Chatuchak, Bangkok 10900, Thailand
[3]Wildlife Conservation Society, Thailand Program, 55/297 Muangthong Thani, Pakkred, Nonthaburi 10210, Thailand

ARTICLE INFO

Received: 11 Apr 2025
Received in revised: 7 Oct 2025
Accepted: 14 Oct 2025
Published online: 12 Nov 2025
DOI: 10.32526/ennrj/24/20250091

Keywords:
Environmental factors/ Density/ Distance sampling/ Hornbills/ QGIS/ Zonal statistics

*** Corresponding author:**
E-mail: mronglarp@gmail.com

ABSTRACT

Hornbills belong to the Bucerotidae Family, and almost all species within this family are vulnerable to extinction. This study examined the population density of four hornbill species in the eastern part of the rainforest of the Huai Kha Khaeng Wildlife Sanctuary. The species studied were the Great Hornbill (*Buceros bicornis* Linnaeus 1758), Rufous-necked Hornbill (*Aceros nipalensis* Hodgson 1829), Wreathed Hornbill (*Rhyticeros undulates* Shaw 1811), and Tickell's Brown Hornbill (*Anorrhinus tickelli* Blyth 1855). Moreover, the study investigated factors influencing hornbill density using distance sampling with point transect methods, as well as the unmarked package in R. The survey was conducted along four 9-km survey lines, covering a total of 36 km, using 45 survey points with 200-m spacing between points. In total, 180 points were surveyed, with each point observed for 10 min. The study was replicated twice, covering an area of approximately 600 km^2, with surveys conducted from November 2023 to January 2024, and again from March 2024 to October 2024. The results showed the following hornbill population densities (individuals/km^2): Great Hornbill 10.16±0.07 (n=108), Rufous-necked Hornbill 5.95±0.07 (n=74), Tickell's Brown Hornbill 4.42±0.03 (n=61), and Wreathed Hornbill 1.52±0.01 (n=22). Factors that significantly influenced hornbill density included elevation, slope, average precipitation, average temperature, and montane forest. These findings contribute to the understanding of hornbill ecology and population dynamics. The results can guide management strategies and promote public awareness of habitat conservation.

HIGHLIGHTS

This study examined the density of four hornbill species: Great Hornbill, Rufous-necked Hornbill, Wreathed Hornbill, and Tickell's Brown Hornbill in the Huai Kha Khaeng Wildlife Sanctuary. The results revealed that the Great Hornbill, Rufous-necked Hornbill, and Tickell's Brown Hornbill had higher densities, whereas the Wreathed Hornbill had a lower density than in previous studies. Factors affecting hornbill densities included elevation, slope, stream, dry evergreen, mixed deciduous, and montane forests, which were critical habitats supporting different hornbill species according to their ecological requirements. In particular, the preservation of large trees is fundamental to sustaining hornbill populations, as nest cavities, food sources, and communal roosting sites represent key limiting resources.

1. INTRODUCTION

Hornbills (Family Bucerotidae) are the largest avian frugivores in Southeast Asia, playing a crucial role in forest ecology through seed dispersal (Jinamoy et al., 2013; Jinamoy et al., 2014). Globally, there are 62 hornbill species, with 32 found in Asia and 30 in Africa (IUCN Hornbill Specialist Group, 2025). Currently, 26 species are classified as Globally Threatened or Near Threatened with extinction, while the remaining species are listed as Least Concern (IUCN, 2025). In Thailand, 13 hornbill species are present (Trisurat et al., 2013; Thailand Hornbill Research Foundation, 2024a), representing approximately 1 in 5 of all hornbill species worldwide.

Citation: Fueakong T, Suksavate W, Pattanavibool A, Jornburom P, Waitanyakarn K, Saisamorn A, Neepai P, Sukmasuang R. Population density estimation of Hornbills in the Eastern Part of Huai Kha Khaeng Wildlife Sanctuary, Thailand. Environ. Nat. Resour. J. 2026;24(1):127-139 (https://doi.org/10.32526/ennrj/24/20250091)

Six hornbill species are found in the Huai Kha Khaeng Wildlife Sanctuary (HKKWS) (Poonswad and Kemp, 1993). There are four Vulnerable species according to the IUCN (2025): Great Hornbill (GH) (*Buceros bicornis*); Rufous-necked Hornbill (RNH) (*Aceros nipalensis*); Wreathed Hornbill (WH) (*Rhyticeros undulatus*), and Plain-pouched Hornbill (*Rhyticeros subruficollis*) IUCN, 2025); also 1 Near Threatened species, Tickell's Brown Hornbill (TBH) (*Anorrhinus tickelli*) (IUCN, 2025); and 1 Least Concern species, the Oriental Pied Hornbill (*Anthracoceros albirostris*). Only four species were found in the survey: the GH, the RNH, the TBH, and the WH. The Plain-pouched Hornbill is found in the southern part of HKKWS, while the Oriental Pied Hornbill is mostly found in the forest edges (IUCN Hornbill Specialist Group, 2025). Neither species was found in the study area. However, hornbill populations have declined significantly in recent years (Annorbah et al., 2016; Wijerathne and Wickramasinghe, 2018; Chaitanya et al., 2024; Monchaithanaphat et al., 2024; Thailand Hornbill Research Foundation, 2024b). As an important part of the ecosystem, hornbills are considered an appropriate proxy for monitoring forest health (Ardiantiono et al., 2020). Hornbills, valued for their conservation importance and key role in forest restoration, rely on natural tree cavities for nesting; therefore, the presence of suitable cavities is vital for their breeding success. (Datta and Rawat, 2004; Jinamoy et al., 2014). Habitat loss and the scarcity of tree cavities are major factors contributing to population declines (Jinamoy et al., 2014). Therefore, population density data provide important insights into the conservation status of a species or target population (Marthy et al., 2016). Establishing density baselines is crucial for wildlife monitoring, enabling researchers to track population trends and evaluate the effectiveness of conservation efforts (Ardiantiono et al., 2020). In addition to species distribution, population abundance and density are important parameters for assessing species status and their responses to forest change and other environmental factors (Callaghan et al., 2024), which vary depending on the natural history and ecological needs of each species. The occurrence of these species in the same area confirms the habitat characteristics and evolutionary relationships that should be studied for a better understanding. Knowledge about population density and environmental relationships for each hornbill species in the area is needed. This study was conducted on four hornbill species found in the high mountain range to the east of the area, where these species have been previously recorded. It also serves as a continuation of hornbill population monitoring in the region, following the work of Jornburom et al. (2010), who reported four hornbill species, namely, GH, RNH, TBH, and WH, using the point transect method. To date, no studies have investigated how these hornbill species respond to environmental variables in this area. This study aimed to address two main hypotheses: (1) changes exist in hornbill population during the non-breeding season, so we need a comparison of hornbill densities between the study area and other regions and (2) there are relationships between the occurrence of each hornbill species and 11 environmental factors, elevation, slope, forest types, normalized difference vegetation index (NDVI), canopy height, precipitation, stream, threat and temperature.

The specific objectives of this study were to estimate hornbill population densities using distance sampling, particularly the point transect method (Tiwari et al., 2021), which can clearly estimate the density, and to identify key environmental variables hypothesized to influence hornbill occurrence using zonal statistics derived from raster analysis in QGIS and the unmarked package (Kellner et al., 2023) within RStudio software. The expected findings will contribute to a deeper understanding of Hornbill ecology and inform future conservation and habitat management strategies.

2. METHODOLOGY

2.1 Ethics statement

This study was conducted with permission from the Department of National Parks, Wildlife and Plant Conservation (DNP) (License No. 0907.404/890, dated Jan 15, 2024).

2.2 Study site

The study area focused on was the eastern part of HKKWS, covering approximately 600 km² of its total area of 2,780 km². HKKWS, a UNESCO World Natural Heritage Site (15°28′16.4″N, 99°13′54.2″E) (Figure 1), is part of the Western Forest Complex (WEFCOM). The sanctuary preserves a pristine forest ecosystem and abundant wildlife, providing habitat for a wide variety of species and essential water and food sources for wildlife, including *Panthera tigris* Linnaeus 1758, *Panthera pardus* Linnaeus 1758, *Elephas maximus* Linnaeus 1758, *Bos javanicus* D'Alton 1823, *Bos gaurus* Smith 1827, *Bubalus arnee* Kerr 1792, *Tapirus indicus* Desmarest 1819, and

Aceros nipalensis Hodgson 1829 (Saisamorn et al., 2024). Forest types include montane, dry evergreen, mixed deciduous, and dry deciduous dipterocarp forests (Trisurat, 2004). Ouithavon et al. (2005) found that the fruits eaten by hornbills belong to the families Moraceae, Myristicaceae, Annonaceae, Meliaceae, and Luaraceae and that the most common trees used for nesting by hornbills in this area are *Dipterocarpus* and *Eugenia* (Poonswad, 1995).

2.3 Data collection

Four 9-km-long survey lines were established in the study area (Figure 1), located in the following areas: (1) Khao Nang Ram Wildlife Research Station, (2) Huai Isa Ranger Station, (3) Wang Pai Ranger Station, and (4) Saiboe Ranger Station. The topography of Khao Nang Ram is primarily covered with mixed deciduous forest, dry evergreen forest, and mountain forest. The Huai Isa and Saiboe areas are covered with dry evergreen forest and hill evergreen forest or mountain forest, respectively. In Wang Phai, the dominant vegetation types are dry evergreen forest and mountain forest. Generally, mountain forest prevails in areas above 1,000 meters above sea level. Lower elevations are dominated by dry evergreen forest, while vegetation in moist areas along streams and valleys may be dominated by moist evergreen forest. Mixed deciduous forests also dominate in the lower elevations. Forty-five survey points were positioned along each line at 200-m intervals (Pawar et al., 2018) to monitor the population of all hornbill species. The locations of the points were recorded using GPS with the UTM coordinate system (Map Datum WGS 84). In total, the survey covered 72 kilometers (four 9-km lines, each with two replications) and included 360 survey points (45 points per line, with two replications) (see Figure 1).

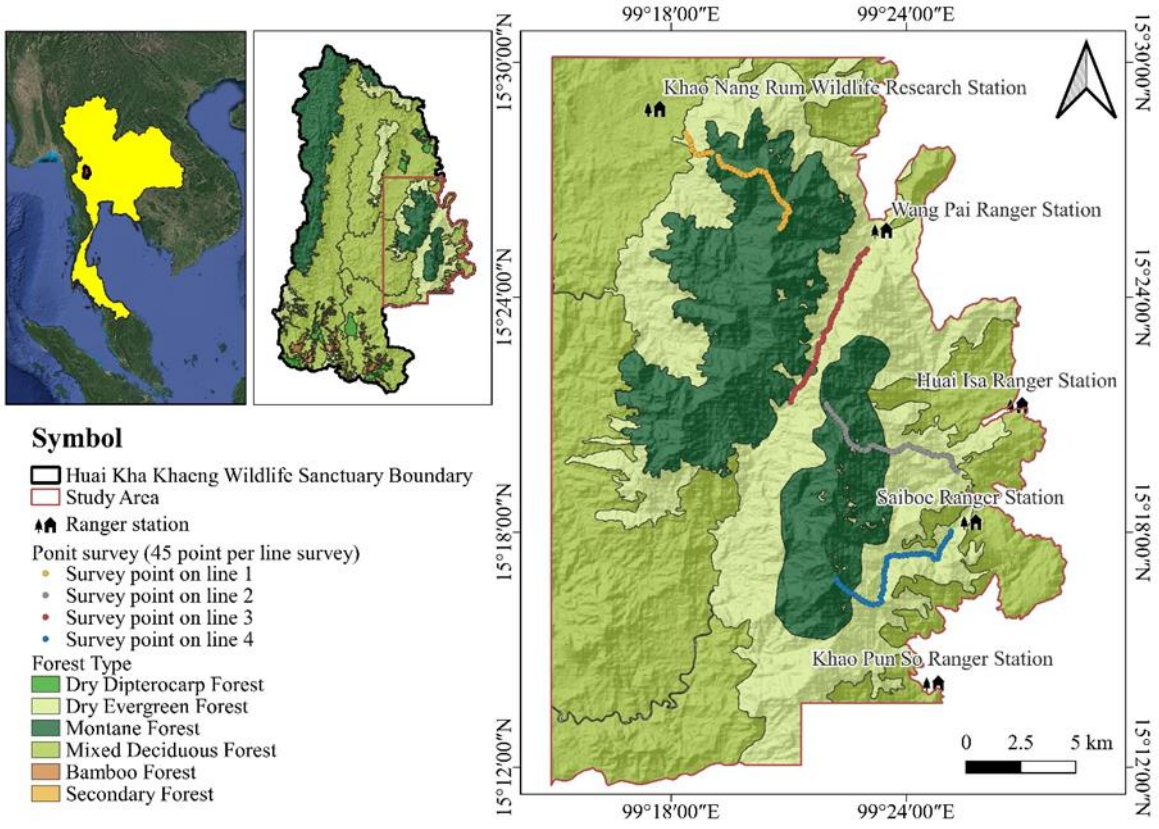

Figure 1. Study area locations in the Eastern part of the Huai Kha Khaeng Wildlife Sanctuary, Thailand

2.4 Population survey

The first survey was conducted primarily during the non-breeding season, from November 2023 to January 2024, and the second from June 2024 to October 2024 (Monchaithanaphat et al., 2024), resulting in two complete replications. The study period was divided into two periods due to the conditions of permission to study in the first period and the exception during the breeding season that occurred in late January to May (Jinamoy et al., 2013).

Surveys were conducted in the morning from 7:00 a.m. to 11:00 a.m. and in the afternoon from 2:00 p.m. to 5:00 p.m. Each survey point was observed for 10 minutes to minimize the risk of double-counting. Since using a survey time of 10 minutes is an appropriate time for population studies and is consistent with the research of Jornburom et al. (2010) used in their research, using too little time may result in an underestimation of the survey population, while using too much time may result in an overestimation of the survey population (Jornburom et al., 2010; Jinamoy et al., 2013; Pawar et al., 2021; Monchaithanaphat et al., 2024).

During data collection, the following information was recorded: (1) hornbill species, (2) detection type (visual or vocal), and (3) estimated distance between the survey point and the hornbill. Since some areas have dense tree canopies, it is not possible to measure distances with a laser rangefinder. Therefore, it is necessary to estimate the hornbill's position from the nearest tree and measure the distance from that tree instead. Sometimes, when moving the survey point, when hornbills are found, even though the data is recorded, it is not included in the density calculation, measured using a laser rangefinder, (4) angle between the survey point and the hornbill, and (5) number of individuals detected. Both visual and vocal detections were used to estimate density, as visibility is often limited in dense canopy forests (Marthy et al., 2016; Ardiantiono et al., 2020). Data were not collected on days with heavy rain, strong winds, or dense fog (Mynott et al., 2021). Hornbills flying over the survey point were recorded but excluded from the density analysis, as accurate distance measurements could not be obtained.

2.5 Data analysis

2.5.1 Population density

Hornbill population density was estimated using the distance sampling method (Chandler, 2020; Monchaithanaphat et al., 2024; Sriprasertsil et al., 2024). The analysis was conducted using a distance sampling model implemented in the unmarked package (version 1.4.3) (Kellner et al., 2023) within RStudio software (version 2024.09.1+394) (RStudio Builds, 2024). Zonal statistics derived from raster analysis in QGIS (version 3.28.13) (QGIS Project, 2024) were used to calculate hornbill density across different forest types: dry evergreen forest, mixed deciduous forest, and montane forest. To estimate the population density of hornbills in this study area, the analysis was performed using R Studio with the unmarked package. After the results were obtained, the density values of each forest type were read using the Zonal statistics tool in QGIS. To identify the most suitable model for the dataset, key detection functions, including half-normal, hazard-rate, and uniform, were evaluated based on the lowest Akaike Information Criterion (AIC) value (Paguntalan et al., 2021; Monchaithanaphat et al., 2024). The detection function curve was truncated at the right tail. Since estimating the distance of a sound is difficult, it relies on measuring the distance from the sound location with a laser rangefinder. To better fit the detection function curve to the survey data, a right truncation of no more than 10% was performed to mitigate bias from imprecise long-distance observations. Environmental factors were removed in a stepwise fashion to determine the best-fitting model for hornbill density estimation.

2.5.2 Environmental factors

Hornbill population density was analyzed in relation to various environmental and climatic factors that influence their distribution and habitat suitability. Key climate variables, such as temperature and precipitation, are critical in determining species distribution, as they directly impact resource availability and biological processes, including reproduction and feeding (Naniwadekar et al., 2020; Monchaithanaphat et al., 2024; Wijerathne et al., 2024). Temperature and precipitation data were obtained from Google Earth Engine for the period January 2023 to October 2024. Average temperature was estimated in relation to land surface conditions derived from the Normalized Difference Vegetation Index (NDVI), following the methodology of Ridho (2023). Average precipitation data were sourced from the Climate Hazards Center InfraRed Precipitation with Station Data (CHIRPS, version 2.0 Final) (USGS, 2024).

Forest type was also considered a key variable, as it directly influences the availability of food and nesting sites, which are factors that significantly affect hornbill populations. Different hornbill species exhibit varying forest type preferences (Patel et al., 2022; Mohd-Azlan et al., 2023). This study employed forest classification data from the Royal Forest Department (2018), which includes montane forest data from 2000 and dry evergreen and mixed deciduous forest data from 2018. In addition, elevation and slope were incorporated as topographic variables influencing

habitat suitability and accessibility. These features also affect water distribution within the habitat, thereby shaping forest structure and wildlife movement patterns (Valderrama-Zafra, 2024). Elevation and slope data were derived from NASA's SRTM Digital Elevation Model at 30 m resolution [Earth Resources Observation and Science (EROS) Center, 2018].

NDVI was used to assess vegetation density, a key indicator of habitat quality. High NDVI values correspond to areas with dense vegetation, which typically offer greater food availability and more suitable nesting sites for hornbills (Setiawana et al., 2023). As hornbills rely heavily on fruiting trees and dense forest canopies, areas with high NDVI values are expected to support larger populations. This highlights the significance of vegetation density in influencing the spatial distribution of hornbills within the study area. Canopy height, representing forest vertical structure, was also included, as it is essential for species that nest in tall, large trees (Chaitanya et al., 2024). NDVI data were sourced from USGS Landsat 9 Level 2, Collection 2, Tier 1 for the period from January 2023 to October 2024 (USGS, 2025).

Streams are vital for the survival of wildlife, significantly influencing the distribution and behavior of species. In HKKWS, streams and other water bodies serve as key foraging habitats for hornbills such as the RNH. At this site, the RNH's diet contains roughly 22% animal matter, including freshwater crabs and frogs (Nepal, 2020; Thailand Hornbill Research Foundation, 2024a). Notably, RNH are often observed feeding on freshwater crabs along stream margins (Nepal, 2020; Saputra, 2024; Thailand Hornbill Research Foundation, 2024a). Data on proximity to human threats, collected by the DNP (2024), offer insights into anthropogenic impacts, such as poaching, habitat degradation, and conservation efforts (Monchaithanaphat et al., 2024; Sriprasertsil et al., 2024). Streams and threat location data were obtained from the DWR (2024) and the DNP (2024), respectively. These datasets were used to calculate distances using QGIS version 3.28.13 (RStudio Builds, 2024) with the r.grow.distance function (GRASS Development Team, 2024). The threat point uses data from January 2023 to October 2024 from the SMART patrol database of the DNP (2024). Together, these factors provide a comprehensive understanding of variables influencing hornbill population density. The contributions of the various data sources are summarized in Table 1 and Figure 2.

3. RESULTS

3.1 Hornbill detection

The results showed that the total number of detections for GH, RNH, TBH, and WH were 191, 74, 61, and 22, respectively. These detections were further categorized into visual detections (108, 18, 54, and 19, respectively) and vocal detections (83, 56, 7, and 3, respectively) (Table 2).

Table 1. Environmental factors used for modelling

Type	Factor name	Code	Data source	Reference from
Climate	Average temperature	TEM	USGS Landsat 9 Level 2, Collection 2, Tier 1	USGS (2025)
	Average precipitation	ARF	Climate Hazards Center InfraRed Precipitation with Station Data (version 2.0 Final)	Funk et al. (2015)
Forest type	Montane Forest	MF	Royal Forest Department (RFD)	RFD (2018)
	Dry Evergreen Forest	DEF		
	Mixed Deciduous Forest	MDF		
Environmental	Elevation	ELV	NASA SRTM Digital Elevation 30 m	Farr et al. (2007)
	Slope	SLP		
	Streams (Distance from nearest stream)	STR	Department of Water Resources (DWR)	DWR (2024)
	Normalized Difference Vegetation Index	NDVI	USGS Landsat 9 Level 2, Collection 2, Tier 1	Cook et al. (2014) USGS (2025)
	Canopy Height	CNP	Global Canopy Height	Tolan et al. (2023)
	Threat (Location of the nearest threat factor)	THR	Department of National Parks, Wildlife and Plant Conservation (DNP)	DNP (2024)

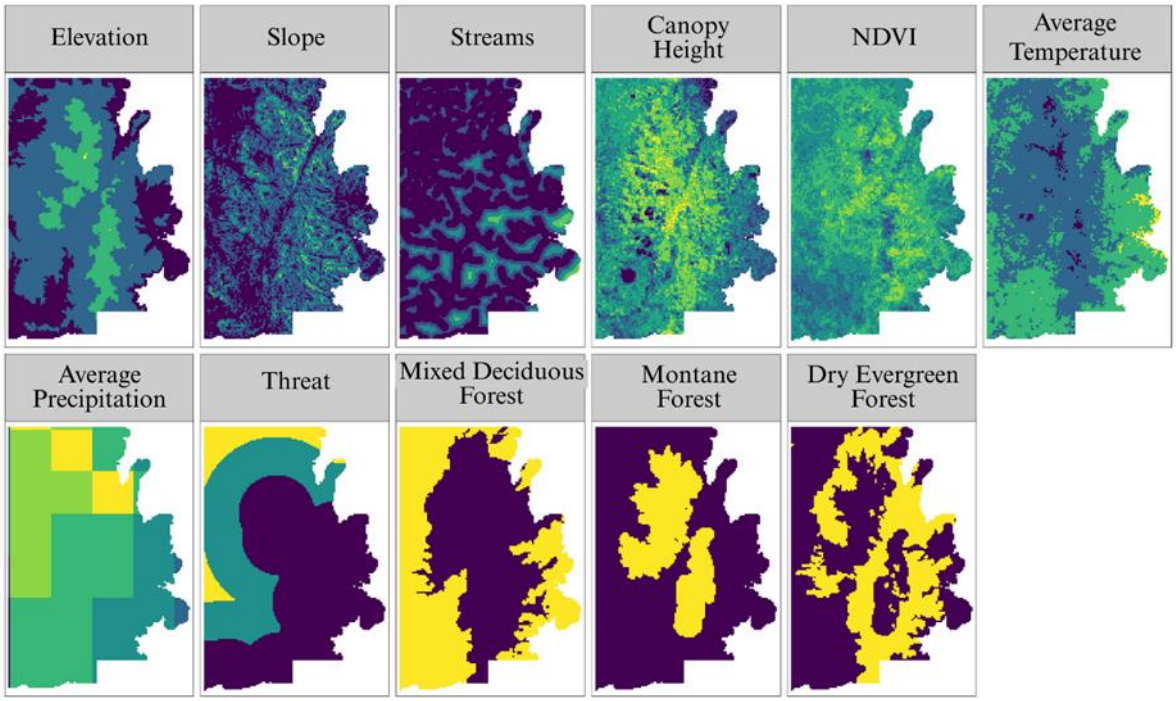

Figure 2. Climate, forest type, and environmental factors in the eastern part of the Huai Kha Khaeng Wildlife Sanctuary, Thailand

Table 2. Observations of hornbills in the eastern part of the Huai Kha Khaeng Wildlife Sanctuary, Thailand, were recorded during the nonbreeding season, spanning from November 2023 to January 2024 and from June 2024 to October 2024.

Hornbill species	Number of detections (Individuals)			%Detection	
	Visual	Vocal	Total	%Visual	%Vocal
Great Hornbill	108	83	191	56.54	43.46
Rufous-necked Hornbill	18	56	74	24.32	75.68
Tickell's Brown Hornbill	54	7	61	88.52	11.48
Wreathed Hornbill	19	3	22	86.36	13.64
Four Hornbill species	199	149	348	57.18	42.82

3.2 Population density

The densities of GH, RNH, TBH, and WH were 10.16, 5.95, 4.42, and 1.52 individuals/km², respectively (Table 3). The study also analyzed hornbill densities across various forest types, including dry evergreen, mixed deciduous, and montane forests. The densities of GH in these forest types were 14.35, 8.85, and 4.07 individuals/km², respectively. RNH densities were 5.94, 6.23, and 5.44 individuals/km², whereas TBH densities were 4.69, 3.73, and 4.75 individuals/km², and WH densities were 1.62, 1.13, and 1.90 individuals/km² (Table 4). In this study, the detection of GH was based on visual observation, while for the other hornbill species, both visual and acoustic observations were used (Ardiantiono et al., 2020). This difference reflects species-specific detection capabilities and methodological limitations during fieldwork.

3.3 Environmental factors affecting the density of hornbill species

The results of the study revealed that the factors that significantly negatively affected the density of GH were Montane Forest (P=0.0003), Average Temperature (P=0.0080), and Average Precipitation (P=0.0115), while the factors that significantly affected negatively the density of RNH were Elevation (P=0.0232), Average Temperature (0.0284), and only a marginal effect for Distance to the Nearest Stream (P=0.0606). In the case of the WH, the factor that significantly affected the density was slope (P=0.0433) (Figure 3 and Table 5).

Table 3. Details of the selected model for hornbill density estimation in the eastern part of the Huai Kha Khaeng Wildlife Sanctuary, Thailand, recorded during the non-breeding season, spanning from November 2023 to January 2024 and from June 2024 to October 2024

Species	Detection	Number of detections (Individuals)	Key function	Right truncation (m)	AIC
Great Hornbill	Visual	108	Half-normal	170	382.83
Rufous-necked Hornbill	Visual and Vocal	74	Hazard	200	471.69
Tickell's Brown Hornbill	Visual and Vocal	61	Half-normal	150	136.17
Wreathed Hornbill	Visual and Vocal	22	Half-normal	100	123.30

Table 4. Population density estimation of four hornbill species in the eastern part of the Huai Kha Khaeng Wildlife Sanctuary, Thailand, during the non-breeding season, from November 2023 to January 2024, and from June 2024 to October 2024

Hornbill species	Density estimation in each area	Density (individuals/km²)	Standard error	95% CI	
				Lower	Upper
Great Hornbill	Study area	10.16	0.07	10.02	10.29
	Dry Evergreen Forest	14.35	0.13	14.10	14.60
	Mixed Deciduous Forest	8.85	0.06	8.74	8.97
	Montane Forest	4.07	0.04	3.98	4.15
Rufous-necked Hornbill	Study area	5.95	0.02	5.91	5.98
	Dry Evergreen Forest	5.94	0.03	5.87	6.00
	Mixed Deciduous Forest	6.23	0.03	6.18	6.28
	Montane Forest	5.44	0.04	5.37	5.52
Tickell's Brown Hornbill	Study area	4.42	0.03	4.35	4.48
	Dry Evergreen Forest	4.69	0.05	4.60	4.78
	Mixed Deciduous Forest	3.73	0.04	3.66	3.81
	Montane Forest	4.75	0.10	4.56	4.94
Wreathed Hornbill	Study area	1.52	0.01	1.50	1.53
	Dry Evergreen Forest	1.62	0.01	1.60	1.64
	Mixed Deciduous Forest	1.13	0.01	1.12	1.15
	Montane Forest	1.90	0.02	1.87	1.93

Table 5. Environmental factors affecting the density of four hornbill species in the eastern part of the Huai Kha Khaeng Wildlife Sanctuary, Thailand, during the non-breeding season, from November 2023 to January 2024, and from June 2024 to October 2024

Hornbill species	Environmental factors affecting the density				
	Environmental factors	AIC	Coefficient	Standard error	p-value
Great Hornbill	Slope (SLP)	382.83	0.228	0.156	0.1450
	Montane Forest (MF)		-0.680**	0.189	0.0003
	Average temperature (TEM)		-0.635**	0.240	0.0080
	Average precipitation (ARF)		-0.539*	0.213	0.0115
Rufous-necked Hornbill	Elevation (ELV)	471.69	-0.572*	0.252	0.0232
	Distance to the Nearest Stream (STR)		0.265	0.141	0.0606
	Average temperature (TEM)		-0.450**	0.205	0.0284
Tickell's Brown Hornbill	Normalized Difference Vegetation Index (NDVI)	136.17	0.609	0.382	0.1108
	Canopy height (CNP)		-0.853	0.583	0.1435
Wreathed Hornbill	Slope (SLP)	123.30	0.514*	0.255	0.0433

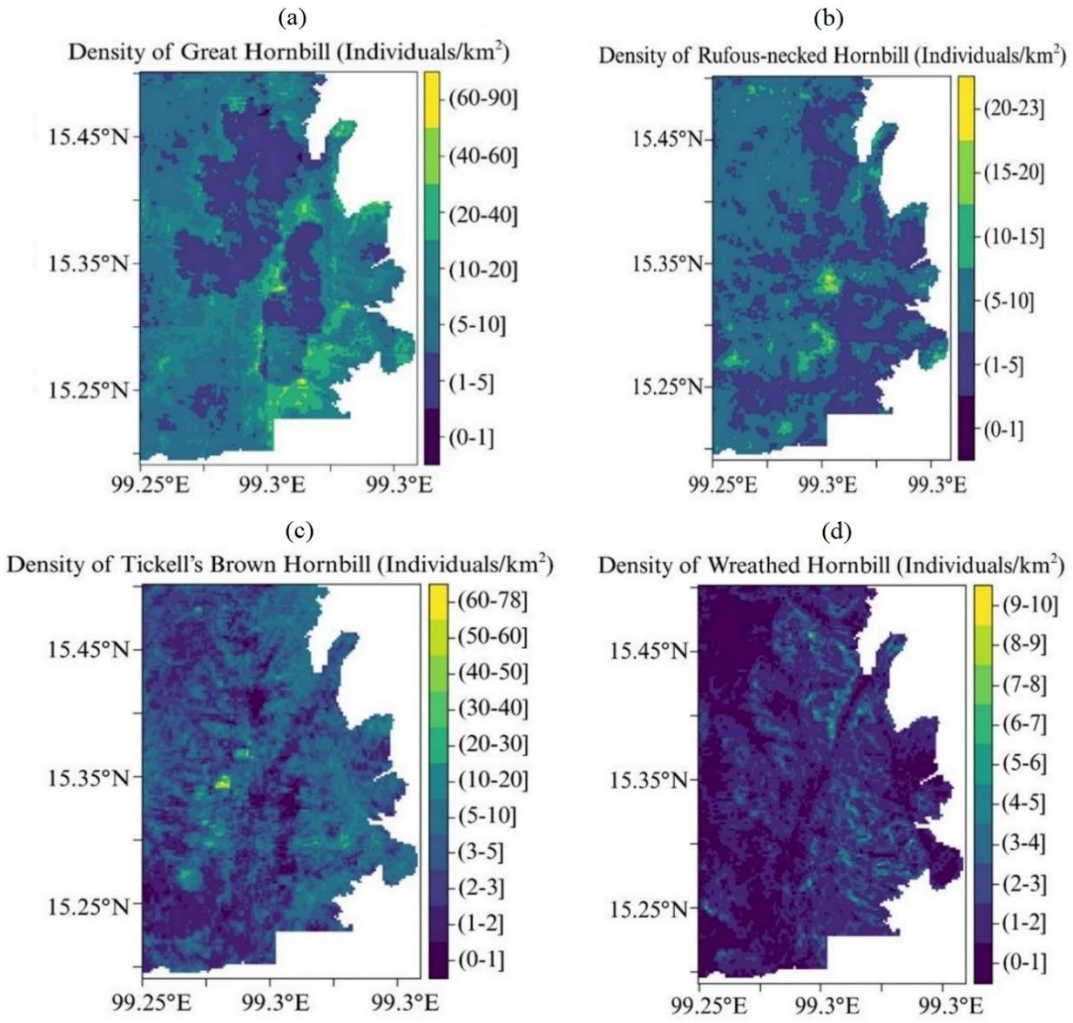

Figure 3. Predicted density (individuals/km^2) of Great Hornbill (a), the Rufous-necked Hornbill (b), the Tickell's Brown Hornbill (c), and the Wreathed Hornbill (d), being density in relation to environmental factors, with 95% confidence interval

4. DISCUSSION

When comparing the results of this study with those of Jornburom et al. (2010), who used the point transect method in the same area, the densities of GH, RNH, and TBH were found to be approximately twice as high as those reported previously. In contrast, the density of WH was more than tenfold lower than reported by both Jornburom et al. (2010) and Naniwadekar and Datta (2013), who recorded 11.47 and 16.1 individuals/km² of WH during the non-breeding season in the study area and the North-East India. However, the WH density in this study was still higher than that reported by Monchaithanaphat et al. (2024), who recorded 2.60 individuals/km² in Khao Yai National Park during the non-breeding season. These findings indicate a significant population increase of GH, RNH, and TBH over the past 15 years, while the sharp decline of WH may suggest population movement or habitat-related factors requiring further investigation. However, WH is a migratory species and not a permanent resident of the HKKWS (Anggraini et al., 2000). It is most abundant in montane evergreen and dry evergreen forests during the non-breeding season, moving to higher elevations to forage in the canopy of large trees (IUCN, 2025). Thus, the population level of the WH in this area remains uncertain because no nesting records or hornbill carcasses have been documented. The absence of such evidence not only limits reliable population estimates but also hinders the evaluation of post-breeding survival and flocking behavior, which are crucial for understanding population dynamics.

RNH is generally sedentary and territorial (Tifong et al., 2007), though seasonal movements to locate patchily distributed fruit resources have been documented. In this study, RNH was observed above 500 mean sea level, consistent with reports that streams in mixed deciduous forests significantly influence its density (Nepal, 2020; Thailand Hornbill Research Foundation, 2024a). This study showed that

RNH densities were highest in mixed deciduous forests, followed by dry evergreen and montane forests. This pattern suggests that a mosaic of forest types provides complementary resources necessary to sustain the species (IUCN, 2025).

A comparison with Jinamoy et al. (2013), who reported 5.55 individuals/km² for RNH in Thung Yai Naresuan (East) Wildlife Sanctuary, indicates that their recorded density was lower than in the present study. This difference is likely due to detectability bias during the breeding season, when females remain sealed inside nest cavities. However, the RNH density reported here was still slightly lower than that documented by Naniwadekar and Datta (2013) in India (6.9 individuals/km²) using the line transect method.

TBH densities were greatest in montane forests, aligning with IUCN (2025), which reports the species as most abundant in dense evergreen and deciduous forests up to 1,500 m, particularly in montane evergreen habitats.

In the case of GH, the largest-bodied hornbill species in Thailand, the highest density was observed in dry evergreen forests. These forests provide moderate moisture, diverse food resources, and large *Dipterocarpus* trees suitable for nesting cavities (Sibarani et al., 2020). Conservation of this forest type is therefore critical to sustain GH populations. Compared with Pawar et al. (2018), who recorded 31 individuals/km² in India, densities in this study were considerably lower. The elevated numbers in India may reflect differences in habitat characteristics, as GH populations there occurred in landscapes adjacent to coffee plantations that are privately managed and protected from major threats such as poaching and large-scale habitat degradation.

The present findings confirm the strong preference of GH for dry evergreen forests, emphasizing the importance of prioritizing their conservation and management, particularly around the three forest protection units. These areas, being adjacent to local communities, are at higher risk of disturbance. In addition to anthropogenic pressures, climate variability poses emerging threats. Excessive rainfall may alter forest structure, reduce fruit availability, or cause nest tree collapse, while rising temperatures could affect foraging and nesting behavior. Similar climate-related influences on hornbill density have been reported in Khao Yai National Park (Naniwadekar et al., 2020; Monchaithanaphat et al., 2024; Wijerathne et al., 2024).

In this study, GH densities were the highest in the dry evergreen forests around Khao Nam Yen, suggesting that food availability and stable climatic conditions in this habitat are critical for sustaining GH populations. Protecting and managing this forest type is thus essential, not only to safeguard key ecological resources but also to enhance the resilience of hornbill populations to the impacts of climate change, thereby ensuring their long-term persistence in the region. Hornbill densities are strongly influenced by food availability, anthropogenic disturbance, and breeding site conditions (Pradhan et al., 2024). Monitoring populations over the long term is therefore essential for detecting changes driven by these factors and for guiding effective conservation strategies (Pawar et al., 2021).

In the case of environmental factors, the distance to streams showed a positive but non-significant effect on RNH density. Streams remain crucial habitats because they provide both foraging opportunities and water for hydration (Saputra, 2024). The proximity of RNH to streams enhances their access to food and other essential resources (Nepal, 2020; Thailand Hornbill Research Foundation, 2024a). Reflecting these ecological benefits, the highest RNH density was recorded in the Khao Nam Yen region, which offers abundant food, a favorable climate, and suitable elevation, creating optimal conditions for the species. The RNH is also found in Mae Wong National Park, Umphang Wildlife Sanctuary (BirdLife International, 2020), and Thung Yai Naresuan Wildlife Sanctuary (Jinamoy et al., 2014). Therefore, it is a species that is specific to high mountain areas covered with mountain forests, as well as countries in the Himalayan Mountain range, such as Nepal, Bhutan, southern China, and northern Burma (Kemp and Kirwan, 2020).

Elevation negatively impacts RNH density, likely average temperatures. Thus, elevation affects RNH density, particularly in challenging regions, as Dahal et al. (2023) reported that the annual mean temperature has a significant influence on the model, followed by elevation, and the least by slope RNH in Bhutan. This suggests that high temperatures may affect foraging and nesting behaviors critical for population sustainability (Monchaithanaphat et al., 2024; Wijerathne et al., 2024).

The analysis included variables such as elevation, slope, distance to streams, canopy height, NDVI, and forest types. The lack of significant relationships suggests that these general habitat

variables may not sufficiently represent the ecological requirements critical to hornbill occurrence. Hornbills depend on specialized resources, particularly suitable nesting cavities and fruiting trees such as those of the *Ficus* genus (Pawar et al., 2021), which were not directly captured by the variables used in this study. This highlights the need for future analyses to incorporate more species-specific ecological factors.

For WH, higher densities were associated with steeper slopes, which can be attributed to several ecological and anthropogenic factors. Steep slopes generally experience reduced human disturbance, provide tall and mature trees for roosting, and support a greater abundance of fruiting trees, thereby offering diverse food sources (Hadiprakarsa and Kinnaird, 2004; Kitamura, 2011; Cheng et al., 2022). This finding is consistent with those from Khao Yai National Park, where hornbills prefer habitats characterized by minimal human activity and abundant food resources (Monchaithanaphat et al., 2024). Additionally, steep slopes often act as natural barriers that protect habitats from anthropogenic threats such as logging and hunting (Cheng et al., 2022). BirdLife International (2018) further noted that during the nonbreeding season, WH tend to move uphill to forage in tree canopies, reinforcing the ecological importance of sloped habitats.

This study has certain limitations, particularly the potential bias introduced by relying on acoustic detections for estimating hornbill densities. Although call-based identification may reduce accuracy, it provides a practical means of achieving the recommended minimum of 40 detections necessary for reliable point transect analysis. To address this issue, if possible, future research should compare density estimates derived from visual encounters with those obtained from acoustic detections to evaluate possible discrepancies. Continued long-term monitoring will also be essential to improve accuracy, enhance ecological understanding, and guide effective conservation planning for hornbills in this landscape. At the habitat level, the study highlights that dry evergreen, montane evergreen, and mixed deciduous forests, when spatially connected across the landscape, serve as critical habitats supporting different hornbill species according to their ecological requirements. Effective management to minimize disturbance in these forests is therefore crucial. In particular, the preservation of large trees is fundamental, as they provide nesting cavities, food sources, and communal roosting sites, which represent key limiting resources for hornbill populations. Most hornbill nesting cavities are found in large Dipterocarpus trees (Poonswad, 1995; Poonswad et al., 2013), underscoring the need to maintain these keystone structures to secure the long-term viability of hornbill populations.

5. CONCLUSION

This study found higher densities of GH, RNH, and TBH but lower densities of WH than those reported in the literature. Factors affecting the hornbill density include (1) elevation and slope, (2) stream, (3) montane forest, (4) precipitation, (5) Normalized Difference Vegetation Index, (6) temperature, and (7) canopy height, though these vary by species. For GH, montane forest, temperature, and precipitation are important, while elevation and temperature impact RNH, and slope significantly affects WH. Based on the analyzed hornbill densities across various forest types, the report emphasizes the preservation of large, continuous forest environments, particularly in these high mountain ranges, which are crucial for maintaining the diversity of hornbill species. Controlling human disturbances over the long term is essential for ongoing conservation efforts.

ACKNOWLEDGEMENTS

This study was funded by the Wildlife Conservation Society (WCS) Thailand to support field surveys. We extend our gratitude to the Department of National Parks, Wildlife, and Plant Conservation for granting access to the study area, facilitating our hornbill population survey, and providing crucial data for the factors analyzed in this study. We also thank the head of the Huai Kha Khaeng Wildlife Sanctuary and his staff for their support of the field research team.

AUTHOR CONTRIBUTIONS

Experimental run and Data Collection: Fueakong T; Pattanavibool A; Jornburom P; Waitanyakarn K; Saisamorn A, Neepai P; Methodology: Suksavate W; Jornburom P; Fueakong T; Validation: Jornburom P; Pattanavibool A, Sukmasuang R; Supervision and Writing Original Draft Preparation: Sukmasuang R; Formal Analysis: Suksavate W; Jornburom P, Fueakong T; Data Curation: Fueakong T, Visualization: Sukmasuang R, Writing-Review and Editing: Sukmasuang R.

DECLARATION OF CONFLICT OF INTEREST

The authors have no conflict of interest to declare.

REFERENCES

Anggraini K, Kinnaird M, O'Brien T. The effects of fruit availability and habitat disturbance on an assemblage of

Sumatran hornbills. Bird Conservation International 2000; 10(3):189-202.

Annorbah NND, Collar NJ, Marsden SJ. Trade and habitat change virtually eliminate the Grey Parrot *Psittacus erithacus* from Ghana. International Journal of Avian Science 2016; 158(1):82-91.

Ardiantiono A, Karyadi, Isa M, Hasibuan AK, Kusara I, Arwin, et al. Hornbill density estimates and fruit availability in a lowland tropical rainforest site of Leuser Landscape, Indonesia: preliminary data towards long-term monitoring. Hornbill Natural History and Conservation 2020;1(1):2-11.

BirdLife International. *Aceros nipalensis*. The IUCN Red List of Threatened Species 2020: e.T22682510A176267243 [Internet]. 2020 [cited 2025 Sep 22]. Available from: https://www.iucnredlist.org/species/22682510/176267243.

BirdLife International. *Rhyticeros undulatus*. The IUCN Red List of Threatened Species 2018: e.T22682528A132400385 [Internet]. 2018 [cited 2025 Sep 22]. Available from: https://www.iucnredlist.org/species/22682528/132400385.

Callaghan CT, Santini L, Spake R, Bowler DE. Population abundance estimates in conservation and biodiversity research. Trends in Ecology and Evolution 2024;39(6):515-23.

Chaitanya R, Naniwadekar R, Meiri S. Why did the hornbill not cross the river? Upland habitats rather than a physical barrier limit the distribution of the Brown Hornbill. Journal of Biogeography 2024;51(11):2156-69.

Chandler R. Distance Sampling Analysis in Unmarked [Internet]. 2020 [cited 2025 Jan 5]. Available from: https://cran.r-project.org/web/packages/unmarked/vignettes/distsamp.html.

Cheng Y, Wen Z, He X, Dong Z, Zhangshang M, Li D, et al. Ecological traits affect the seasonal migration patterns of breeding birds along a subtropical altitudinal gradient. Avian Research 2022;13:Article No. 100066.

Cook M, Schott JR, Mandel J, Raqueno N. Development of an operational calibration methodology for the land sat thermal data archive and initial testing of the atmospheric compensation component of a land surface temperature (LST) product from the archive. Remote Sensing 2014;6(11):11244-66.

Dahal D, Nepal A, Rai CM, Sapkota S. Understanding the impact of climate change on the habitat of the rufous-necked hornbill (*Aceros nipalensis*) (Hodgson, 1829) using MaxEnt modeling in Bhutan. Ornithology Research 2023;31:182-92.

Datta A, Rawat GS. Nest-site selection and nesting success of three hornbill species in Arunachal Pradesh, north-east India: Great Hornbill *Buceros bicornis*, Wreathed Hornbill *Aceros undulatus*, and Oriental Pied Hornbill *Anthracoceros albirostris*. Bird Conservation International 2004;14:35-92.

Department of National Parks, Wildlife and Plant Conservation (DNP). Huai Kha Khaeng Wildlife Sanctuary [Internet]. 2024 [cited 2024 Dec 6]. Available from: www.dnp.go.th.

Department of Water Resources (DWR). National maps [Internet]. 2024 [cited 2024 Nov 8]. Available from: www.opendata.onde.go.th/en/dataset/9-national-maps.

Earth Resources Observation and Science (EROS) Center. USGS EROS Archive - Digital Elevation - Shuttle Radar Topography Mission (SRTM) 1 Arc-Second Global [Internet]. 2018 [cited 2024 Nov 10]. Available from: https://usgs.gov/centers/eros/science/usgs-eros-archive-digital-elevation-shuttle-radar-topography-mission-srtm-1.

Farr TG, Rosen PA, Caro E, Crippen R, Duren R, Hensley S, et al. The Shuttle radar topography mission. Reviews of Geophysics 2007;45(2):Article No. 2005RG00018.

Funk C, Peterson P, Landsfeld M, Pedreros D, Verdin J, Shukla S, et al. The climate hazards infrared precipitation with stations: A new environmental record for monitoring extremes. Scientific Data 2015;2:Article No. 150066.

GRASS Development Team. r.grow - Generates a raster map layer with contiguous areas grown by one cell [Internet]. 2024 [cited 2024 Oct 20]. Available from: https://grass.osgeo.org/grass-stable/manuals/r.grow.html.

Hadiprakarsa YY, Kinnaird MF. Foraging characteristics of an assemblage of four Sumatran hornbill species. Bird Conservation International 2004;14(1):53-62.

International Union for Conservation of Nature (IUCN). The IUCN Red List of threatened species. Version 2025-1 [Internet]. 2025 [cited 2025 Jan 20]. Available from: https://iucnredlist.org.

International Union for Conservation of Nature (IUCN) Hornbill Specialist Group. Hornbills of the world [Internet]. 2025 [cited 2025 Sep 22]. Available from: https://iucnhornbills.org/hornbills-of-the-world/.

Jinamoy S, Poonswad P, Pattanavibool A, Chimchome V, Thongsikem S. Estimating density of rufous-necked hornbill (*Aceros nipalensis*) using distance sampling in Thung Yai Naresuan (East) Wildlife Sanctuary. Journal of Wildlife in Thailand 2013;20(1):1-14 (in Thai).

Jinamoy S, Trisurat Y, Pattanavibool A, Pisdamkham C, Thongsikem S, Veerasamphan V, et al. Predictive distribution modelling for rufous-necked hornbill *Aceros nipalensis* (Hodgson, 1829) in the core area of the Western Forest Complex, Thailand. Raffles Bulletin of Zoology 2014;62:12-20.

Jornburom P, Chimchome V, Pattnavibool A, Poonswad P. Density estimation of hornbills in Huai Kha Khaeng Wildlife Sanctuary, Uthai Thani Province. Thai Journal of Forestry 2010;29(1):1-11 (in Thai).

Kellner KF, Smith AD, Royle JA, Kéry M, Belant JL, Chandler RB. The unmarked R package: Twelve years of advances in occurrence and abundance modelling in ecology. Methods in Ecology and Evolution 2023;14(6):1408-15.

Kemp AC, Kirwan GM. Rufous-necked Hornbill (*Aceros nipalensis*), version 1.0. In birds of the world, Cornell Lab of Ornithology, Ithaca, NY, USA [Internet]. 2020 [cited 2025 Sep 25]. Available from: https://birdsoftheworld.org/bow/species/runhor1/1.0/introduction.

Kitamura S. Frugivory and seed dispersal by hornbills (Bucerotidae) in tropical forests. Acta Oecologica 2011; 37(6):531-41.

Marthy W, Clough Y, Tscharntke T. Assessing the biodiversity value of degraded lowland forest in Sumatra, Indonesia. Kukila 2016;19:1-20.

Mohd-Azlan J, Pengiran P, Maiwald MJ, Chas NBJ, Robert LA, Noske RA. Diversity and relative abundance of hornbills in selectively-logged production forests in Central Sarawak, Malaysian Borneo. Kukila 2023;24(1):1-10.

Monchaithanaphat N, Trisurat Y, Chimchome V. Non-breeding season population density of hornbills in the core area of Khao Yai National Park, Thailand. Hornbill Natural History and Conservation 2024;5:1-14.

Mynott HI, Lee DC, Santillan RA, Schwarz CJ, Tacud B, Fernandez AD, et al. Population assessment and habitat associations of the Visayan Hornbill (*Penelopides panini*) in

Northwest Panay, Philippines. Avian Research 2021; 12:Article No. 67.

Naniwadekar R, Datta A. Spatial and temporal variation in hornbill densities in Namdapha Tiger Reserve, Arunachal Pradesh, North-East India. Tropical Conservation Science 2013;6(6):734-48.

Naniwadekar R, Ghuman S, Gopal A, Page N, Ramachandran V. Characteristics of Narcondam Hornbill *Rhyticeros narcondami* nest trees. Hornbill Natural History and Conservation 2020;1(2):1-9.

Nepal TK. Distribution and threats of Rufous-necked Hornbill (*Aceros nipalensis*) in Bhutan. International Journal of Science and Research 2020;9(11):797-800.

Ouithavon K, Poonswad P, Bhumbhakpan N, Laohajinda V. A comparative study of the feeding ecology of two sympatric hornbill species (Aves: Bucerotidae) during their breeding season in Huai Kha Khaeng Wildlife Sanctuary, Thailand. Proceedings of the Third Hornbill Workshop, The Ecology of Hornbills: Reproduction and Populations; 2005; Mahidol University, Bangkok: Thailand; 2005.

Paguntalan LJ, Reintar ART, Jakosalem PGC. Population density of Visayan Tarictic hornbill *Penelopides panini* on Negros Island, Philippines. Journal of Asian Ornithology 2021; 37:93-8.

Patel B, Sivaraman S, Balakrishnan P. Nesting ecology of Malabar Grey Hornbill *Ocyceros griseus* in a mosaic landscape in the Southern Western Ghats, India. Proceedings of the Zoological Society 2022;75:337-48.

Pawar P, Naniwadekar R, Raman T, Mudappa D. Seasonal variation in hornbill densities in coffee plantations in the Anaimalai Hills, Western Ghats, India. Sarawak Museum [Internet]. 2018 [cited 2024 Oct 12]. Available from: https://museum.sarawak.gov.my/web/subpage/webpage_view/314.

Pawar PY, Mudappa D, Raman TRS. Hornbill abundance and breeding incidence in relation to habitat modification and fig fruit availability. IBIS-International Journal of Avian Science 2021;163(2):473-85.

Poonswad P. Nest site characteristics of four sympatric species of hornbills in Khao Yai National Park, Thailand. IBIS-International Journal of Avian Science 1995;137(2):183-91.

Poonswad P, Chimchome V, Mahannop N, Mudsri S. Conservation of hornbills in Thailand. In: Sodhi NS, Gibson L, Raven PH, editors. Conservation Biology: Voices from the Tropics. 1st ed. John Wiley and Sons, Ltd.; 2013. p. 157-66.

Poonswad P, Kemp AC. Manual to the Conservation of Asian Hornbills. Bangkok, Thailand: Sirvatana Interprint; 1993.

Pradhan K, Datta A, Ganguly D, Naniwadekar R, Mahato S, Dukpa K, et al. Hornbill abundance and habitat relationships in a human-impacted protected area in the Indian Eastern Himalaya. Global Ecology and Conservation 2024;5:e02868.

QGIS Project. QGIS Desktop 3.28 User guide [Internet]. 2024 [cited 2024 Jun 20]. Available from: https://docs.qgis.org/3.28/pdf/en/QGIS-3.28-DesktopUserGuide-en.pdf.

Ridho M. Analyzing land surface temperature (LST) with Landsat 8 data in Google Earth Engine [Internet]. 2023 [cited 2025 Jan 5]. Available from: https://medium.com/@ridhomuh002/analyzing-land-surface-temperature-lst-with-landsat-8-data-in-google-earth-engine-f4dd7ca28e70.

Royal Forest Department (RFD). Forest type database [Internet]. 2018 [cited 2024 Feb 17]. Available from: https://data.forest.go.th/.

RStudio Builds. RStudio desktop [Internet]. 2024 [cited 2024 Dec 15]. Available from: http://dailies.rstudio.com/version/2024.09.1+394/.

Saisamorn A, Duangchantrasiri S, Sornsa M, Suksavate W, Pattanavibool A, Duengkae P. Recovery of globally threatened ungulate species in Huai Kha Khaeng Wildlife Sanctuary, Thailand. Global Ecology and Conservation 2024;53:e03012.

Saputra RA. Prediction of bird habitat suitability: Determination and use of environmental parameters. Journal of Geographical Sciences and Education 2024;2(1):1-8.

Sibarani MC, Utoyo L, Pratama RD, Danus MA, Sudrajat R, Surahmat F, et al. Long-term monitoring of nesting behavior and nesting habitat of four sympatric hornbill species in a Sumatran lowland tropical rainforest of Bukit Barisan Selatan National Park. Hornbill Natural History and Conservation 2020;1(1):17-29.

Setiawana T, Prasetyob LB, Mulyanib YA, Jarulisc. The habitat suitability modelling of Rhinoceros Hornbills (*Buceros rhinoceros*) in Java Island, Indonesia. Journal of Natural Resources and Environmental Management 2023;14(2): Article No. 253.

Sriprasertsil V, Da-ouli N, Chootongkhum C, Strange BC, Khamcha D, Jinamoy S, et al. Changes in endangered hornbill populations over space and time and potential ecological impacts in peninsular Thailand. Global Ecology and Conservation 2024;53:e03006.

Thailand Hornbill Research Foundation. Hornbill species: Rufous-necked Hornbill [Internet]. 2024a [cited 2024 Feb 17]. Available from: www.hornbill.or.th/about-hornbills/hornbill-species/rufous-necked-hornbill.

Thailand Hornbill Research Foundation. Hornbill species [Internet]. 2024b [cited 2024 Oct 10]. Available from: http://hornbill.or.th.

Tifong J, Chimchome V, Poonswad P, Pattnavibool A. Home range and habitat use of rufous-necked hornbill (*Aceros nipalensis*) by radio tracking in Huai Kha Khaeng Wildlife Sanctuary, Uthai Thani Province. Thailand Journal of Forestry 2007;26:28-39 (in Thai).

Tiwari G, Pandey P, Kaul R, Lee H, Singh R. Comparison of point and roadside transect methods to evaluate the abundance and richness of diurnal raptors in the arid region of Rajasthan. Public Library of Science ONE 2021;16(12):e0259805.

Tolan J, Yang H-I, Nosarzewski B, Couairon G, Vo H, Brandt J, et al. Sub-meter resolution canopy height maps using self-supervised learning and a vision transformer trained on Aerial and GEDI Lidar [Internet]. 2023 [cited 2024 Feb 9]. Available from: http://arxiv.org/pdf/2304.07213.

Trisurat Y. GIS Database and Its Applications for Ecosystem Management. Bangkok, Thailand: Western Forest Complex, Ecosystem Management Project (WEFCOM), Kasetsart University; 2004.

Trisurat Y, Chimchome V, Pattanavibool A, Jinamoy S, Thongaree S, Kanchanasakha B, et al. An assessment of the distribution and conservation status of hornbill species in Thailand. Oryx 2013;47(3):441-50.

US Geological Survey (USGS). CHIRPS, version 2.0 Final [Internet]. 2024 [cited 2024 Feb 9]. Available from: https://www.chc.ucsb.edu/data/chirps.

US Geological Survey (USGS). USGS Landsat 9 level 2, collection 2, tier 1 [Internet]. 2025 [cited 2025 Feb 20]. Available from: https://developers.google.com/earth-engine/datasets/catalog/LANDSAT_LC09_C02_T1_L2.

Valderrama-Zafra JM, Rubio-Paramio MA, Garcia-Molina DF, Mercado-Colmenero JM, Oya A, Carrasco R, et al. Impact of topographic factors on animal field pathings: Analysis and prediction of deer movement patterns. Ecological Informatics 2024;80:Article No. 102487.

Wijerathne I, Wickramasinghe S. Behavioral pattern of endemic Sri Lanka Grey Hornbill (*Ocyceros gingalensis*) within the breeding and nonbreeding seasons. International Journal of Biodiversity 2018;2018:Article No. 509785.

Wijerathne IL, Vidanapathirana DR, Panduwawala PP, Nirath T, Kirambakanda K, Sarathchandra C, et al. Distribution status and influence of climate change on patterns of distribution of hornbills in Sri Lanka. Global Ecology and Conservation 2024;51:e02903.

INSTRUCTION FOR AUTHORS

Publication and Peer-reviewing processes of Environment and Natural Resources Journal

Environment and Natural Resources Journal is a peer reviewed and open access journal that is published in six issues per year. Manuscripts should be submitted online at https://ph02.tci-thaijo.org/index.php/ennrj/about/submissions by registering and logging into this website. Submitted manuscripts should not have been published previously, nor be under consideration for publication elsewhere (except conference proceedings papers). A guide for authors and relevant information for the submission of manuscripts are provided in this section and also online at: https://ph02.tci-thaijo.org/index.php/ennrj/author. All manuscripts are refereed through a **single-blind peer-review** process.

Submitted manuscripts are reviewed by outside experts or editorial board members of **Environment and Natural Resources Journal**. This journal uses double-blind review, which means that both the reviewer and author identities are concealed from the reviewers, and vice versa, throughout the review process. Steps in the process are as follows:

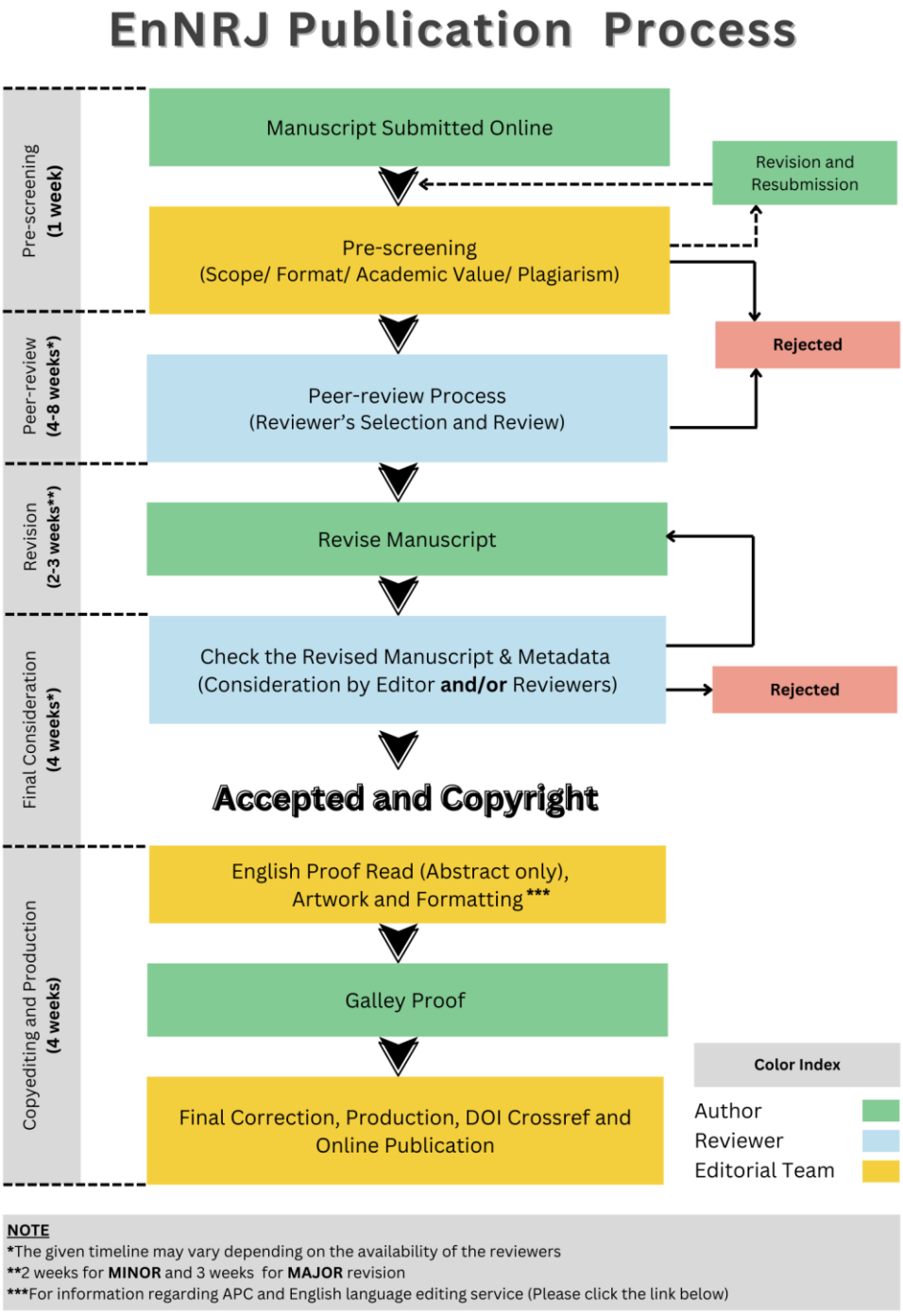

NOTE
*The given timeline may vary depending on the availability of the reviewers
2 weeks for **MINOR and 3 weeks for **MAJOR** revision
***For information regarding APC and English language editing service (Please click the link below)

The Environment and Natural Resources Journal (EnNRJ) considers and accepts two types of articles for publication as follows:

- *Original Research Article*: This is the most common type of article. It showcases new, innovative or unique findings surrounding a focused research question. Manuscripts should not exceed 4,000 words (excluding references) - see more details in the Preparation of Manuscript section below.
- *Review Article (by invitation)*: This type of article focuses on the in-depth critical review of a special aspect of an environmental-related research question, issue, or topic. It provides a synthesis and critical evaluation of the state of the knowledge of the subject. Manuscripts should not exceed 6,000 words (excluding references).

Submission of Manuscript

The items that the author needs to upload for the submission are as follows:

Manuscript: The manuscript must be submitted as a Microsoft Word file (.doc or .docx). Refer to the **Preparation of Manuscript** section below for detailed formatting instructions.

Cover Letter: The letter should address the Editor and include the following: a statement declaring that the author's paper has not been previously published and is not currently under consideration by another journal.

- a brief description of the research the author reports in the paper, including why the findings are important and why the journal readers should be interested
- contact information of the author and any co-authors
- a confirmation that the author has no competing interests to disclose

Graphical Abstract (Optional): The author is encouraged to submit a graphical abstract with the manuscript. The graphical abstract depicts the research and findings with visuals. It attracts more potential readers as it lets them understand the overall picture of the article within a few glances. Note that the graphical abstract must be original and unpublished artwork. It should be a high-quality illustration or diagram in any of the following formats: TIFF, PDF, JPEG, or PNG. The minimum required size is 750 × 750 pixels (height × width). The size should be of high quality (600 dpi or larger) in order to reproduce well.

Reviewers Suggestion (mandatory): Please provide the names of three potential reviewers, with information about their affiliations as well as their email addresses. The recommended reviewers should not have any conflict of interest with the authors. Each reviewer must represent a different affiliation and not have the same nationality as the author. Please note that the editorial board retains the sole right to decide whether or not the recommended reviewers will be selected.

Declaration of Competing Interest: The author must include a declaration of competing interest form during submission. If there is no conflict of interest, please state, "The authors declare no conflict of interest." Otherwise, authors should declare all interests to avoid inappropriate influence or bias in their published work. Examples of potential conflicts of interest in research projects include but are not limited to financial interests (such as employment, consultancies, grants, and other funding) and non-financial interests (such as personal or professional relationships, affiliations, and personal beliefs).

CrediT (Contributor Roles Taxonomy) Author Statement or Author Contributions: For research articles with several authors, we require corresponding authors to provide co-author contributions to the manuscript using the relevant CRediT roles. CRediT is a taxonomy that shows the contributions of the author and co-author(s), reduces possible authorship disputes, and facilitates collaboration among research team members. The CRediT taxonomy includes 14 different roles describing each contributor's specific contribution to the scholarly output.

The roles are: Conceptualization; Data curation; Formal analysis; Funding acquisition; Investigation; Methodology; Project administration; Resources; Software; Supervision; Validation; Visualization; Roles/Writing – original draft; and Writing – review & editing.

Note that authors may have contributed through multiple roles, and those who contributed to the research work but do not qualify for authorship should be listed in the acknowledgments.

An example of a CRediT author statement is given below:
"Conceptualization, X.X. and Y.Y.; Methodology, X.X.; Software, X.X.; Validation, X.X., Y.Y. and Z.Z.; Formal Analysis, X.X.; Investigation, X.X.; Resources, X.X.; Data Curation, X.X.; Writing – Original Draft Preparation, X.X.; Writing – Review & Editing, X.X.; Visualization, X.X.; Supervision, X.X.; Project Administration, X.X.; Funding Acquisition, Y.Y."

Artwork for the Journal Cover: The author may provide and propose a piece of artwork (with a description) for the journal issue cover. This is an excellent opportunity for the author to promote their article, if accepted, on the cover of a published issue. Alternatively, the editorial team may invite the author to submit a piece of artwork for the cover after their manuscript has been accepted for publication. The final cover artwork selection will be made by the editorial team.

Final Author Checks: In addition to the basic requirements, the author should review this checklist before submitting their manuscript. Following it ensures the manuscript is complete and in accordance with all standards.

Preparation of Manuscript

Format and Style

The manuscript should be prepared strictly as per the guidelines given below. Any manuscript with an incorrect format will be returned, and the corresponding author may have to resubmit a new manuscript with the correct format.

Overall Format

The manuscript must be submitted as a Microsoft Word file (.doc or .docx). The formatting should be as follows:

- File format - .doc or .docx
- Page size - A4
- Page orientation - portrait (some landscape pages are accepted if necessary)
- Page margin - 2.54 cm (left and the right margin) and 1.9 cm (bottom and the top margin)
- Page number (bottom of the page)
- Line number
- Line spacing - 1.5
- Font - 12 point, Times New Roman (unless stated otherwise)

Unit - The use of abbreviation must follow the International System of Units (SI Unit) format.

- The unit separator is a virgule (/) and not a negative coefficient: 10 mg/L not 10 mgL^{-1}
- Liter always has a capital letter: mg/L

Equations

- Insert equations using the dedicated tool in Microsoft Word. Do not use pictures or text boxes.
- Equations that are referenced in the text should be identified by parenthetical numbers, such as (1), and should be referred to in the manuscript as “Equation 1”.

Inclusive Language: The language used in the manuscript acknowledges diversity, promotes equal opportunity, respects all people, and is sensitive to all aspects of differences. The manuscript content should not make assumptions about the beliefs or commitments of any individual. It should not imply superiority regarding age, race, ethnicity, culture, gender, sexual orientation, disability, or health conditions. Moreover, the manuscript must be free from bias, stereotypes, slang, and derogatory terms.

Reference Style: Vancouver style should be used for the reference list and in-text citations throughout the manuscript. Please follow the format of the sample references and citations, as shown in the Body Text Sections portion below.

Front Page

Title: The title of the manuscript should be concise and not longer than necessary. The title should be bold, 12-point size, and Times New Roman. The first letter of major words should be capitalized (as in standard title case).

Author(s) Name: The first and last names of all authors must be given, in bold, Times New Roman, and 12-point font.

Affiliation of All Author(s): Affiliation(s) must be in italics, Times New Roman, and 11-point font. Specify the Department/School/Faculty, University, City/Province/or State, and Country of each affiliation. Do not include positions or fellowships, or postal zip codes.
Each affiliation should be indicated with superscript Arabic numerals. The Arabic numeral(s) should appear immediately after the author’s name, and represent the respective affiliation(s).

Corresponding Author: One author should be responsible for correspondence, and their name must be identified in the author list using an asterisk (*).

- All correspondence with the journal, including article submission and status updates, must be handled by the corresponding author.

- The online submission and all associated processes should be operated by the corresponding author.

*Corresponding author: followed by the corresponding author's email address.

Example:

Papitchaya Chookaew[1], Apiradee Sukmilin[2], and Chalor Jarusutthirak[1*]
[1]Department of Environmental Technology and Management, Faculty of Environment, Kasetsart University, Bangkok, Thailand
[2]Environmental Science and Technology Program, Faculty of Science and Technology, Phranakhon Rajabhat University, Bangkok, Thailand
**Corresponding author: abcxx@xx.ac.th*

Abstract Page

Abstract: The abstract should include the significant findings paired with relevant data. A good abstract is presented in one paragraph and is limited to 250 words. Do not include a table, figure, or references.
Keywords - Up to six keywords are allowed, and they should adequately index the subject matter.

Highlights: Please include 3-5 concise sentences describing innovative methods and the findings of the study. Each sentence should contain at most 85 characters (not words).

Body Text Sections
The main body text of the manuscript normally includes the following sections: 1. Introduction 2. Methodology 3. Results and Discussion 4. Conclusions 5. Acknowledgments 6. Author Contributions 7. Declaration of Competing Interests 8. References

Introduction should include the aims of the study. It should be as concise as possible, with no subheadings. The significance of the problem and the essential background should also be given.

Methodology is sufficiently detailed so that the experiments can be reproduced. The techniques and methods adopted should be supported with standard references.
There should be no more than three levels of headings in the **Methodology and Results and Discussion** sections. Main headings are in bold letters, second-level headings are in bold and italic letters, and third-level headings are in normal letters.

Here is an example:

2. Methodology
2.1 Sub-heading
2.1.1 Sub-sub-heading

Results presents the key findings in figures and tables with descriptive explanations in the text.

Tables
- Tables - look best if all the cells are not bordered; place horizontal borders only under the legend, the column headings, and the bottom.

Figures
- Figures - should be submitted in color. The author must ensure that the figures are clear and understandable. Regardless of the application used to create them, when electronic artworks are finalized, please 'save as' or convert the images to TIFF or JPG and send them separately to EnNRJ. Images require a resolution of at least 600 dpi (dots per inch) for publication. The labels of the figures and tables must be Times New Roman, and their size should be adjusted to fit the figures without borderlines.
- Graph - The font style in all graphs must be Times New Roman, 9-10 size, and black color. Please avoid bold formatting, and set the border width of the graphs to 0.75 pt.

- Graph from MS Excel: Please attach an editable graph from MS Excel within your manuscript. Then please also submit the full MS Excel file used to prepare the graph as a separate document. This helps us customize our layout for aesthetic beauty.
- Graph from another program: Feel free to use whichever program best suits your needs. But as noted above, when your artwork is finalized, please convert the image to TIFF or JPG and send them separately Again, images should be at least 600 dpi. Do not directly cut and paste.

***All figures and tables should be embedded in the text, and also mentioned in the text.**

Discussion shows the interpretation of findings with supporting theory and comparisons to other studies. The Results and Discussion sections can be either separated, or combined. If combined, the section should be named Results and Discussion. **Conclusions** should include a summary of the key findings and take-home messages. This should not be too long, or repetitive but this section is absolutely necessary so that the argument of the manuscript is not uncertain or left unfinished.

Acknowledgments should include the names of those who contributed substantially to the work, but do not fulfill the requirements for authorship. It should also include any sponsor or funding agency that supported the work.

Author Contributions: For research articles with several authors, we require corresponding author contributions listed using the relevant CRediT roles. This should be done by the author responsible for correspondence.

Declaration of Competing Interest: The author must include a declaration of competing interest form during submission. If there is no conflict of interest, please state, "The authors declare no conflict of interest." Otherwise, authors should declare all interests to avoid inappropriate influence or bias in their published work.

References should be cited in the text by the surname of the author(s) and the year. This journal uses the author-date method of citation. The author's last name and date of publication are inserted in the text in the appropriate place. If there are more than two authors, “et al.” must be added after the first author’s name. Examples: (Frits, 1976; Pandey and Shukla, 2003; Kungsuwas et al., 1996). If the author’s name is part of the sentence, only the date is placed in parentheses: “Frits (1976) argued that . . .”

Please ensure that every reference cited in the text is also in the reference list (and vice versa).

In the list at the end of the manuscript, complete references must be arranged alphabetically by the surnames of the first author in each citation. Examples are given below.

Book

Tyree MT, Zimmermann MH. Xylem Structure and the Ascent of Sap. Heidelberg, Germany: Springer; 2002.

Chapter in a book

Kungsuwan A, Ittipong B, Chandrkrachang S. Preservative effect of chitosan on fish products. In: Steven WF, Rao MS, Chandrkachang S, editors. Chitin and Chitosan: Environmental and Friendly and Versatile Biomaterials. Bangkok: Asian Institute of Technology; 1996. p. 193-9.

Journal article

Muenmee S, Chiemchaisri W, Chiemchaisri C. Microbial consortium involving biological methane oxidation in relation to the biodegradation of waste plastics in a solid waste disposal open dump site. International Biodeterioration and Biodegradation 2015;102(3):172-81.

Journal article with Article Number

Sah D. Concentration, source apportionment and human health risk assessment of elements in $PM_{2.5}$ at Agra, India. Urban Climate 2023;49:Article No. 101477.

Non-English articles

Suebsuk P, Pongnumkul A, Leartsudkanung D, Sareewiwatthana P. Predicting factors of lung function among motorcycle taxi drivers in the Bangkok metropolitan area. Journal of Public Health 2014;44(1):79-92 (in Thai).

Article in press

Dhiman V, Kumar A. Biomass and carbon stock estimation through remote sensing and field methods of subtropical Himalayan Forest under threat due to developmental activities. Environment and Natural Resources Journal 2024. DOI: 10.32526/ennrj/22/20240018.

Published in conference proceedings

Wiwattanakantang P, To-im J. Tourist satisfaction on sustainable tourism development, Amphawa floating market Samut Songkhram, Thailand. Proceedings of the 1st Environment and Natural Resources International Conference; 2014 Nov 6-7; The Sukosol hotel, Bangkok: Thailand; 2014.

Ph.D./Master thesis

Shrestha MK. Relative Ungulate Abundance in a Fragmented Landscape: Implications for Tiger Conservation [dissertation]. Saint Paul, University of Minnesota; 2004.

Website

Orzel C. Wind and temperature: why doesn't windy equal hot? [Internet]. 2010 [cited 2016 Jun 20]. Available from: http://scienceblogs.com/principles/2010/08/17/wind-and-temperature-why-doesn/.

Report organization

Intergovernmental Panel on Climate Change (IPCC). IPCC Guidelines for National Greenhouse Gas Inventories: Volume 1-5. Hayama, Japan: Institute for Global Environmental Strategies; 2006.

Royal Gazette

Royal Gazette. Promotion of Marine and Coastal Resources Management Act 2059. Volume 132, Part 21, Dated 26 Mar B.E. 2558. Bangkok, Thailand: Office of the Council of State; 2015a. (in Thai).

Remark

** Please be note that manuscripts should usually contain at least 15 references and some of them must be up-to-date research articles.*

** Please strictly check all references cited in text, they should be added in the list of references. Our Journal does not publish papers with incomplete citations.*

Changes to Authorship

This policy of journal concerns the addition, removal, or rearrangement of author names in the authorship of accepted manuscripts:

Before the accepted manuscript

For all submissions, that request of authorship change during review process should be made to the form below and sent to the Editorial Office of EnNRJ. Approval of the change during revision is at the discretion of the Editor-in-Chief. The form that the corresponding author must fill out includes: (a) the reason for the change in author list and (b) written confirmation from all authors who have been added, removed, or reordered need to confirm that they agree to the change by signing the form. Requests form submitted must be consented by corresponding author only.

After the accepted manuscript

The journal does not accept the change request in all of the addition, removal, or rearrangement of author names in the authorship. Only in exceptional circumstances will the Editor consider the addition, deletion or rearrangement of authors after the manuscript has been accepted.

Copyright transfer

The copyright to the published article is transferred to Environment and Natural Resources Journal (EnNRJ) which is organized by Faculty of Environment and Resource Studies, Mahidol University. The accepted article cannot be published until the Journal Editorial Officer has received the appropriate signed copyright transfer.

Online First Articles

The article will be published online after receipt of the corrected proofs. This is the official first publication citable with the Digital Object Identifier (DOI). After release of the printed version, the paper can also be cited by issue and page numbers. DOI may be used to cite and link to electronic documents. The DOI consists of a unique alpha-numeric character string which is assigned to a document by the publisher upon the initial electronic publication. The assigned DOI never changes.

Mahidol University

Wisdom of the Land

Faculty of Environment and Resource Studies, Mahidol University, Thailand
999 Phutthamonthon Sai 4 Rd, Salaya, Phutthamonthon District, Nakhon Pathom 73170
E-mail: ennrjournal@gmail.com